

Copyright

by

Harrey Jeong Shuler

2009

The Dissertation Committee for Harrey Jeong Shuler certifies that this is the approved version of the following dissertation:

**RECOVERY OF THE LOCAL GRAVITY FIELD BY
SPHERICAL REGULARIZATION WAVELETS APPROXIMATION
AND ITS NUMERICAL IMPLEMENTATION**

Committee:

Byron D. Tapley, Supervisor

Bob E. Schutz

Wallace T. Fowler

Clark R. Wilson

Don P. Chambers

**RECOVERY OF THE LOCAL GRAVITY FIELD BY
SPHERICAL REGULARIZATION WAVELETS APPROXIMATION
AND ITS NUMERICAL IMPLEMENTATION**

by

Harrey Jeong Shuler, B.S.; M.S.

Dissertation

Presented to the Faculty of the Graduate School of
The University of Texas at Austin
in Partial Fulfillment
of the Requirements
for the Degree of

Doctor of Philosophy

The University of Texas at Austin

May 2009

DEDICATION

To my husband Andrew and my son Jeremy
– the two men who complete my world

ACKNOWLEDGMENTS

I would like to express my deepest appreciation to Dr. Byron D. Tapley for his continuing support and guidance throughout my work as well as allowing me the precious research opportunities at the Center for Space Research. His insight and expertise have been invaluable in completing this dissertation while his unflagging dedication to the spectrum of research subjects has been truly inspiring.

My sincere gratitude extends to the other members of the dissertation committee: Dr. Bob E. Schutz, Dr. Wallace T. Fowler, Dr. Clark R. Wilson and Dr. Don P. Chambers for their interest in my work and valuable suggestions to improve my dissertation.

Special thanks go to my fellow student Hyo-Jin Kim, who helped me with the registration paperwork every semester while I was residing in Dallas. Further thanks are due to the staffs at the Center for Space Research.

I am also indebted to Jae-Won and Mi-Ae, my parents in Korea, and Michael and Karen, my parents-in-law, for their love and support over the years. Their unwavering confidence in me has been beyond appreciation.

My fondest thanks are reserved to my son Jeremy whose mere existence has brought such joy and contentment to my everyday life.

Last of all, my warmest gratitude goes to Andrew, my husband, for his unceasing love, support, dedication, understanding, encouragement, advice and inspiration through the long journey of my research. I truly cannot thank him enough for everything he has done for me, especially for believing in me even in my darkest hours. This work would not have been possible without him.

RECOVERY OF THE LOCAL GRAVITY FIELD BY SPHERICAL REGULARIZATION WAVELETS APPROXIMATION AND ITS NUMERICAL IMPLEMENTATION

Harrey Jeong Shuler, Ph.D.

The University of Texas at Austin, 2009

Supervisor: Byron D. Tapley

As an alternative to spherical harmonics in modeling the gravity field of the Earth, we built a multiresolution gravity model by employing spherical regularization wavelets in solving the inverse problem, *i.e.* downward propagation of the gravity signal to the Earth's surface. Scale discrete Tikhonov spherical regularization scaling function and wavelet packets were used to decompose and reconstruct the signal. We recovered the local gravity anomaly using only localized gravity measurements at the observing satellite's altitude of 300 km. When the upward continued gravity anomaly to the satellite altitude with a resolution 0.5° was used as simulated measurement inputs, our model could recover the local surface gravity anomaly at a spatial resolution of 1° with an RMS error between 1 and 10 mGal, depending on the topography of the gravity field. Our study of the effect of varying the data volume and altering the maximum degree of Legendre polynomials on the accuracy of the recovered gravity solution suggests that the short wavelength signals and the regions with high magnitude gravity gradients respond more strongly to such changes. When tested with simulated SGG measurements, *i.e.* the second order radial derivative of the gravity anomaly, at an altitude of 300 km with a 0.7° spatial resolution as input data, our model could obtain the gravity anomaly with an RMS

error of 1 ~ 7 mGal at a surface resolution of 0.7° (< 80 km). The study of the impact of measurement noise on the recovered gravity anomaly implies that the solutions from SGG measurements are less susceptible to measurement errors than those recovered from the upward continued gravity anomaly, indicating that the SGG type mission such as GOCE would be an ideal choice for implementing our model. Our simulation results demonstrate the model's potential in determining the local gravity field at a finer scale than could be achieved through spherical harmonics, *i.e.* less than 100 km, with excellent performance in edge detection.

TABLE OF CONTENTS

Chapter 1.	Introduction	1
Chapter 2.	Preliminaries	6
2.1.	Harmonic Analysis: Spherical Harmonics and Legendre Polynomials	6
2.2.	Spherical Pseudo-differential Operators	13
2.3.	Basics of Multiresolution Analysis	16
2.4.	Spherical Wavelets	21
Chapter 3.	Solving Inverse Problem by Spherical Regularization Wavelets Approximation	27
3.1.	Inverse Problem and Scale Discrete Spherical Regularization Wavelets	27
3.2.	Approximate Solution to the Inverse Problem and Tikhonov Spherical Regularization Wavelets	35
3.3.	Local Gravity Solution	44
3.4.	Choice of Regularization Parameter by Discrepancy Principle	46
3.5.	Upward Continuation	49
Chapter 4.	Numerical Aspect of Implementing the Spherical Wavelets Gravity Model	51
4.1.	Numerical Integration Schemes	51
4.2.	Numerical Implementation of the Spherical Wavelets Gravity Model	57
Chapter 5.	Simulation Result: Region I ($30.25^{\circ}\text{W} \sim 109.75^{\circ}\text{W}$ and $24.75^{\circ}\text{S} \sim 19.75^{\circ}\text{N}$)	71

5.1.	Region I	71
5.2.	Region I with Four Times the Volume of Input Data	96
5.3.	Region I with $N = 150$	102
5.4.	Region I with $N = 600$	108
Chapter 6.	Simulation Result: Region II ($160.25^{\circ}\text{E} \sim 100.25^{\circ}\text{W}$ and $24.75^{\circ}\text{S} \sim 24.75^{\circ}\text{N}$)	114
Chapter 7.	Gravity Solution for SGG Mission	131
7.1.	A Brief Review of SGG Mission	131
7.2.	Simulation Result (Region of $29.82^{\circ}\text{W} \sim 109.82^{\circ}\text{W}$ and $24.51^{\circ}\text{S} \sim 20.31^{\circ}\text{N}$)	133
Chapter 8.	Effect of Measurement Noise on the Recovered Gravity Anomaly	148
8.1.	Noise and Errors in Satellite Remote Sensing Missions	148
8.2.	By Using the Upward Propagated Gravity Anomaly.....	153
8.3.	By Using the SGG Measurements	162
Chapter 9.	Satellite Gravity Measurement Data on Ground Track	169
9.1.	Satellite Ground Track Data	169
9.2.	By Using the Upward Propagated Gravity Anomaly.....	171
9.3.	By Using the SGG Measurements	178
Chapter 10.	Conclusions and Discussion	185
	Bibliography	197
	Vita	200

Chapter 1. Introduction

For precise determination of the satellites' orbits around the Earth to support their numerous applications, it is extremely important to have an accurate model of the Earth's gravity field. In satellite geodesy, the conventional method has been the spherical harmonics approach. The traditional spherical harmonics model of the gravity potential takes the following form:

$$V(r, \lambda, \varphi) = \frac{\mu}{r} \left\{ 1 + \sum_{n=2}^N \left(\frac{R}{r} \right)^n Y_n(\varphi, \lambda) \right\} , \quad (1.1)$$

where V is the gravity potential, μ is the Earth's gravitational constant, R is the equatorial radius of the Earth, r is the satellite orbit radius from the Earth's center of mass, λ is the geocentric longitude ($0 \leq \lambda \leq 2\pi$) and φ is the geocentric latitude ($-\frac{\pi}{2} \leq \varphi \leq \frac{\pi}{2}$). $Y_n(\varphi, \lambda)$, the spherical harmonics of degree n , is defined by

$$Y_n(\varphi, \lambda) = \sum_{m=0}^n \bar{P}_n^m(\sin \varphi) \left(\bar{C}_n^m \cos m\lambda + \bar{S}_n^m \sin m\lambda \right) , \quad (1.2)$$

where $\left\{ \bar{C}_n^0, \bar{C}_n^1, \dots, \bar{C}_n^n, \bar{S}_n^1, \dots, \bar{S}_n^n \right\}$ are the normalized spherical harmonics coefficients and \bar{P}_n^m is the normalized associated Legendre function of degree n and order m .

In the spherical harmonics model, the gravity potential can be determined by estimating the spherical harmonics coefficients \bar{C}_n^m and \bar{S}_n^m from satellite observations. Increasing the degree n and the order m ensures more accurate evaluation of the gravity potential up to a certain degree, provided accurate data at sufficient resolution.

Constructing gravity models from satellite measurements using spherical harmonics, however, leads to several problems. Two of the most frequently discussed problems are the cost of evaluating V , which grows rapidly with the increasing degree and order, and the model's inadequacy in handling local problems.

For a spherical harmonics model with degree and order N , the number of operations required to evaluate V is proportional to N^2 . The estimation procedure using the satellite measurements requires the formation of correlation matrices whose size is roughly $N^2 \times N^2$, which are dense (full) because spherical harmonics coefficients are not associated with any particular spatial location, and therefore the number of operations needed to store and manipulate them grows rapidly as N increases. Since the spherical harmonics model is globally supported, it is impossible to increase resolution of the model without increasing the degree and order globally. As evaluating the gravity potential at a fine scale requires estimating the coefficients with high degree and order, spherical harmonics model incurs a huge cost to perform such an operation. In addition, it is extremely difficult, if not impossible, to adjust the spatial frequency content of a spherical harmonic expansion locally. As a result, there is a difficulty in incorporating data from different sources (*e.g.* observations obtained near the Earth's surface and those from satellites), due to the different spectral contents of the data. (Beylkin and Cramer, 2002)

Some of the aforementioned problems can be solved, however, especially for the satellite missions whose ground track covers the entire Earth almost uniformly such as the GRACE (Gravity Recovery And Climate Experiment) mission, where its covariance matrix is near diagonal instead of dense (Tapley, 2008). Moreover, the introduction of fast processors and the implementation of parallel algorithms in recent years have reduced the cost and time of the operation associated with spherical harmonics expansions to high degree and order, and thus the spherical harmonics model still remains the best tool to obtain the global gravity solution by providing very good low frequency representation of the gravity field. A recent gravity model, GGM02C from the GRACE

mission output, has recovered the global gravity field to approximately 7 mm geoid height RMS error at degree/order 70 (Tapley *et al.*, 2005).

Despite the certain achievements in the ability of the spherical harmonics model to represent the global gravity field, a number of the weaknesses, especially in treating local problems as discussed by Schneider (1997) and Beylkin and Cramer (2002), still remain:

1. A local change in the measurements affects all coefficients of the global gravity field, which makes it difficult to handle local problems.
2. Due to its global nature, the overall resolution that could be reached by the spherical harmonics model is limited by the most poorly sampled region, unable to take advantage of the regions with better measurements than others.
3. Spherical harmonics provide localization only in the frequency domain, not in the space domain.
4. Spherical harmonics show large oscillations in high degree coefficients.
5. Spherical harmonics tend to smooth the high frequency signals.

A multiresolution model of the gravity field, such as the spherical wavelets approximation, uses basis functions with localized support in both space and frequency domains and has several advantages over the spherical harmonics model in applications to local problems (Schneider 1997):

1. Local changes in the parameters produce only local changes in the model.
2. The inherent spatial localization nature of wavelets provides a strong local meaning to its coefficients.
3. High frequency signals that the spherical harmonics model cannot process can be practically handled by wavelet approaches.
4. Using the wavelets approximation, a finer scale gravity field determination can be achieved.

While spherical harmonics remains the tool of choice for applications requiring a global solution, we took the multiresolution model approach in order to overcome some of the spherical harmonics model's weaknesses in handling local problems. In this study, we aim to show that the spherical wavelets model can recover fine resolution gravity signals in the local region, using only localized measurements. As Schneider (1997) showed in his study of the inverse problems in satellite geodesy, we employed scale discrete Tikhonov spherical regularization wavelets to derive an approximate solution to the inverse problem, *i.e.* the inverse of the upward continuation of the gravity potential, which is also interpreted as a downward propagation of the gravity measurements at the satellite altitude to the Earth's surface. We also derived the mathematical formulae to provide the optimal regularization parameters as well as the upward continuation equation. Based on these equations and formulae we could build several numerical algorithms to test and evaluate our spherical wavelets model.

In order to test our gravity model we first generated the gravity anomaly field on the Earth's surface at a 0.5° resolution assuming a spherical Earth, based on GGM02 and EGM96 gravity models. We then simulated the gravity field at the satellite altitude of 300 km by upward continuation of the surface gravity anomaly. The simulated at-altitude gravity data on the local region of interest was used as an input to be fed into the numerical algorithms to solve the inverse problem. The localized solution thus obtained was compared to the initial surface gravity anomaly for the evaluation of the model. In validating our spherical wavelets gravity model and the numerical algorithms, we studied the effect of varying the data volume and the maximum degree of Legendre polynomials on the accuracy of the recovered gravity anomaly as well as the impact of the measurement noise and the irregularity of the data arrangement.

Unlike the traditional method to recover the surface gravity by finding the spherical harmonics coefficients that best fit the satellite's orbit elements, our model requires different type of measurements at the satellite altitude: the radial derivatives of gravity or gravitational potential. In the course of our study, we tested our model using two types of simulated gravity measurements at the satellite altitude: upward continued

gravity anomaly and the second order radial derivative of gravity anomaly, the former being a nominal data set to test the algorithms while the latter corresponding to the SGG (Satellite Gravity Gradiometry) measurements. We excluded the SST (Satellite-to-Satellite Tracking) measurements (*i.e.* the first order radial derivative of gravity potential or anomaly) from our tests because it is very difficult to separate the radial component from the inter-satellite range and its derivatives in a practical SST mission such as GRACE.

This dissertation is arranged as follows:

In **Chapter 2**, we will briefly review preliminary mathematics and the basics of multiresolution analysis as well as a cursory introduction to spherical wavelets, which is a necessary step to understand the contents that will be discussed in the following chapters. The theory of the inverse problem and the implementation of the spherical regularization wavelets as an approximate solution, treatment of local problems, the discrepancy principle and upward continuation will be discussed in **Chapter 3**. In **Chapter 4**, we will look into the numerical aspect of implementing the spherical wavelets model in recovering the local gravity field. **Chapter 5** and **Chapter 6** provide the simulation results of two local regions with different gravity gradients profiles. The effect of the data volume and the degree of Legendre polynomials on the recovered gravity anomaly is also studied in **Chapter 5**. In **Chapter 7**, we will review the results of the numerical simulation for a SGG type mission, which provides a more practical input format for our model. We will also examine the impact of the measurement noise on the recovered gravity solution in **Chapter 8**. In **Chapter 9**, we will study the surface gravity anomaly recovered from the data on a ground track rather than on a regular grid in order to understand the effect of irregularity in the data arrangement on the gravity solution. Finally, we will discuss the implications of the result and the application possibilities of the spherical wavelets model in **Chapter 10**.

Chapter 2. Preliminaries

In this chapter, we will review the mathematical background that will lay the basic foundation for **Chapter 3**. In section **2.1**, the properties of spherical harmonics and Legendre polynomials and their roles in harmonic analysis will be reviewed. The spherical pseudo-differential operators will be introduced in section **2.2** and section **2.3** will provide a brief insight to multiresolution analysis. In section **2.4**, we will present both continuous and scale discrete spherical wavelets and their properties, which will allow an opportunity for a better understanding of the spherical regularization wavelets that we will discuss in the following chapter.

2.1. Harmonic Analysis: Spherical Harmonics and Legendre Polynomials

We start with harmonic analysis, focusing on spherical harmonics and Legendre polynomials. The results and theorems in this section are based on Müller (1966) and Freeden (1979). We followed the mathematical notations and definitions presented by Schneider (1997).

Let $\mathcal{L}^2(\Omega)$ be the Hilbert space with the inner product of two scalar functions $F: \Omega \rightarrow \mathbb{R}$ and $G: \Omega \rightarrow \mathbb{R}$ defined as

$$(F, G)_{\mathcal{L}^2(\Omega)} = \int_{\Omega} F(\bar{y})G(\bar{y})d\omega(\bar{y}) \quad , \quad (2.1.1)$$

where $d\omega$ is the surface-element on Ω , a spherical surface with the unit radius. Then, $F \in \mathcal{L}^2(\Omega)$ can be represented by a spherical harmonics expansion such that

$$F = \sum_{n=0}^{\infty} \sum_{j=1}^{2n+1} F_{n,j} Y_{n,j} \quad , \quad (2.1.2)$$

where

$$F_{n,j} = \int_{\Omega} F(\vec{y}) Y_{n,j}(\vec{y}) d\omega(\vec{y}) \quad , \quad n \in \mathbb{N}_0 \quad , \quad j = 1, 2, \dots, 2n+1 \quad (2.1.3)$$

is the Fourier coefficient of F and $\{Y_{n,j} \mid n \in \mathbb{N}_0, j = 1, 2, \dots, 2n+1\}$ is the system of spherical harmonics of degree n defined by

$$Y_{n,j}(\vec{y}) = Y_n^{j-n-1}(\varphi, \lambda) \quad , \quad (2.1.4.a)$$

$$Y_n^m(\varphi, \lambda) = \sqrt{\frac{(2n+1)(n-m)!}{4\pi(n+m)!}} P_n^m(\sin \varphi) (\cos m\lambda + i \sin m\lambda) \quad , \quad m = 0, 1, \dots, n \quad , \quad (2.1.4.b)$$

$$Y_n^{-m}(\varphi, \lambda) = (-1)^m \overline{Y_n^m(\varphi, \lambda)} \quad , \quad (2.1.4.c)$$

for a unit vector $\vec{y} = (y_1, y_2, y_3) = (\lambda, \varphi)$ with $y_1 = \cos \varphi \cos \lambda$, $y_2 = \cos \varphi \sin \lambda$ and $y_3 = \sin \varphi$, where $\overline{Y_n^m}$ is the conjugate of Y_n^m . The function P_n^m in (2.1.4.b) is the associated Legendre function of degree n and order m defined as

$$P_n^m(t) = (-1)^m (1-t^2)^{m/2} \frac{d^m}{dt^m} (P_n(t)) \quad , \quad \text{for } t \in [-1, 1] \quad (2.1.5)$$

where

$$P_n(t) = \frac{1}{2^n n!} \frac{d^n}{dt^n} \left[(t^2 - 1)^n \right] \quad (2.1.6)$$

is the Legendre polynomial of degree n , defined by Rodrigue's formula.

The system $\{Y_{n,j}\}$ is $\mathcal{L}^2(\Omega)$ - orthonormalized, with the following properties:

$$\int_{\Omega} Y_{n,j}(\vec{y}) Y_{m,i}(\vec{y}) d\omega(\vec{y}) = \delta_{nm} \delta_{ji} \quad , \quad (2.1.7)$$

where $\delta_{aa} = 1$, $\delta_{ab} = 0$ if $a \neq b$, is Kronecker delta. The inner product of F and G in equation (2.1.1) is then represented as

$$(F, G)_{\mathcal{L}^2(\Omega)} = \sum_{n=0}^{\infty} \sum_{j=1}^{2n+1} F_{n,j} G_{n,j} \quad , \quad (2.1.8)$$

and thus $\|F\|_{\mathcal{L}^2(\Omega)}$, the norm of F on $\mathcal{L}^2(\Omega)$, becomes

$$\|F\|_{\mathcal{L}^2(\Omega)} = \left(\sum_{n=0}^{\infty} \sum_{j=1}^{2n+1} F_{n,j}^2 \right)^{1/2} \quad . \quad (2.1.9)$$

Now let us consider a system on Ω_R , a spherical surface with the radius R . Then

$F \in \mathcal{L}^2(\Omega_R)$ can be represented by the spherical harmonics expansion as

$$F = \sum_{n=0}^{\infty} \sum_{j=1}^{2n+1} F_{n,j}^R Y_{n,j}^R \quad , \quad (2.1.10)$$

where $F_{n,j}^R$ is the Fourier coefficient of F and $\{Y_{n,j}^R\}$ is the spherical harmonics system that is $\mathcal{L}^2(\Omega_R)$ - orthonormalized with the following properties:

$$F_{n,j}^R = \int_{\Omega_R} F(\bar{y}) Y_{n,j}^R(\bar{y}) d\omega_R(\bar{y}) \quad , \quad n \in \mathbb{N}_0 \quad , \quad j = 1, 2, \dots, 2n+1 \quad , \quad (2.1.11)$$

and

$$Y_{n,j}^R(\bar{y}) = \frac{1}{R} Y_{n,j} \left(\frac{\bar{y}}{|\bar{y}|} \right) \quad , \quad \bar{y} \in \Omega_R \quad . \quad (2.1.12)$$

Hence replacing $F_{n,j}^R$ in the equation (2.1.10) with the right-hand side of (2.1.11) yields,

$$F(\bar{x}) = \int_{\Omega_R} F(\bar{y}) \sum_{n=0}^{\infty} \sum_{j=1}^{2n+1} Y_{n,j}^R(\bar{y}) Y_{n,j}^R(\bar{x}) d\omega_R(\bar{y}) \quad . \quad (2.1.13)$$

Now let us examine some important properties of spherical harmonics and Legendre polynomials. Consider the scalar functions $G: [-1,1] \rightarrow \mathbb{R}$ and $H: [-1,1] \rightarrow \mathbb{R}$ on a Hilbert space $\mathcal{L}^2[-1,1]$. Their inner product is defined as

$$(G, H)_{\mathcal{L}^2[-1,1]} = 2\pi \int_{-1}^1 G(t) H(t) dt \quad , \quad (2.1.14)$$

and thus the norm of G on $\mathcal{L}^2[-1,1]$ becomes

$$\|G\|_{\mathcal{L}^2[-1,1]} = \left(2\pi \int_{-1}^1 |G(t)|^2 dt \right)^{\frac{1}{2}} \quad . \quad (2.1.15)$$

Any function $G \in \mathcal{L}^2[-1,1]$ can be represented by Legendre series as

$$G = \sum_{n=0}^{\infty} \frac{2n+1}{4\pi} G^{\wedge}(n) P_n \quad , \quad (2.1.16)$$

where

$$G^{\wedge}(n) = 2\pi \int_{-1}^1 G(t) P_n(t) dt \quad , \quad n \in \mathbb{N}_0 \quad (2.1.17)$$

is the Legendre coefficient of G . P_n , the Legendre polynomial of degree n , has the following orthogonal property:

$$\int_{-1}^1 P_n(t) P_m(t) dt = \frac{2}{2n+1} \delta_{nm} \quad , \quad \delta_{mm} = 1 \quad , \quad \delta_{nm} = 0 \quad \text{if } n \neq m \quad . \quad (2.1.18)$$

By replacing $G(t)$ in (2.1.15) with the right-hand side of (2.1.16) and utilizing the orthogonal property of $P_n(t)$ in (2.1.18), we obtain the norm of G as

$$\|G\|_{\mathcal{L}^2[-1,1]} = \left(\sum_{n=0}^{\infty} \frac{2n+1}{4\pi} (G^{\wedge}(n))^2 \right)^{\frac{1}{2}} \quad . \quad (2.1.19)$$

Now we introduce Funk-Hecke formula. Let G be a function on $\mathcal{L}^2[-1,1]$ and $n \in \mathbb{N}_0$. Then,

$$\int_{\Omega} G(\vec{\xi} \cdot \vec{\eta}) P_n(\vec{\eta} \cdot \vec{\zeta}) d\omega(\vec{\eta}) = G^{\wedge}(n) P_n(\vec{\xi} \cdot \vec{\zeta}) \quad (2.1.20)$$

holds valid for all $\vec{\xi}, \vec{\zeta} \in \Omega$. In addition, Y_n , any spherical harmonics of degree n , satisfies

$$\int_{\Omega} G(\vec{\xi} \cdot \vec{\eta}) Y_n(\vec{\eta}) d\omega(\vec{\eta}) = G^\wedge(n) Y_n(\vec{\xi}) \quad (2.1.21)$$

for all $\vec{\xi} \in \Omega$.

In order to examine the relation between the spherical harmonics and Legendre functions, we now define the spherical convolution of $G \in \mathcal{L}^2[-1, 1]$ and $F \in \mathcal{L}^2(\Omega)$ with respect to a unit sphere Ω as

$$\int_{\Omega} G(\cdot \vec{\eta}) F(\vec{\eta}) d\omega(\vec{\eta}) \quad , \quad (2.1.22)$$

which is of class $\mathcal{L}^2(\Omega)$. The spherical harmonics coefficients of the convolution of G and F satisfy

$$\left(\int_{\Omega} G(\cdot \vec{\eta}) F(\vec{\eta}) d\omega(\vec{\eta}) \right)_{n,j} = G^\wedge(n) F_{n,j} \quad , \quad n \in \mathbb{N}_0 \quad , \quad j = 1, 2, \dots, 2n+1 \quad . \quad (2.1.23)$$

Let $G_1, G_2 \in \mathcal{L}^2[-1, 1]$. Then the spherical convolution of G_1 and G_2 is of class $\mathcal{C}[-1, 1]$ (*i.e.* continuous on $[-1, 1]$) and its Legendre coefficients satisfy

$$\left(\int_{\Omega} G_1(\cdot \vec{\eta}) G_2(\vec{\eta}) d\omega(\vec{\eta}) \right)^\wedge(n) = G_1^\wedge(n) G_2^\wedge(n) \quad . \quad (2.1.24)$$

Now let us introduce the Addition theorem, one of the most widely used formulas in numerical implementation of regularization methods. For the orthonormal spherical harmonics system $\{Y_{n,j}\}$ on $\mathcal{L}^2(\Omega)$,

$$\sum_{j=1}^{2n+1} Y_{n,j}(\vec{\xi}) Y_{n,j}(\vec{\eta}) = \frac{2n+1}{4\pi} P_n(\vec{\xi} \cdot \vec{\eta}) \quad (2.1.25)$$

holds for all $\vec{\xi}, \vec{\eta} \in \Omega$.

2.2. Spherical Pseudo-differential Operators

In this section, we introduce spherical pseudo-differential operators (hereafter SPDO), which is necessary to understand the inverse problem we will discuss shortly in **Chapter 3**. The following definitions and results are based on Èskin (1981) and Svensson (1983), as presented by Schneider (1997).

First, with a sequence of real numbers $\{A_n \mid n=0,1,\dots\}$, let us introduce the space $\mathcal{E}(\{A_n\};\Omega_R)$:

$$\mathcal{E}(\{A_n\};\Omega_R) = \left\{ F \in C^{(\infty)}(\Omega_R) \mid \sum_{n=0}^{\infty} \sum_{j=1}^{2n+1} A_n^2 (F_{n,j}^R)^2 < \infty \right\}, \quad (2.2.1)$$

where F being of class $C^{(\infty)}$ means being smooth and having derivatives of all orders.

On $\mathcal{E}(\{A_n\};\Omega_R)$, the inner product and norm are defined as

$$(F, G)_{\mathcal{H}(\{A_n\};\Omega_R)} = \sum_{n=0}^{\infty} \sum_{j=1}^{2n+1} A_n^2 F_{n,j}^R G_{n,j}^R, \quad (2.2.2)$$

$$\|F\|_{\mathcal{H}(\{A_n\};\Omega_R)} = \left((F, F)_{\mathcal{H}(\{A_n\};\Omega_R)} \right)^{\frac{1}{2}}. \quad (2.2.3)$$

The Sobolev space $\mathcal{H}(\{A_n\};\Omega_R)$ is the completion of the space $\mathcal{E}(\{A_n\};\Omega_R)$ under the norm (2.2.3) and

$$\mathcal{H}_s(\Omega_R) = \mathcal{H}\left(\left\{\left(n + \frac{1}{2}\right)^s\right\};\Omega_R\right) \quad \text{for } s \in \mathbb{R}, \quad (2.2.4)$$

with $\mathcal{H}_0(\Omega_R) = \mathcal{L}^2(\Omega_R)$, the Hilbert space.

Now let us consider a sequence of real numbers $\{\Lambda^\wedge(n)\}$ in Sobolev space that satisfies

$$\lim_{n \rightarrow \infty} \frac{|\Lambda^\wedge(n)|}{\left(n + \frac{1}{2}\right)^t} = \text{const} \neq 0 \quad (2.2.5)$$

for $t \in \mathbb{R}$. Then the operator $\Lambda : \mathcal{H}_s(\Omega_R) \rightarrow \mathcal{H}_{s-t}(\Omega_r)$ defined as

$$\Lambda F = \sum_{n=0}^{\infty} \sum_{j=1}^{2n+1} \Lambda^\wedge(n) F_{n,j}^R Y_{n,j}^r \quad (2.2.6)$$

is called the spherical pseudo-differential operator of order t , and $\{\Lambda^\wedge(n)\}$ is called the spherical symbol of Λ . If

$$\lim_{n \rightarrow \infty} \frac{|\Lambda^\wedge(n)|}{\left(n + \frac{1}{2}\right)^t} = 0 \quad (2.2.7)$$

for all $t \in \mathbb{R}$, then the operator $\Lambda : \mathcal{H}_s(\Omega_R) \rightarrow \mathcal{C}^{(\infty)}(\Omega_r)$ is called the SPDO of order $-\infty$. In particular, if $s \geq 0$ and

$$\sum_{n=0}^{\infty} \frac{2n+1}{4\pi} |\Lambda^\wedge(n)| < \infty \quad , \quad (2.2.8)$$

then (2.2.6) can be represented in a convolution form such that

$$(\Lambda F)(\vec{x}) = \int_{\Omega_R} K_\Lambda(\vec{x}, \vec{y}) F(\vec{y}) d\omega_R(\vec{y}) \quad , \quad (2.2.9)$$

where

$$K_\Lambda(\vec{x}, \vec{y}) = \sum_{n=0}^{\infty} \sum_{j=1}^{2n+1} \Lambda^\wedge(n) Y_{n,j}^R(\vec{y}) Y_{n,j}^r(\vec{x}) \quad , \quad \vec{x} \in \Omega_r \quad , \quad \vec{y} \in \Omega_R \quad (2.2.10)$$

is the C -kernel of the SPDO Λ , which is of class $C(\Omega_r) \times C(\Omega_R)$. Now by replacing $K_\Lambda(\vec{x}, \vec{y})$ in (2.2.9) with the right-hand side of (2.2.10) we arrive at

$$(\Lambda F)(\vec{x}) = \int_{\Omega_R} F(\vec{y}) \sum_{n=0}^{\infty} \sum_{j=1}^{2n+1} \Lambda^\wedge(n) Y_{n,j}^R(\vec{y}) Y_{n,j}^r(\vec{x}) d\omega_R(\vec{y}) \quad . \quad (2.2.11)$$

The role of the SPDO in the inverse problem in satellite geodesy will be discussed in **Chapter 3**.

2.3. Basics of Multiresolution Analysis

The wavelet transform, first proposed by Morlet as an alternative method to Fourier transform in seismic data modeling (Grossman and Morlet, 1984), has been recognized as a part of harmonic analysis (Meyer 1993). Wavelets provide a mathematical tool to decompose a signal or a function into different frequency domains and to study each component with a resolution that matches to its scale (Daubechies, 1992). Multiresolution analysis, developed by Mallat (1989) and Meyer (1993) consists of a sequence of nested subspaces of different resolutions and uses discrete orthonormal wavelets as a tool to link the different resolution levels. In this section, we review the basic theory of multiresolution analysis and wavelet transform. The following definitions and notations are largely based on J. Gilbert (2001), Kaiser (1994) and Daubechies and Gilbert (1998).

A multiresolution analysis (hereafter MRA) is a sequence of V_j , which denotes nested subspaces of $\mathcal{L}^2(\mathbb{R})$, satisfying the following properties:

1. $V_j \subset V_{j+1}$, $j \in \mathbb{Z}$.
2. $\bigcap_{j \in \mathbb{Z}} V_j = \{0\}$, $\overline{\bigcup_{j \in \mathbb{Z}} V_j} = \mathcal{L}^2(\mathbb{R})$.
3. For $f(x) \in V_j$, $j \in \mathbb{Z}$, then $f(2x) \in V_{j+1}$. This relation is called the dilation property. It implies that each successive V_j corresponds to a resolution increasing by a factor 2 from the previous level.
4. For $f(x) \in V_j$, $j \in \mathbb{Z}$, then $f(x-k) \in V_j$, $k \in \mathbb{Z}$. This relation is called the translation property.
5. For $\exists f(x) \in V_0$ such that $\{f(x-k)$, $k \in \mathbb{Z}\}$ is an orthonormal basis of V_0 , then $f(x)$ is called a mother scaling function and

$\left\{ 2^{\frac{j}{2}} f(2^j x - k) \ , \ j, k \in \mathbb{Z} \right\}$ is an orthonormal basis of V_j . Any function in

$V_j \subset V_{j+1}$ can be expressed in terms of basis functions of V_{j+1} .

Now let us define a subspace W_j , the orthogonal complements of V_j in V_{j+1} , by

$$W_j \equiv \left\{ f \in V_{j+1} \mid \langle f, g \rangle = 0 \text{ for all } g \in V_j \right\} \ , \quad (2.3.1)$$

which together with V_j constructs the MRA such that

$$V_{j+1} = V_j \oplus W_j \quad , \quad W_j = V_{j+1} \cap V_j^\perp \quad , \quad (2.3.2)$$

where \oplus denotes the orthogonal sum of subspaces. MRA can also be decomposed as

$$\begin{aligned} V_j &= W_{j-1} \oplus V_{j-1} \\ &= W_{j-1} \oplus W_{j-2} \oplus V_{j-2} \\ &\dots \\ &= W_{j-1} \oplus \dots \oplus W_0 \oplus V_0 \\ &\dots \\ &= W_{j-1} \oplus \dots \oplus W_{-k} \oplus V_{-k} \quad . \end{aligned} \quad (2.3.3)$$

Now we introduce the mother scaling function $\phi(x)$ and mother wavelet $\psi(x)$ which satisfy the following properties with $\overline{\phi(x)}$ and $\overline{\psi(x)}$ respectively being the conjugate of $\phi(x)$ and $\psi(x)$:

1. 2-scale dilation equations

$$\phi(x) = \sqrt{2} \sum_{k=-\infty}^{\infty} h_k \phi(2x - k) \quad (2.3.4)$$

$$h_k = \int_{-\infty}^{\infty} \phi(x) \overline{\phi(2x - k)} dx \quad (2.3.5)$$

$$\sum_{k=-\infty}^{\infty} |h_k|^2 = 1 \quad (2.3.6)$$

2. wavelet equations

$$\psi(x) = \sqrt{2} \sum_{k=-\infty}^{\infty} g_k \phi(2x - k) \quad (2.3.7)$$

$$g_k = (-1)^{k-1} h_{1-k} \quad (2.3.8)$$

3. orthonormality

$$\int_{-\infty}^{\infty} \phi(x - n) \overline{\phi(x - m)} dx = \delta_{nm} \quad (2.3.9)$$

$$\int_{-\infty}^{\infty} \psi(x - n) \overline{\psi(x - m)} dx = \delta_{nm} \quad (2.3.10)$$

$$\int_{-\infty}^{\infty} \phi(x - n) \overline{\psi(x - m)} dx = 0 \quad (2.3.11)$$

Then, the scaling function $\phi_{j,k}$, defined as a dilated-translated copy of a mother scaling function ϕ , is represented as

$$\phi_{j,k}(x) = 2^{-\frac{j}{2}} \phi(2^j x - k) \quad , \quad j, k \in \mathbb{Z} \quad , \quad (2.3.12)$$

and it forms an orthonormal basis of V_j . The wavelet $\psi_{j,k}$, a dilated-translated copy of mother wavelet ψ , is similarly defined by

$$\psi_{j,k}(x) = 2^{\frac{j}{2}} \psi(2^j x - k) \quad , \quad j, k \in \mathbb{Z} \quad , \quad (2.3.13)$$

and is an orthonormal basis of W_j .

Now we decompose a signal into a set of scaling functions and wavelets. Let us define an operator $P_j : \mathcal{L}^2(\mathbb{R}) \rightarrow \mathcal{L}^2(\mathbb{R})$, the orthogonal projection of a signal f onto V_j , by

$$P_j f = \sum_{k=-\infty}^{\infty} \langle f, \phi_{j,k} \rangle \phi_{j,k} \quad , \quad (2.3.14)$$

where the coefficient in the sum is given by

$$\langle f, \phi_{j,k} \rangle = \int_{-\infty}^{\infty} f(y) \overline{\phi_{j,k}(y)} dy \quad . \quad (2.3.15)$$

Then, $P_j f$ represents the coarse version of f and it satisfies

$$\lim_{j \rightarrow \infty} P_j f = f \quad , \quad \lim_{j \rightarrow -\infty} P_j f = 0 \quad . \quad (2.3.16)$$

Similarly, the operator $Q_j : \mathcal{L}^2(\mathbb{R}) \rightarrow \mathcal{L}^2(\mathbb{R})$, the orthogonal projection of f onto W_j , is defined by

$$Q_j f = \sum_{k=-\infty}^{\infty} \langle f, \psi_{j,k} \rangle \psi_{j,k} \quad , \quad (2.3.17)$$

where

$$\langle f, \psi_{j,k} \rangle = \int_{-\infty}^{\infty} f(y) \overline{\psi_{j,k}(y)} dy \quad (2.3.18)$$

denotes the wavelet coefficient, and is called the wavelet transform. We can interpret that $Q_j f$ represents the fine details of the signal f in V_{j+1} . Now, we can construct the finer version of signal f such that

$$P_{j+1}f = P_j f + Q_j f \quad , \quad (2.3.19)$$

which is equivalent to (2.3.2) and represents the approximate solution of f .

2.4. Spherical Wavelets

The essence of the wavelet analysis is to find the scaling and wavelet basis functions best fitting to the nature of the signals or functions of the problem we treat. Since the Earth's surface is near spherical, the geodetic problems we are interested in have a spherical nature. In this section, we introduce the spherical wavelets, with both continuous and scale discrete cases, which will lay the foundation for the understanding of spherical regularization wavelets we will discuss in **Chapter 3**. The following definitions and properties of spherical wavelets are based on Freeden and Windheuser (1996, 1997) and Schneider (1997).

Let $\alpha : (0, \infty) \rightarrow \mathbb{R}$ be a positive weight function, $\{\Psi_\rho \mid \rho \in (0, \infty)\}$ be a subfamily of $\mathcal{L}^2[-1, 1]$ and $m \in \mathbb{Z}$, $m \geq -1$, satisfying

1. $\int_0^\infty (\Psi_\rho^\wedge(n))^2 \alpha(\rho) d\rho = 1$ for $n \geq m+1$,
2. $\sum_{n=m+1}^\infty \frac{2n+1}{4\pi} \int_\gamma^\infty (\Psi_\rho^\wedge(n))^2 \alpha(\rho) d\rho < \infty$ for all $\gamma > 0$,
3. $\Psi_\rho^\wedge(n) = 0$ for $n = 0, \dots, m$ (this condition must be omitted for $m = -1$).

Then, $\{\Psi_\rho \mid \rho \in (0, \infty)\}$ with the following form

$$\Psi_\rho = \sum_{n=m+1}^\infty \frac{2n+1}{4\pi} \Psi_\rho^\wedge(n) P_n, \quad (2.4.1)$$

where P_n is Legendre polynomial of degree n , is called the scale continuous spherical wavelet of order m . The spherical wavelet can be defined on Ω_R , where $\bar{y} \in \Omega_R$, by using the Addition theorem in (2.1.25) in the following way:

$$\Psi_{\rho;y}^R = \frac{1}{R^2} \sum_{n=m+1}^{\infty} \frac{2n+1}{4\pi} \Psi_{\rho}^{\wedge}(n) P_n \left(\frac{\bar{y}}{R} \cdot \frac{\cdot}{R} \right) = \sum_{n=m+1}^{\infty} \sum_{j=1}^{2n+1} \Psi_{\rho}^{\wedge}(n) Y_{n,j}^R(\bar{y}) Y_{n,j}^R(\cdot) \quad . \quad (2.4.2)$$

The wavelet transform $(WT)_{\Psi} : \mathcal{L}^2(\Omega_R) \rightarrow \mathcal{L}^2((0, \infty) \times \Omega_R)$ is then defined as

$$(WT)_{\Psi}(F)(\rho; \bar{y}) = (F, \Psi_{\rho;y}^R)_{\mathcal{L}^2(\Omega_R)} = \int_{\Omega_R} \Psi_{\rho;y}^R(\bar{z}) F(\bar{z}) d\omega_R(\bar{z}) \quad , \quad (2.4.3)$$

and we can now formulate the reconstruction formula:

$$\begin{aligned} F &= \int_{\Omega_R} \int_0^{\infty} (WT)_{\Psi}(F)(\rho; \bar{y}) \Psi_{\rho;y}^R(\cdot) \alpha(\rho) d\rho d\omega_R(\bar{y}) \\ &= \int_{\Omega_R} \int_0^{\infty} \int_{\Omega_R} \Psi_{\rho;y}^R(\bar{z}) F(\bar{z}) d\omega_R(\bar{z}) \Psi_{\rho;y}^R(\cdot) \alpha(\rho) d\rho d\omega_R(\bar{y}) \\ &= \int_{\Omega_R} F(\bar{z}) \sum_{n=m+1}^{\infty} \sum_{j=1}^{2n+1} \int_0^{\infty} (\Psi_{\rho}^{\wedge}(n))^2 \alpha(\rho) d\rho Y_{n,j}^R(\bar{z}) Y_{n,j}^R(\cdot) d\omega_R(\bar{z}) \quad . \end{aligned} \quad (2.4.4)$$

We used (2.4.2) and the orthonormality of the spherical harmonics in (2.1.7) to arrive at (2.4.4). We now introduce the mother wavelet Ψ_1 , from which all other wavelets can be derived by rotation and dilation such that

$$\Psi_1 = \sum_{n=0}^{\infty} \frac{2n+1}{4\pi} \Psi_1^{\wedge}(n) P_n \quad , \quad (2.4.5)$$

$$\Psi_{\rho;y}^R = R_y^R D_{\rho} \Psi_1 \quad , \quad (2.4.6)$$

where R_y^R represents the rotation operator and D_{ρ} is the dilation operator.

The (scale continuous) scaling function $\{\Phi_{\gamma} \mid \gamma \in (0, \infty)\}$ corresponding to the spherical wavelet $\{\Psi_{\rho} \mid \rho \in (0, \infty)\}$ is defined as

$$\Phi_\gamma = \sum_{n=0}^{\infty} \frac{2n+1}{4\pi} \Phi_\gamma^\wedge(n) P_n \quad , \quad (2.4.7)$$

with

$$\Phi_\gamma^\wedge(n) = \begin{cases} \left(\int_\gamma^\infty (\Psi_\rho^\wedge(n))^2 \alpha(\rho) d\rho \right)^{\frac{1}{2}} & : n \geq m+1 \\ 1 & : n = 0, \dots, m \end{cases} . \quad (2.4.8)$$

As with the wavelet, we can define the mother scaling function Φ_1 and its rotated-dilated copies $\{\Phi_{\gamma;y}^R\}$ on Ω_R by

$$\Phi_1 = \sum_{n=0}^{\infty} \frac{2n+1}{4\pi} \Phi_1^\wedge(n) P_n \quad , \quad (2.4.9)$$

$$\Phi_{\gamma;y}^R = R_y^R D_\gamma \Phi_1 = \sum_{n=0}^{\infty} \sum_{j=1}^{2n+1} \Phi_\gamma^\wedge(n) Y_{n,j}^R(\bar{y}) Y_{n,j}^R \quad , \quad (2.4.10)$$

and the reconstruction formula (2.4.4) can be reformulated in the following form:

$$\begin{aligned} F &= \lim_{\gamma \rightarrow +0} \int_{\Omega_R} (F, R_y^R D_\gamma \Phi_1)_{\mathcal{L}^2(\Omega_R)} (R_y^R D_\gamma \Phi_1)(\cdot) d\omega_R(\bar{y}) \\ &= \lim_{\gamma \rightarrow +0} \int_{\Omega_R} (F, \Phi_{\gamma;y}^R)_{\mathcal{L}^2(\Omega_R)} \Phi_{\gamma;y}^R(\cdot) d\omega_R(\bar{y}) \quad . \end{aligned} \quad (2.4.11)$$

Now we discretize the spherical wavelet to the continuous scale interval to obtain scale discrete spherical wavelet packets first by introducing a strict monotonously decreasing sequence $\{\gamma_j\}$ of real numbers satisfying

$$\lim_{j \rightarrow \infty} \gamma_j = 0 \quad \text{and} \quad \lim_{j \rightarrow -\infty} \gamma_j = \infty \quad , \quad (2.4.12)$$

and then by defining the spherical wavelet packet $\{\Psi_j^p \mid j \in \mathbb{Z}\}$ of order m as

$$\Psi_j^p = \sum_{n=0}^{\infty} \frac{2n+1}{4\pi} (\Psi_j^p)^\wedge(n) P_n \quad , \quad (2.4.13)$$

with

$$(\Psi_j^p)^\wedge(n) = \begin{cases} \left(\int_{\gamma_{j+1}}^{\gamma_j} (\Psi_\rho^\wedge(n))^2 \alpha(\rho) d\rho \right)^{\frac{1}{2}} & : n \geq m+1 \\ 0 & : n = 0, \dots, m \end{cases} . \quad (2.4.14)$$

The mother wavelet packet Ψ_0^p and its rotated-dilated copies $\{\Psi_{j;y}^{R;p}\}$ on Ω_R is given by

$$\Psi_0^p = \sum_{n=0}^{\infty} \frac{2n+1}{4\pi} (\Psi_0^p)^\wedge(n) P_n \quad , \quad (2.4.15)$$

$$\Psi_{j;y}^{R;p} = R_y^R D_j \Psi_0^p = \sum_{n=0}^{\infty} \sum_{i=1}^{2n+1} (\Psi_j^p)^\wedge(n) Y_{n,i}^R(\bar{y}) Y_{n,i}^R \quad , \quad (2.4.16)$$

and the reconstruction formula takes the following form

$$F = \sum_{j=-\infty}^{\infty} \int_{\Omega_R} (WT)_\Psi^p(F)(j; \bar{y}) \Psi_{j;y}^{R;p}(\cdot) d\omega_R(\bar{y}) \quad , \quad (2.4.17)$$

(Note that the integration over the scale interval ρ in (2.4.4) has been replaced with infinite summation over j for the scale discrete case) with

$$(WT)_{\Psi}^p(F)(j; \bar{y}) = (F, \Psi_{j;y}^{R;p})_{\mathcal{L}^2(\Omega_R)} = \int_{\Omega_R} \Psi_{j;y}^{R;p}(\bar{z}) F(\bar{z}) d\omega_R(\bar{z}) \quad . \quad (2.4.18)$$

As a last step, we define the scale discrete scaling function $\{\Phi_J^p \mid J \in \mathbb{Z}\}$ by

$$\Phi_J^p = \sum_{n=0}^{\infty} \frac{2n+1}{4\pi} (\Phi_J^p)^{\wedge}(n) P_n \quad , \quad (2.4.19)$$

with

$$(\Phi_J^p)^{\wedge}(n) = \begin{cases} \left(\sum_{j=-\infty}^{J-1} ((\Psi_j^p)^{\wedge}(n))^2 \right)^{\frac{1}{2}} & : n \geq m+1 \\ 1 & : n = 0, \dots, m \end{cases} \quad , \quad (2.4.20)$$

and the mother scaling function Φ_0^p and the rotated-dilated copies $\{\Phi_{J;y}^{R;p}\}$ on Ω_R in the following way

$$\Phi_0^p = \sum_{n=0}^{\infty} \frac{2n+1}{4\pi} (\Phi_0^p)^{\wedge}(n) P_n \quad , \quad (2.4.21)$$

$$\Phi_{J;y}^{R;p} = R_y^R D_J \Phi_0^p = \sum_{n=0}^{\infty} \sum_{j=1}^{2n+1} (\Phi_J^p)^{\wedge}(n) Y_{n,j}^R(\bar{y}) Y_{n,j}^R \quad . \quad (2.4.22)$$

The reconstruction formula is then given by

$$\begin{aligned} F &= \lim_{J \rightarrow \infty} \int_{\Omega_R} (F, R_y^R D_J \Phi_0^p)_{\mathcal{L}^2(\Omega_R)} (R_y^R D_J \Phi_0^p)(\cdot) d\omega_R(\bar{y}) \\ &= \lim_{J \rightarrow \infty} \int_{\Omega_R} (F, \Phi_{J;y}^{R;p})_{\mathcal{L}^2(\Omega_R)} \Phi_{J;y}^{R;p}(\cdot) d\omega_R(\bar{y}) \quad . \end{aligned} \quad (2.4.23)$$

Finally, we will derive the relation between the scale discrete scaling function and the wavelet packet. Combining the reconstruction formula in (2.4.17) and (2.4.23) leads us to

$$F = \int_{\Omega_R} (F, \Phi_{J;y}^{R;p})_{\mathcal{L}^2(\Omega_R)} \Phi_{J;y}^{R;p}(\cdot) d\omega_R(\bar{y}) + \sum_{j=J}^{\infty} \int_{\Omega_R} (WT)_{\Psi}^p(F)(j; \bar{y}) \Psi_{j;y}^{R;p}(\cdot) d\omega_R(\bar{y}) \quad . \quad (2.4.24)$$

It is easy to verify the following property by examining condition 1 in defining the scale continuous spherical wavelet and the definition of the scale discrete wavelet packet and scaling function in (2.4.14) and (2.4.20):

$$1 = \int_0^{\infty} (\Psi_{\rho}^{\wedge}(n))^2 \alpha(\rho) d\rho = \sum_{j=-\infty}^{\infty} \left((\Psi_j^p)^{\wedge}(n) \right)^2 = \left((\Phi_J^p)^{\wedge}(n) \right)^2 + \sum_{j=J}^{\infty} \left((\Psi_j^p)^{\wedge}(n) \right)^2 \quad , \quad (2.4.25)$$

for $n \geq m+1$. From (2.4.25) we finally arrive at

$$\left((\Psi_j^p)^{\wedge}(n) \right)^2 = \left((\Phi_{j+1}^p)^{\wedge}(n) \right)^2 - \left((\Phi_j^p)^{\wedge}(n) \right)^2 \quad , \quad j \in \mathbb{Z} \quad , \quad n \in \mathbb{N}_0 \quad . \quad (2.4.26)$$

Now we are ready to introduce the scale discrete spherical regularization wavelets approximation as a solution to the inverse problem in the next chapter.

Chapter 3. Solving Inverse Problem by Spherical Regularization Wavelets Approximation

3.1. Inverse Problem and Scale Discrete Spherical Regularization Wavelets

In this section we follow Schneider's (1997) approach to the inverse problem and its solution by employing spherical regularization wavelets, including definitions and notations.

We begin by introducing an SPDO equation frequently encountered in satellite geodesy. Let us consider an equation:

$$\Lambda_{\frac{R}{r}} F(\vec{z}) = G(\vec{x}) \quad , \quad \vec{x} \in \Omega_r \quad , \quad \vec{z} \in \Omega_R \quad , \quad R < r \quad , \quad (3.1.1)$$

where R is the surface radius of the spherical Earth, r is the satellite's orbit radius from the Earth's center of mass, $F(\vec{z})$ is the gravity potential at the Earth's surface and $G(\vec{x})$ is the gravity measurements at the satellite's altitude. The equation (3.1.1) is a well-posed problem, where a unique solution exists which is dependent continuously on the data in some reasonable topology, a definition forwarded by French mathematician Jacques Hadamard. The SPDO $\Lambda_{\frac{R}{r}}$ in the equation (3.1.1) is of order $-\infty$ and takes a different form depending on the measurements and satellite mission type: direct upward propagation, Satellite-to-Satellite Tracking (SST) or Satellite Gravity Gradiometry (SGG).

In direct upward propagation, the outputs are the gravity potential at the satellite altitude. In an SST or SGG mission, the satellite measurements take the respective form of the first or second order radial derivative of the gravity potential (Vermeer, 1989;

Seeber 2003). The corresponding spherical symbol of the SPDO for each type of mission is listed below:

$$\text{direct upward propagation operator: } \left(\Lambda_{\frac{R}{r}}\right)^\wedge(n) = \left(\frac{R}{r}\right)^n \quad (3.1.2)$$

$$\text{SST operator: } \left(\Lambda_{\frac{R}{r}}\right)^\wedge(n) = \left(\frac{R}{r}\right)^n \frac{n+1}{r} \quad (3.1.3)$$

$$\text{SGG operator: } \left(\Lambda_{\frac{R}{r}}\right)^\wedge(n) = \left(\frac{R}{r}\right)^n \frac{(n+1)(n+2)}{r^2} \quad (3.1.4)$$

Now we consider the inverse of the equation (3.1.1), where the surface gravity anomaly or gravity potential is to be obtained from the satellite measurements, such that

$$F(\vec{z}) = \Lambda_{\frac{R}{r}}^{-1} G(\vec{x}) \quad , \quad \vec{x} \in \Omega_r \quad , \quad \vec{z} \in \Omega_R \quad , \quad R < r \quad . \quad (3.1.5)$$

This equation is widely known as the inverse problem in satellite geodesy. It is ill-posed due to the fact that $\left(\left(\Lambda_{\frac{R}{r}}\right)^\wedge(n)\right)^{-1}$, the spherical symbol of $\Lambda_{\frac{R}{r}}^{-1}$, diverges exponentially as $n \rightarrow \infty$ (Louis, 1989). Since it is ill-posed, we regularize the SPDO to solve the problem.

Let us consider an inverse operator $\Lambda_{\frac{R}{r}}^{-1} : \mathcal{L}^2(\Omega_r) \rightarrow \mathcal{L}^2(\Omega_R)$ and let $\sigma_n = \left(\Lambda_{\frac{R}{r}}\right)^\wedge(n)$ be the spherical symbol of the SPDO $\Lambda_{\frac{R}{r}}$. We can regularize the operator $\Lambda_{\frac{R}{r}}^{-1}$ by introducing a regularizing filter $f_\gamma(\sigma_n)$ that satisfies:

1. $\sup_{n \in \mathbb{N}_0} \left| f_\gamma(\sigma_n) \sigma_n^{-1} \right| = c(\gamma) < \infty \quad , \quad \gamma > 0 \quad ,$
2. $\lim_{\gamma \rightarrow 0} f_\gamma(\sigma_n) = 1 \quad , \quad n \in \mathbb{N}_0 \quad ,$

3. $|f_\gamma(\sigma_n)| \leq c$ for all $\gamma > 0$ and $n \in \mathbb{N}_0$.

Now we define the operator $T_\gamma : \mathcal{L}^2(\Omega_r) \rightarrow \mathcal{L}^2(\Omega_R)$ by

$$T_\gamma G(\vec{x}) = \sum_{n=0}^{\infty} \sum_{j=1}^{2n+1} \sigma_n^{-1} f_\gamma(\sigma_n) G_{n,j}^r Y_{n,j}^R(\vec{x}) \quad , \quad (3.1.6)$$

which is the realization of the equation (2.2.6) for the inverse problem. The operator T_γ is called the regularization of the inverse operator $\Lambda_{\frac{R}{r}}^{-1}$ (Louis, 1989) with $\sigma_n^{-1} f_\gamma(\sigma_n)$ being its spherical symbol.

Now, we solve the inverse problem using the wavelets approximation. Let F_J be the regularized solution to (3.1.5) satisfying

$$\lim_{J \rightarrow \infty} F_J = \Lambda_{\frac{R}{r}}^{-1} G \quad . \quad (3.1.7)$$

F_J is also represented as

$$F_J = T_J G \quad , \quad (3.1.8)$$

where T_J is the regularization of $\Lambda_{\frac{R}{r}}^{-1}$ of wavelet resolution level J and $G \in \mathcal{R}(\Lambda_{\frac{R}{r}})$ (*i.e.* G belongs to the range of $\Lambda_{\frac{R}{r}}$). Let us consider $V_J = \{F_J = T_J G \mid G \in \mathcal{R}(\Lambda_{\frac{R}{r}})\}$ that satisfies:

1. $\{0\} \subset V_J \subset V_{J'} \subset \mathcal{L}^2(\Omega_R)$ for all $J < J'$,

2. $\left\{ \lim_{J \rightarrow -\infty} T_J G \mid G \in \mathcal{R}(\Lambda_{\frac{R}{r}}) \right\} = \{0\}$,
3. $\overline{\left\{ F \in \mathcal{L}^2(\Omega_R) \mid F \in V_J \text{ for some } J \in \mathbb{Z} \right\}}^{\|\cdot\|_{\mathcal{L}^2(\Omega_R)}} = \mathcal{L}^2(\Omega_R)$.

Then a collection of scale discrete regularization subspaces V_J is called a scale discrete regularization of multiresolution analysis (hereafter RMRA), and it satisfies

$$V_J = V_{J-1} \oplus W_{J-1}, \quad J \in \mathbb{Z}, \quad (3.1.9)$$

where W_{J-1} contains the “detailed information” of G which corresponds to the regularization of wavelet resolution level J .

Now let $\{\Phi_J^p\}$, $J \in \mathbb{Z}$, defined by

$$\Phi_J^p = \sum_{n=0}^{\infty} \frac{2n+1}{4\pi} (\Phi_J^p)^\wedge(n) P_n \quad (3.1.10)$$

be a subfamily of $\mathcal{L}^2[-1,1]$ that satisfies:

1. $\lim_{J \rightarrow \infty} \sigma_n \left((\Phi_J^p)^\wedge(n) \right)^2 = 1$ for $n \geq 0$,
2. $\left((\Phi_{J+1}^p)^\wedge(n) \right)^2 \geq \left((\Phi_J^p)^\wedge(n) \right)^2$ for $J \in \mathbb{Z}$ and $n \in \mathbb{N}_0$.

Then $\{\Phi_J^p\}$ is called a scale discrete spherical regularization scaling function and $(\Phi_J^p)^\wedge(n)$ denotes the Legendre coefficient of the spherical regularization scaling function. In particular, if $J = 0$, then

$$\Phi_0^p = \sum_{n=0}^{\infty} \frac{2n+1}{4\pi} (\Phi_0^p)^\wedge(n) P_n \quad (3.1.11)$$

is the scale discrete spherical regularization mother scaling function. We define $\{\Phi_{J;y}^{r;p}\}$ and $\{\tilde{\Phi}_{J;y}^{R;p}\}$, the rotated-dilated copies of Φ_0^p respectively on Ω_r and Ω_R , where $\bar{y} \in \Omega_R$, as

$$\Phi_{J;y}^{r;p} = R_y^r D_J \Phi_0^p = \sum_{n=0}^{\infty} \sum_{j=1}^{2n+1} (\Phi_J^p)^\wedge(n) Y_{n,j}^R(\bar{y}) Y_{n,j}^r \quad , \quad (3.1.12)$$

$$\tilde{\Phi}_{J;y}^{R;p} = R_y^R D_J \Phi_0^p = \sum_{n=0}^{\infty} \sum_{j=1}^{2n+1} (\Phi_J^p)^\wedge(n) Y_{n,j}^R(\bar{y}) Y_{n,j}^R \quad . \quad (3.1.13)$$

We now employ (2.2.9) for the regularized problem (3.1.8). For $\bar{x} \in \Omega_r$ and $\bar{z} \in \Omega_R$,

$$\begin{aligned} F_J(\bar{z}) &= T_J G(\bar{x}) = \int_{\Omega_r} G(\bar{x}) K_J(\bar{x}, \bar{z}) d\omega_r(\bar{x}) \\ &= \int_{\Omega_R} \int_{\Omega_r} \Phi_{J;y}^{r;p}(\bar{x}) G(\bar{x}) d\omega_r(\bar{x}) \tilde{\Phi}_{J;y}^{R;p}(\bar{z}) d\omega_R(\bar{y}) \quad , \quad (3.1.14) \end{aligned}$$

where

$$K_J(\bar{x}, \bar{z}) = \int_{\Omega_R} \Phi_{J;y}^{r;p}(\bar{x}) \tilde{\Phi}_{J;y}^{R;p}(\bar{z}) d\omega_R(\bar{y}) \quad (3.1.15)$$

is the \mathcal{C} -kernel of the regularization operator T_J . We can replace $\Phi_{J;y}^{r;p}$ and $\tilde{\Phi}_{J;y}^{R;p}$ in (3.1.15) with the right-hand side of (3.1.12) and (3.1.13), and by using the orthonormal

property of the spherical harmonics as presented in (2.1.7) we obtain the representation of $K_J(\bar{x}, \bar{z})$ analogous to (2.2.10):

$$K_J(\bar{x}, \bar{z}) = \sum_{n=0}^{\infty} \sum_{j=1}^{2n+1} \left((\Phi_j^p)^\wedge(n) \right)^2 Y_{n,j}^r(\bar{x}) Y_{n,j}^R(\bar{z}) \quad . \quad (3.1.16)$$

The equation (3.1.16) implies that $\left((\Phi_j^p)^\wedge(n) \right)^2$ corresponds to the spherical symbol of the regularization operator T_J , providing the link between the regularized inverse problem and the spherical regularization scaling functions and wavelets. The second line in (3.1.14) is also the reconstruction formula for the regularized solution of wavelet resolution level J .

Along with the scale discrete spherical regularization scaling function, we introduce the scale discrete spherical regularization wavelet packet $\{\Psi_j^p\}$, which is defined by

$$\Psi_j^p = \sum_{n=0}^{\infty} \frac{2n+1}{4\pi} (\Psi_j^p)^\wedge(n) P_n \quad , \quad (3.1.17)$$

with

$$(\Psi_j^p)^\wedge(n) = \left(\left((\Phi_{j+1}^p)^\wedge(n) \right)^2 - \left((\Phi_j^p)^\wedge(n) \right)^2 \right)^{\frac{1}{2}} \quad , \quad n \in \mathbb{N}_0 \quad , \quad (3.1.18)$$

being the Legendre coefficient of the spherical regularization wavelet packet. The scale discrete spherical regularization mother wavelet Ψ_0^p and its rotated-dilated copies $\{\Psi_{j;y}^{r;p}\}$ and $\{\tilde{\Psi}_{j;y}^{R;p}\}$ are defined in a similar way as in the scaling function:

$$\Psi_0^p = \sum_{n=0}^{\infty} \frac{2n+1}{4\pi} (\Psi_0^p)^\wedge(n) P_n \quad , \quad (3.1.19)$$

$$\Psi_{j;y}^{r;p} = R_y^r D_j \Psi_0^p = \sum_{n=0}^{\infty} \sum_{i=1}^{2n+1} (\Psi_j^p)^\wedge(n) Y_{n,i}^R(\bar{y}) Y_{n,i}^r \quad , \quad (3.1.20)$$

$$\tilde{\Psi}_{j;y}^{R;p} = R_y^R D_j \Psi_0^p = \sum_{n=0}^{\infty} \sum_{i=1}^{2n+1} (\Psi_j^p)^\wedge(n) Y_{n,i}^R(\bar{y}) Y_{n,i}^R \quad . \quad (3.1.21)$$

Now let us consider the scale discrete RMRA:

$$V_J = V_{J-1} \oplus W_{J-1} = V_0 \oplus \bigoplus_{j=0}^{J-1} W_j \quad . \quad (3.1.22)$$

We can use (3.1.14) to represent $V_0 = \left\{ F_0 = T_0 G \mid G \in \mathcal{R}(\Lambda_{\frac{R}{r}}) \right\}$ such that

$$V_0 = \left\{ \int_{\Omega_R} \int_{\Omega_r} \Phi_{0;y}^{r;p}(\bar{x}) G(\bar{x}) d\omega_r(\bar{x}) \tilde{\Phi}_{0;y}^{R;p}(\cdot) d\omega_R(\bar{y}) \mid G \in \mathcal{R}(\Lambda_{\frac{R}{r}}) \right\} \quad , \quad (3.1.23)$$

and similarly, W_j is represented as

$$W_j = \left\{ \int_{\Omega_R} (RWT)_{\Psi}^p(G)(j; \bar{y}) \tilde{\Psi}_{j;y}^{R;p}(\cdot) d\omega_R(\bar{y}) \mid G \in \mathcal{R}(\Lambda_{\frac{R}{r}}) \right\} \quad , \quad (3.1.24)$$

where

$$(RWT)_{\Psi}^p(G)(j; \bar{y}) = \int_{\Omega_r} \Psi_{j;y}^{r;p}(\bar{x}) G(\bar{x}) d\omega_r(\bar{x}) \quad (3.1.25)$$

denotes the regularization wavelet transform of $G(\bar{x})$.

By substituting (3.1.23) and (3.1.24) for V_0 and W_j in (3.1.22), we acquire the representation of scale discrete RMRA V_j and in turn obtain the approximate solution to the regularized problem as

$$F_j(\vec{z}) = \int_{\Omega_R} \int_{\Omega_r} \Phi_{0;y}^{r;p}(\vec{x}) G(\vec{x}) d\omega_r(\vec{x}) \tilde{\Phi}_{0;y}^{R;p}(\vec{z}) d\omega_R(\vec{y}) + \sum_{j=0}^{J-1} \int_{\Omega_R} (RWT)_{\Psi}^p(G)(j; \vec{y}) \tilde{\Psi}_{j;y}^{R;p}(\vec{z}) d\omega_R(\vec{y}) \quad , \quad (3.1.26)$$

which is the result of the decomposition and the reconstruction of the gravity signal in terms of spherical regularization scaling function and wavelet packets, and

$$F(\vec{z}) = \lim_{J \rightarrow \infty} F_j(\vec{z}) = \lim_{J \rightarrow \infty} T_j G(\vec{x}) \quad , \quad \vec{x} \in \Omega_r \quad , \quad \vec{z} \in \Omega_R \quad (3.1.27)$$

is the regularized solution to the inverse problem (3.1.5).

3.2. Approximate Solution to the Inverse Problem and Tikhonov Spherical Regularization Wavelets

In this section, we obtain the formula for the approximate solution to the inverse problem that can be realized in numerical implementation.

Let F_J , the regularized solution to the inverse problem of wavelet resolution level J , be represented as

$$F_J(\bar{z}) = F_0(\bar{z}) + \sum_{j=0}^{J-1} d_j(\bar{z}) \quad , \quad \bar{z} \in \Omega_R \quad , \quad (3.2.1)$$

where $F_0(\bar{z})$ denotes the regularized solution of wavelet resolution level 0, which is the first term of the right-hand side of the equation (3.1.26), and $d_j(\bar{z})$ is the added details at each wavelet resolution level j , whose sum over j corresponds to the second term of the right-hand side of (3.1.26).

Now we rewrite $F_0(\bar{z})$ using the definition of $\Phi_{0;y}^{r;p}$ and $\tilde{\Phi}_{0;y}^{R;p}$ and the orthonormal property of the spherical harmonics in (2.1.7):

$$\begin{aligned} F_0(\bar{z}) &= \int_{\Omega_R} \int_{\Omega_r} \Phi_{0;y}^{r;p}(\bar{x}) G(\bar{x}) d\omega_r(\bar{x}) \tilde{\Phi}_{0;y}^{R;p}(\bar{z}) d\omega_R(\bar{y}) \\ &= \int_{\Omega_R} \int_{\Omega_r} G(\bar{x}) \sum_{n=0}^{\infty} \sum_{j=1}^{2n+1} \left(\Phi_0^p \right)^\wedge(n) Y_{n,j}^R(\bar{y}) Y_{n,j}^r(\bar{x}) d\omega_r(\bar{x}) \sum_{m=0}^{\infty} \sum_{i=1}^{2m+1} \left(\Phi_0^p \right)^\wedge(m) Y_{m,i}^R(\bar{y}) Y_{m,i}^R(\bar{z}) d\omega_R(\bar{y}) \\ &= \int_{\Omega_r} G(\bar{x}) \sum_{n=0}^{\infty} \sum_{j=1}^{2n+1} \left(\left(\Phi_0^p \right)^\wedge(n) \right)^2 Y_{n,j}^r(\bar{x}) Y_{n,j}^R(\bar{z}) d\omega_r(\bar{x}) \quad , \end{aligned} \quad (3.2.2)$$

for $\bar{x} \in \Omega_r$ and $\bar{z}, \bar{y} \in \Omega_R$.

By utilizing (2.1.12), equation (3.2.2) yields,

$$F_0(\bar{z}) = \int_{\Omega_r} G(\bar{x}) \sum_{n=0}^{\infty} \left((\Phi_0^p)^\wedge(n) \right)^2 \sum_{j=1}^{2n+1} \frac{1}{rR} Y_{n,j} \left(\frac{\bar{x}}{|\bar{x}|} \right) Y_{n,j} \left(\frac{\bar{z}}{|\bar{z}|} \right) d\omega_r(\bar{x}) \quad . \quad (3.2.3)$$

Now by applying the Addition theorem (2.1.25) to (3.2.3), we get

$$F_0(\bar{z}) = \frac{1}{rR} \sum_{n=0}^{\infty} \frac{2n+1}{4\pi} \left((\Phi_0^p)^\wedge(n) \right)^2 \int_{\Omega_r} G(\bar{x}) P_n \left(\frac{\bar{x}}{|\bar{x}|} \cdot \frac{\bar{z}}{|\bar{z}|} \right) d\omega_r(\bar{x}) \quad . \quad (3.2.4)$$

Similarly, $d_j(\bar{z})$ becomes:

$$\begin{aligned} d_j(\bar{z}) &= \int_{\Omega_R} (RWT)_{\Psi}^p(G)(j; \bar{y}) \tilde{\Psi}_{j;y}^{R;p}(\bar{z}) d\omega_R(\bar{y}) \\ &= \int_{\Omega_R} \int_{\Omega_r} \Psi_{j;y}^{r;p}(\bar{x}) G(\bar{x}) d\omega_r(\bar{x}) \tilde{\Psi}_{j;y}^{R;p}(\bar{z}) d\omega_R(\bar{y}) \\ &= \int_{\Omega_R} \int_{\Omega_r} G(\bar{x}) \sum_{n=0}^{\infty} \sum_{i=1}^{2n+1} \left(\Psi_j^p \right)^\wedge(n) Y_{n,i}^R(\bar{y}) Y_{n,i}^r(\bar{x}) d\omega_r(\bar{x}) \sum_{m=0}^{\infty} \sum_{k=1}^{2m+1} \left(\Psi_j^p \right)^\wedge(m) Y_{m,k}^R(\bar{y}) Y_{m,k}^R(\bar{z}) d\omega_R(\bar{y}) \\ &= \int_{\Omega_r} G(\bar{x}) \sum_{n=0}^{\infty} \sum_{i=1}^{2n+1} \left(\Psi_j^p \right)^\wedge(n) Y_{n,i}^r(\bar{x}) Y_{n,i}^R(\bar{z}) d\omega_r(\bar{x}) \quad . \end{aligned} \quad (3.2.5)$$

Again, applying (2.1.12) to (3.2.5) yields,

$$d_j(\bar{z}) = \int_{\Omega_r} G(\bar{x}) \sum_{n=0}^{\infty} \left((\Psi_j^p)^\wedge(n) \right)^2 \sum_{i=1}^{2n+1} \frac{1}{rR} Y_{n,i} \left(\frac{\bar{x}}{|\bar{x}|} \right) Y_{n,i} \left(\frac{\bar{z}}{|\bar{z}|} \right) d\omega_r(\bar{x}) \quad . \quad (3.2.6)$$

By using the Addition theorem, we obtain

$$d_j(\bar{z}) = \frac{1}{rR} \sum_{n=0}^{\infty} \frac{2n+1}{4\pi} \left((\Psi_j^p)^\wedge(n) \right)^2 \int_{\Omega_r} G(\bar{x}) P_n \left(\frac{\bar{x}}{|\bar{x}|} \cdot \frac{\bar{z}}{|\bar{z}|} \right) d\omega_r(\bar{x}) \quad . \quad (3.2.7)$$

The equation (3.2.4) and (3.2.7) are of the form that can easily be realized in numerical algorithms. By combining those two equations we acquire the approximate solution to the inverse problem (3.1.5) that is numerically implementable:

$$\begin{aligned} F_J(\bar{z}) &= \frac{1}{rR} \sum_{n=0}^N \frac{2n+1}{4\pi} \left((\Phi_0^p)^\wedge(n) \right)^2 \int_{\Omega_r} G(\bar{x}) P_n \left(\frac{\bar{x}}{|\bar{x}|} \cdot \frac{\bar{z}}{|\bar{z}|} \right) d\omega_r(\bar{x}) \\ &+ \sum_{j=0}^{J-1} \frac{1}{rR} \sum_{n=0}^N \frac{2n+1}{4\pi} \left((\Psi_j^p)^\wedge(n) \right)^2 \int_{\Omega_r} G(\bar{x}) P_n \left(\frac{\bar{x}}{|\bar{x}|} \cdot \frac{\bar{z}}{|\bar{z}|} \right) d\omega_r(\bar{x}) \quad , \quad (3.2.8) \end{aligned}$$

for $\bar{x} \in \Omega_r$ and $\bar{z} \in \Omega_R$, where N denotes the maximum degree of Legendre polynomials.

Now, we introduce the scale discrete Tikhonov spherical regularization scaling function and wavelet packet (Schneider, 1997), whose Legendre coefficients are to be used in (3.2.8) in solving the inverse problem:

$$\left(\Phi_j^p \right)^\wedge(n) = \left(\frac{\sigma_n}{\sigma_n^2 + \gamma_j^2} \right)^{\frac{1}{2}} \quad \text{for } j \in \mathbb{Z} \quad , \quad n \in \mathbb{N}_0 \quad , \quad (3.2.9)$$

$$\left(\Psi_j^p \right)^\wedge(n) = \left(\frac{\sigma_n}{\sigma_n^2 + \gamma_{j+1}^2} - \frac{\sigma_n}{\sigma_n^2 + \gamma_j^2} \right)^{\frac{1}{2}} \quad \text{for } j \in \mathbb{Z} \quad , \quad n \in \mathbb{N}_0 \quad , \quad (3.2.10)$$

where γ_j denotes the regularization parameter of wavelet level j , which is of great importance as it controls the regularization level as well as determines how much

“detailed information” will be added at each wavelet resolution level. The method to find the optimal value of γ_j will be discussed in section 3.4.

Recalling (2.2.6), (2.2.10), (3.1.6) and (3.1.16), the regularization filter $f_{\gamma_j}(\sigma_n)$ of wavelet level J takes the form

$$f_{\gamma_j}(\sigma_n) = \frac{\sigma_n^2}{\sigma_n^2 + \gamma_j^2} \quad \text{for } J \in \mathbb{Z}, \quad n \in \mathbb{N}_0, \quad (3.2.11)$$

for the scale discrete Tikhonov spherical regularization scaling function and wavelet packets. It is a simple task to confirm that $f_{\gamma_j}(\sigma_n)$ meets the properties of the regularization filter illustrated in section 3.1.

Fig. 3.2.1 and **Fig. 3.2.2** are the sample plots for the Legendre coefficient of scale discrete Tikhonov spherical regularization mother scaling function $(\Phi_0^p)^\wedge(n)$ (for $j = 0$) and wavelet packet $(\Psi_j^p)^\wedge(n)$ (for $j = 2, 4, 6$), respectively employing the spherical symbol of the direct upward propagation operator $\sigma_n = \left(\frac{R}{r}\right)^n$ and the SGG operator

$\sigma_n = \left(\frac{R}{r}\right)^n \frac{(n+1)(n+2)}{r^2}$. The regularization parameters used in the plots are: $\gamma_0 = 9.0 \times 10^{-2}$, $\gamma_1 = 5.0 \times 10^{-2}$, $\gamma_2 = 2.0 \times 10^{-2}$, $\gamma_3 = 4.0 \times 10^{-3}$, $\gamma_4 = 1.0 \times 10^{-3}$, $\gamma_5 = 2.0 \times 10^{-4}$ and $\gamma_6 = 5.0 \times 10^{-5}$ for **Fig. 3.2.1** and $\gamma_0 = 2.0 \times 10^{-12}$, $\gamma_1 = 7.0 \times 10^{-13}$, $\gamma_2 = 2.0 \times 10^{-13}$, $\gamma_3 = 8.0 \times 10^{-14}$, $\gamma_4 = 4.0 \times 10^{-14}$, $\gamma_5 = 2.0 \times 10^{-14}$ and $\gamma_6 = 5.0 \times 10^{-15}$ for **Fig. 3.2.2**. The parameter choices for the Earth’s surface radius R and the satellite’s orbit radius r are $R = 6378136.3$ m and $r = 6678136.3$ m, assuming a satellite altitude of 300 km. Either plot plainly exhibits the essential properties of the spherical regularization wavelets in frequency domain:

1. The scaling function and wavelet packets act as band pass filters for the gravity signal.
2. As the wavelet resolution level increases, the wavelet filter moves toward the higher frequency (*i.e.* larger n), correlating the wavelet level with the frequency of the signal.
3. The amplitude of the Legendre coefficient of the wavelet increases with the wavelet level due to the ill-posed nature of the inverse problem (Schneider 1997).

In **Fig. 3.2.3** and **Fig. 3.2.4** are the sample plots for the scale discrete Tikhonov spherical regularization mother scaling function $\Phi_0^p = \sum_{n=0}^{\infty} \frac{2n+1}{4\pi} (\Phi_0^p)^\wedge(n) P_n$ (for $j = 0$) and wavelet packet $\Psi_j^p = \sum_{n=0}^{\infty} \frac{2n+1}{4\pi} (\Psi_j^p)^\wedge(n) P_n$ (for $j = 2, 4, 6$) with respect to the angular distance from the location where the signal is to be decomposed and reconstructed, in both the direct and the SGG case, with the same regularization parameters as were used to plot **Fig. 3.2.1** and **Fig. 3.2.2**. The upper limit of the summation was set to be $N = 600$. Either plot shows the wavelet's localization property in space domain:

1. The scaling function and wavelet packets exhibit localized support in scales.
2. As the wavelet resolution level increases, the localization becomes stronger – the higher the wavelet level is, the finer scale localization of the signal occurs.
3. The amplitude of wavelet increases with the wavelet level, attesting to the ill-posed nature of the problem.

The numerical solution to the inverse problem applying Tikhonov spherical regularization wavelet packets will be presented in later chapters.

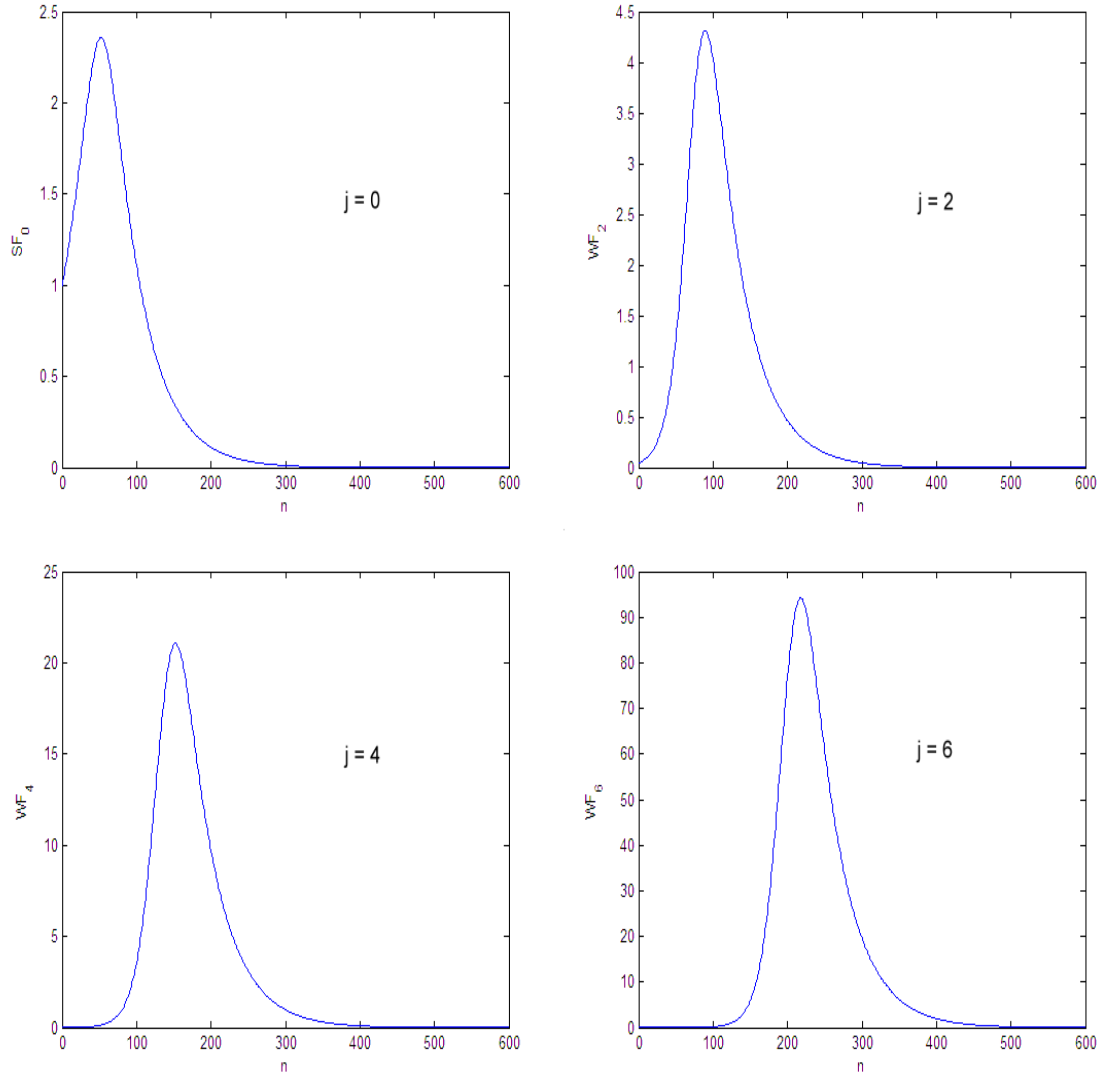


Fig. 3.2.1. The plots of the Legendre coefficient of scale discrete Tikhonov spherical regularization scaling function $(\Phi_0^p)^\wedge(n)$ ($j = 0$) and wavelet packet $(\Psi_j^p)^\wedge(n)$ ($j = 2, 4, 6$) for the spherical symbol of the direct upward propagation operator $\sigma_n = \left(\frac{R}{r}\right)^n$.

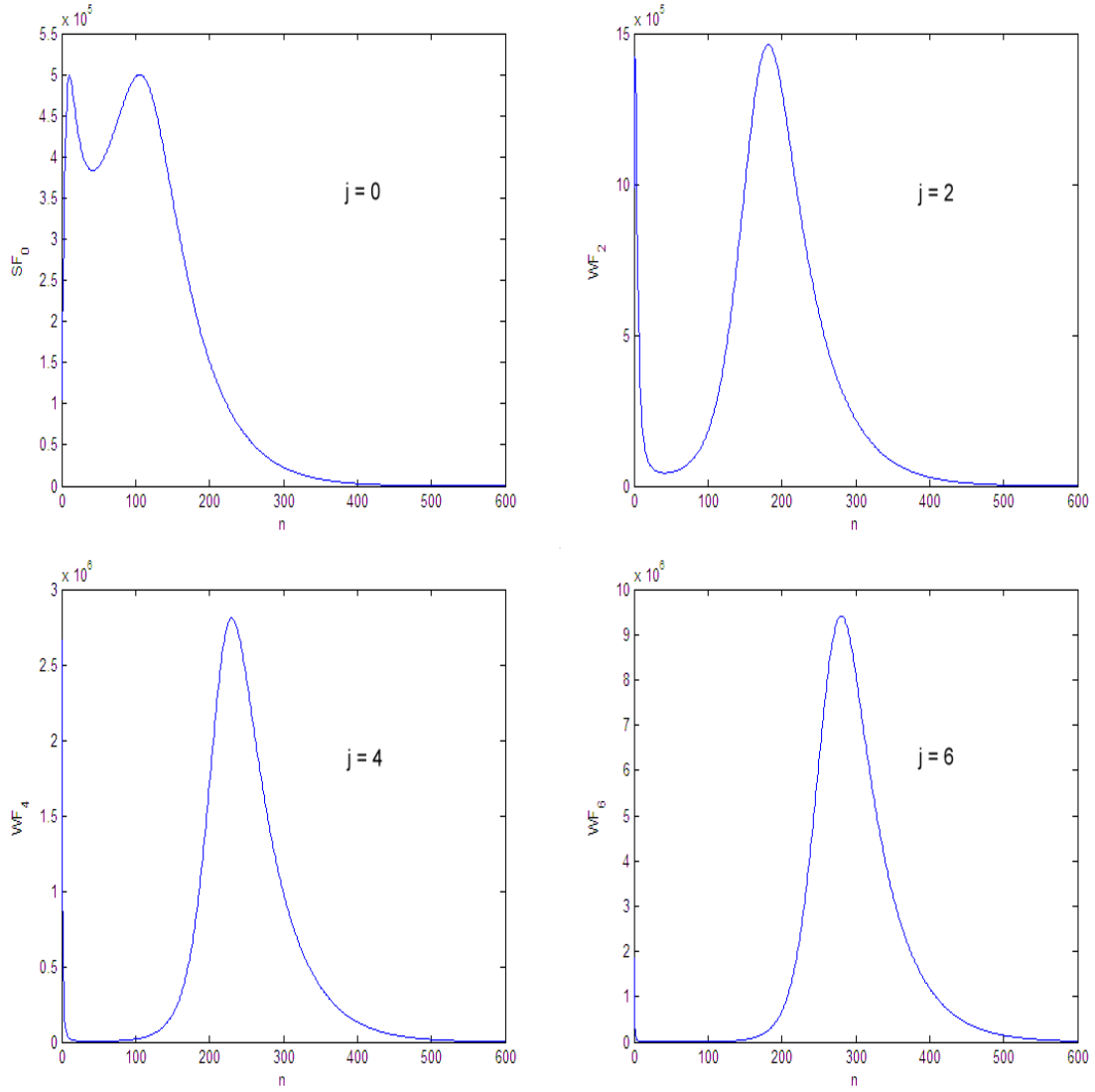


Fig. 3.2.2. The plots of the Legendre coefficient of scale discrete Tikhonov spherical regularization scaling function $(\Phi_0^p)^\wedge(n)$ ($j = 0$) and wavelet packet $(\Psi_j^p)^\wedge(n)$ ($j = 2, 4, 6$) for the spherical symbol of the SGG operator $\sigma_n = \left(\frac{R}{r}\right)^n \frac{(n+1)(n+2)}{r^2}$.

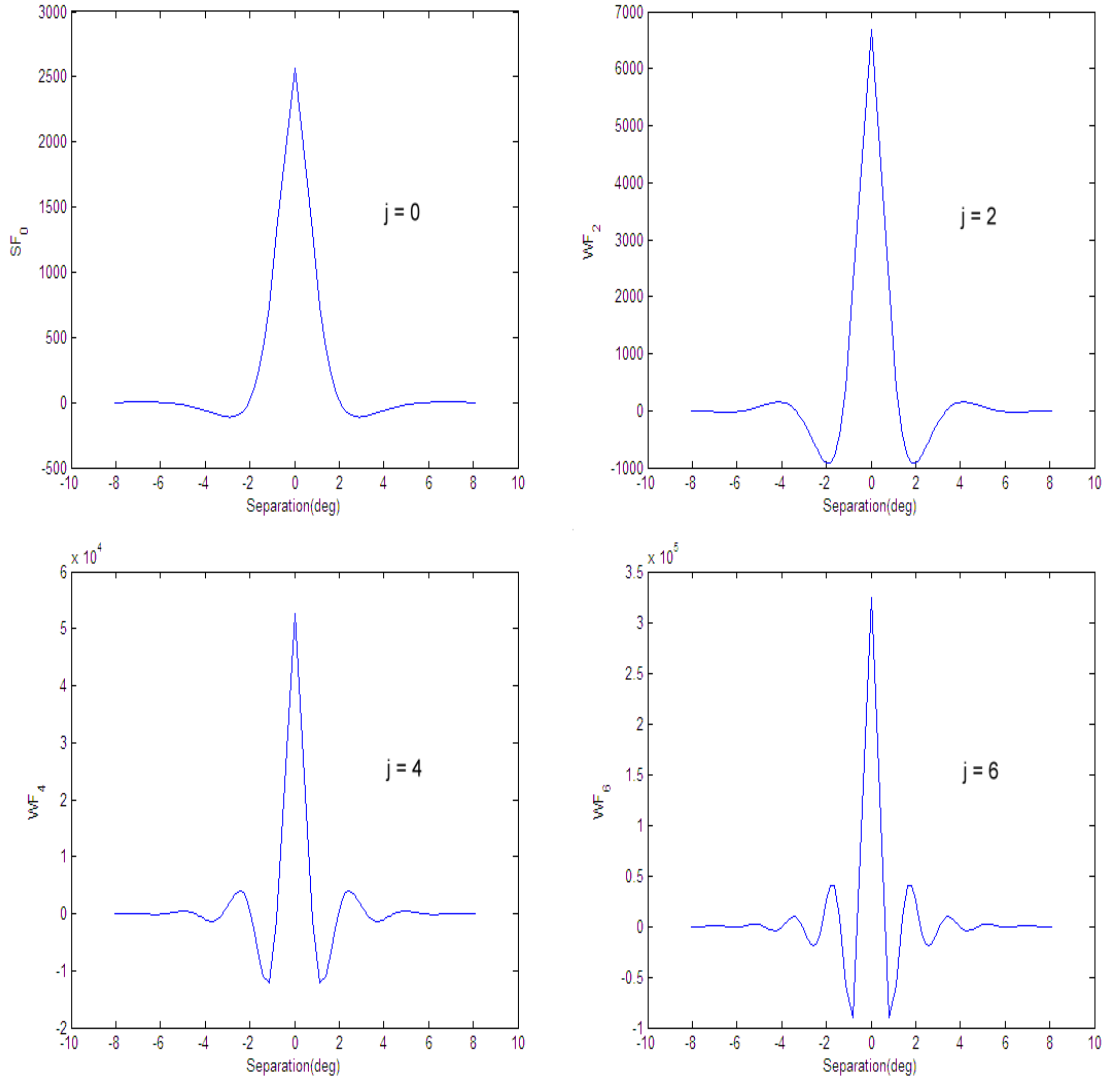


Fig. 3.2.3. The plots of the scale discrete Tikhonov spherical regularization scaling function $\Phi_0^p = \sum_{n=0}^{600} \frac{2n+1}{4\pi} (\Phi_0^p)^\wedge(n) P_n$ and wavelet packet $\Psi_j^p = \sum_{n=0}^{600} \frac{2n+1}{4\pi} (\Psi_j^p)^\wedge(n) P_n$ for the direct upward propagation operator, with respect to the angular distance (in degrees) from the location where the signal is decomposed and reconstructed.

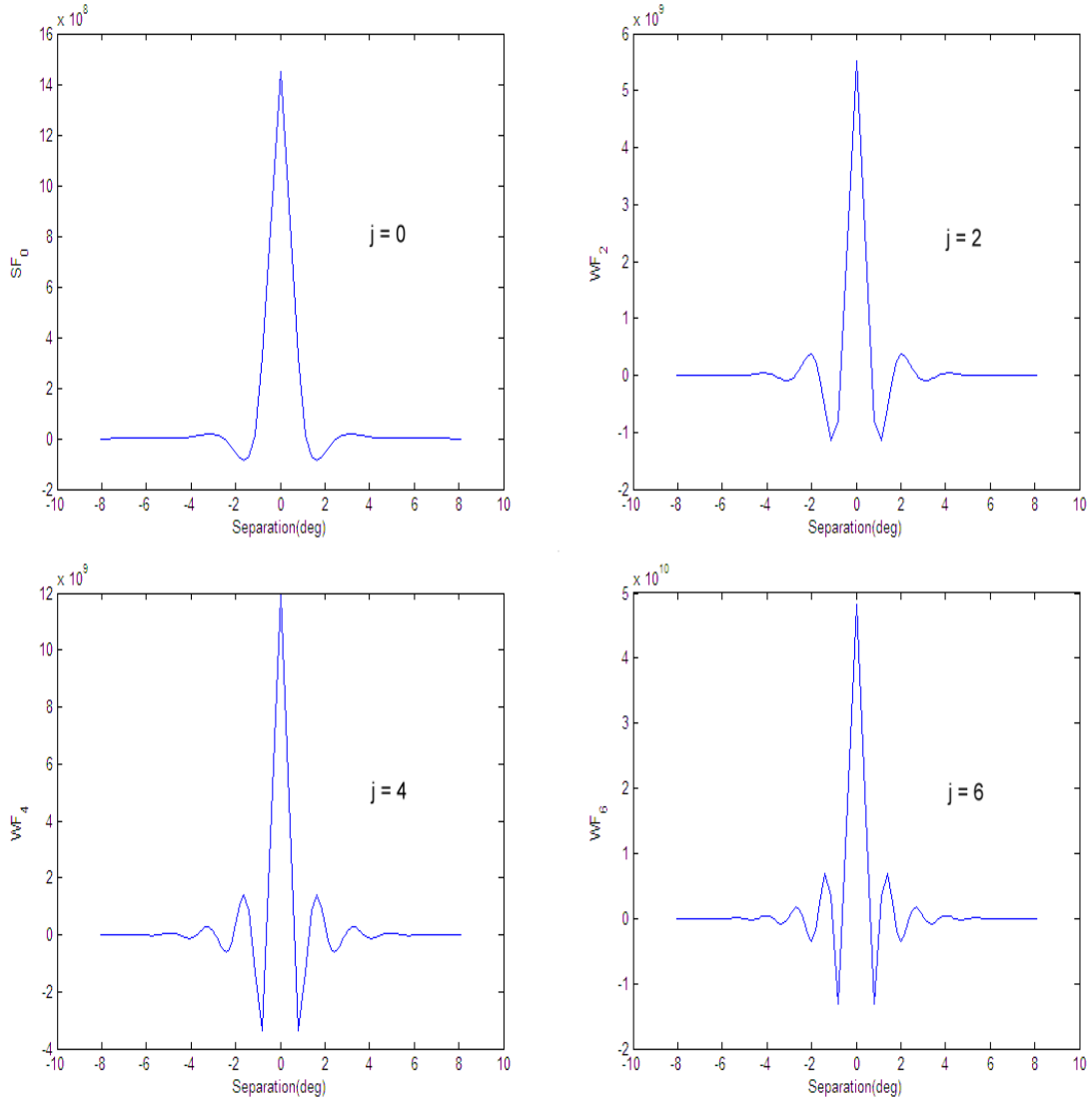


Fig. 3.2.4. The plots of the scale discrete Tikhonov spherical regularization scaling function $\Phi_0^p = \sum_{n=0}^{600} \frac{2n+1}{4\pi} (\Phi_0^p)^{\wedge}(n) P_n$ and wavelet packet $\Psi_j^p = \sum_{n=0}^{600} \frac{2n+1}{4\pi} (\Psi_j^p)^{\wedge}(n) P_n$ for the SGG operator, with respect to the angular distance (in degree) from the location where the signal is decomposed and reconstructed.

3.3. Local Gravity Solution

Unlike the spherical harmonics representation of the gravity field where only one set of global solutions for the spherical harmonics coefficients is available, a wavelet model uses locally supported basis functions. Our spherical regularization wavelets model allows us to locally solve the inverse problem to recover only the local gravity solution and to take advantage of the regions with better sampled measurements than others, which is one of the greatest advantages of the wavelet model and the focus of this study.

Let us consider local regions on the spherical surfaces Ω_r^S and $\Omega_R^{\tilde{S}}$. The regularization of the inverse problem for these local regions can be represented as

$$F_J^{\tilde{S}}(\vec{z}) = T_J G^S(\vec{x}) \quad , \quad (3.3.1)$$

where $F_J^{\tilde{S}}(\vec{z})$ and $G^S(\vec{x})$ are defined by

$$G^S(\vec{x}) = \begin{cases} G(\vec{x}) & \text{for } \vec{x} \in \Omega_r^S \\ 0 & \text{elsewhere} \end{cases} \quad , \quad (3.3.2)$$

$$F_J^{\tilde{S}}(\vec{z}) = \begin{cases} T_J G^S(\vec{x}) & \text{for } \vec{z} \in \Omega_R^{\tilde{S}} \\ 0 & \text{elsewhere} \end{cases} \quad , \quad (3.3.3)$$

and T_J denotes the regularization of the inverse operator $\Lambda_{\frac{R}{r}}^{-1}$ of wavelet resolution level J (Schneider, 1997).

Now the approximate solution to the inverse problem in (3.2.8) can be adapted for the local problem in the following way:

$$\begin{aligned}
F_J^{\tilde{s}}(\bar{z}) &= \frac{1}{rR} \sum_{n=0}^N \frac{2n+1}{4\pi} \left((\Phi_0^p)^\wedge(n) \right)^2 \int_{\Omega_r^s} G^s(\bar{x}) P_n \left(\frac{\bar{x}}{|\bar{x}|} \cdot \frac{\bar{z}}{|\bar{z}|} \right) d\omega_r(\bar{x}) \\
&+ \sum_{j=0}^{J-1} \frac{1}{rR} \sum_{n=0}^N \frac{2n+1}{4\pi} \left((\Psi_j^p)^\wedge(n) \right)^2 \int_{\Omega_r^s} G^s(\bar{x}) P_n \left(\frac{\bar{x}}{|\bar{x}|} \cdot \frac{\bar{z}}{|\bar{z}|} \right) d\omega_r(\bar{x}) \quad , \quad (3.3.4)
\end{aligned}$$

which is the approximate local solution to the regularized inverse problem and the one we will utilize to recover the local surface gravity field in the following numerical simulations.

3.4. Choice of Regularization Parameter by Discrepancy Principle

The Legendre coefficient of the spherical regularization scaling function and wavelet packet contains γ_j , the regularization parameter of the wavelet resolution level j . An optimal value for γ_j can be determined by satisfying the Discrepancy principle (Morozov, 1966) in the following way:

$$\|G^\varepsilon - G\|_{\mathcal{L}^2(\Omega_r)} = \left\| \Lambda_{\frac{R}{r}} T_{(\gamma_j)_{opt}} G - G \right\|_{\mathcal{L}^2(\Omega_r)} \leq \varepsilon \quad , \quad (3.4.1)$$

where G is the gravity signal at the satellite's orbit radius r (the gravity measurements at the satellite's altitude), $G^\varepsilon = \Lambda_{\frac{R}{r}} T_{(\gamma_j)_{opt}} G$ is the regularized signal of G and $T_{(\gamma_j)_{opt}} : \mathcal{L}^2(\Omega_r) \rightarrow \mathcal{L}^2(\Omega_R)$ denotes the regularization of the inverse operator $\Lambda_{\frac{R}{r}}^{-1}$ of wavelet resolution level J with the optimal regularization parameter $(\gamma_j)_{opt}$. Schneider (1997) used the Discrepancy principle to find the regularization parameter for scale continuous wavelets. We are, however, required to find the formula for the scale discrete case because our regularized solution uses a scale discrete scaling function and wavelet packet for the numerical implementation purpose.

Let us consider the spherical symbol of the operator $\Lambda_{\frac{R}{r}} T_{(\gamma_j)_{opt}}$. In the preceding section 3.1, we defined $(\Lambda_{\frac{R}{r}})^\wedge(n) = \sigma_n$ and from (3.1.16) we could determine $(T_J)^\wedge(n) = ((\Phi_J^p)^\wedge(n))^2$. If we now define the spherical symbol $(\Phi_J^p)_{(\gamma_j)_{opt}}^\wedge(n)$ as

$$(\Phi_J^p)_{(\gamma_j)_{opt}}^\wedge(n) = \left(\frac{\sigma_n}{\sigma_n^2 + (\gamma_j)_{opt}^2} \right)^{\frac{1}{2}} \quad (3.4.2)$$

in accordance with the scale discrete Tikhonov spherical regularization scaling function, $\left(\Lambda_{\frac{r}{r}} T_{(\gamma_J)_{opt}}\right)^\wedge(n) = \left(\left(\Phi_J^p\right)_{(\gamma_J)_{opt}}^\wedge(n)\right)^2 \sigma_n$ satisfies (2.2.7) and (2.2.8). The operator $\Lambda_{\frac{r}{r}} T_{(\gamma_J)_{opt}}$ is thus SPDO of order $-\infty$ and the function $G^\varepsilon : \Omega_r \rightarrow \mathbb{R}$ can be represented by the following convolution form:

$$G^\varepsilon(\bar{y}) = \Lambda_{\frac{r}{r}} T_{(\gamma_J)_{opt}} G(\bar{x}) = \int_{\Omega_r} G(\bar{x}) K_{(\gamma_J)_{opt}}(\bar{x}, \bar{y}) d\omega_r(\bar{x}) \quad , \quad \bar{x}, \bar{y} \in \Omega_r \quad , \quad (3.4.3)$$

where $K_{(\gamma_J)_{opt}}(\bar{x}, \bar{y})$ is the C -kernel of $\Lambda_{\frac{r}{r}} T_{(\gamma_J)_{opt}}$ defined by

$$K_{(\gamma_J)_{opt}}(\bar{x}, \bar{y}) = \sum_{n=0}^{\infty} \sum_{j=1}^{2n+1} \left(\left(\Phi_J^p\right)_{(\gamma_J)_{opt}}^\wedge(n)\right)^2 \sigma_n Y_{n,j}^r(\bar{x}) Y_{n,j}^r(\bar{y}) \quad . \quad (3.4.4)$$

Substituting (3.4.4) for $K_{(\gamma_J)_{opt}}(\bar{x}, \bar{y})$ in the equation (3.4.3) and regrouping leads us to

$$G^\varepsilon(\bar{y}) = \sum_{n=0}^{\infty} \left(\left(\Phi_J^p\right)_{(\gamma_J)_{opt}}^\wedge(n)\right)^2 \sigma_n \int_{\Omega_r} G(\bar{x}) \sum_{j=1}^{2n+1} Y_{n,j}^r(\bar{x}) Y_{n,j}^r(\bar{y}) d\omega_r(\bar{x}) \quad . \quad (3.4.5)$$

Now applying (2.1.12) and the Addition theorem (2.1.25) to the equation (3.4.5) yields

$$G^\varepsilon(\bar{y}) = \frac{1}{r^2} \sum_{n=0}^{\infty} \frac{2n+1}{4\pi} \left(\left(\Phi_J^p\right)_{(\gamma_J)_{opt}}^\wedge(n)\right)^2 \sigma_n \int_{\Omega_r} G(\bar{x}) P_n\left(\frac{\bar{x}}{|\bar{x}|} \cdot \frac{\bar{y}}{|\bar{y}|}\right) d\omega_r(\bar{x}) \quad , \quad (3.4.6)$$

and (3.4.1) thus becomes

$$\left\| \frac{1}{r^2} \sum_{n=0}^N \frac{2n+1}{4\pi} \left(\left(\Phi_J^p \right)_{(\gamma_J)_{opt}}^\wedge (n) \right)^2 \sigma_n \int_{\Omega_r} G(\bar{x}) P_n \left(\frac{\bar{x} \cdot \bar{y}}{|\bar{x}| |\bar{y}|} \right) d\omega_r(\bar{x}) - G(\bar{y}) \right\|_{\mathcal{L}^2(\Omega_r)} \leq \varepsilon \quad . \quad (3.4.7)$$

In (3.4.7), we changed the upper limit of the sum from ∞ to N for numerical implementation. Now by finding $(\gamma_J)_{opt}$ that satisfies (3.4.7), we can obtain the optimal regularization parameter for an arbitrary wavelet resolution level J . In practice, however, we set the largest value of $(\gamma_J)_{opt}$ satisfying the condition (3.4.7) with a given ε (e.g. 10% of the amplitude of $|G|$) to be γ_0 , the regularization parameter for the mother scaling function Φ_0^p . Since the scaling function must satisfy the requirement $\left(\left(\Phi_{J+1}^p \right)^\wedge (n) \right)^2 \geq \left(\left(\Phi_J^p \right)^\wedge (n) \right)^2$, the regularization parameter at each successive wavelet level should be smaller than the previous one. Therefore, the regularization parameters can be chosen as a set of monotonously decreasing sequence $\{\gamma_j\}$, starting from γ_0 .

3.5. Upward Continuation

In numerical application, we often need to convert the original surface gravity anomaly or gravity potential to a certain form of gravity measurements at the satellite's altitude according to the type of mission (*e.g.* second order radial derivative of gravity potential for SGG mission) in order to compare the recovered gravity solution to the original surface gravity data. This process is called upward continuation, which is a well-posed problem. The obtained gravity measurement data at the satellite altitude is then used to recover the surface gravity solution by solving the inverse problem through the spherical regularization wavelet transform as explained in the section 3.1.

Let us assume a spherical Earth. The gravity potential or its derivative $U(\vec{x})$ on the spherical surface Ω_r , where $\vec{x} \in \Omega_r$, can be propagated from $F(\vec{z})$, the gravity potential on the Earth's surface Ω_R , where $\vec{z} \in \Omega_R$ and $r > R$, through upward continuation by solving the following SPDO equation (Svensson 1983; Schneider 1997):

$$U(\vec{x}) = \left(A_{\frac{R}{r}} F \right) (\vec{x}) \quad , \quad (3.5.1)$$

where $A_{\frac{R}{r}}$ is the SPDO of order $-\infty$ whose spherical symbol denotes:

$$\text{direct upward propagation operator: } \left(A_{\frac{R}{r}} \right)^\wedge(n) = \left(\frac{R}{r} \right)^n \quad (3.5.2)$$

$$\text{SST operator: } \left(A_{\frac{R}{r}} \right)^\wedge(n) = \left(\frac{R}{r} \right)^n \frac{n+1}{r} \quad (3.5.3)$$

$$\text{SGG operator: } \left(A_{\frac{R}{r}} \right)^\wedge(n) = \left(\frac{R}{r} \right)^n \frac{(n+1)(n+2)}{r^2} \quad (3.5.4)$$

Then the equation (3.5.1) can be represented by a convolution form such that

$$U(\vec{x}) = \int_{\Omega_R} K_{A_{\frac{R}{r}}}(\vec{x}, \vec{z}) F(\vec{z}) d\omega_R(\vec{z}) \quad , \quad \vec{x} \in \Omega_r \quad , \quad \vec{z} \in \Omega_R \quad , \quad (3.5.5)$$

where

$$K_{A_{\frac{R}{r}}}(\vec{x}, \vec{z}) = \sum_{n=0}^{\infty} \sum_{j=1}^{2n+1} \left(A_{\frac{R}{r}}\right)^{\wedge}(n) Y_{n,j}^r(\vec{x}) Y_{n,j}^R(\vec{z}) \quad (3.5.6)$$

is the \mathcal{C} -kernel of $A_{\frac{R}{r}}$ (Schneider 1997).

Now we take a similar approach as in section 3.2 and rewrite (3.5.5) as,

$$\begin{aligned} U(\vec{x}) &= \int_{\Omega_R} \sum_{n=0}^{\infty} \sum_{j=1}^{2n+1} \left(A_{\frac{R}{r}}\right)^{\wedge}(n) Y_{n,j}^r(\vec{x}) Y_{n,j}^R(\vec{z}) F(\vec{z}) d\omega_R(\vec{z}) \\ &= \frac{1}{rR} \sum_{n=0}^{\infty} \left(A_{\frac{R}{r}}\right)^{\wedge}(n) \int_{\Omega_R} F(\vec{z}) \sum_{j=1}^{2n+1} Y_{n,j}^r\left(\frac{\vec{x}}{|\vec{x}|}\right) Y_{n,j}^R\left(\frac{\vec{z}}{|\vec{z}|}\right) d\omega_R(\vec{z}) \\ &= \frac{1}{rR} \sum_{n=0}^{\infty} \frac{2n+1}{4\pi} \left(A_{\frac{R}{r}}\right)^{\wedge}(n) \int_{\Omega_R} F(\vec{z}) P_n\left(\frac{\vec{x} \cdot \vec{z}}{|\vec{x}| |\vec{z}|}\right) d\omega_R(\vec{z}) \quad . \end{aligned} \quad (3.5.7)$$

Therefore, by changing the limit of the sum from ∞ to N , we obtain the following equation:

$$U(\vec{x}) = \frac{1}{rR} \sum_{n=0}^N \frac{2n+1}{4\pi} \left(A_{\frac{R}{r}}\right)^{\wedge}(n) \int_{\Omega_R} F(\vec{z}) P_n\left(\frac{\vec{x} \cdot \vec{z}}{|\vec{x}| |\vec{z}|}\right) d\omega_R(\vec{z}) \quad , \quad (3.5.8)$$

which is the formula to numerically obtain the gravity measurements at the satellite altitude by upward continuation.

Chapter 4. Numerical Aspect of Implementing the Spherical Wavelets Gravity Model

We have developed three different algorithms – the solution to equation (3.2.8) and (3.3.4), the approximate solution to the inverse problem; for satisfying the inequality (3.4.7) to obtain the optimal regularization parameter; and for solving the equation (3.5.8) for the upward continuation. In this chapter, we will discuss the numerical schemes for the surface integration presented in the aforementioned equations and the numerical implementation of the spherical wavelets gravity model for recovering the surface gravity.

4.1. Numerical Integration Schemes

In order to evaluate the surface integral, we built and tested several numerical integrators for the tabulated functions including the trapezoidal rule and Gaussian quadrature. Gaussian quadrature rule approximates a definite integral to a weighted sum of the function values at specific points within the integral limit $[-1,1]$ as

$$\int_{-1}^1 f(x)dx \approx \sum_{i=1}^N w_i f(x_i) \quad , \quad (4.1.1)$$

where w_i is the weight at the point or abscissa x_i . For the integration over the interval $[a, b]$, it takes a more general form:

$$\int_a^b W(x)f(x)dx \approx \sum_{i=1}^N w_i f(x_i) \quad , \quad (4.1.2)$$

where $W(x)$ is a positive weight function. Gaussian quadrature is designed to provide the freedom to choose not only the weighted coefficients, but also the location of the abscissas at which the function is evaluated by employing orthogonal polynomials to remove integrable singularities from the desired integral (*Numerical Recipes*, 1986). One of the most commonly used weight functions is the Gauss-Legendre formula which is given by

$$w_i = \frac{2}{(1-x_i^2)[P'_N(x_i)]^2} \quad \text{for} \quad -1 < x_i < 1 \quad , \quad (4.1.3)$$

where P'_N is the derivative of Legendre polynomial of degree N , given N abscissas to evaluate the integral. The Gauss-Legendre formula scales the integration limit $[a, b]$ to $[-1, 1]$ and provides the abscissas and weights for Gaussian quadrature in the following way:

$$\int_a^b f(x)dx = \frac{b-a}{2} \int_{-1}^1 f\left(\frac{b-a}{2}x + \frac{a+b}{2}\right)dx \approx \frac{b-a}{2} \sum_{i=1}^N w_i f\left(\frac{b-a}{2}x_i + \frac{a+b}{2}\right) \quad . \quad (4.1.4)$$

Gaussian quadrature, however, yields a high order-high accuracy result only when the integrand is very smooth (*Numerical Recipes*, 1986). For the tabulated functions of our interest such as the gravity anomaly on evenly spaced grid points, which is not necessarily very smooth, we found the extended trapezoidal rule to be a better choice for the integration scheme.

The most basic and crudest trapezoidal rule calculates a definite integral of function $f(x)$ by approximating

$$\int_a^b f(x)dx \approx (b-a) \cdot \frac{f(a)+f(b)}{2} \quad . \quad (4.1.5)$$

For M evenly spaced abscissas the extended trapezoidal rule can be applied as

$$\int_a^b f(x)dx \approx \frac{(b-a)}{M-1} \left(\frac{f(x_1)}{2} + f(x_2) + f(x_3) + \dots + f(x_{M-1}) + \frac{f(x_M)}{2} \right) \quad , \quad (4.1.6)$$

where $x_1 = a$ and $x_M = b$ (*Numerical Recipes*, 1986).

One of the most commonly used algorithms for extended trapezoidal rule adds new mid-points to the previously defined grid points at each sequence and makes sequential calls that incorporates the information from previous calls and evaluate the integrand only at the new points necessary to refine the grid (*Numerical Recipes*, 1986).

Fig. 4.1.1 shows how the new mid-points are added with respect to the previous points on the grid at each sequential call following the extended trapezoidal rule.

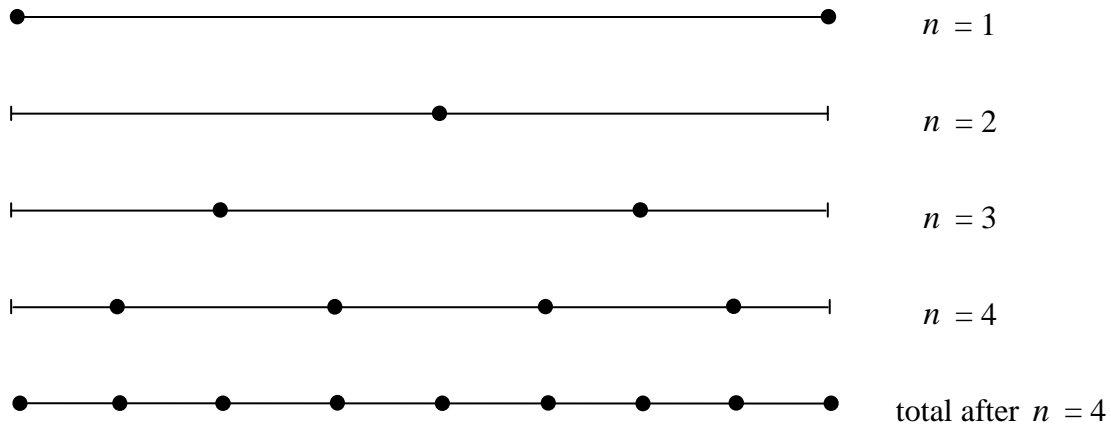


Fig. 4.1.1. Added new mid-points with respect to the previous points on the grid at each sequential call. After fourth call, the total number of points for evaluating the integral is 9. (*Numerical Recipes*, 1986)

The extended trapezoidal rule adds new 2^{n-2} points at n 'th sequence and requires total $2^{n-1} + 1$ evenly spaced grid points for the integration. The integral is evaluated in the following way:

$$x_1 = a + \frac{1}{2} \cdot \frac{(b-a)}{2^{n-2}} \quad , \quad (4.1.7)$$

$$x_i = x_1 + (i-1) \cdot \frac{(b-a)}{2^{n-2}} \quad , \quad (4.1.8)$$

$$S_1 = (b-a) \cdot \frac{f(a) + f(b)}{2} \quad , \quad (4.1.9)$$

$$S_n = \frac{1}{2} \left(S_{n-1} + \frac{(b-a)}{2^{n-2}} \sum_{i=1}^{2^{n-2}} f(x_i) \right) \quad \text{for } n = 2, 3, 4, \dots \quad , \quad (4.1.10)$$

where S_n is the evaluation of the definite integral $\int_a^b f(x)dx$ after n 'th call of the trapezoidal routine. This algorithm is especially handy when one desires to evaluate the integral of an analytic function within a certain level of accuracy because it can be used repeatedly to refine the grid by adding new points until the desired level of accuracy ε is achieved by satisfying the following condition:

$$|S_n - S_{n-1}| \leq \varepsilon \quad \text{for } n = 2, 3, 4, \dots \quad . \quad (4.1.11)$$

Our interest is to establish the integration scheme for the tabulated function $\{ FUNC(i), i = 1, 2, \dots, M \}$ on a total of $M = 2^{N_{\max}-1} + 1$ evenly spaced points, where $FUNC(i)$ denotes the i 'th function value in the array of the tabulated function of size M .

We recovered the integral for $FUNC(i)$ by applying the extended trapezoidal rule such that

$$S_1 = (b-a) \cdot \frac{FUNC(1) + FUNC(M)}{2} \quad , \quad (4.1.12)$$

$$S_n = \frac{1}{2} \left(S_{n-1} + \frac{(b-a)}{2^{n-2}} \sum_{i=1}^{2^{n-2}} FUNC(1 + (2i-1) \cdot 2^{N_{\max}-n}) \right) \quad \text{for } n = 2, 3, 4, \dots, N_{\max} \quad . \quad (4.1.13)$$

The requirement of $2^{n-1} + 1$ abscissas, however, is not an absolute condition to execute the extended trapezoidal rule. In our simulation, we had the global data field and choosing a local region encompassing $2^{n-1} + 1$ points along the either longitude or latitude for recovering surface gravity solution did not pose a problem. In other situations where only a fixed number of data points are available, which do not necessarily satisfy the requirement of $2^{n-1} + 1$ abscissas, we can take a direct approach to the extended trapezoidal rule in (4.1.6) by evaluating the integral in one single step instead of sequential calls of trapezoidal routine in the following way:

$$S = \frac{(b-a)}{M-1} \left(\frac{FUNC(1) + FUNC(M)}{2} + \sum_{i=2}^{M-1} FUNC(i) \right) \quad . \quad (4.1.14)$$

Now let us consider a two-dimensional surface integral of a function $f(\lambda, \varphi)$ on the spherical surface Ω_r , where λ is the longitude ($0 \leq \lambda \leq 2\pi$) and φ is the latitude ($-\frac{\pi}{2} \leq \varphi \leq \frac{\pi}{2}$) in a spherical coordinate. The surface integral can be broken down into two linear integrals:

$$\int_{\Omega_r} f(\lambda, \varphi) d\omega_r = r^2 \int_0^{2\pi} \int_{-\frac{\pi}{2}}^{\frac{\pi}{2}} f(\lambda, \varphi) \cos(\varphi) d\varphi d\lambda \quad , \quad (4.1.15)$$

$$S(\lambda) = \int_{-\frac{\pi}{2}}^{\frac{\pi}{2}} f(\lambda, \varphi) \cos(\varphi) d\varphi \quad , \quad (4.1.16)$$

$$\int_{\Omega_r} f(\lambda, \varphi) d\omega_r = r^2 \int_0^{2\pi} S(\lambda) d\lambda \quad . \quad (4.1.17)$$

The linear integral in the equation (4.1.16) and (4.1.17) then can now be evaluated by employing extended trapezoidal rule.

4.2. Numerical Implementation of the Spherical Wavelets Gravity Model

From several preliminary tests with simulated data sets (which do not necessarily represent the Earth's geodetic signal), we have learned that when using the spherical wavelets model, the local surface gravity solutions recovered from the local satellite measurements can be nearly as accurate as those recovered from the global measurements if the local area where the gravity measurements are acquired is at least 70% larger in both longitudinal and latitudinal directions than the desired solution region.

In order to test our numerical algorithms in a more realistic situation, we generated the Earth's global surface gravity anomaly. In geophysics, the gravity anomaly is defined as the difference between $|\bar{g}|_{geoid}$, the gravity on the geoid, and $|\bar{g}|_{reference}$, the normal gravity on the reference ellipsoid, in the following way:

$$\Delta g \text{ (gravity anomaly)} = |\bar{g}|_{geoid} - |\bar{g}|_{reference} . \quad (4.2.1)$$

Gravity anomaly is often measured in a unit of mGal (milli-Galileo), where 1 mGal is equivalent to 10^{-5} m/s² of acceleration. The Earth's surface gravity acceleration ranges between 976 and 983 Gal. The standard choice of the reference ellipsoid is WGS84, an equipotential ellipsoid with the semi-major axis $a = 6378137.0$ m, the reciprocal of flattening $1/f = 298.257223563$, the theoretical gravity potential $U_0 = 62636851.7146$ m²/s² and the Earth's gravitational constant $\mu = 3986004.418 \times 10^8$ m³/s² (NIMA Technical Report TR8350.2, 2000).

The anomaly we generated, however, is not the actual gravity anomaly, but rather a spherical anomaly, or gravity disturbance, while the Earth as well as the reference system is assumed as a sphere with the same radius. In computing the spherical surface gravity anomaly, we assumed the Earth is spherical with the radius $R = 6378136.3$ m

(real Earth's equatorial radius). For a reference system, we used a sphere with the same radius R with the gravity potential on the surface $V_0 = \frac{\mu}{R} = 62494814.0102 \text{ m}^2/\text{s}^2$, where μ is the Earth's gravitational constant defined in the WGS84 system. We generated the surface gravity potential $V(R, \lambda, \varphi)$ on a 720×360 evenly spaced longitude-latitude grid at a 0.5° resolution from the equation (1.1) and (1.2) using spherical harmonics coefficients of the gravity models GGM02C (with n , the degree and order of spherical harmonics coefficient, up to 200) and EGM96 (for higher n : up to 360). The spherical surface anomaly was then computed by:

$$\Delta g_0 = \frac{V(R, \lambda, \varphi)}{R} - \frac{V_0}{R} \quad , \quad (4.2.2)$$

where, λ denotes geocentric longitude and φ geocentric latitude.

The anomaly at the satellite altitude $h = 300 \text{ km}$ (*i.e.* the orbit radius $r = 6678136.3 \text{ m}$) was generated in a similar way on a 720×360 grid, using the same spherical harmonics coefficients of the GGM02C/EGM96 hybrid model to compute $V(r, \lambda, \varphi)$, the gravity potential at the orbit radius r , and V_r , the gravity potential of the reference sphere at r (the radial distance from the center of the reference sphere), as $V_r = \frac{\mu}{r} = 59687377.4200 \text{ m}^2/\text{s}^2$. The anomaly at the satellite altitude was then computed in the following way:

$$\Delta g_r = \frac{V(r, \lambda, \varphi)}{r} - \frac{V_r}{r} \quad . \quad (4.2.3)$$

It is noteworthy that this at-altitude anomaly can also be obtained with an alternative method by applying a direct upward propagation operator (3.1.2) to the gravity anomaly itself in solving the upward continuation equation (3.5.8). The upward

continued solution was then multiplied by a factor $\frac{R}{r}$, because the upward continuation operator affects the gravity potentials and their difference, but not the radius of the sphere, which is set to be constant.

The simulated at-altitude anomaly was then used as the simulated gravity measurements at the satellite altitude and the surface gravity anomaly was recovered by solving the inverse problem, which was multiplied by a factor of $\frac{r}{R}$ in the final solution.

Fig. 4.2.1 and **Fig. 4.2.2** show the contour maps of the gravity anomaly at the Earth's surface and at the altitude of 300 km. Note how much fine details are lost as the gravity anomaly is smoothed out at altitude, giving another illustration to the nature of the ill-posed problem in treating the downward propagation of the gravity signals.

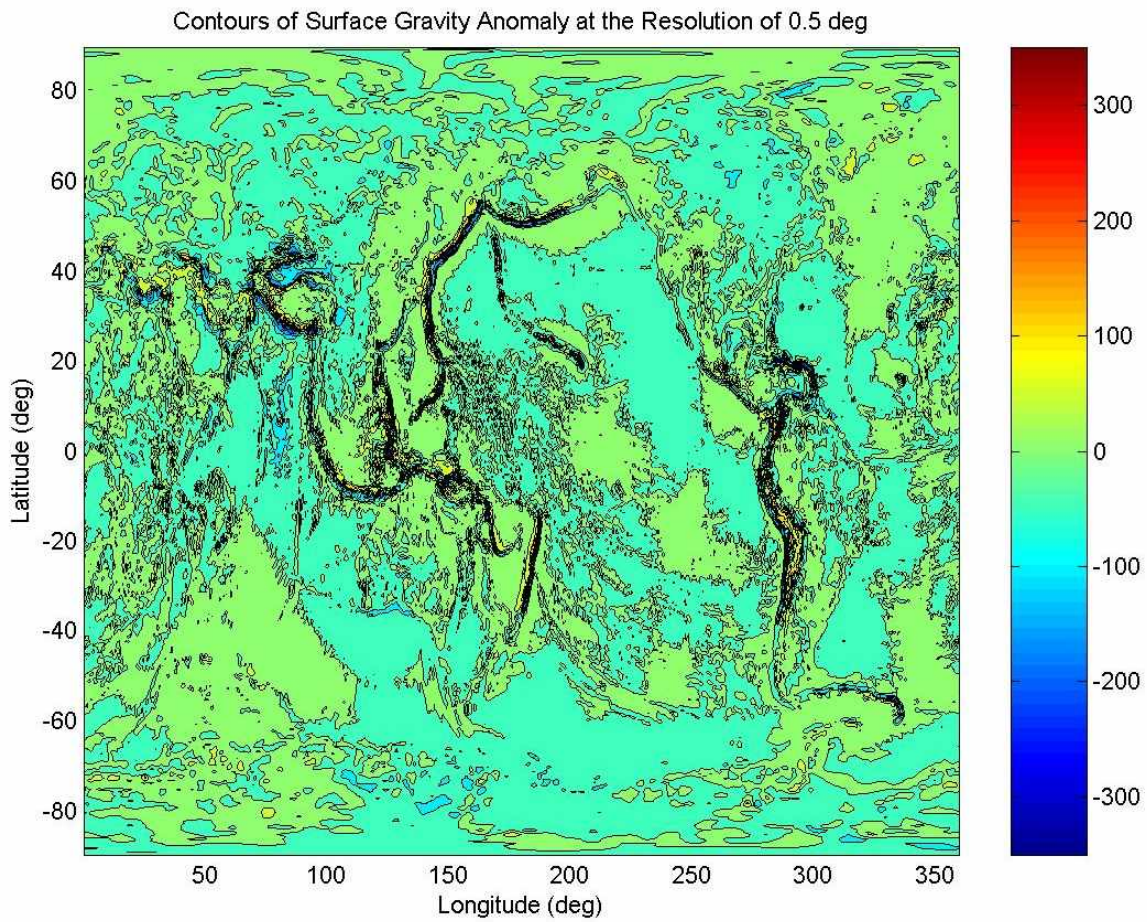


Fig. 4.2.1. Contour map of the global surface gravity anomaly at the resolution of 0.5° . Each contour represents 50 mGal of gravity anomaly difference.

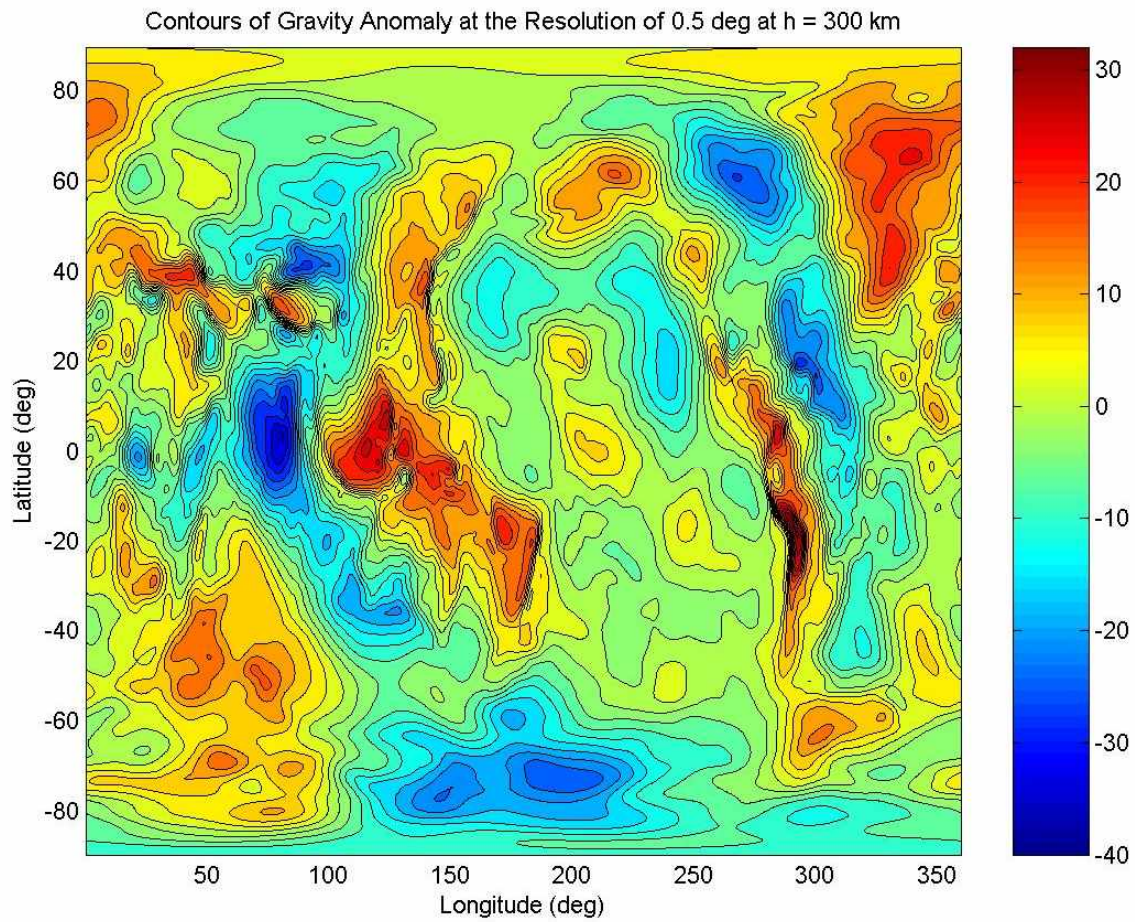


Fig. 4.2.2. Contour map of the simulated gravity anomaly at the satellite altitude $h = 300$ km. Each contour represents 3 mGal of difference.

In order to validate our gravity model and the numerical algorithms, we studied two different local regions, one is the area of $30.25^\circ\text{W} \sim 109.75^\circ\text{W}$ in longitude and $24.75^\circ\text{S} \sim 19.75^\circ\text{N}$ latitude (Region I) and the other $160.25^\circ\text{E} \sim 100.25^\circ\text{W}$ longitude (counterclockwise) and $24.75^\circ\text{S} \sim 24.75^\circ\text{N}$ latitude (Region II). After the local surface regions of interest were chosen, the corresponding local gravity anomaly at the altitude of $h = 300$ km was used to recover the local surface gravity signals. In our simulations we chose the local area at the satellite altitude, from which the gravity measurement data is obtained to solve the inverse problem, to encompass $2^n + 1$ grid points along longitude and $2^{n-1} + 1$ points along latitude (*e.g.* 257 points through longitude and 129 points through latitude), where n is an arbitrary positive integer (except those of **Chapter 9**). The number of data points on the grid or abscissas was chosen such that it could be accommodated in the sequential scheme of the extended trapezoidal rule, as mentioned in section **4.1**, although the restriction would not have been necessary if we employed the single-step extended trapezoidal routine. We set N , the maximum degree of Legendre polynomials included in the solution to the inverse problem to be 300 as the default.

The regularization parameters used in the spherical wavelet transform were obtained as follows. We used (3.4.2) for the Legendre coefficient of the mother scaling function $(\Phi_0^p)^\wedge(n)$ and found γ_0 that satisfies the condition imposed by (3.4.7) within the error set to be 10% of the amplitude of $|G^\varepsilon|$. Since the recovered solution gets closer to the true gravity anomaly as the wavelet resolution level is added, we could perform our simulation in the following way: Starting from γ_0 , generate a monotonously decreasing sequence of γ_j for each added wavelet resolution level j and solve the inverse problem to recover the surface gravity anomaly for each wavelet level until the recovered gravity solution displays “forced” fine signals, which are induced by high frequency wavelets, interfering with the true gravity signals and causing the RMS error $|G - G_j|_{RMS}$ to increase.

The flowcharts of the numerical algorithms for finding the optimal regularization parameter, solving the inverse problem, and performing upward continuation are provided in **Fig. 4.2.3** to **Fig. 4.2.5**.

Once the regularization parameters were determined and the local surface gravity anomaly was recovered from the gravity measurements at the satellite altitude by solving equation (3.3.4), the solution then was compared to the truth data, *i.e.* the surface gravity anomaly generated from GGM02C/EGM96 gravity models. A mean filter was used to the truth data to obtain F_s , the surface gravity anomaly at the different spatial resolutions, in the following way:

$$F_s(\vec{z}_i) = \frac{\sum_j F(\vec{z}_j)}{N_s} \quad \text{for } |\vec{z}_i - \vec{z}_j| \leq \frac{r_s}{2}, \quad (4.2.4)$$

where \vec{z}_i and \vec{z}_j are the grid points on a 720×360 grid set, $F(\vec{z}_j)$ is the surface gravity anomaly at \vec{z}_j , r_s is the spatial resolution and N_s is the total number of grid points \vec{z}_j that satisfies $|\vec{z}_i - \vec{z}_j| \leq \frac{r_s}{2}$ at a given surface position \vec{z}_i . We thus obtained the surface gravity anomaly at the spatial resolution of 1° to 5° to be compared to the recovered gravity solution with the different wavelet resolution levels.

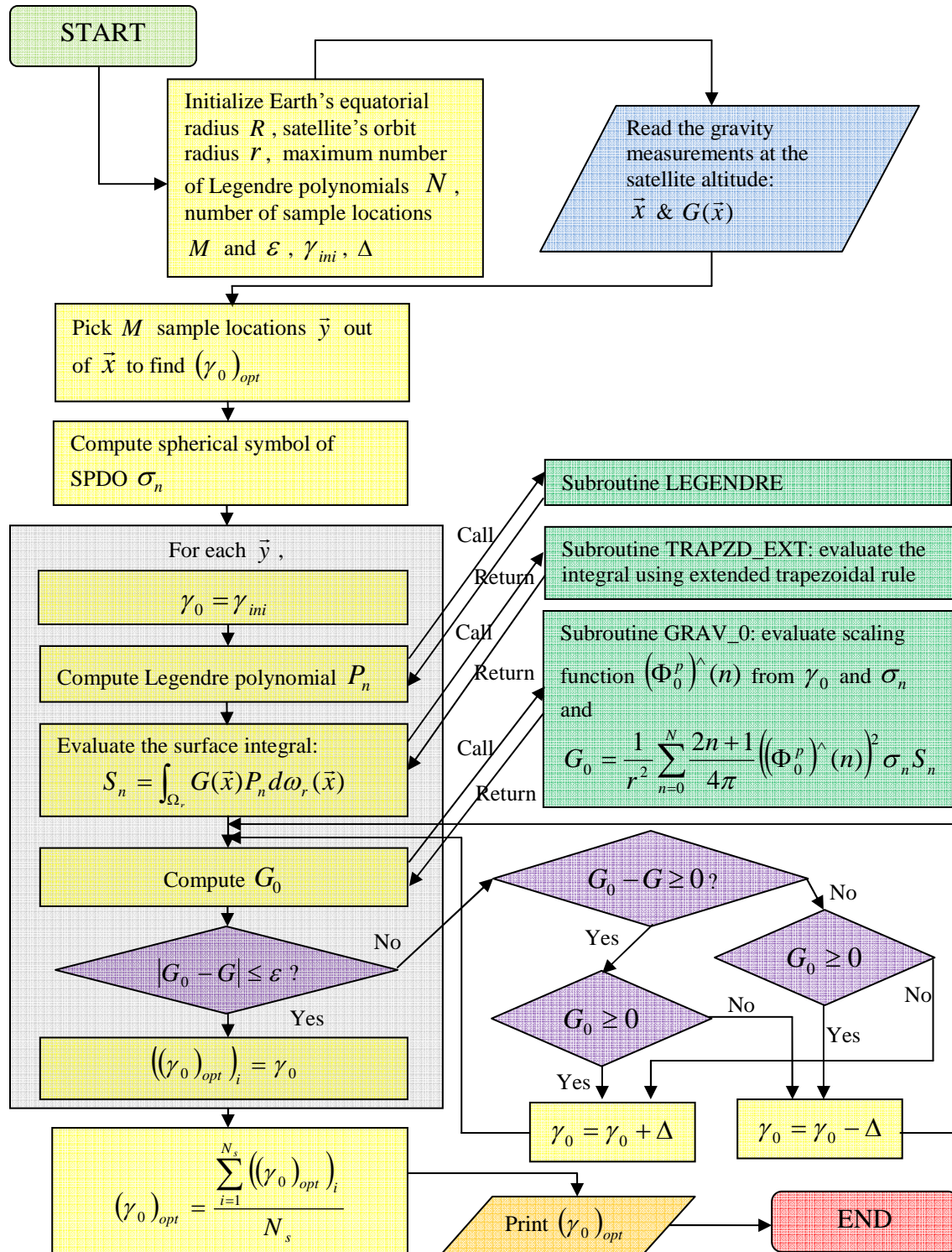


Fig. 4.2.3. Flowchart for finding optimal regularization parameter $(\gamma_0)_{opt}$ for $J = 0$.

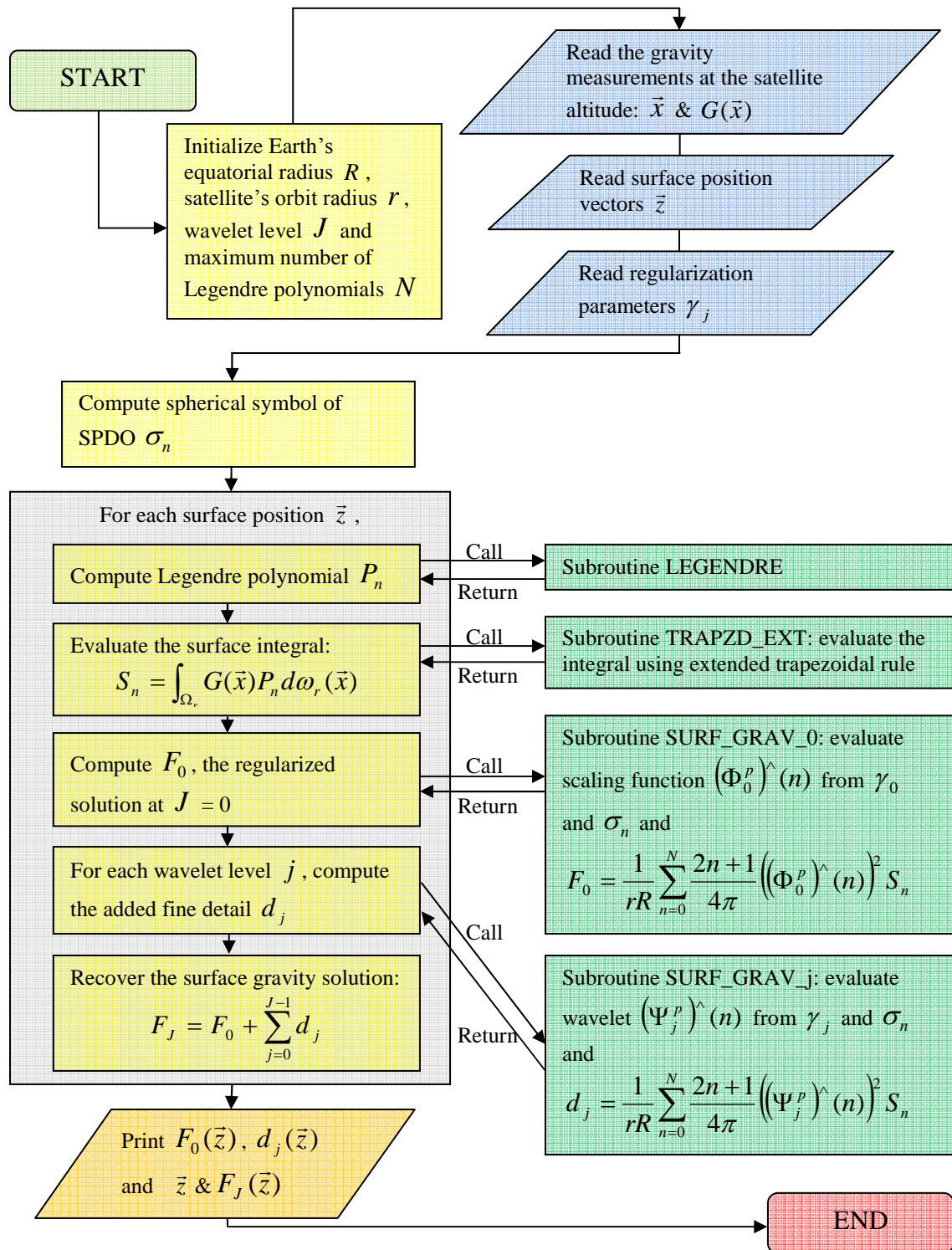


Fig. 4.2.4. Flowchart to recover the surface gravity anomaly $F_j(\bar{z})$ with wavelet level J .

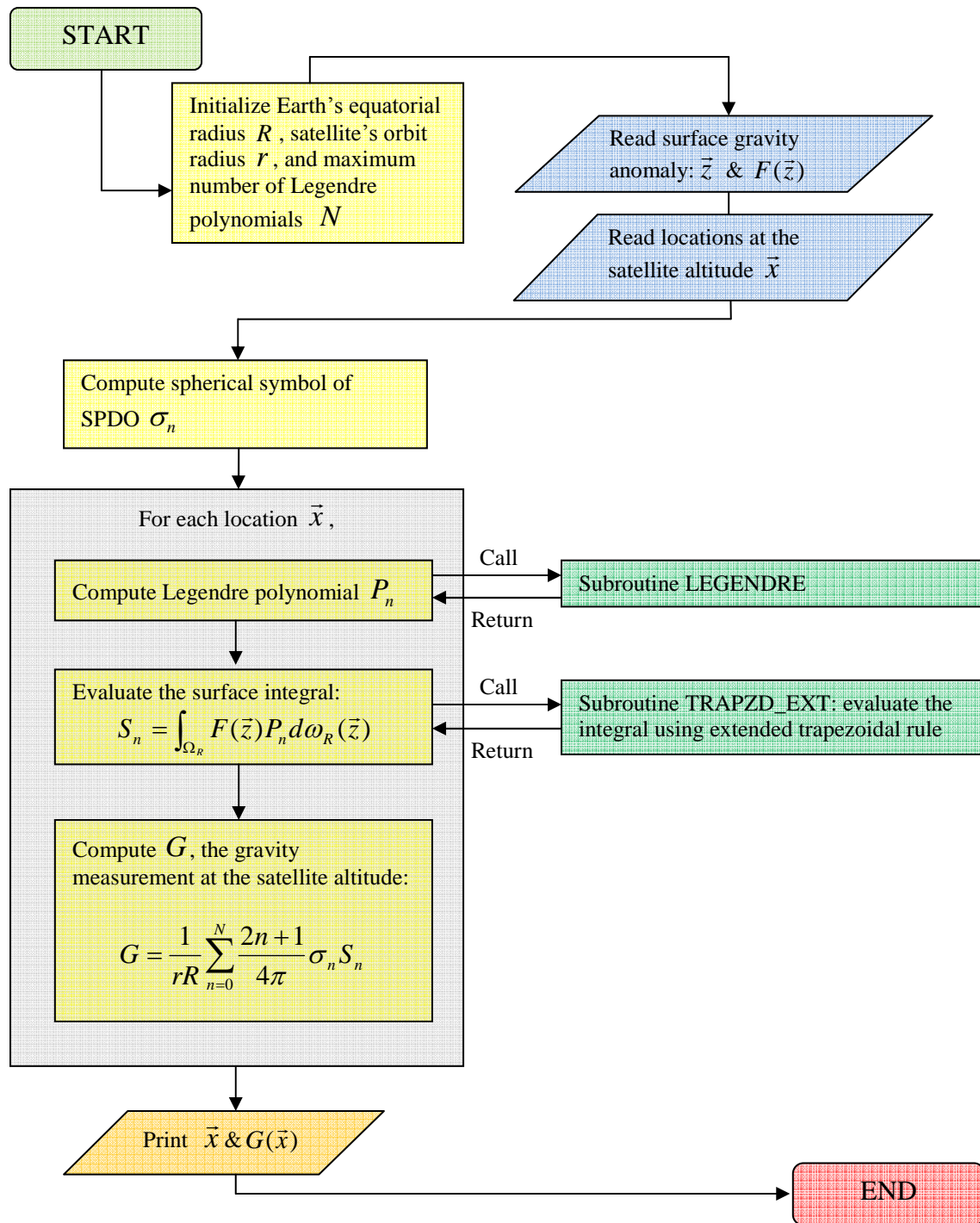


Fig. 4.2.5. Flowchart for the upward continuation to obtain $G(\vec{x})$, the simulated measurements at the satellite altitude, from the surface gravity anomaly $F(\vec{z})$.

We investigated the effect of changes in N , the maximum degree of the Legendre polynomials, on the recovered surface gravity anomaly, with both reduced ($N = 150$) and increased value ($N = 600$) for the Region I. We also studied how the volume of the gravity measurement data at the satellite altitude affects the accuracy of the recovered surface gravity.

In addition to the numerical simulations for the cases where the upward propagated gravity anomaly at the satellite altitude was used as input data, we tested our gravity model for an SGG case. We re-sampled the surface gravity anomaly on a 513×257 longitude-latitude grid from the truth data set on a 720×360 grid by Gaussian smoothing and obtained the second order radial derivative of the gravity anomaly at the satellite altitude by the upward continuation of this new set of surface gravity data. A local set of the SGG type data at the altitude of 300 km with a spatial resolution 0.7° was obtained in such a manner and was then used to recover the surface gravity anomaly for the local region corresponding to Region I.

We also investigated the impact of the measurement noise on the recovered gravity solution. We imposed Gaussian random noise on the gravity measurements and solved the inverse problem to recover the surface gravity anomaly. Two sets of Gaussian random noise with varying amplitude, whose respective standard deviation is 0.1% and 0.5% of that of the gravity measurements at the satellite altitude, were tested in the cases with both the upward propagated gravity anomaly and the SGG measurements.

Finally, in order to understand the effect of irregularity in the measurement data arrangement on the gravity solution, we studied the surface gravity anomaly recovered from the at-altitude gravity measurement data on ground tracks rather than on a regular grid with the equal spacing along the longitude and latitude. We generated two sets of ground track profiles of the Track A (ground tracks are separated by 1° with the data along the track 0.5° apart) and the Track B (ground tracks are 1.5° apart with the data along the track separated by 0.5°) and compared the result to the one obtained from the data set on a regular grid with 0.5° spacing in both longitudinal and latitudinal directions.

The block diagrams to summarize the numerical procedure for the simulations using either type of gravity measurements at the satellite altitude are provided in **Fig. 4.2.6** and **Fig. 4.2.7**. Simulation findings and results will follow in the next five chapters.

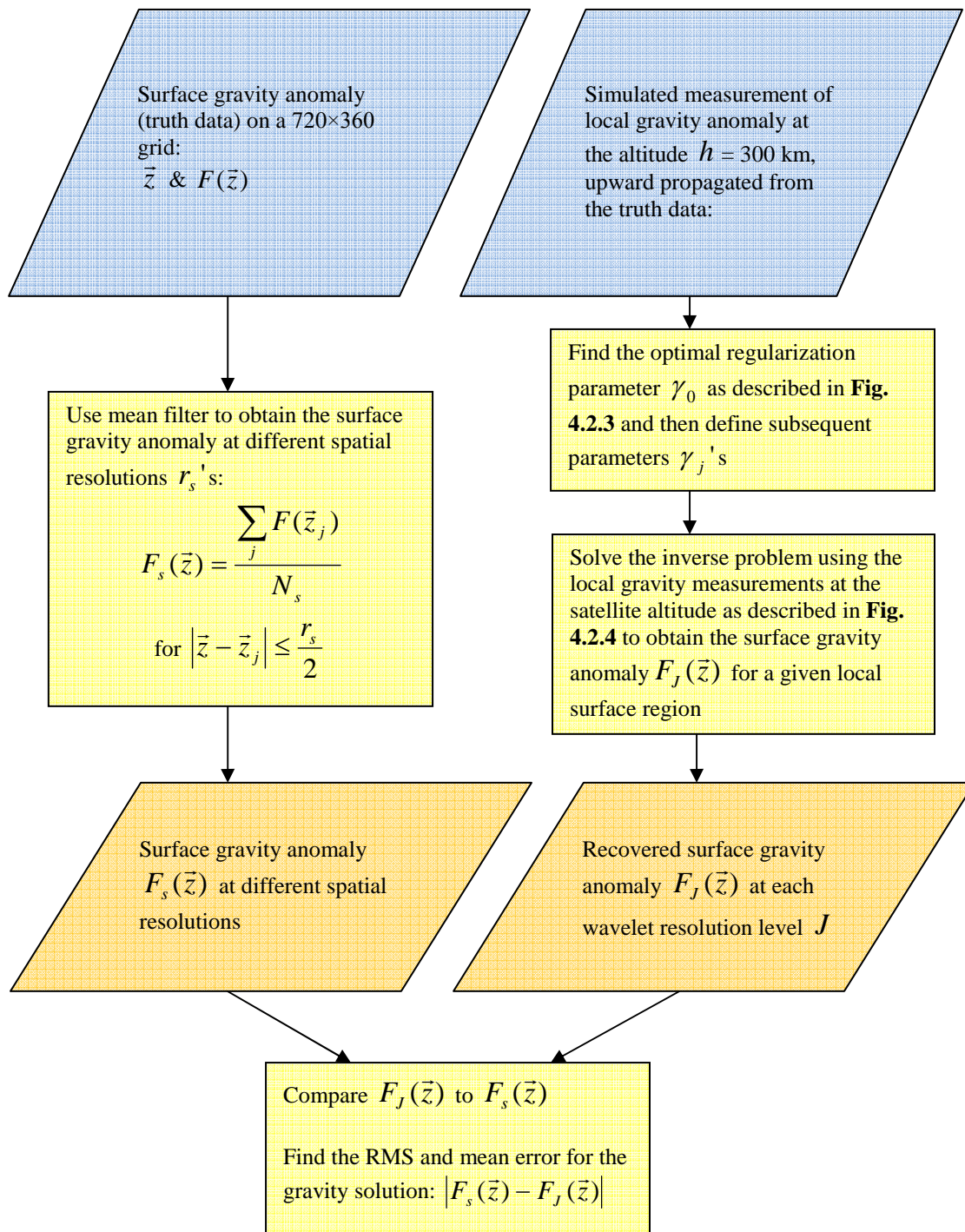


Fig. 4.2.6. Numerical procedure for the simulation when using the upward propagated gravity anomaly as input data to recover the surface gravity anomaly.

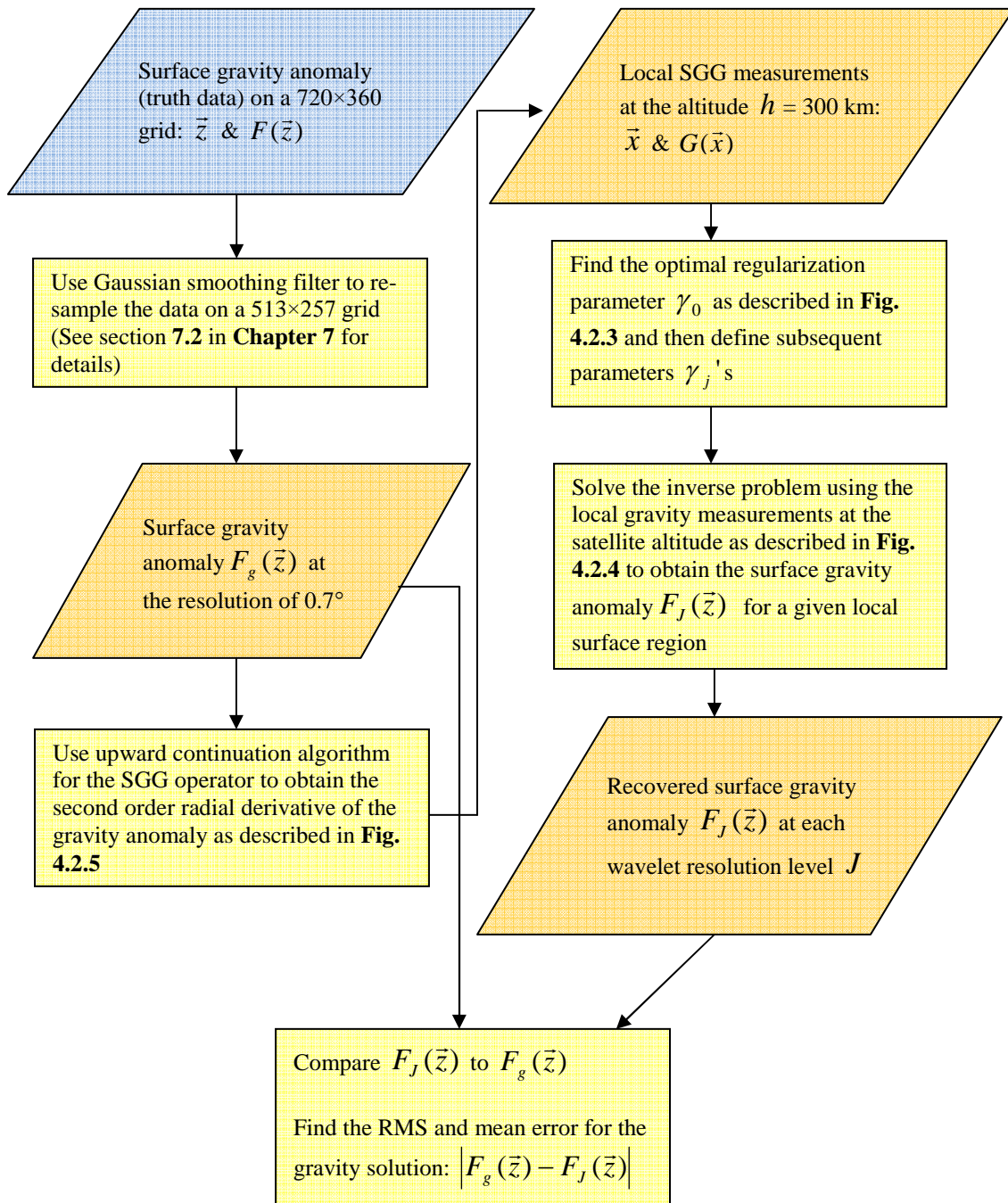


Fig. 4.2.7. Numerical procedure for the simulation when using the simulated SGG measurements at the satellite altitude as input data to recover the surface gravity anomaly.

Chapter 5. Simulation Result: Region I (30.25°W ~ 109.75°W and 24.75°S ~ 19.75°N)

5.1. Region I

Region I includes the Pacific – Central-South America where the Andes Mountain Range starts off the Pacific in the west and the Amazon Basin continues to the east toward the Atlantic. The local surface gravity anomaly on a 160×90 grid for the region of $250.25^\circ \sim 329.75^\circ$ in longitude (equivalent to $30.25^\circ\text{W} \sim 109.75^\circ\text{W}$) and $-24.75^\circ \sim 19.75^\circ$ latitude ($24.75^\circ\text{S} \sim 19.75^\circ\text{N}$) was recovered from the gravity anomaly data of the local region of $226.25^\circ \sim 354.25^\circ$ in longitude ($5.75^\circ\text{W} \sim 133.75^\circ\text{W}$) and $-34.25^\circ \sim 29.75^\circ$ in latitude ($34.25^\circ\text{S} \sim 29.75^\circ\text{N}$) on a 257×129 regular grid at the satellite altitude of 300 km. This area was selected mainly because it contains regions with three distinct gravity profiles and thus was considered a good candidate to stress our model: the Pacific with the low gravity gradients, the Andes with high gradients and the Continental South America with medium strength gravity gradients. The contour maps of the truth data at a resolution of 0.5° and the gravity anomaly at the satellite altitude of corresponding local area are shown in **Fig. 5.1.1**. The 3-D surface plots are presented in **Fig. 5.1.2**.

A mean filter was used to the truth data to obtain the surface gravity anomaly at the different spatial resolutions from 1° to 5° to be compared to the recovered surface gravity anomaly with the different wavelet resolution levels from $J = 0$ to $J = 6$. The regularization parameters used in the simulation are $\gamma_0 = 9.0 \times 10^{-2}$, $\gamma_1 = 5.0 \times 10^{-2}$, $\gamma_2 = 2.0 \times 10^{-2}$, $\gamma_3 = 4.0 \times 10^{-3}$, $\gamma_4 = 1.0 \times 10^{-3}$, $\gamma_5 = 2.0 \times 10^{-4}$ and $\gamma_6 = 5.0 \times 10^{-5}$. The maximum degree of the Legendre polynomials N was set to be 300 throughout the simulation.

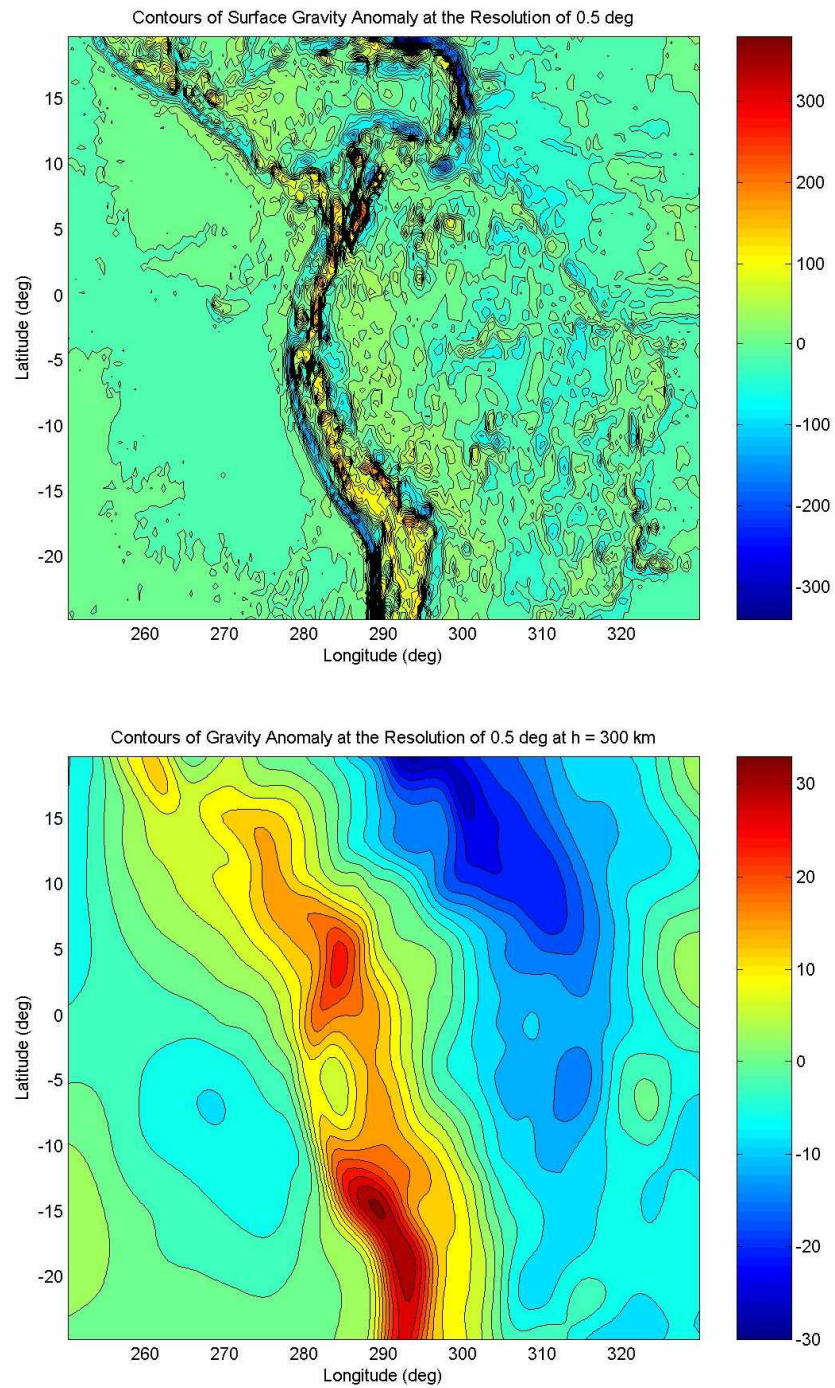


Fig. 5.1.1. The contour map of the surface gravity anomaly of the truth data at the resolution of 0.5° and the corresponding gravity anomaly at the satellite altitude $h = 300$ km with each contour respectively representing 20 mGal and 3 mGal of difference in gravity anomaly.

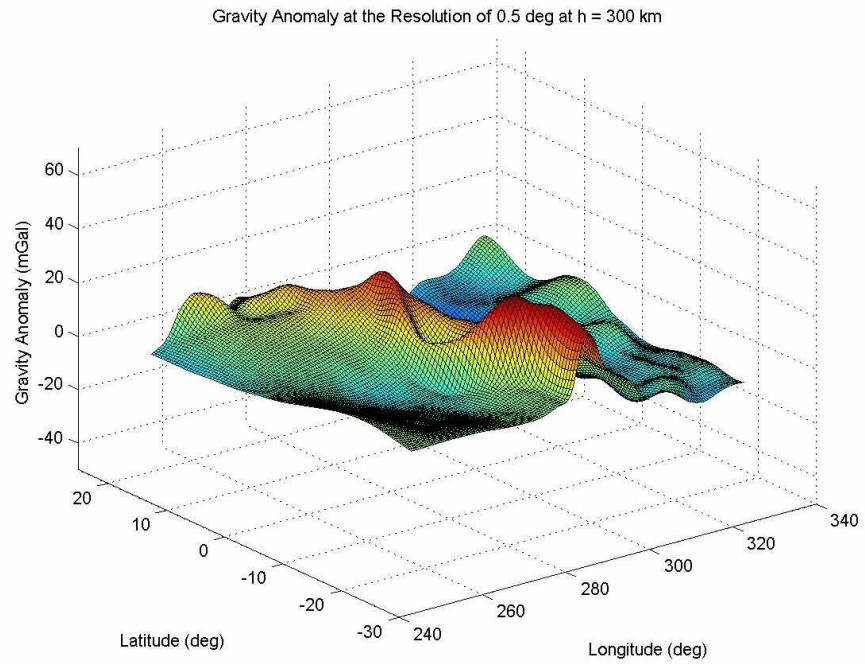
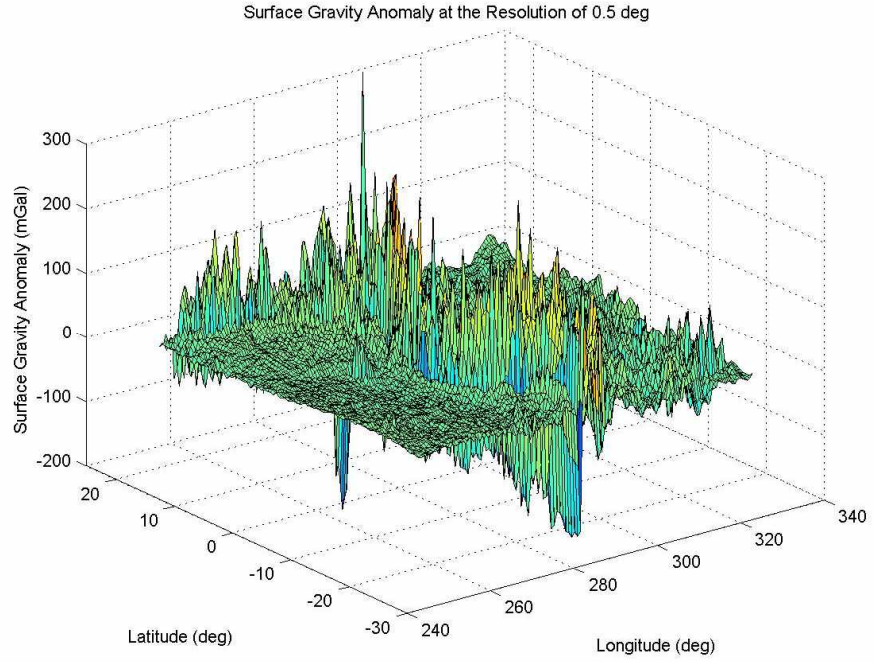


Fig. 5.1.2. 3-D surface plot of the surface gravity anomaly of the truth data at the resolution of 0.5° and the corresponding gravity anomaly at the satellite altitude $h = 300$ km to be used to recover the surface gravity anomaly by solving the inverse problem. The surface gravity information was smoothed out a great deal by upward propagation.

Since the wavelet resolution level J can be determined to an arbitrary degree – one can set a hundred different resolution levels or just one – and because how much of the fine details that can be added at each increased wavelet level depends on the regularization parameter γ_j , we chose the parameters so that each wavelet resolution level corresponds to a spatial resolution: The gravity signal of $J = 0$ corresponds to that of the spatial resolution 5° , $J = 1$ to the resolution 4° , $J = 2$ to 3° , $J = 3$ to 2° , $J = 4$ to 1.5° and $J = 5$ to 1° .

Fig. 5.1.3 to **Fig. 5.1.14** show the comparison between the recovered surface gravity anomaly at each wavelet resolution and the truth data at its corresponding spatial resolution both in contour maps and 3-D plots. In all of the contour maps, each contour represents 20 mGal of difference in gravity anomaly. As is expected from wavelet theory, finer details are recovered as the wavelet resolution level J increases, until high frequency wavelets produce “forced” fine signals over the area with low-medium strength gravity gradients to interfere with the real gravity signals (*i.e.* $J = 6$ in this case), as is shown in **Fig. 5.1.15**.

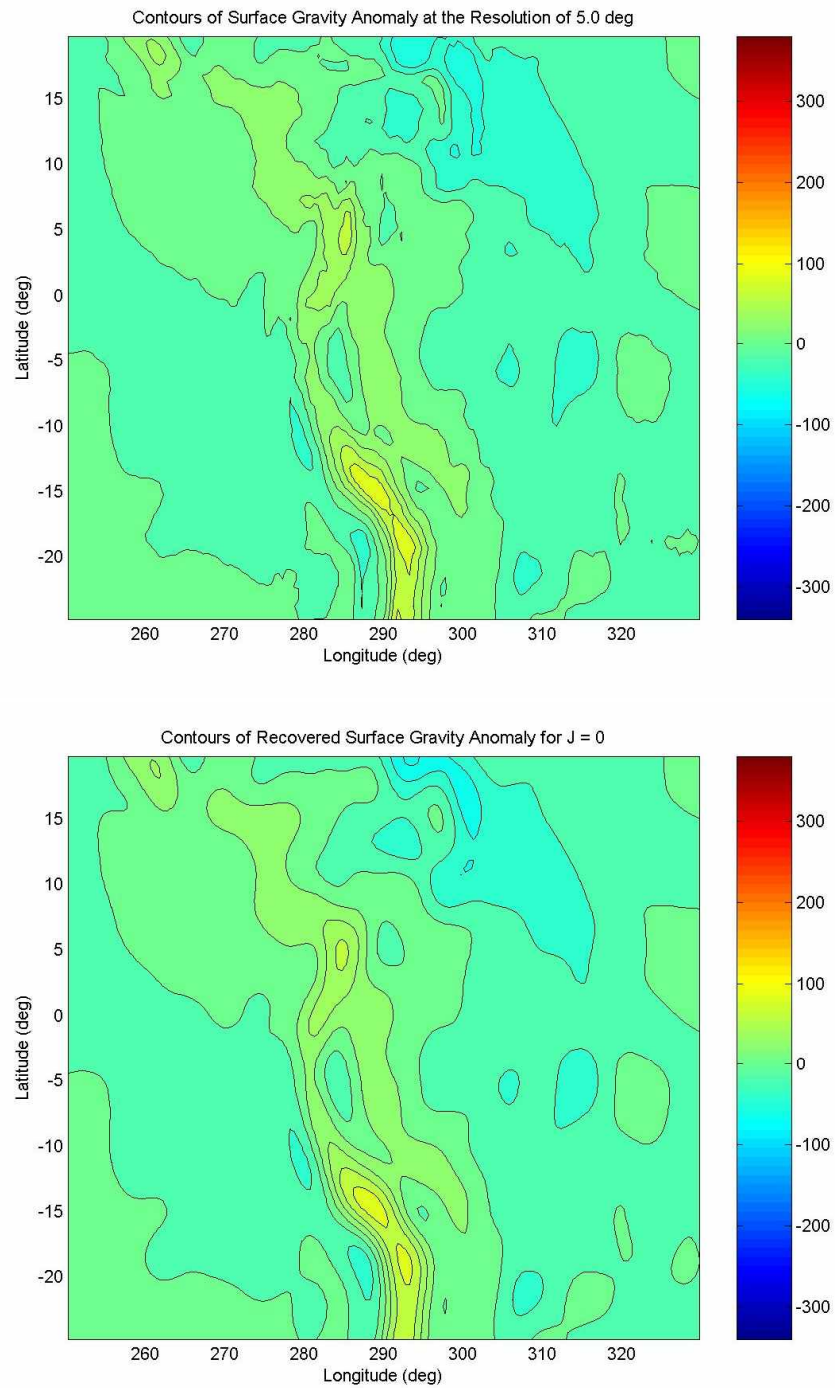


Fig. 5.1.3. The contour map of the truth data at the spatial resolution 5° and the recovered gravity anomaly for the wavelet resolution level $J = 0$, with each contour representing 20 mGal difference in gravity anomaly. The RMS error in the region is 2.3 mGal and the mean error magnitude is 1.5 mGal.

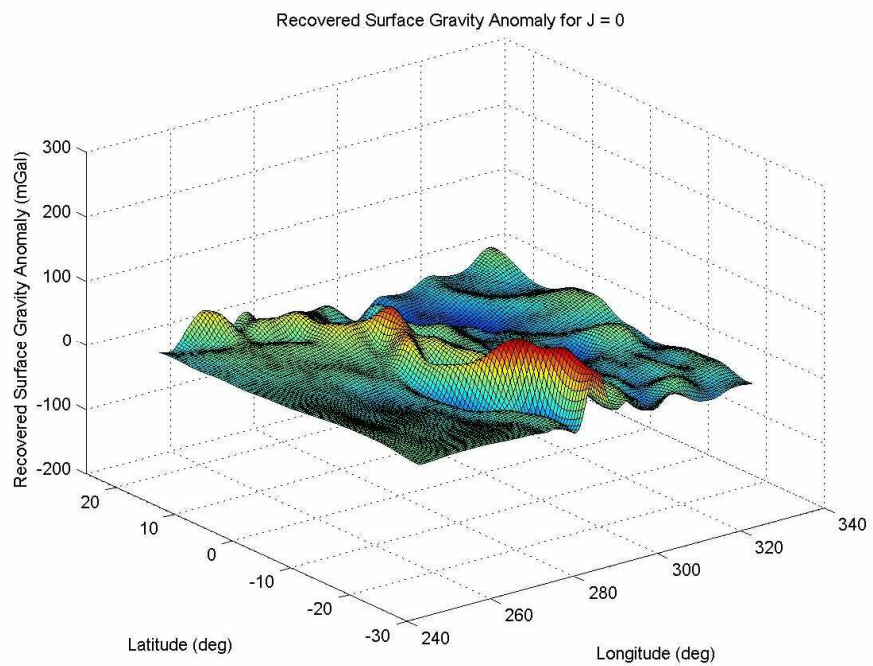
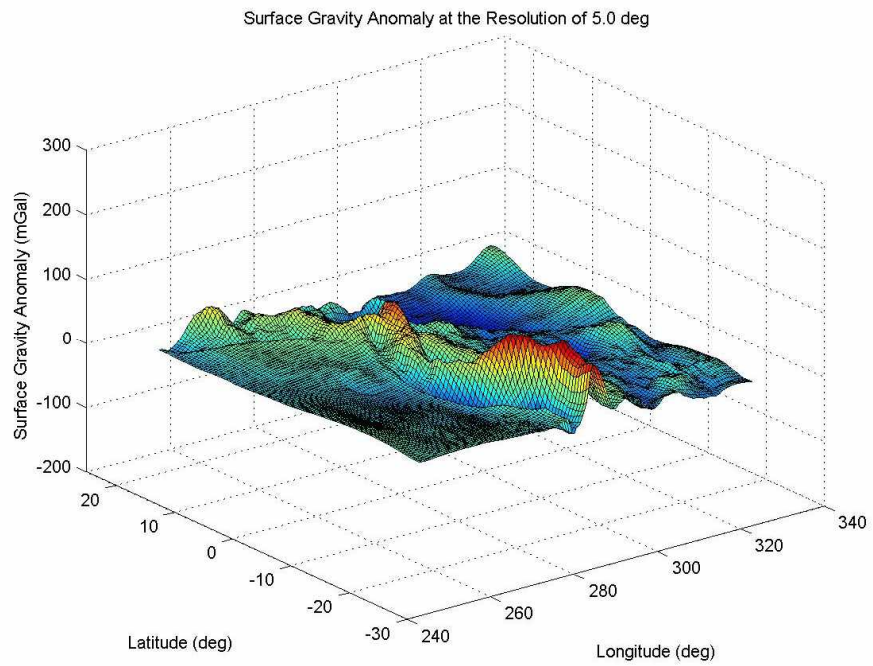


Fig. 5.1.4. 3-D surface map of the truth data at the spatial resolution 5° and the recovered gravity anomaly for the wavelet resolution level $J = 0$.

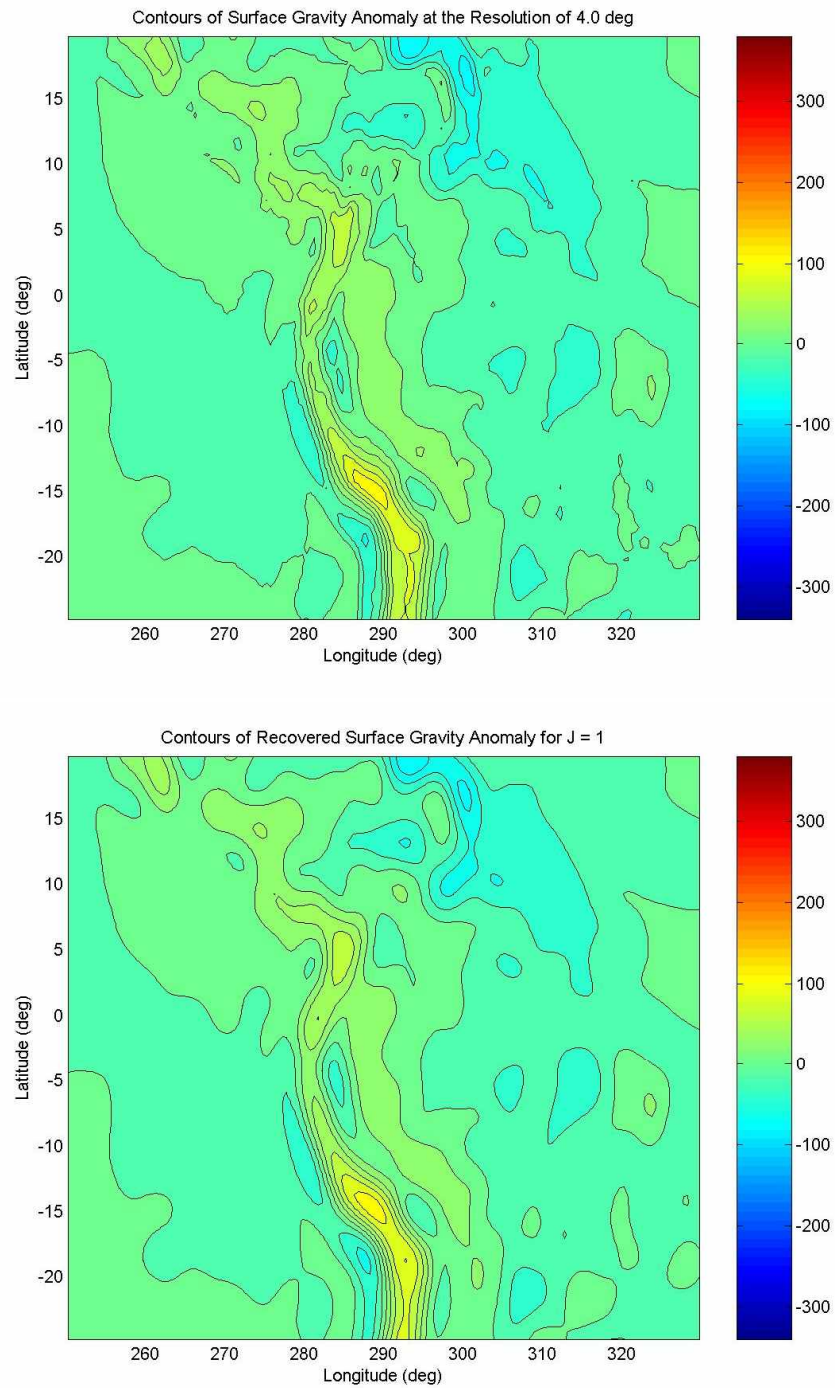


Fig. 5.1.5. The contour map of the truth data at the spatial resolution 4° and the recovered gravity anomaly for the wavelet resolution level $J = 1$. The RMS error in the region is 2.6 mGal and the mean error is 1.7 mGal.

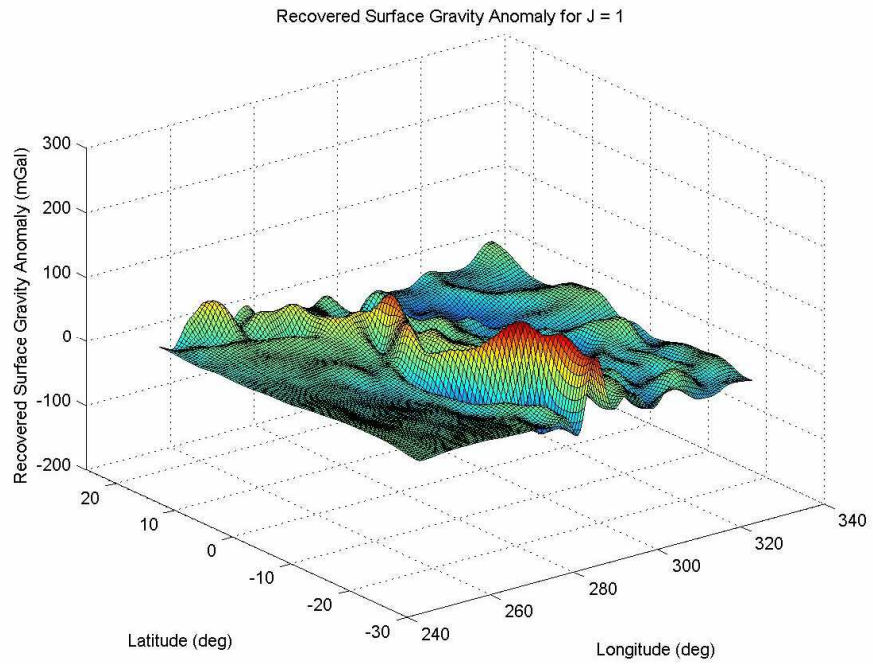
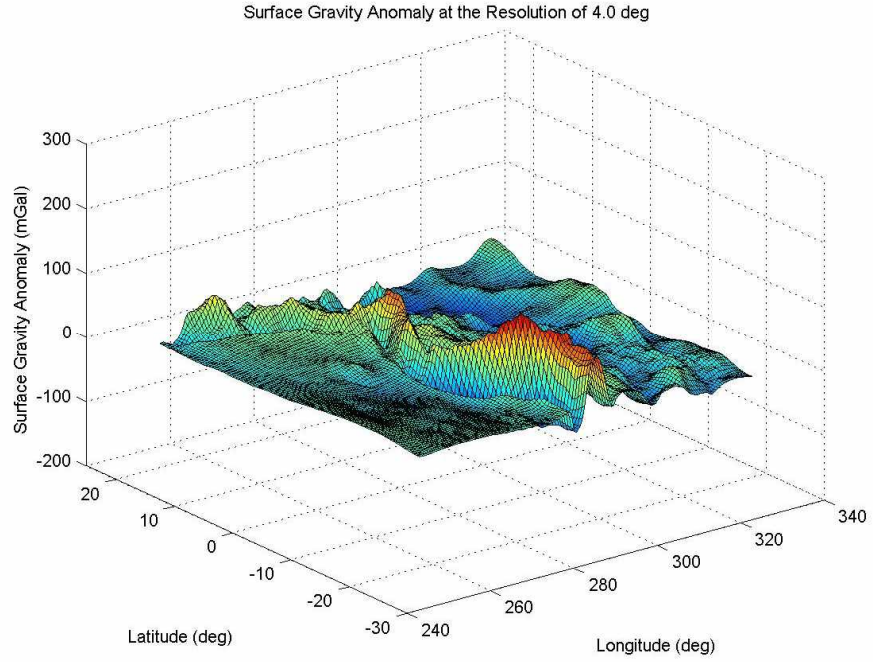


Fig. 5.1.6. 3-D surface map of the truth data at the spatial resolution 4° and the recovered gravity anomaly for the wavelet resolution level $J = 1$.

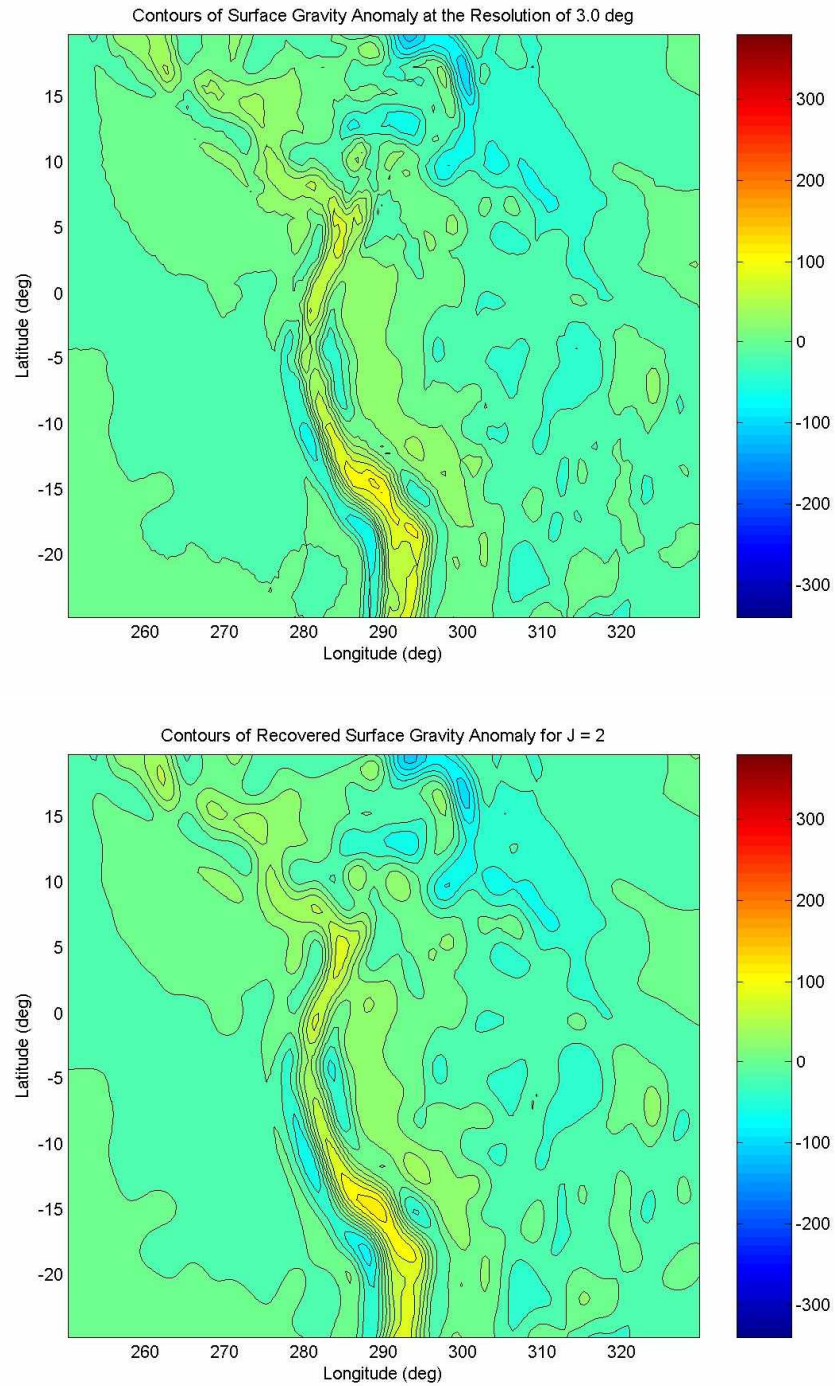


Fig. 5.1.7. The contour map of the truth data at the spatial resolution 3° and the recovered gravity anomaly for the wavelet resolution level $J = 2$. The RMS and mean error in the region is reduced to 3.5 mGal and 2.1 mGal, respectively.

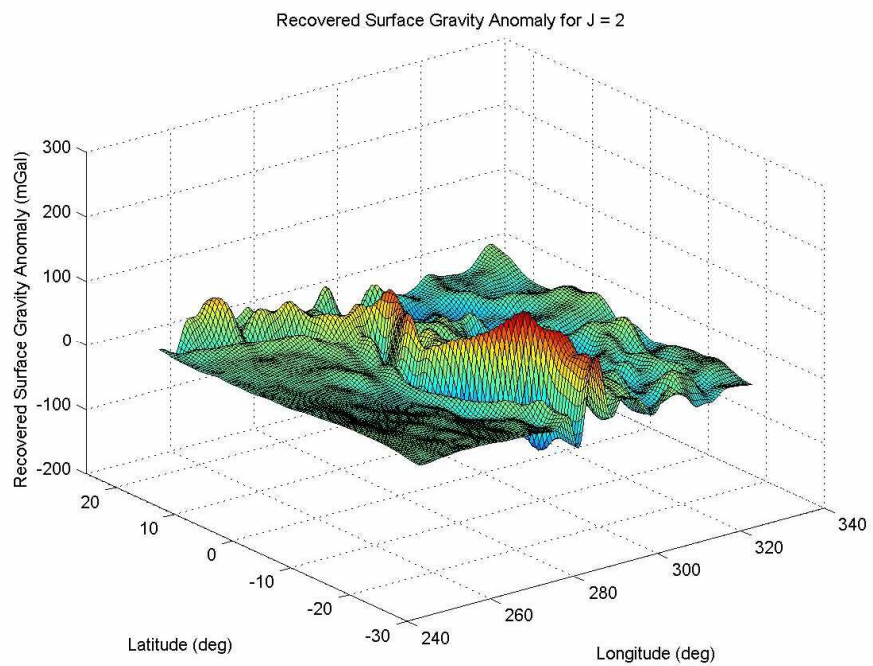
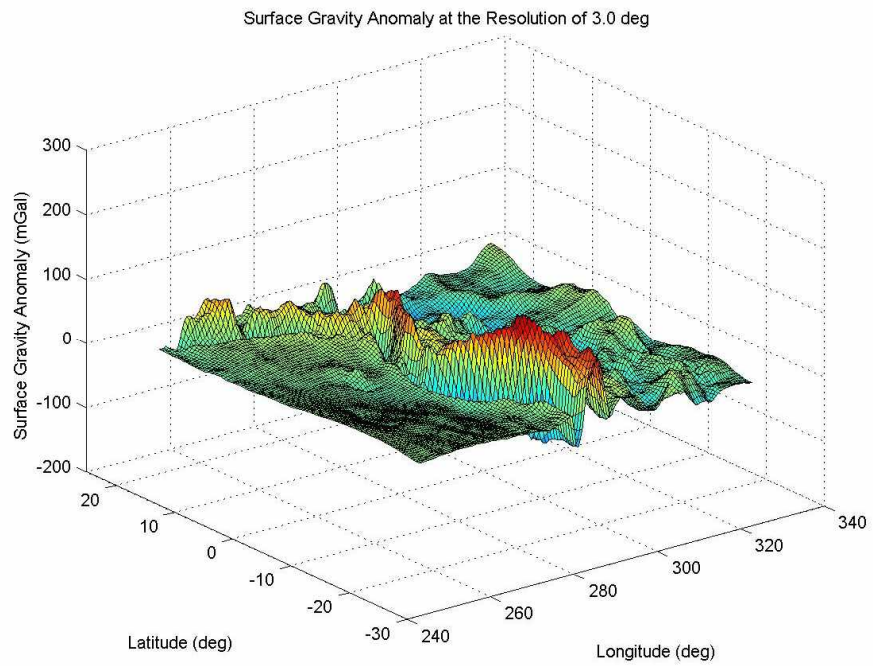


Fig. 5.1.8. 3-D surface map of the truth data at the spatial resolution 3° and the recovered gravity anomaly for the wavelet resolution level $J = 2$.

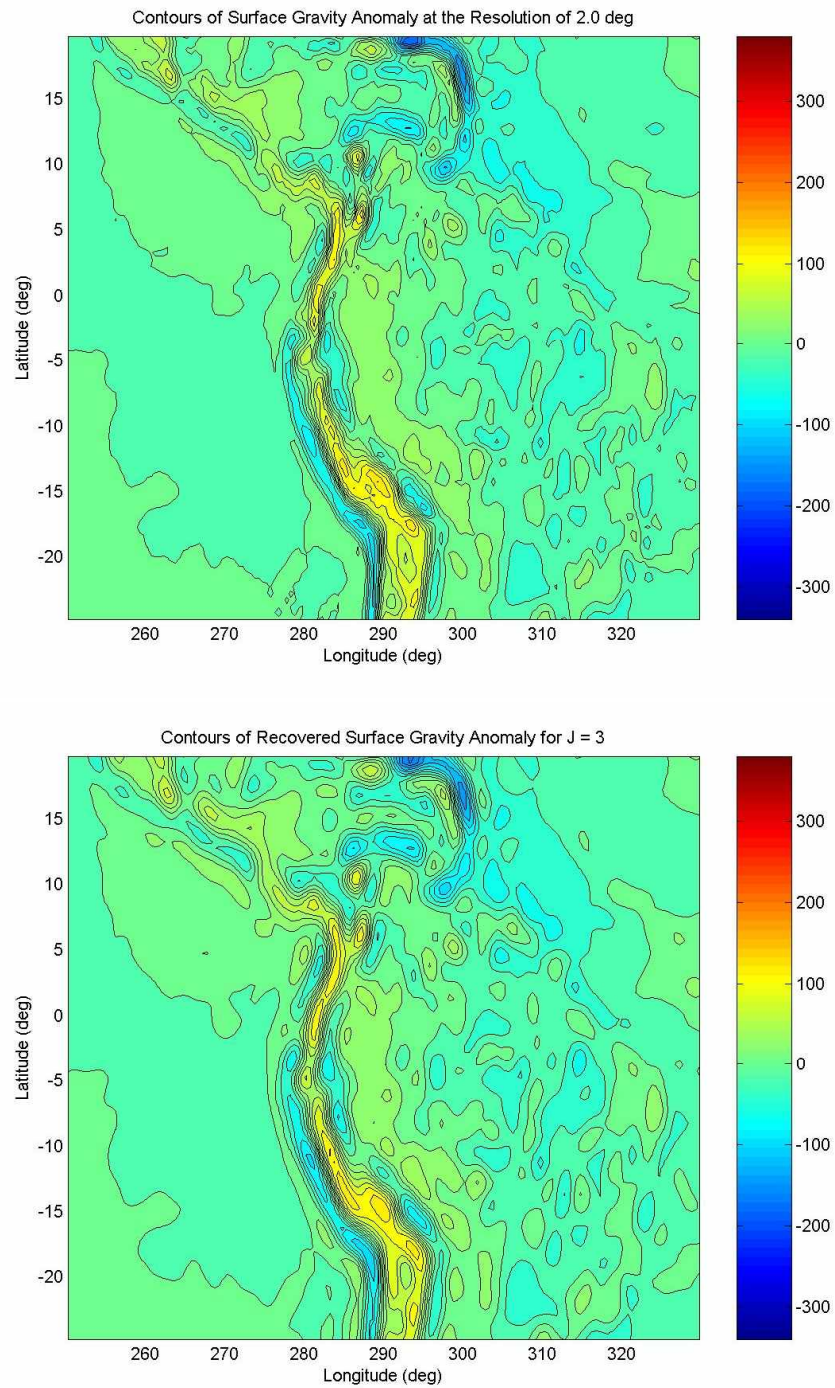


Fig. 5.1.9. The contour map of the truth data at the spatial resolution 2° and the recovered gravity anomaly for the wavelet resolution level $J = 3$. The RMS error in the region is 5.0 mGal and the mean error is 3.0 mGal.

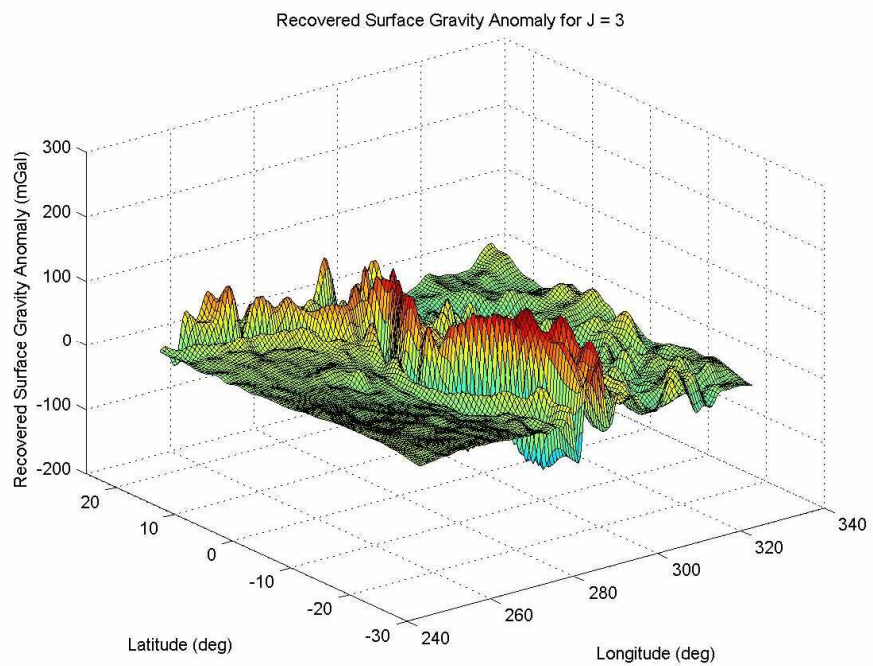
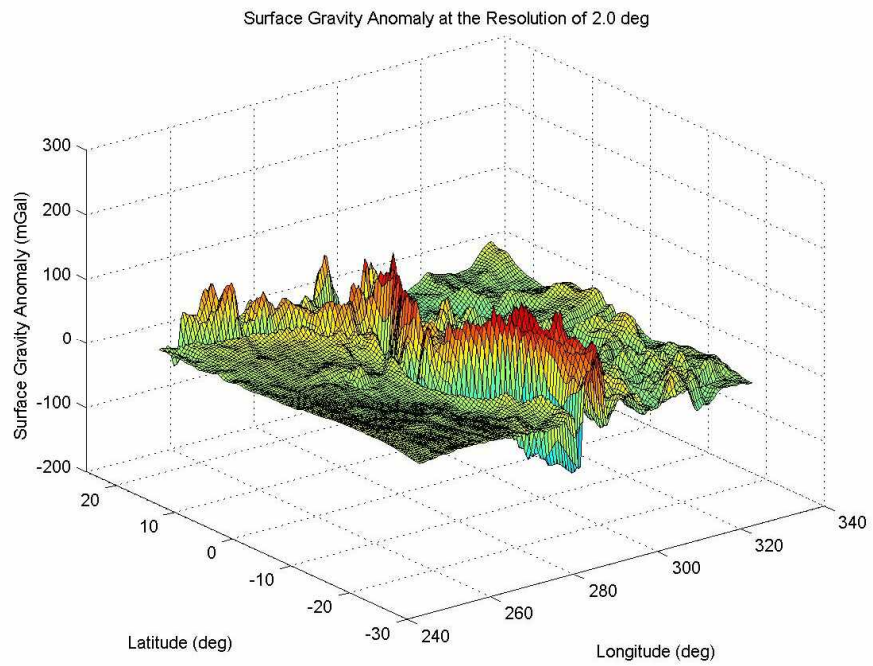


Fig. 5.1.10. 3-D surface map of the truth data at the spatial resolution 2° and the recovered gravity anomaly for the wavelet resolution level $J = 3$.

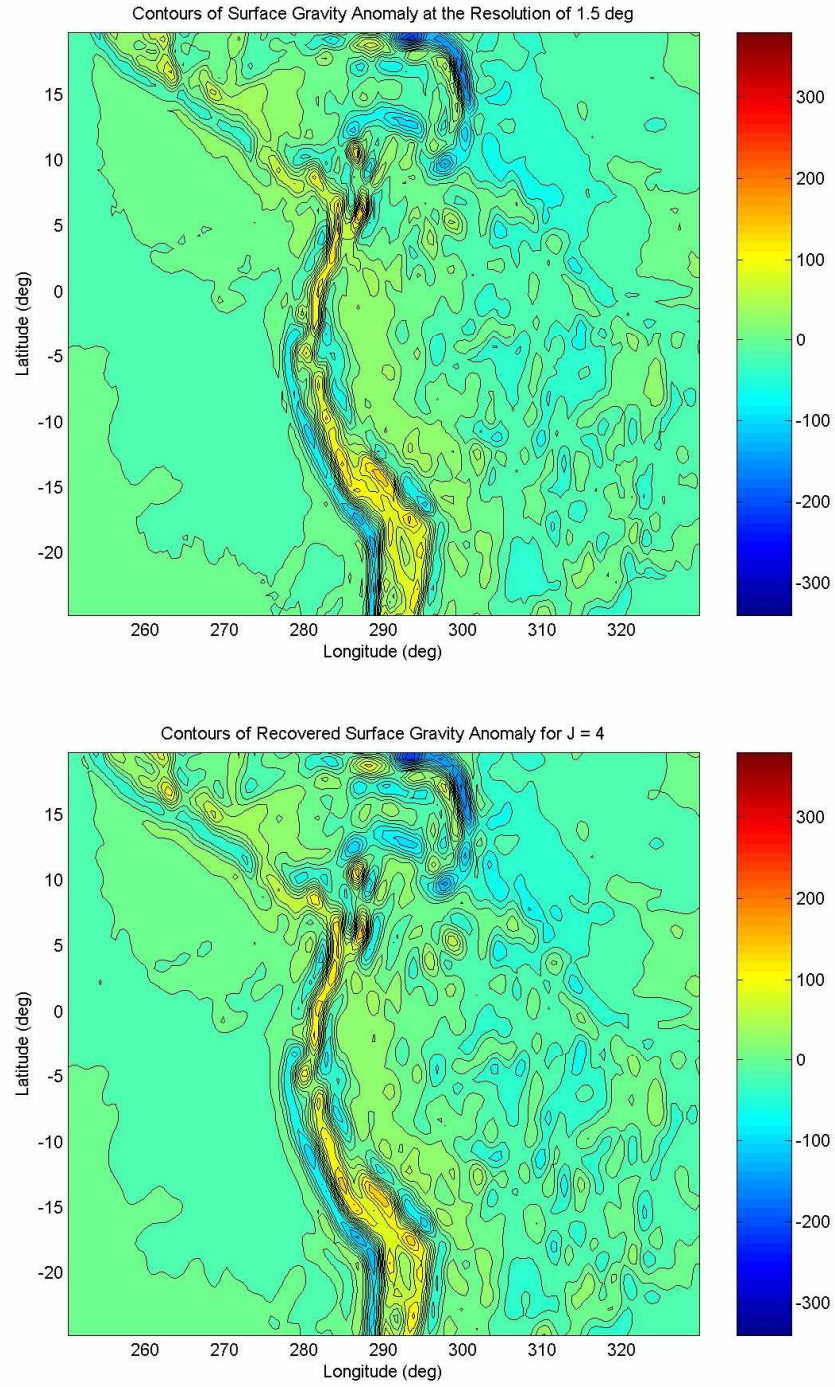


Fig. 5.1.11. The contour map of the truth data at the spatial resolution 1.5° and the recovered gravity anomaly for the wavelet resolution level $J = 4$. The RMS error in the region is 5.2 mGal and the mean error is 3.1 mGal.

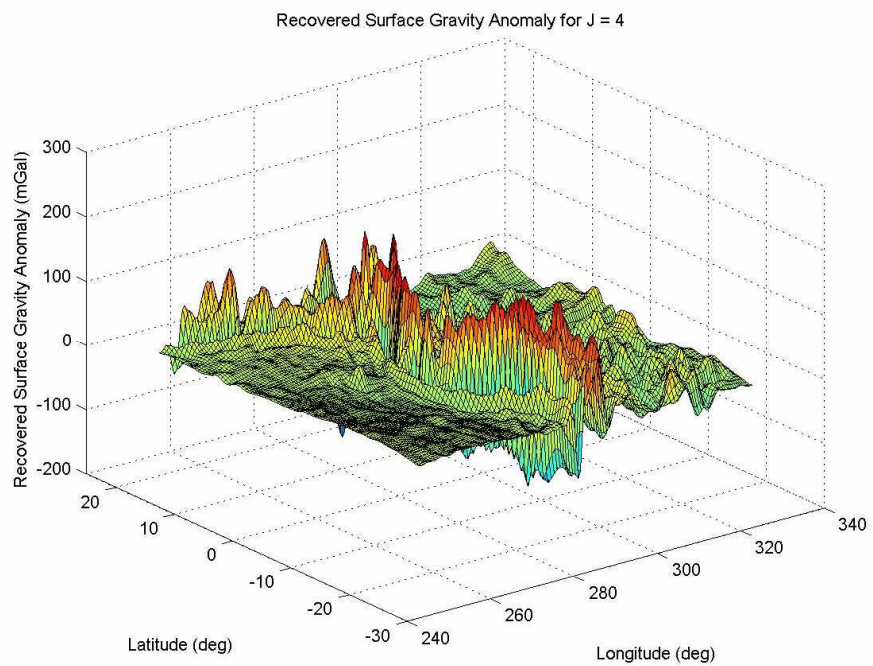
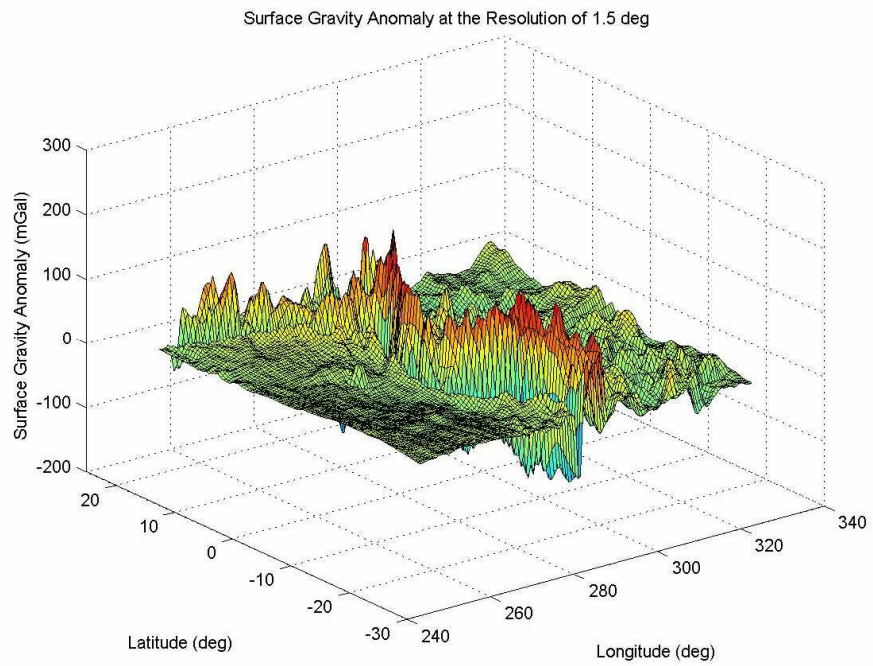


Fig. 5.1.12. 3-D surface map of the truth data at the spatial resolution 1.5° and the recovered gravity anomaly for the wavelet resolution level $J = 4$.

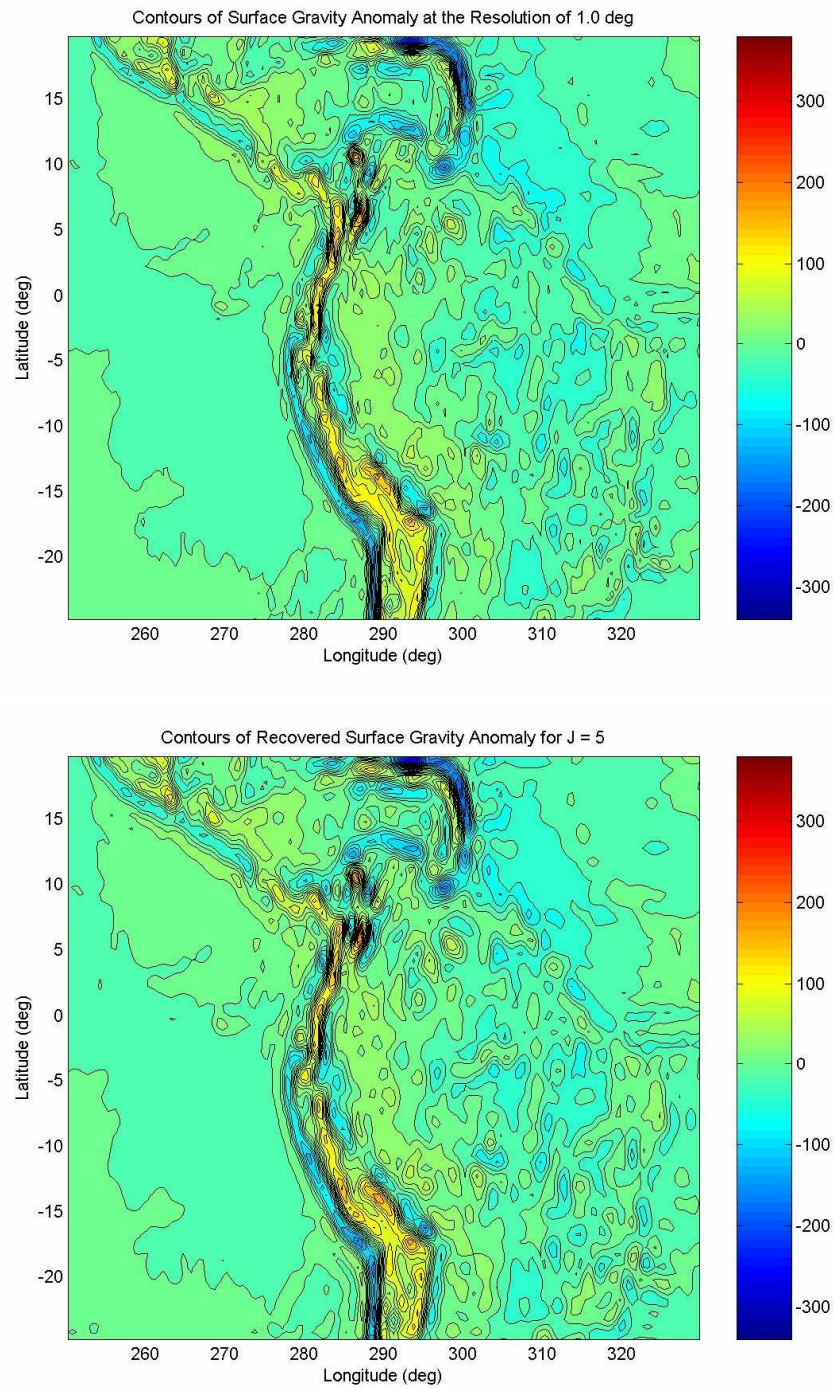


Fig. 5.1.13. The contour map of the truth data at the spatial resolution 1° and the recovered gravity anomaly for the wavelet resolution level $J = 5$. The RMS error in the region is 5.9 mGal and the mean error is 3.5 mGal.

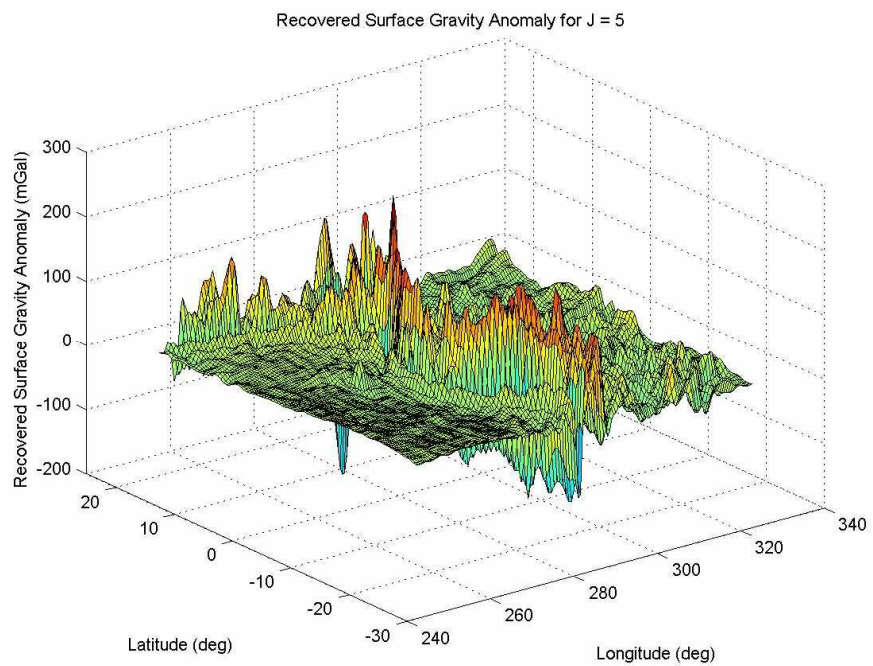
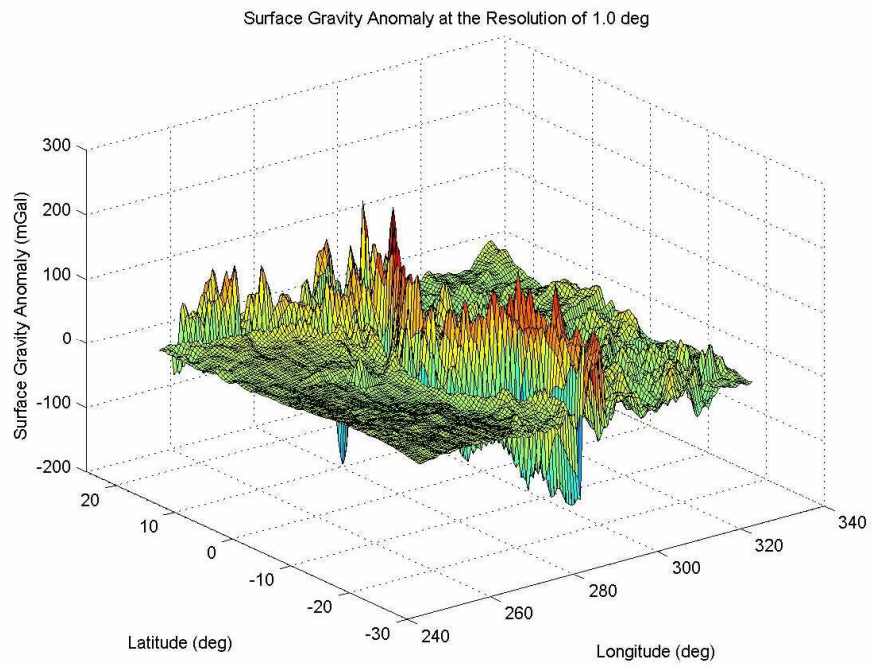


Fig. 5.1.14. 3-D surface map of the truth data at the spatial resolution 1° and the recovered gravity anomaly for the wavelet resolution level $J = 5$.

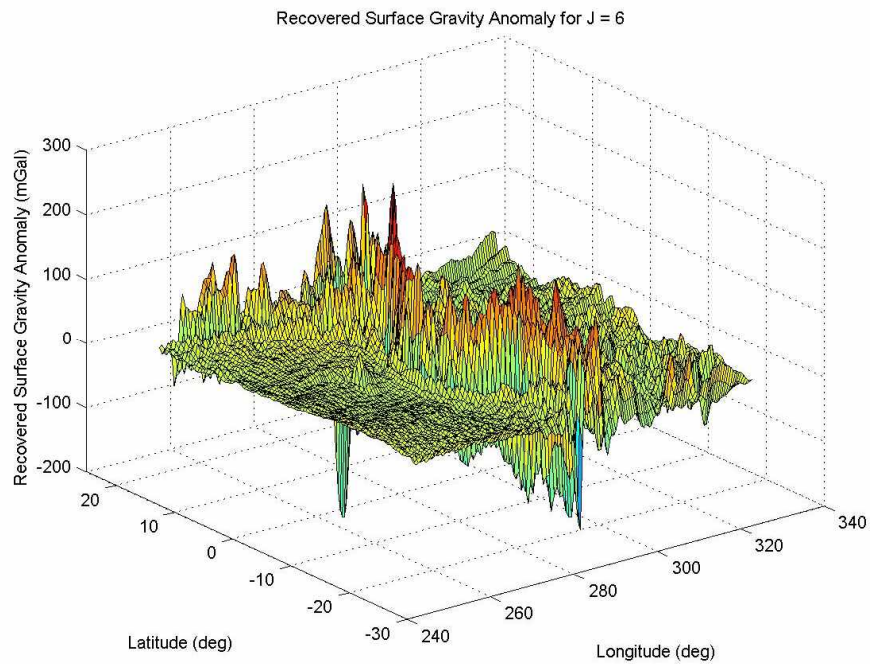
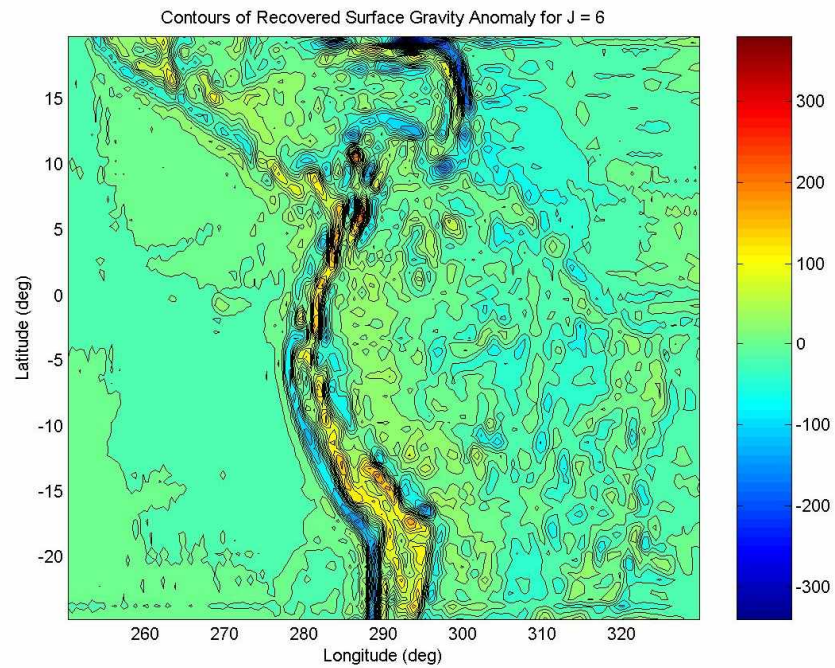


Fig. 5.1.15. Contour and 3-D surface map of the recovered gravity anomaly for the wavelet resolution level $J = 6$. Note the interference caused by “forced” signals along the grid lines near the horizontal edges of the region.

The contour map and 3-D plots in **Fig. 5.1.16** and **Fig. 5.1.17** show $|G - G_J|$, the surface gravity anomaly error at different spatial resolutions and wavelet levels. With the truth surface gravity anomaly at each spatial resolution, the wavelet solution that yields the least RMS error was chosen for the plot, *i.e.* the solution with $J = 5$ for 1° resolution, $J = 4$ for 1.5° resolution, *etc.* In both of the pictures, the error plots are arranged in the following order: error map with the spatial resolution of 1° at the top left, 1.5° top right, 2° middle left, 3° middle right, 4° bottom left and 5° bottom right. As is obvious from the error plots, the surface gravity anomaly error decreases as the spatial resolution increases. Comparing the contour map of the error to the contours of the initial surface gravity anomaly in **Fig. 5.1.1** (top figure) reveals that the largest errors come from the area with the high gravity gradient signals (*i.e.* along the Andes Mountain Range), while modest errors are observed from the area with moderate gravity gradients (the Continental South America including the Amazon Basin) and the smallest errors from the low gravity gradients region (the Pacific), implying a strong correlation between the error and the gravity gradients – the higher the magnitude of the gravity gradient, the larger the error of the recovered solution.

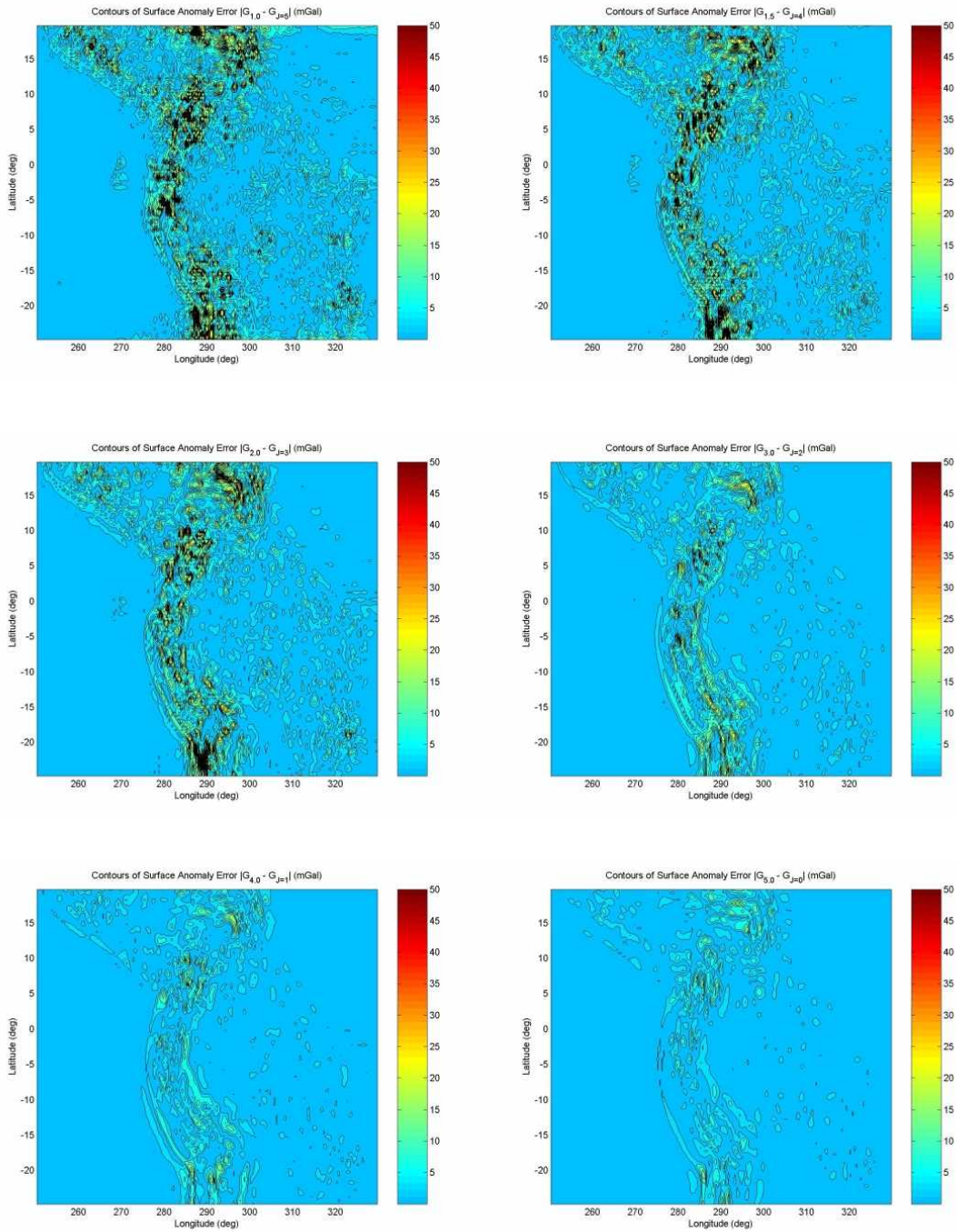


Fig. 5.1.16. Contour map of the surface gravity anomaly error in different spatial and wavelet resolution levels. Each contour represents 3 mGal of difference in the error. The wavelet resolution level J was chosen at each spatial resolution that yields the least RMS error.

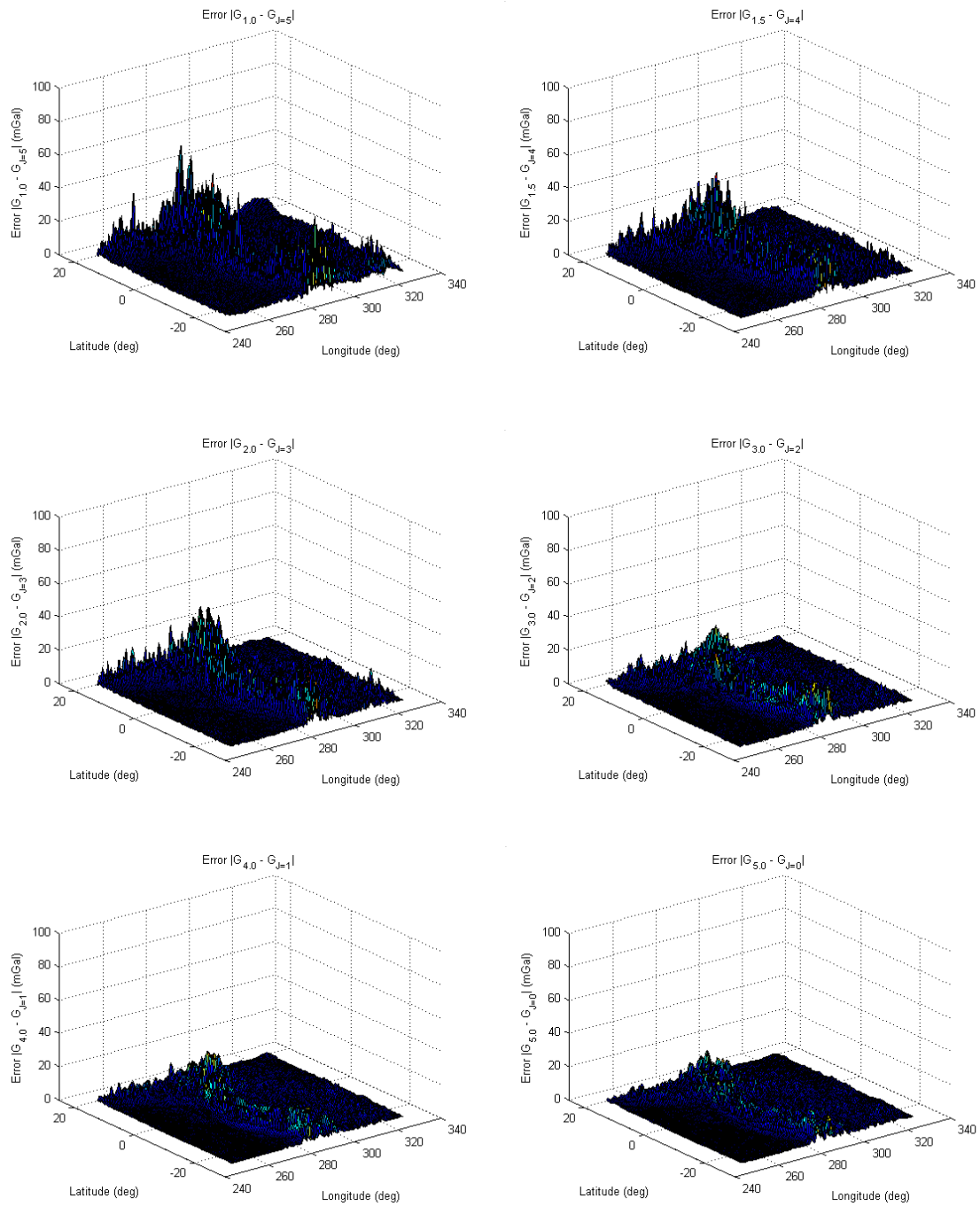


Fig. 5.1.17. 3-D surface gravity anomaly error plots in different spatial and wavelet resolution levels. The wavelet resolution level J was chosen at each spatial resolution that yields the least RMS error.

Table 5.1.1 and **Table 5.1.2** summarize the results. Bold faced numbers indicate the minimum RMS and mean error magnitude for the wavelet resolution level J at each spatial resolution. The RMS error in the overall region ranges between 5.9 mGal at the resolution 1° and 2.3 mGal at the resolution 5° . The significant difference between RMS and mean error at each spatial resolution suggests that the error is not evenly distributed throughout the region.

Table 5.1.3 to **Table 5.1.8** provide RMS and mean error of the sub-regions: $278.25^\circ \sim 299.75^\circ$ in longitude and $-24.75^\circ \sim 19.75^\circ$ latitude, $304.25^\circ \sim 329.75^\circ$ in longitude and $-14.75^\circ \sim 19.75^\circ$ latitude and $250.25^\circ \sim 275.25^\circ$ in longitude and $-20.75^\circ \sim 4.75^\circ$ latitude, respectively representing the area with high, moderate and low magnitude gravity gradients. As mentioned above, the RMS error is the largest in the region with high gravity gradients (ranging from 9.6 mGal at the resolution 1° to 3.8 mGal at the resolution 5°) and the smallest with the low gradient signals (from 1.0 mGal at the resolution 1° to 0.5 mGal at the resolution 5°).

Spatial Resolution	$ G - G_0 _{RMS}$	$ G - G_1 _{RMS}$	$ G - G_2 _{RMS}$	$ G - G_3 _{RMS}$	$ G - G_4 _{RMS}$	$ G - G_5 _{RMS}$	$ G - G_6 _{RMS}$
0.5°	28.90	27.54	25.37	21.27	17.93	14.65	13.43
1.0°	20.51	18.78	16.06	11.11	7.65	5.87	8.36
1.5°	17.26	15.35	12.38	7.33	5.19	6.96	10.88
2.0°	14.13	12.05	8.93	4.97	6.45	10.32	14.26
3.0°	8.05	5.64	3.46	8.11	13.30	17.88	21.21
4.0°	4.29	2.63	5.37	12.78	17.89	21.81	24.42
5.0°	2.29	4.44	9.23	16.61	20.92	23.97	26.17

Table 5.1.1. The RMS surface gravity anomaly error $|G - G_J|_{RMS}$ in mGal at the wavelet resolution level $J = 0$ to $J = 6$ for each spatial resolution of the truth data. Bold faced numbers indicate the minimum RMS error for the wavelet resolution level J at each spatial resolution.

Spatial Resolution	$ G - G_0 _{mean}$	$ G - G_1 _{mean}$	$ G - G_2 _{mean}$	$ G - G_3 _{mean}$	$ G - G_4 _{mean}$	$ G - G_5 _{mean}$	$ G - G_6 _{mean}$
0.5°	15.29	14.60	13.41	11.31	9.65	8.12	7.88
1.0°	10.98	10.08	8.60	6.04	4.32	3.46	4.89
1.5°	9.36	8.36	6.78	4.18	3.06	3.98	6.18
2.0°	7.79	6.67	5.01	2.95	3.73	5.70	7.96
3.0°	4.69	3.35	2.11	4.59	7.26	9.59	11.54
4.0°	2.61	1.65	3.16	7.12	9.75	11.71	13.24
5.0°	1.45	2.62	5.33	9.35	11.48	12.85	14.16

Table 5.1.2. The mean surface gravity anomaly error $|G - G_J|_{mean}$ in mGal at the wavelet resolution level $J = 0$ to $J = 6$ for each spatial resolution of the truth data. Bold faced numbers are the minimum mean error for the wavelet level J at each spatial resolution.

Spatial Resolution	$ G - G_0 _{RMS}$	$ G - G_1 _{RMS}$	$ G - G_2 _{RMS}$	$ G - G_3 _{RMS}$	$ G - G_4 _{RMS}$	$ G - G_5 _{RMS}$	$ G - G_6 _{RMS}$
0.5°	48.70	46.29	42.49	35.24	29.46	23.69	21.04
1.0°	34.90	31.88	27.18	18.58	12.67	9.55	13.04
1.5°	29.38	26.06	20.96	12.17	8.60	11.64	17.70
2.0°	24.06	20.45	15.11	8.23	10.88	17.37	23.53
3.0°	13.64	9.47	5.79	13.81	22.59	30.27	35.56
4.0°	7.17	4.31	9.13	21.79	30.43	37.02	41.14
5.0°	3.77	7.58	15.71	28.29	35.62	40.78	44.25

Table 5.1.3. The RMS surface gravity anomaly error $|G - G_J|_{RMS}$ in mGal for the sub-region of $278.25^\circ \sim 299.75^\circ$ in longitude and $-24.75^\circ \sim 19.75^\circ$ in latitude: the region with high gravity gradients profile.

Spatial Resolution	$ G - G_0 _{mean}$	$ G - G_1 _{mean}$	$ G - G_2 _{mean}$	$ G - G_3 _{mean}$	$ G - G_4 _{mean}$	$ G - G_5 _{mean}$	$ G - G_6 _{mean}$
0.5°	31.98	30.47	27.77	22.87	19.13	15.49	14.04
1.0°	23.52	21.59	18.29	12.47	8.71	6.68	8.70
1.5°	20.11	17.97	14.48	8.57	6.18	8.04	11.62
2.0°	16.78	14.34	10.69	5.97	7.91	11.81	15.50
3.0°	10.06	7.10	4.29	9.93	15.62	20.22	23.33
4.0°	5.42	3.25	6.64	15.49	21.07	24.89	27.23
5.0°	2.85	5.59	11.41	20.36	24.83	27.47	29.38

Table 5.1.4. The mean surface gravity anomaly error $|G - G_J|_{mean}$ in mGal for the sub-region of $278.25^\circ \sim 299.75^\circ$ in longitude and $-24.75^\circ \sim 19.75^\circ$ in latitude.

Spatial Resolution	$ G - G_0 _{RMS}$	$ G - G_1 _{RMS}$	$ G - G_2 _{RMS}$	$ G - G_3 _{RMS}$	$ G - G_4 _{RMS}$	$ G - G_5 _{RMS}$	$ G - G_6 _{RMS}$
0.5°	14.03	13.36	12.24	10.43	9.01	7.75	7.90
1.0°	9.81	8.94	7.49	5.25	3.75	3.17	5.23
1.5°	8.29	7.33	5.74	3.47	2.60	3.48	6.05
2.0°	6.86	5.83	4.17	2.50	3.20	4.96	7.40
3.0°	4.04	2.87	1.75	4.05	6.37	8.40	10.36
4.0°	2.25	1.43	2.74	6.27	8.55	10.27	11.81
5.0°	1.35	2.23	4.68	8.21	10.10	11.40	12.73

Table 5.1.5. The RMS surface gravity anomaly error $|G - G_J|_{RMS}$ in mGal for the sub-region of $304.25^\circ \sim 329.75^\circ$ in longitude and $-14.75^\circ \sim 19.75^\circ$ in latitude: the region with moderate gravity gradients.

Spatial Resolution	$ G - G_0 _{mean}$	$ G - G_1 _{mean}$	$ G - G_2 _{mean}$	$ G - G_3 _{mean}$	$ G - G_4 _{mean}$	$ G - G_5 _{mean}$	$ G - G_6 _{mean}$
0.5°	9.75	9.20	8.37	7.13	6.20	5.45	5.76
1.0°	6.91	6.22	5.22	3.71	2.74	2.34	3.74
1.5°	5.87	5.12	4.02	2.53	1.95	2.61	4.46
2.0°	4.89	4.10	2.97	1.87	2.32	3.61	5.46
3.0°	2.94	2.08	1.35	2.85	4.45	6.01	7.63
4.0°	1.68	1.11	2.04	4.38	5.96	7.29	8.65
5.0°	1.06	1.70	3.43	5.78	7.08	8.08	9.30

Table 5.1.6. The mean surface gravity anomaly error $|G - G_J|_{mean}$ in mGal for the sub-region of $304.25^\circ \sim 329.75^\circ$ in longitude and $-14.75^\circ \sim 19.75^\circ$ in latitude.

Spatial Resolution	$ G - G_0 _{RMS}$	$ G - G_1 _{RMS}$	$ G - G_2 _{RMS}$	$ G - G_3 _{RMS}$	$ G - G_4 _{RMS}$	$ G - G_5 _{RMS}$	$ G - G_6 _{RMS}$
0.5°	3.98	3.90	3.79	3.53	3.31	2.96	2.81
1.0°	2.24	2.11	1.94	1.56	1.28	0.99	1.39
1.5°	1.78	1.62	1.42	1.01	0.83	0.93	1.65
2.0°	1.45	1.28	1.08	0.75	0.84	1.24	2.00
3.0°	0.90	0.72	0.65	0.89	1.41	2.01	2.69
4.0°	0.61	0.52	0.72	1.27	1.80	2.30	2.86
5.0°	0.49	0.61	1.01	1.61	2.05	2.42	2.93

Table 5.1.7. The RMS surface gravity anomaly error $|G - G_J|_{RMS}$ in mGal for the sub-region of $250.25^\circ \sim 275.25^\circ$ in longitude and $-20.75^\circ \sim 4.75^\circ$ in latitude: the region with low gravity gradients.

Spatial Resolution	$ G - G_0 _{mean}$	$ G - G_1 _{mean}$	$ G - G_2 _{mean}$	$ G - G_3 _{mean}$	$ G - G_4 _{mean}$	$ G - G_5 _{mean}$	$ G - G_6 _{mean}$
0.5°	2.21	2.14	2.06	1.91	1.81	1.67	1.78
1.0°	1.32	1.20	1.08	0.86	0.72	0.61	1.05
1.5°	1.12	0.98	0.84	0.62	0.53	0.60	1.15
2.0°	0.95	0.81	0.65	0.48	0.53	0.74	1.31
3.0°	0.63	0.47	0.40	0.58	0.83	1.14	1.64
4.0°	0.42	0.33	0.47	0.81	1.08	1.33	1.75
5.0°	0.32	0.41	0.68	1.06	1.27	1.44	1.80

Table 5.1.8. The mean surface gravity anomaly error $|G - G_J|_{mean}$ in mGal for the sub-region of $250.25^\circ \sim 275.25^\circ$ in longitude and $-20.75^\circ \sim 4.75^\circ$ in latitude.

5.2. Region I with Four Times the Volume of Input Data

In order to study how the size of the local area at altitude, where the satellite gravity measurements are attained to solve the inverse problem, affects the accuracy of the recovered surface gravity, we increased the area of the input data 4 times (twice in longitude and twice in latitude) of the original one for the same solution region as in **5.1**, *i.e.* $162.25^\circ \sim 58.25^\circ$ in longitude (counterclockwise) and $-66.25^\circ \sim 61.75^\circ$ latitude, which is equivalent to $58.25^\circ\text{E} \sim 162.25^\circ\text{E}$ in longitude (clockwise) and $66.25^\circ\text{S} \sim 61.75^\circ\text{N}$ latitude. The gravity anomaly data at $h = 300$ km on a 513×257 grid was used to recover the surface gravity for the Region I. The maximum degree of Legendre polynomials N was set to be 300 and the regularization parameters used are: $\gamma_0 = 9.0 \times 10^{-2}$, $\gamma_1 = 5.0 \times 10^{-2}$, $\gamma_2 = 2.0 \times 10^{-2}$, $\gamma_3 = 4.0 \times 10^{-3}$, $\gamma_4 = 1.0 \times 10^{-3}$, $\gamma_5 = 2.0 \times 10^{-4}$ and $\gamma_6 = 5.0 \times 10^{-5}$, and all other parameters remained the same as in section **5.1**. The result follows below.

Fig. 5.2.1 and **Fig. 5.2.2** in the next pages are the contour and 3-D surface plots for the recovered surface gravity anomaly for wavelet resolution level $J = 5$ and $J = 6$. The gravity solutions at these two resolutions are the ones with the most improved results by the change in the input data.

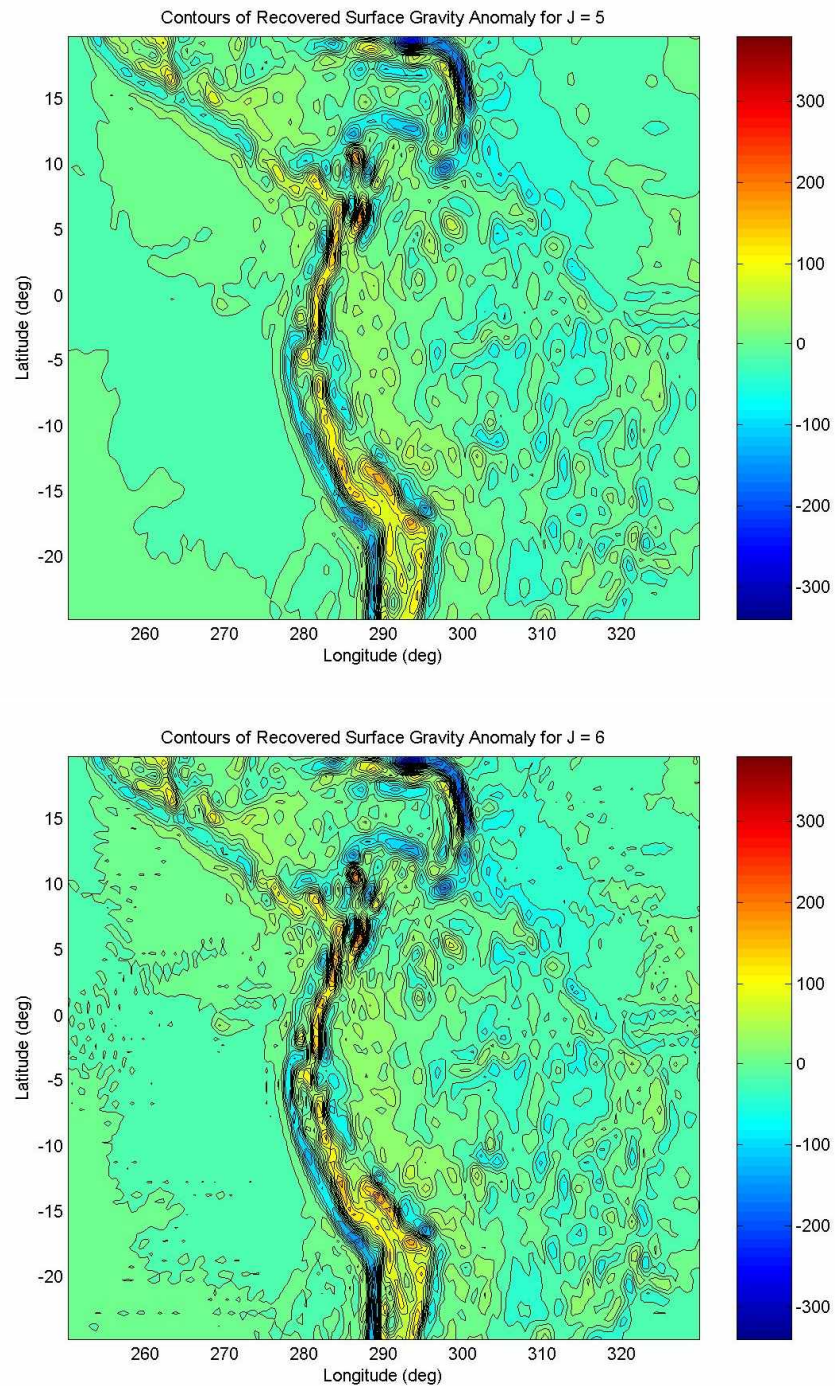


Fig. 5.2.1. The contour map of the recovered gravity anomaly for the wavelet resolution level $J = 5$ and $J = 6$ with the 4 times more data volume. “Forced” fine signals appear at $J = 6$. They are more prominent in the low gravity gradient region, in contrast to the high-moderate gravity gradient area.

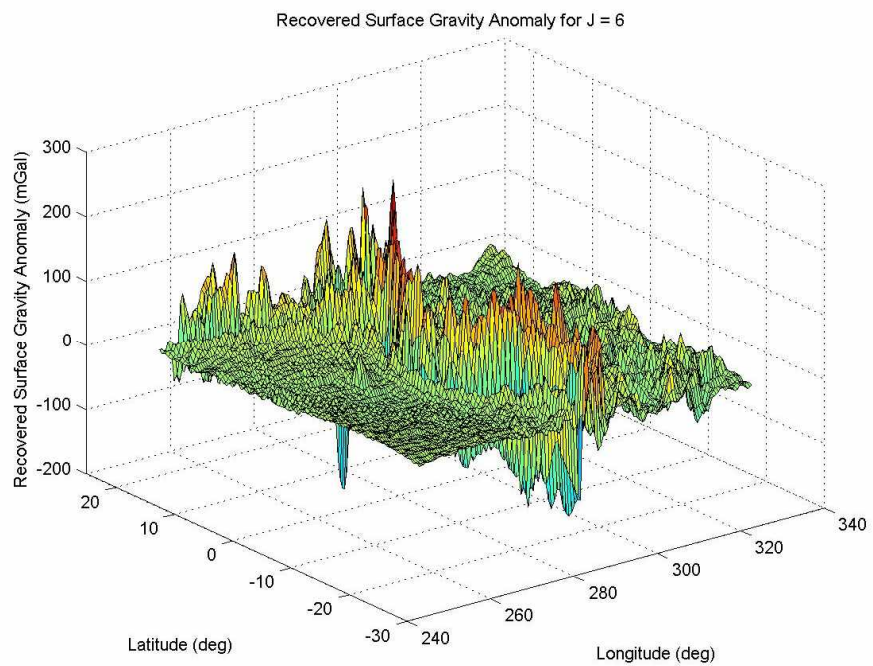
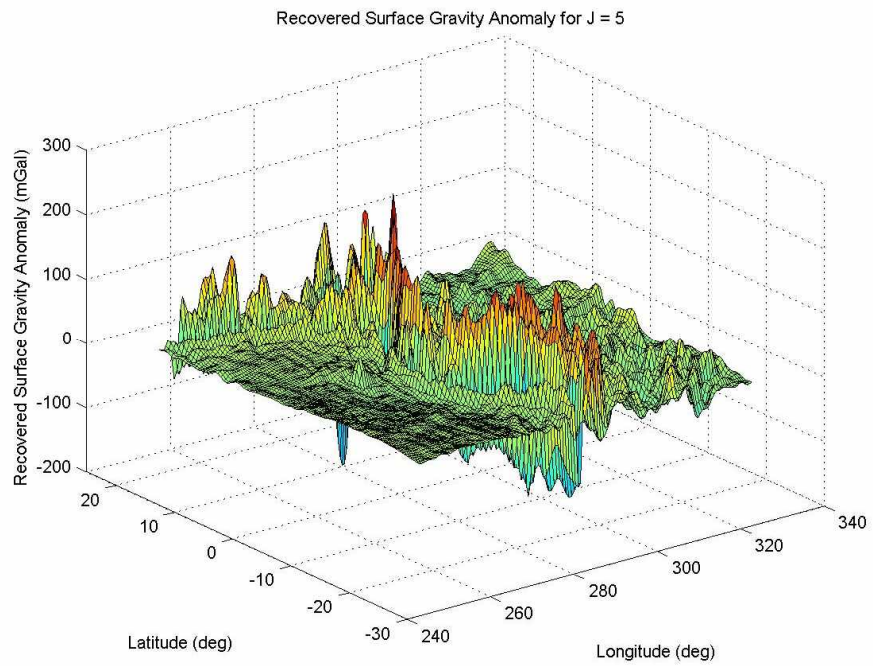


Fig. 5.2.2. 3-D surface map of the recovered gravity anomaly for the wavelet resolution level $J = 5$ and $J = 6$ with the 4 times more data volume.

Table 5.2.1 in comparison to **Table 5.1.1** shows that the RMS error has improved by 1.3 mGal at the resolution of 0.5° and 0.3 mGal at the resolution 1°, whereas the lower resolution signals were little affected by the change in the input data.

Spatial Resolution	$ G - G_0 _{RMS}$	$ G - G_1 _{RMS}$	$ G - G_2 _{RMS}$	$ G - G_3 _{RMS}$	$ G - G_4 _{RMS}$	$ G - G_5 _{RMS}$	$ G - G_6 _{RMS}$
0.5°	28.90	27.54	25.38	21.28	17.96	14.59	12.18
1.0°	20.51	18.78	16.06	11.13	7.66	5.56	5.96
1.5°	17.26	15.35	12.39	7.34	5.16	6.61	9.07
2.0°	14.13	12.05	8.94	4.97	6.41	10.05	12.88
3.0°	8.05	5.64	3.46	8.10	13.25	17.66	20.22
4.0°	4.29	2.62	5.36	12.77	17.84	21.62	23.55
5.0°	2.29	4.44	9.23	16.59	20.88	23.80	25.38

Table 5.2.1. The RMS surface gravity anomaly error $|G - G_J|_{RMS}$ in mGal at the wavelet resolution level $J = 0$ to $J = 6$ for each spatial resolution of the truth data.

Table 5.2.2 to **Table 5.2.4** provide the RMS error of the recovered surface gravity anomaly with different wavelet resolutions at each spatial resolution. It is noted that the increase of the volume of input data improved the accuracy significantly (by 1.8 mGal for the resolution 0.5° and by 0.4 mGal for 1°) in the region with high gravity gradients whereas it barely affected the accuracy in the region with low gravity gradients profile except for the solution with $J = 6$.

Spatial Resolution	$ G - G_0 _{RMS}$	$ G - G_1 _{RMS}$	$ G - G_2 _{RMS}$	$ G - G_3 _{RMS}$	$ G - G_4 _{RMS}$	$ G - G_5 _{RMS}$	$ G - G_6 _{RMS}$
0.5°	48.70	46.29	42.50	35.27	29.52	23.66	19.29
1.0°	34.90	31.88	27.19	18.61	12.72	9.11	9.34
1.5°	29.39	26.06	20.97	12.20	8.58	11.07	14.89
2.0°	24.07	20.45	15.12	8.25	10.82	16.92	21.39
3.0°	13.64	9.47	5.79	13.78	22.49	29.87	33.97
4.0°	7.18	4.32	9.12	21.76	30.34	36.66	39.77
5.0°	3.78	7.59	15.71	28.26	35.53	40.45	42.99

Table 5.2.2. The RMS surface gravity anomaly error $|G - G_J|_{RMS}$ in mGal for the sub-region of $278.25^\circ \sim 299.75^\circ$ in longitude and $-24.75^\circ \sim 19.75^\circ$ in latitude: the region with high gravity gradients profile.

Spatial Resolution	$ G - G_0 _{RMS}$	$ G - G_1 _{RMS}$	$ G - G_2 _{RMS}$	$ G - G_3 _{RMS}$	$ G - G_4 _{RMS}$	$ G - G_5 _{RMS}$	$ G - G_6 _{RMS}$
0.5°	14.03	13.36	12.23	10.43	9.00	7.63	6.94
1.0°	9.80	8.94	7.48	5.24	3.72	2.88	3.78
1.5°	8.28	7.33	5.73	3.46	2.55	3.23	4.92
2.0°	6.85	5.82	4.16	2.49	3.16	4.78	6.49
3.0°	4.03	2.86	1.73	4.04	6.34	8.30	9.72
4.0°	2.23	1.41	2.73	6.26	8.53	10.18	11.25
5.0°	1.32	2.22	4.67	8.20	10.08	11.32	12.21

Table 5.2.3. The RMS surface gravity anomaly error $|G - G_J|_{RMS}$ in mGal for the sub-region of $304.25^\circ \sim 329.75^\circ$ in longitude and $-14.75^\circ \sim 19.75^\circ$ in latitude: the region with moderate gravity gradients.

Spatial Resolution	$ G - G_0 _{RMS}$	$ G - G_1 _{RMS}$	$ G - G_2 _{RMS}$	$ G - G_3 _{RMS}$	$ G - G_4 _{RMS}$	$ G - G_5 _{RMS}$	$ G - G_6 _{RMS}$
0.5°	3.98	3.90	3.79	3.53	3.31	2.97	3.59
1.0°	2.24	2.11	1.94	1.56	1.28	1.00	2.56
1.5°	1.78	1.62	1.42	1.00	0.83	0.94	2.70
2.0°	1.45	1.28	1.08	0.75	0.84	1.25	2.93
3.0°	0.90	0.72	0.65	0.89	1.41	2.01	3.45
4.0°	0.61	0.52	0.72	1.27	1.80	2.31	3.58
5.0°	0.49	0.61	1.01	1.61	2.05	2.43	3.63

Table 5.2.4. The RMS surface gravity anomaly error $|G - G_J|_{RMS}$ in mGal for the sub-region of $250.25^\circ \sim 275.25^\circ$ in longitude and $-20.75^\circ \sim 4.75^\circ$ in latitude: the region with low gravity gradients.

From the result, we can conclude that the increased volume of the input data improves the recovery of the gravity anomaly at finer resolutions as well as the recovery of the high gravity gradients signals. It also appears that in an attempt to recover the fine details in the high gradient gravity anomaly, the wavelet solution with high resolution level (*i.e.* $J = 6$) overcompensates the low gravity gradient region resulting in producing “forced” signals. **Table 5.2.4** confirms this: for the spatial resolution 0.5° , $J = 5$ is a better solution than $J = 6$ in the region with the low gravity gradient profile. If the overcompensated region is removed, $J = 6$ appears to successfully represent the gravity solution for the spatial resolution between 0.5° and 1° , which is a definite improvement over the solution in section **5.1**.

5.3. Region I with $N = 150$

In equation (3.2.8), the wavelet solution to the inverse problem takes the form of the summation of the surface integral up to the maximum degree of Legendre polynomials N . In order to study the effect of N on the recovery of the surface gravity anomaly, we reduced N from 300 to 150. We used the gravity anomaly data at the satellite altitude from the region of $226.25^\circ \sim 354.25^\circ$ in longitude ($5.75^\circ\text{W} \sim 133.75^\circ\text{W}$) and $-34.25^\circ \sim 29.75^\circ$ in latitude ($34.25^\circ\text{S} \sim 29.75^\circ\text{N}$) on a 257×129 regular grid, the same region for the gravity data used in **5.1**. The regularization parameters used for the simulation are $\gamma_0 = 9.0 \times 10^{-2}$, $\gamma_1 = 5.0 \times 10^{-2}$, $\gamma_2 = 2.0 \times 10^{-2}$, $\gamma_3 = 6.0 \times 10^{-3}$, $\gamma_4 = 4.0 \times 10^{-3}$ and $\gamma_5 = 2.0 \times 10^{-3}$.

The contour and 3-D surface maps of the gravity anomaly for the wavelet resolution levels $J = 4$ and $J = 5$, the two with the result most affected by the change in N , are shown in **Fig. 5.3.1** and **Fig. 5.3.2**. A notable difference compared to the results in section **5.1** is that the solution with the wavelet resolution level $J = 5$ failed to recover the gravity anomaly for the spatial resolution of 1° . The contour map **Fig. 5.3.1** shows the interferences caused by “forced” fine signals for the wavelet resolution level $J = 5$, indicating that the model is incapable of recovering the gravity signals finer than 1.5° resolution. The gravity anomaly peaks shown in the 3-D surface map in **Fig. 5.3.2** are not as sharply defined as is the case with $N = 300$.

The result is expected from the **Fig. 3.2.1** and **Fig. 3.2.2**, the plots for the Legendre coefficient of the scale discrete Tikhonov spherical regularization scaling function and wavelet packets. Higher wavelet level filters correspond to the larger degree of Legendre polynomials, and thus the small N means the high level wavelet solution becomes unreliable.

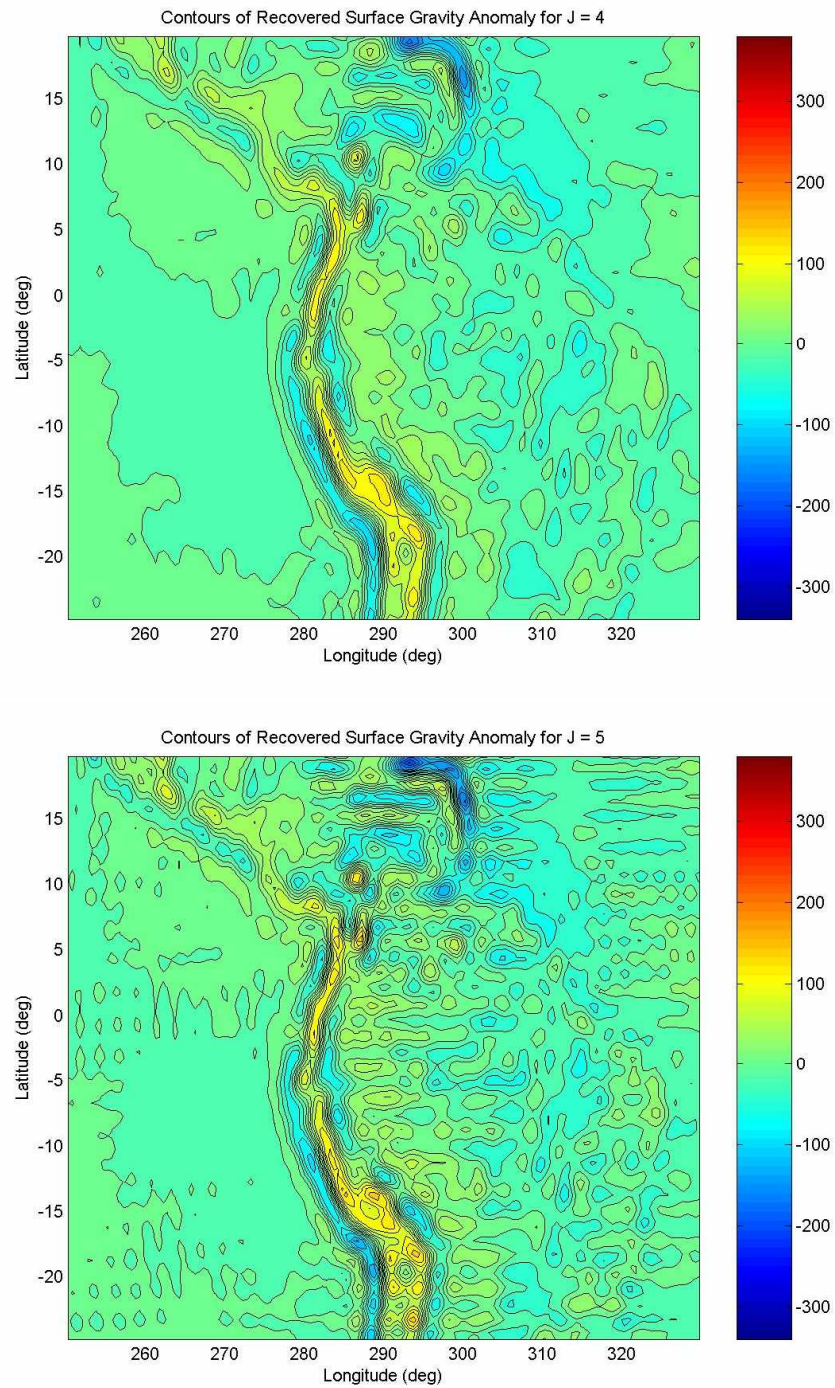


Fig. 5.3.1. The contour map of the recovered gravity anomaly for the wavelet resolution level $J = 4$ and $J = 5$ when N was set to be 150. “Forced” fine signals along the grid lines are very prominent at $J = 5$.

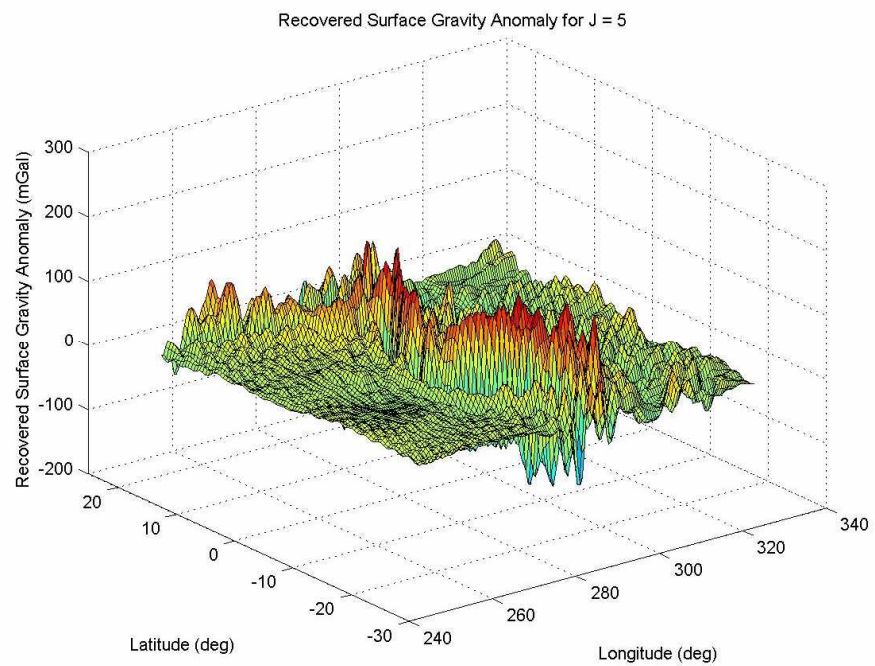
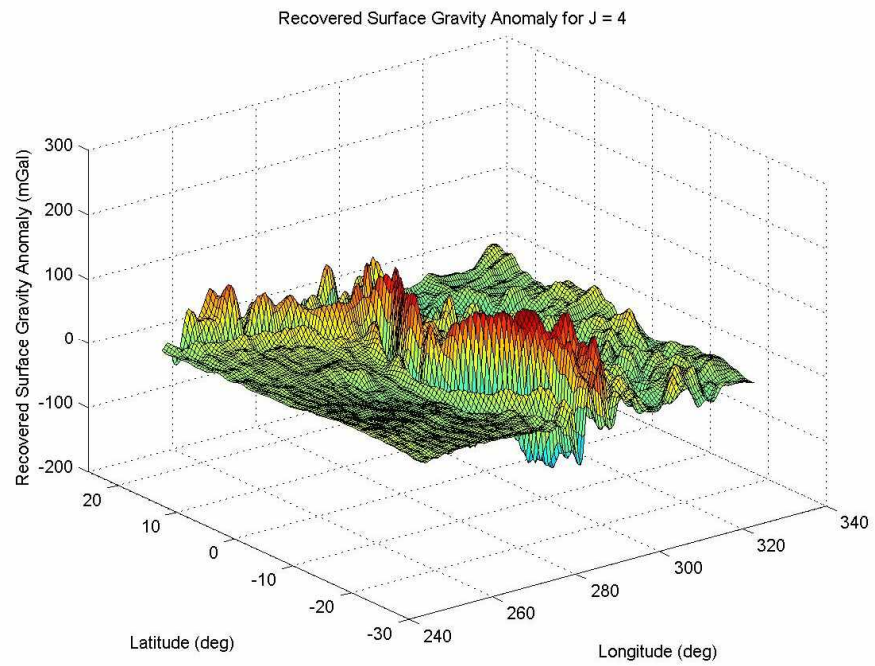


Fig. 5.3.2. 3-D surface map of the recovered gravity anomaly for the wavelet resolution level $J = 4$ and $J = 5$, with $N = 150$.

As is confirmed in **Table 5.3.1** in comparison with **Table 5.1.1**, the change in N appears to affect the shorter wavelength signals only. The anomaly error has scarcely changed for the spatial resolution $3^\circ \sim 5^\circ$, while it has increased significantly for the resolution $1^\circ \sim 2^\circ$. The RMS error increased by 5.8 mGal for the resolution 1° , by 2.8 mGal for 1.5° and by 0.8 mGal for 2° .

Spatial Resolution	$ G - G_0 _{RMS}$	$ G - G_1 _{RMS}$	$ G - G_2 _{RMS}$	$ G - G_3 _{RMS}$	$ G - G_4 _{RMS}$	$ G - G_5 _{RMS}$
1.0°	20.51	18.78	16.06	12.47	11.64	13.86
1.5°	17.26	15.36	12.39	8.65	8.01	11.65
2.0°	14.13	12.05	8.94	5.72	5.84	11.16
3.0°	8.05	5.64	3.46	6.59	8.54	14.36
4.0°	4.29	2.62	5.36	11.03	13.05	18.17
5.0°	2.29	4.44	9.23	15.00	16.84	21.28

Table 5.3.1. The RMS surface gravity anomaly error $|G - G_J|_{RMS}$ in mGal at the wavelet resolution level $J = 0$ to $J = 5$ for each spatial resolution of the truth data.

Table 5.3.2 to **Table 5.3.4** provide the insight of how the change in N affected the result for the regions with different gravity gradients. The change affected the region with the high gravity gradients most severely, while the effect is less noticeable for the region with low gravity gradients profile.

Spatial Resolution	$ G - G_0 _{RMS}$	$ G - G_1 _{RMS}$	$ G - G_2 _{RMS}$	$ G - G_3 _{RMS}$	$ G - G_4 _{RMS}$	$ G - G_5 _{RMS}$
1.0°	34.90	31.88	27.19	20.89	19.37	22.09
1.5°	29.38	26.06	20.97	14.41	13.19	18.11
2.0°	24.06	20.45	15.12	9.44	9.49	17.27
3.0°	13.64	9.47	5.78	11.11	14.35	23.14
4.0°	7.17	4.31	9.12	18.76	22.14	29.95
5.0°	3.77	7.58	15.72	25.51	28.61	35.42

Table 5.3.2. The RMS surface gravity anomaly error $|G - G_J|_{RMS}$ in mGal for the sub-region of $278.25^\circ \sim 299.75^\circ$ in longitude and $-24.75^\circ \sim 19.75^\circ$ in latitude: the region with high gravity gradients profile.

Spatial Resolution	$ G - G_0 _{RMS}$	$ G - G_1 _{RMS}$	$ G - G_2 _{RMS}$	$ G - G_3 _{RMS}$	$ G - G_4 _{RMS}$	$ G - G_5 _{RMS}$
1.0°	9.81	8.94	7.49	5.91	5.84	9.49
1.5°	8.29	7.33	5.74	4.14	4.27	8.80
2.0°	6.86	5.83	4.17	2.93	3.50	8.68
3.0°	4.04	2.87	1.75	3.50	4.68	9.71
4.0°	2.25	1.43	2.74	5.57	6.69	11.07
5.0°	1.35	2.23	4.68	7.55	8.54	12.35

Table 5.3.3. The RMS surface gravity anomaly error $|G - G_J|_{RMS}$ in mGal for the sub-region of $304.25^\circ \sim 329.75^\circ$ in longitude and $-14.75^\circ \sim 19.75^\circ$ in latitude: the region with moderate gravity gradients.

Spatial Resolution	$ G - G_0 _{RMS}$	$ G - G_1 _{RMS}$	$ G - G_2 _{RMS}$	$ G - G_3 _{RMS}$	$ G - G_4 _{RMS}$	$ G - G_5 _{RMS}$
1.0°	2.24	2.11	1.94	1.68	1.71	2.77
1.5°	1.78	1.62	1.42	1.15	1.23	2.54
2.0°	1.45	1.28	1.08	0.86	1.03	2.50
3.0°	0.90	0.72	0.65	0.83	1.13	2.64
4.0°	0.61	0.52	0.72	1.16	1.45	2.85
5.0°	0.49	0.61	1.01	1.50	1.77	3.03

Table 5.3.4. The RMS surface gravity anomaly error $|G - G_J|_{RMS}$ in mGal for the sub-region of $250.25^\circ \sim 275.25^\circ$ in longitude and $-20.75^\circ \sim 4.75^\circ$ in latitude – the region with low gravity gradients.

5.4. Region I with $N = 600$

In this case, we increased the maximum degree of Legendre polynomials N from the baseline of 300 up to 600. We employed the at-altitude gravity anomaly from the region of $226.25^\circ \sim 354.25^\circ$ in longitude ($5.75^\circ\text{W} \sim 133.75^\circ\text{W}$) and $-34.25^\circ \sim 29.75^\circ$ in latitude ($34.25^\circ\text{S} \sim 29.75^\circ\text{N}$) on a 257×129 regular grid as was used in section 5.1. The regularization parameters for the simulation are $\gamma_0 = 9.0 \times 10^{-2}$, $\gamma_1 = 5.0 \times 10^{-2}$, $\gamma_2 = 2.0 \times 10^{-2}$, $\gamma_3 = 4.0 \times 10^{-3}$, $\gamma_4 = 1.0 \times 10^{-3}$, $\gamma_5 = 2.0 \times 10^{-4}$ and $\gamma_6 = 5.0 \times 10^{-5}$.

The contour and 3-D surface maps of the gravity anomaly for the wavelet resolution levels $J = 5$ and $J = 6$ are shown in **Fig. 5.4.1** and **Fig. 5.4.2**. When compared to the results in 5.1, the recovered gravity anomaly with $J = 6$ exhibits less noticeable “forced” signals in the low gravity gradient region. If the area near the horizontal edges with the interference signals is removed, this wavelet resolution represents the gravity solution with the spatial resolution between 0.5° and 1° .

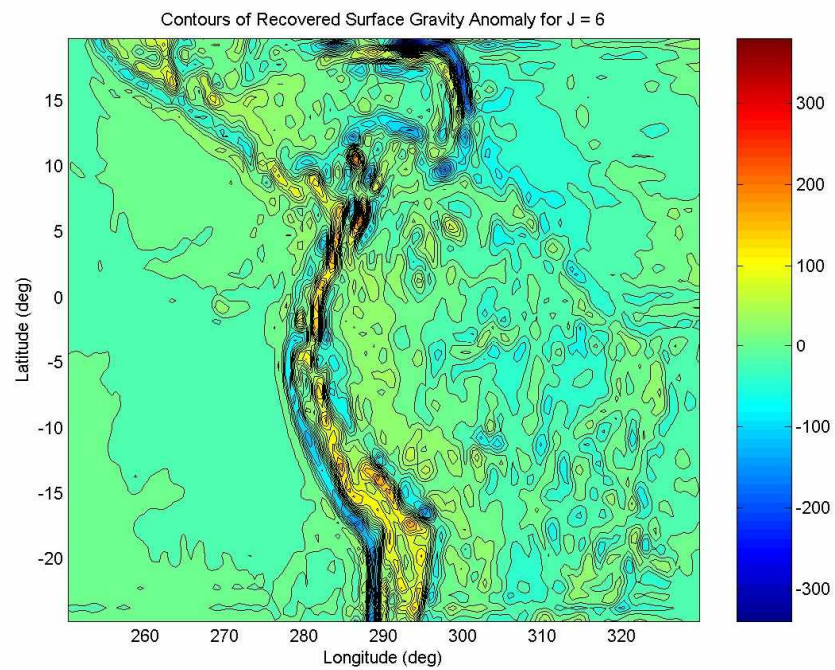
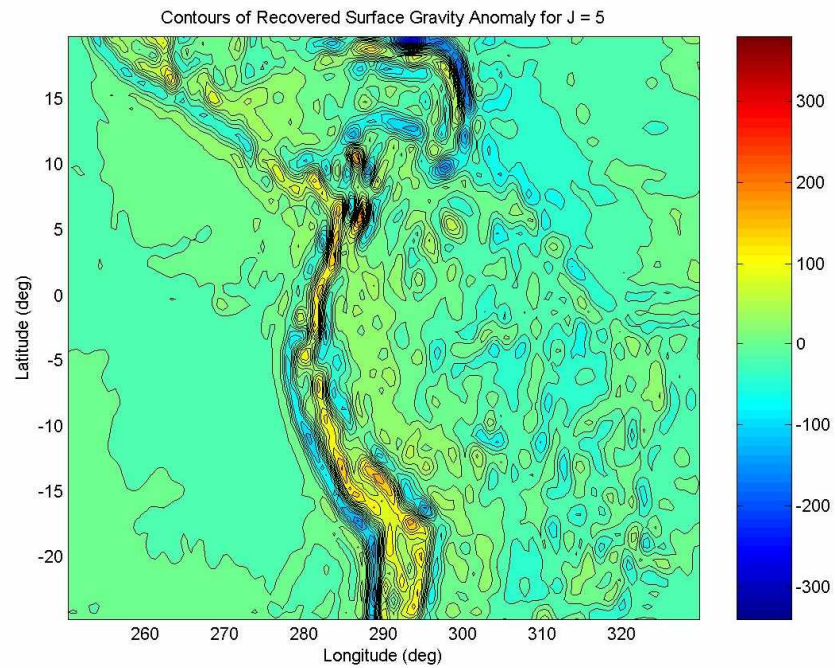


Fig. 5.4.1. The contour map of the recovered gravity anomaly for the wavelet resolution level $J = 5$ and $J = 6$ when N was set to be 600.

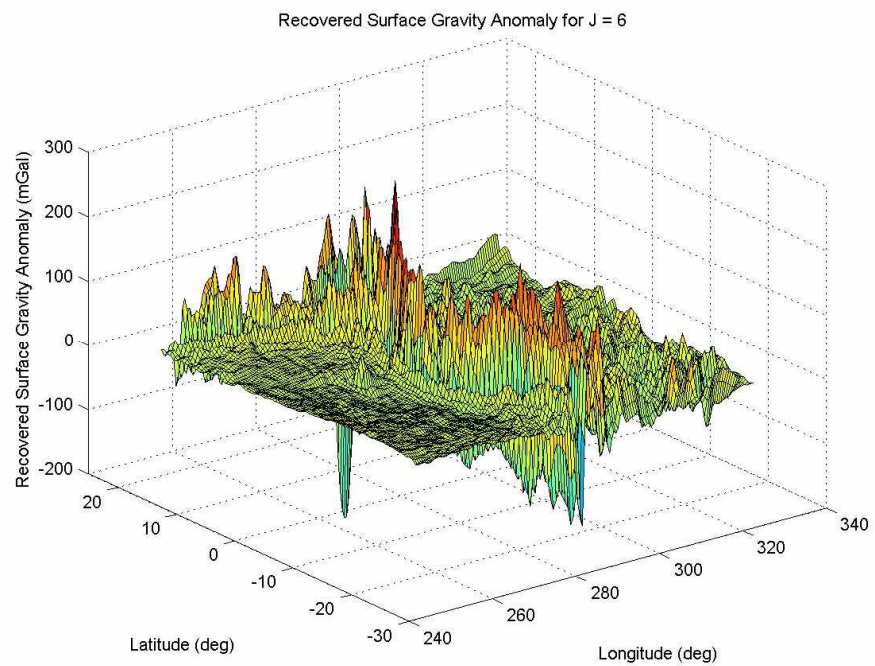
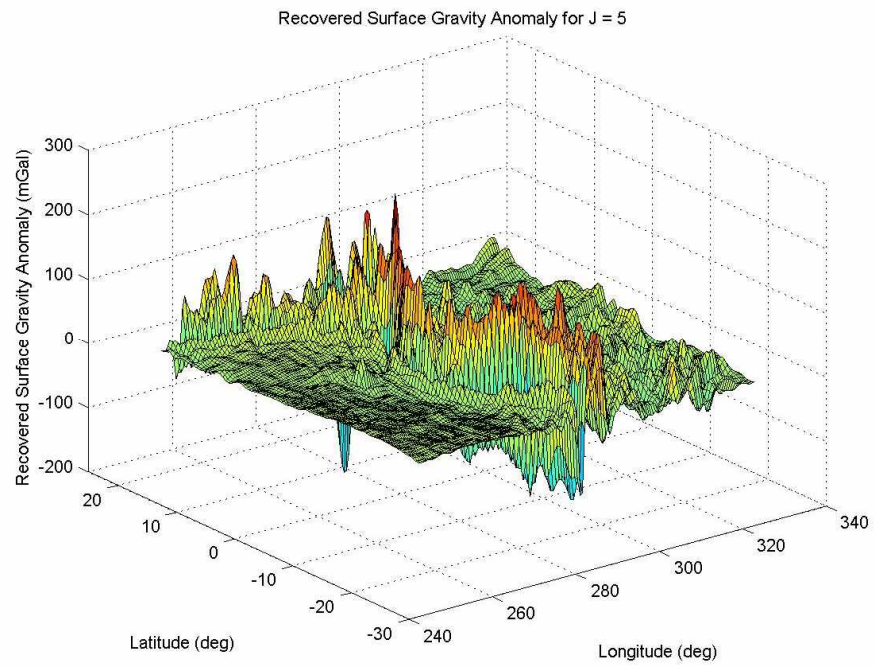


Fig. 5.4.2. 3-D surface map of the recovered gravity anomaly for the wavelet resolution level $J = 5$ and $J = 6$, with $N = 600$.

Table 5.4.1 shows that the improvement in RMS error by increasing N is very minimal except for the spatial resolution 0.5° . It has improved by 0.5 mGal at the resolution of 0.5° when compared to **Table 5.1.1**, whereas the gravity signals in the other resolutions were little affected by the change in N .

Spatial Resolution	$ G - G_0 _{RMS}$	$ G - G_1 _{RMS}$	$ G - G_2 _{RMS}$	$ G - G_3 _{RMS}$	$ G - G_4 _{RMS}$	$ G - G_5 _{RMS}$	$ G - G_6 _{RMS}$
0.5°	28.90	27.54	25.37	21.27	17.93	14.64	12.90
1.0°	20.51	18.78	16.06	11.11	7.65	5.86	7.58
1.5°	17.26	15.35	12.38	7.33	5.19	6.95	10.33
2.0°	14.13	12.05	8.93	4.97	6.45	10.31	13.83
3.0°	8.05	5.64	3.46	8.11	13.30	17.87	20.92
4.0°	4.29	2.63	5.37	12.78	17.89	21.81	24.16
5.0°	2.29	4.44	9.23	16.61	20.92	23.97	25.93

Table 5.4.1. The RMS surface gravity anomaly error $|G - G_J|_{RMS}$ in mGal at the wavelet resolution level $J = 0$ to $J = 6$ for each spatial resolution of the truth data.

Table 5.4.2 to **Table 5.4.4** provide the RMS error of the recovered surface gravity anomaly with different wavelet resolution levels at each spatial resolution. As is the case with the increased data volume, the increase in N improved the accuracy (by 0.7 mGal for the resolution 0.5°) in the region with high gravity gradients whereas the effect in the region with low gravity gradients profile are less noticeable.

Spatial Resolution	$ G - G_0 _{RMS}$	$ G - G_1 _{RMS}$	$ G - G_2 _{RMS}$	$ G - G_3 _{RMS}$	$ G - G_4 _{RMS}$	$ G - G_5 _{RMS}$	$ G - G_6 _{RMS}$
0.5°	48.70	46.29	42.49	35.24	29.46	23.68	20.37
1.0°	34.90	31.88	27.18	18.58	12.67	9.53	12.02
1.5°	29.38	26.06	20.96	12.17	8.60	11.63	17.00
2.0°	24.06	20.45	15.11	8.23	10.88	17.36	22.99
3.0°	13.64	9.47	5.79	13.81	22.59	30.26	35.20
4.0°	7.17	4.31	9.13	21.79	30.43	37.01	40.82
5.0°	3.77	7.58	15.71	28.29	35.62	40.77	43.94

Table 5.4.2. The RMS surface gravity anomaly error $|G - G_J|_{RMS}$ in mGal for the sub-region of $278.25^\circ \sim 299.75^\circ$ in longitude and $-24.75^\circ \sim 19.75^\circ$ in latitude: the region with high gravity gradients profile.

Spatial Resolution	$ G - G_0 _{RMS}$	$ G - G_1 _{RMS}$	$ G - G_2 _{RMS}$	$ G - G_3 _{RMS}$	$ G - G_4 _{RMS}$	$ G - G_5 _{RMS}$	$ G - G_6 _{RMS}$
0.5°	14.03	13.36	12.24	10.43	9.01	7.74	7.34
1.0°	9.81	8.94	7.49	5.25	3.75	3.15	4.39
1.5°	8.29	7.33	5.74	3.47	2.60	3.47	5.38
2.0°	6.86	5.83	4.17	2.50	3.20	4.95	6.84
3.0°	4.04	2.87	1.75	4.05	6.37	8.40	9.96
4.0°	2.25	1.43	2.74	6.27	8.55	10.27	11.47
5.0°	1.35	2.23	4.68	8.21	10.10	11.40	12.42

Table 5.4.3. The RMS surface gravity anomaly error $|G - G_J|_{RMS}$ in mGal for the sub-region of $304.25^\circ \sim 329.75^\circ$ in longitude and $-14.75^\circ \sim 19.75^\circ$ in latitude: the region with moderate gravity gradients.

Spatial Resolution	$ G - G_0 _{RMS}$	$ G - G_1 _{RMS}$	$ G - G_2 _{RMS}$	$ G - G_3 _{RMS}$	$ G - G_4 _{RMS}$	$ G - G_5 _{RMS}$	$ G - G_6 _{RMS}$
0.5°	3.98	3.90	3.79	3.53	3.31	2.96	2.61
1.0°	2.24	2.11	1.94	1.56	1.28	0.99	0.93
1.5°	1.78	1.62	1.42	1.01	0.83	0.93	1.31
2.0°	1.45	1.28	1.08	0.75	0.84	1.24	1.71
3.0°	0.90	0.72	0.65	0.89	1.41	2.01	2.49
4.0°	0.61	0.52	0.72	1.27	1.80	2.30	2.67
5.0°	0.49	0.61	1.01	1.61	2.05	2.42	2.74

Table 5.4.4. The RMS surface gravity anomaly error $|G - G_J|_{RMS}$ in mGal for the sub-region of $250.25^\circ \sim 275.25^\circ$ in longitude and $-20.75^\circ \sim 4.75^\circ$ in latitude: the region with low gravity gradients.

Recalling the result from section 5.3, it appears that the increase in N from 150 to 300 improved the accuracy of the recovered gravity anomaly significantly as well as it allowed the solution to recover shorter wavelength gravity signals. When N was increased to 600, however, the wavelet solution did not show noticeable improvement over the solution with $N = 300$, even for the short wavelength signals with the exception of the slight enhancement for the 0.5° resolution. The conclusion then follows that increasing the Legendre polynomial degree N does not improve the gravity solution indefinitely, since there exists a limit in improving the spatial resolution by increasing wavelet level.

Chapter 6. Simulation Result: Region II (160.25°E ~ 100.25°W and 24.75°S ~ 24.75°N)

Region II is the Pacific Ocean – a mainly low-moderate gravity gradient region except that South Solomon, New Hebrides and Tonga Trenches constitute sharp rises and plunges in the gravity anomaly in the south-west corner of the map and the Hawaiian Islands account for the sudden high rise in the north-west part and the tip of North America (Mexico) forms the peaks in the north-east corner of the area. The local surface gravity anomaly on a 200×100 grid for the region of $160.25^\circ \sim 259.75^\circ$ in longitude (equivalent to $160.25^\circ\text{E} \sim 100.25^\circ\text{W}$ in counterclockwise) and $-24.75^\circ \sim 24.75^\circ$ latitude ($24.75^\circ\text{S} \sim 24.75^\circ\text{N}$) was recovered from the gravity anomaly data of the local region of $146.25^\circ \sim 274.25^\circ$ in longitude ($146.25^\circ\text{E} \sim 85.75^\circ\text{W}$ counterclockwise) and $-31.75^\circ \sim 32.25^\circ$ in latitude ($31.75^\circ\text{S} \sim 32.25^\circ\text{N}$) on a 257×129 regular grid at the altitude of 300 km. The contour maps of the truth data at a resolution 0.5° and the gravity anomaly at the satellite altitude of corresponding local area are shown in **Fig. 6.1**. The 3-D surface plots are provided in **Fig. 6.2**.

Again, a mean filter was applied to the truth data to obtain the surface gravity anomaly at the different spatial resolutions from 1° to 5° to be compared to the recovered surface gravity anomaly with the different wavelet resolution levels from $J = 0$ to $J = 6$. The regularization parameters used in the simulation are $\gamma_0 = 9.0 \times 10^{-2}$, $\gamma_1 = 5.0 \times 10^{-2}$, $\gamma_2 = 2.0 \times 10^{-2}$, $\gamma_3 = 3.0 \times 10^{-3}$, $\gamma_4 = 1.0 \times 10^{-3}$, $\gamma_5 = 6.0 \times 10^{-4}$ and $\gamma_6 = 3.0 \times 10^{-4}$. The maximum degree of the Legendre polynomials N was set to be 300.

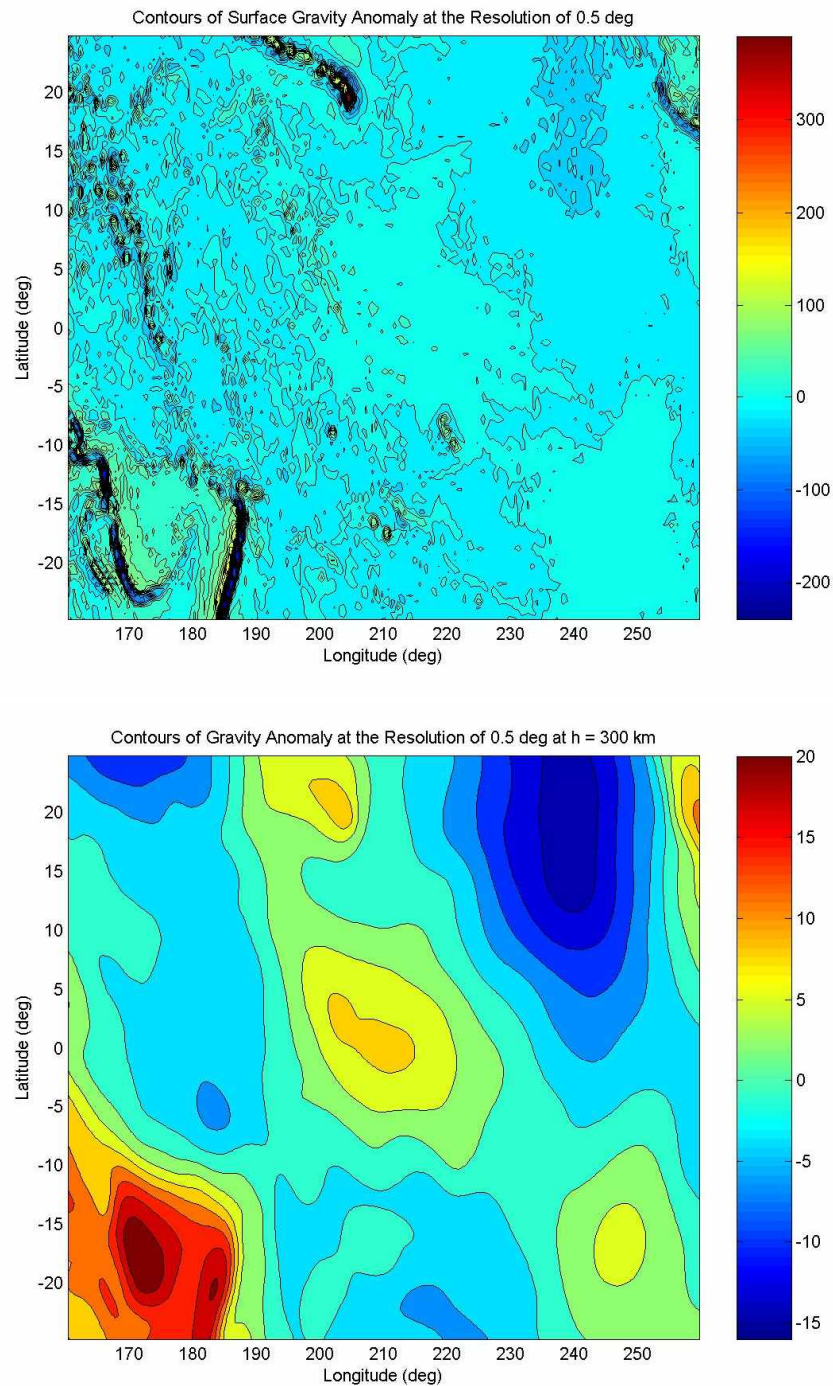


Fig. 6.1. The contour map of the surface gravity anomaly of the truth data at the resolution of 0.5° and the corresponding gravity anomaly at the satellite altitude $h = 300$ km with each contour respectively representing 20 mGal and 3 mGal of gravity anomaly difference.

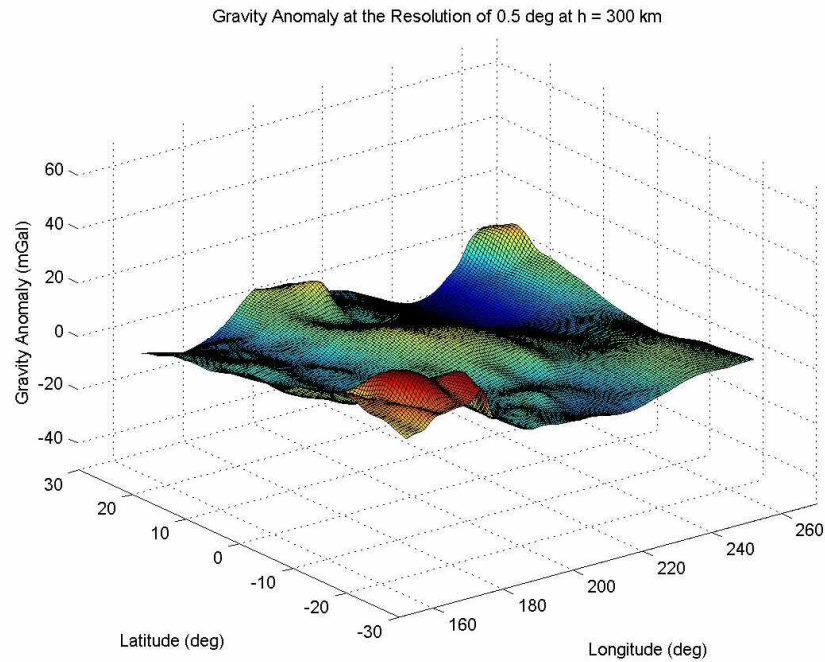
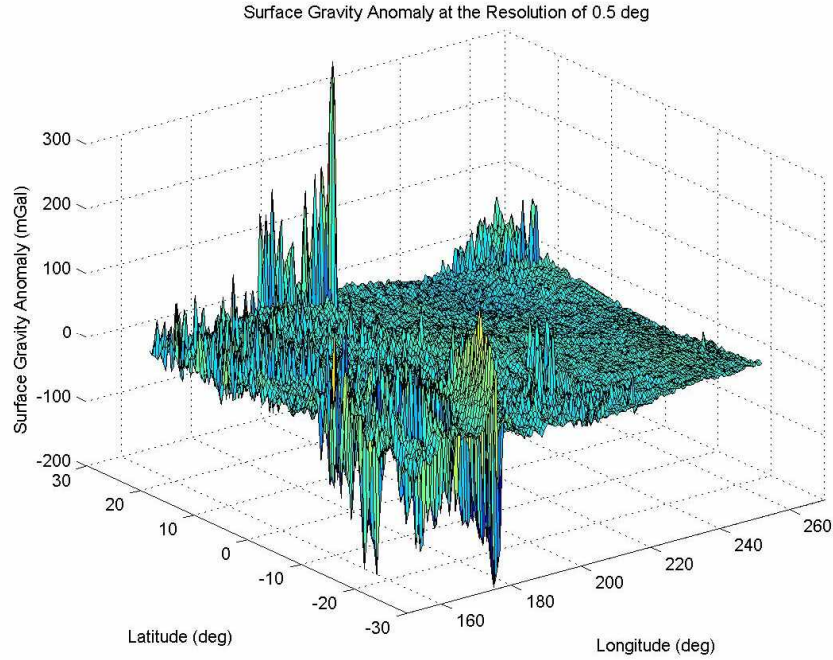


Fig. 6.2. 3-D surface plot of the surface gravity anomaly of the truth data at the resolution of 0.5° and the corresponding gravity anomaly at the satellite altitude $h = 300$ km to be used to recover the surface gravity anomaly by solving the inverse problem. The surface gravity information was smoothed out a great deal by upward propagation.

Fig. 6.3 to **Fig. 6.8** compare the recovered surface gravity anomaly at the wavelet resolution levels $J = 3$ to $J = 5$ to the truth data at its corresponding spatial resolution of 2° to 1° . In the contour maps, each contour accounts for 20 mGal of increment in gravity anomaly. The regularization parameters were chosen so that each wavelet resolution level corresponds to the different spatial resolution: The wavelet resolution level $J = 0$ corresponds to the spatial resolution 5° , $J = 1$ to the resolution 4° , $J = 2$ to 3° , $J = 3$ to 2° , $J = 4$ to 1.5° and $J = 5$ to 1° . As mentioned in section 5.1, finer details are recovered as the wavelet resolution level J increases up to $J = 5$, even if some of the interferences from the “forced” signals were observed near the horizontal edges starting from the wavelet resolution level $J = 4$. **Fig. 6.9** shows the interference is more prominent with the recovered gravity anomaly with the wavelet level $J = 6$.

Fig. 6.10 and **Fig. 6.11** provide the contour map and the 3-D plots of $|G - G_j|$, the surface gravity anomaly error, in different spatial and wavelet resolutions. With the truth surface gravity anomaly at each spatial resolution, wavelet solution that yields the least RMS error was chosen to create the plot. The error plots are arranged in the following order: error map with the spatial resolution of 1° at the top left, 1.5° top right, 2° middle left, 3° middle right, 4° bottom left and 5° bottom right. It is apparent that the error decreases as the spatial resolution increases. As is the case with Region I, here the largest errors also result from the area with the high gravity gradient signals (*i.e.* Southwestern Trenches and Hawaiian Islands), while the most of the ocean region with lower gravity gradients yields smaller errors.

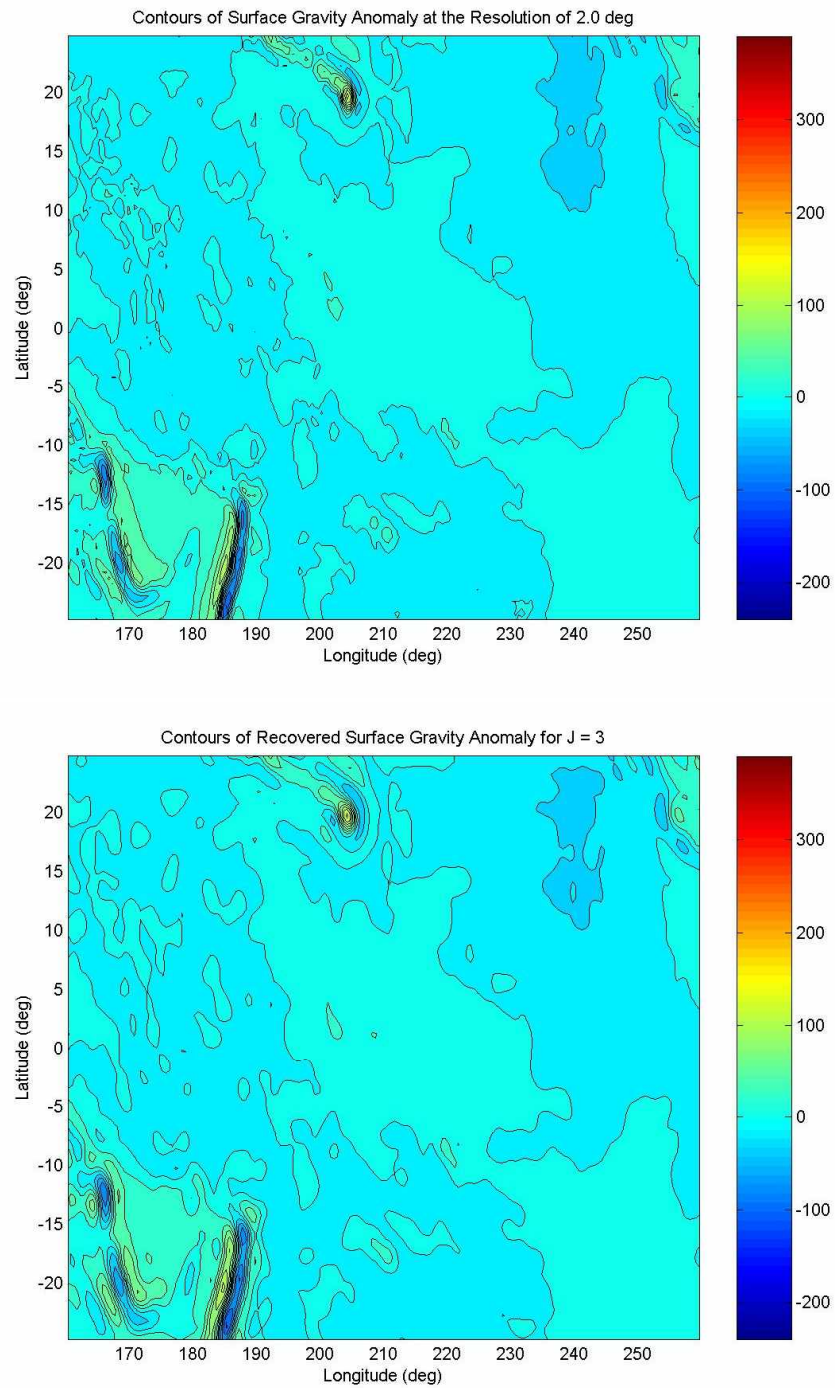


Fig. 6.3. The contour map of the truth data at the spatial resolution 2° and the recovered gravity anomaly for the wavelet resolution level $J = 3$. The RMS error in the region is 3.1 mGal and the mean error is 1.6 mGal.

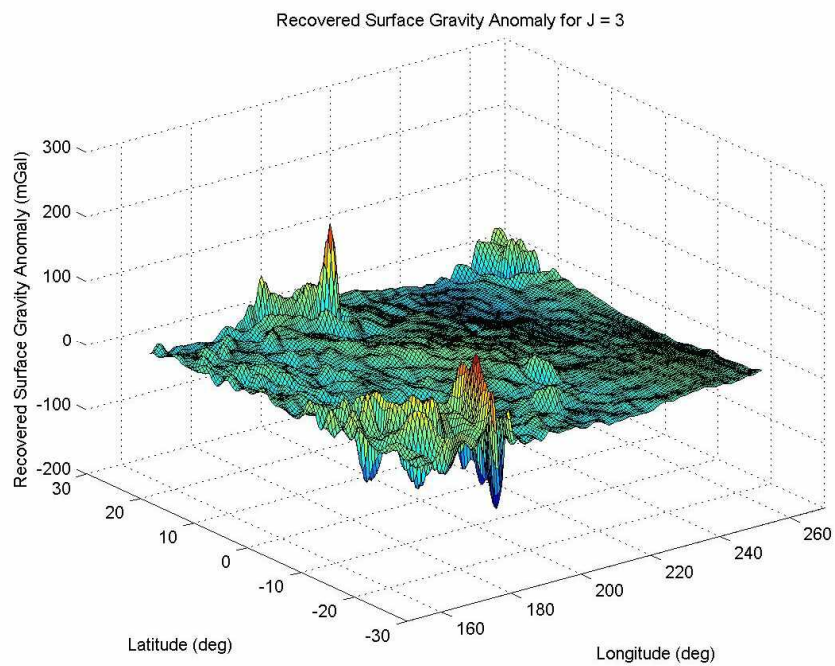
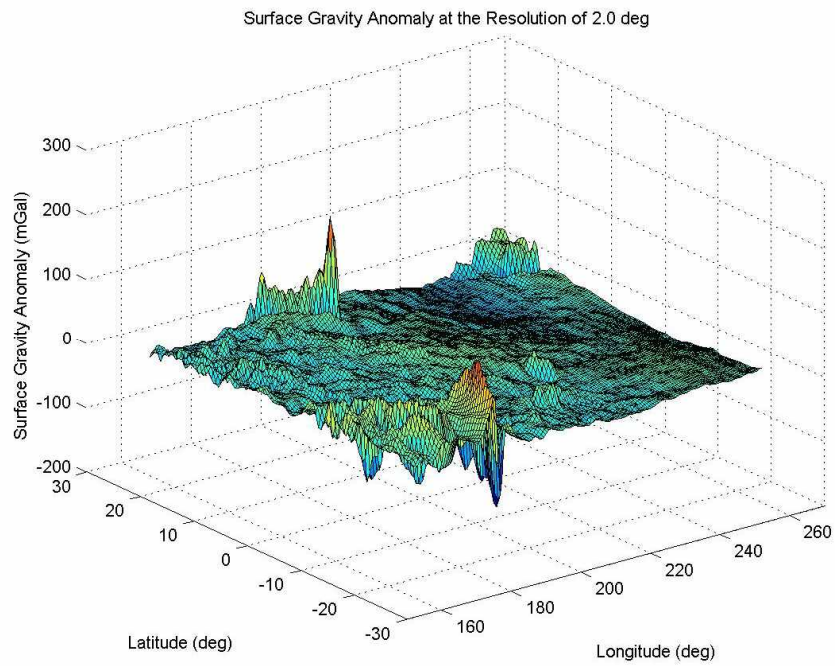


Fig. 6.4. 3-D surface map of the truth data at the spatial resolution 2° and the recovered gravity anomaly for the wavelet resolution level $J = 3$.

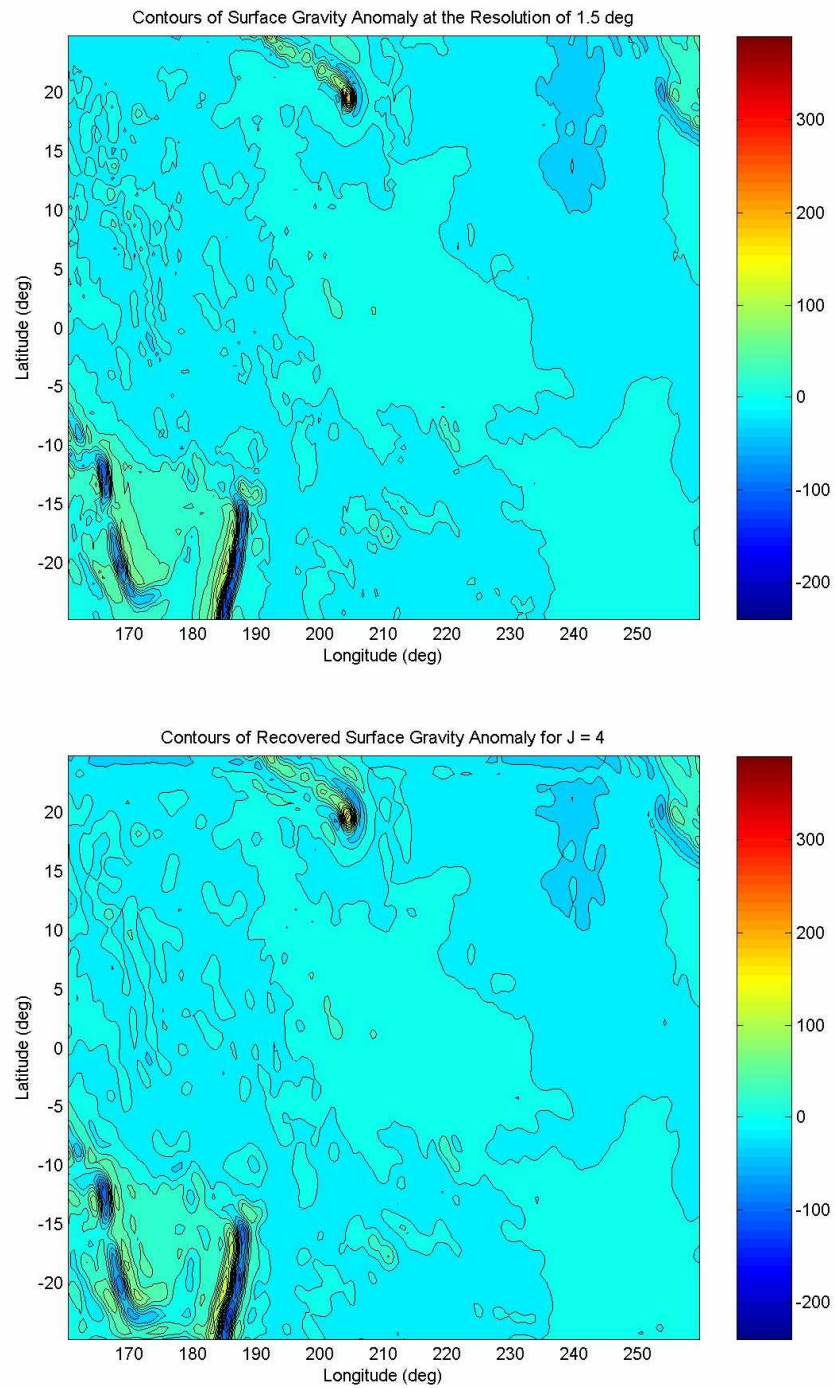


Fig. 6.5. The contour map of the truth data at the spatial resolution 1.5° and the recovered gravity anomaly for the wavelet resolution level $J = 4$. The RMS error in the region is 3.8 mGal and the mean error is 2.0 mGal.

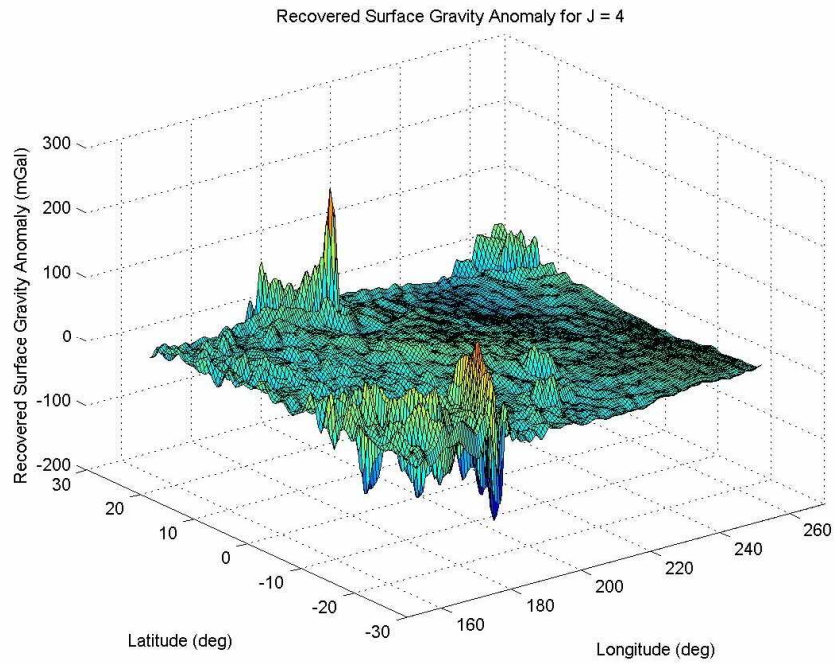
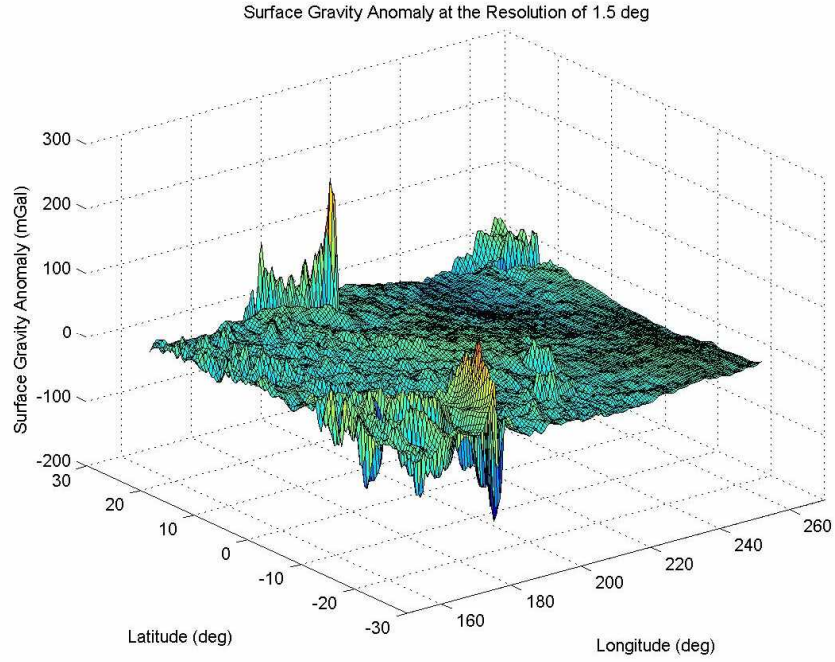


Fig. 6.6. 3-D surface map of the truth data at the spatial resolution 1.5° and the recovered gravity anomaly for the wavelet resolution level $J = 4$.

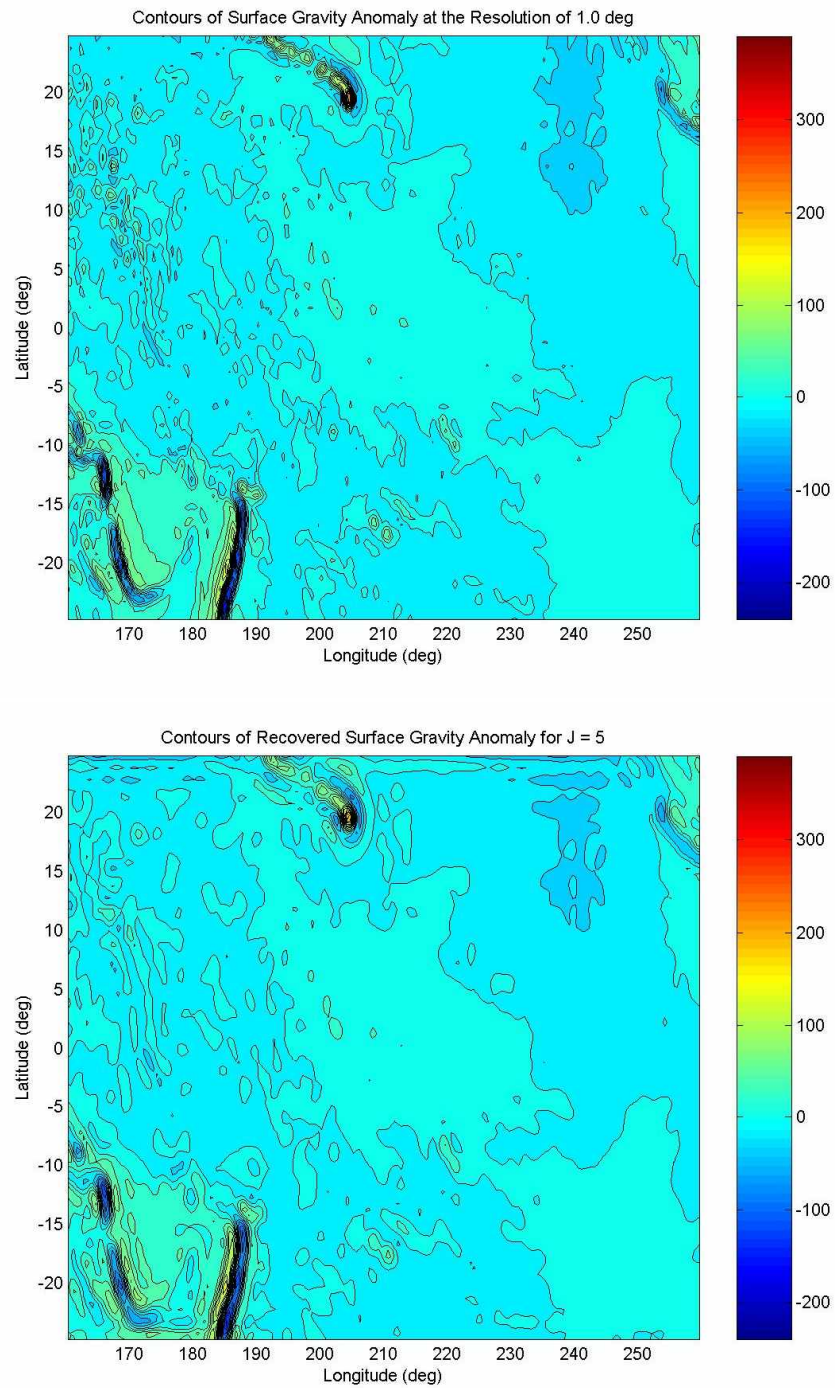


Fig. 6.7. The contour map of the truth data at the spatial resolution 1° and the recovered gravity anomaly for the wavelet resolution level $J = 5$. The RMS error in the region is 5.5 mGal and the mean error is 2.8 mGal.

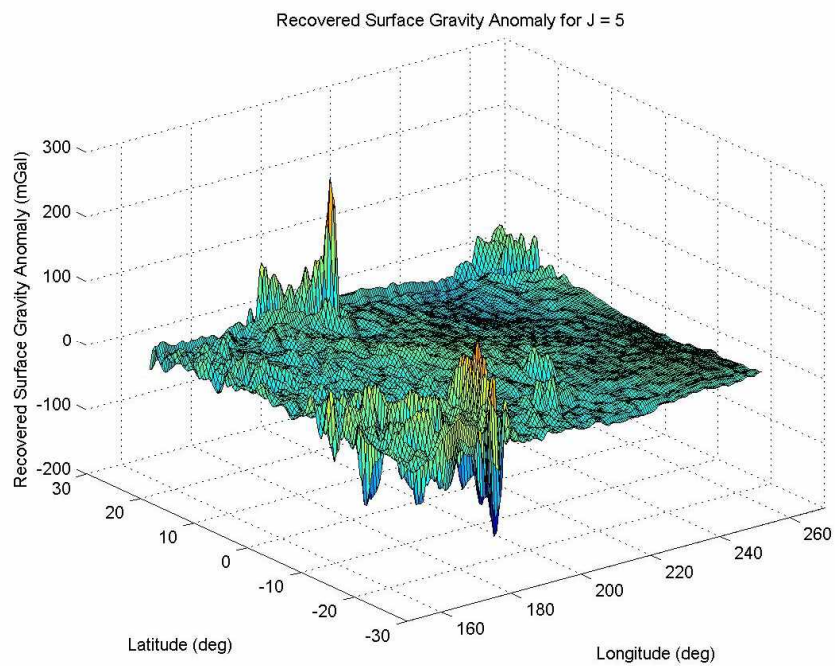
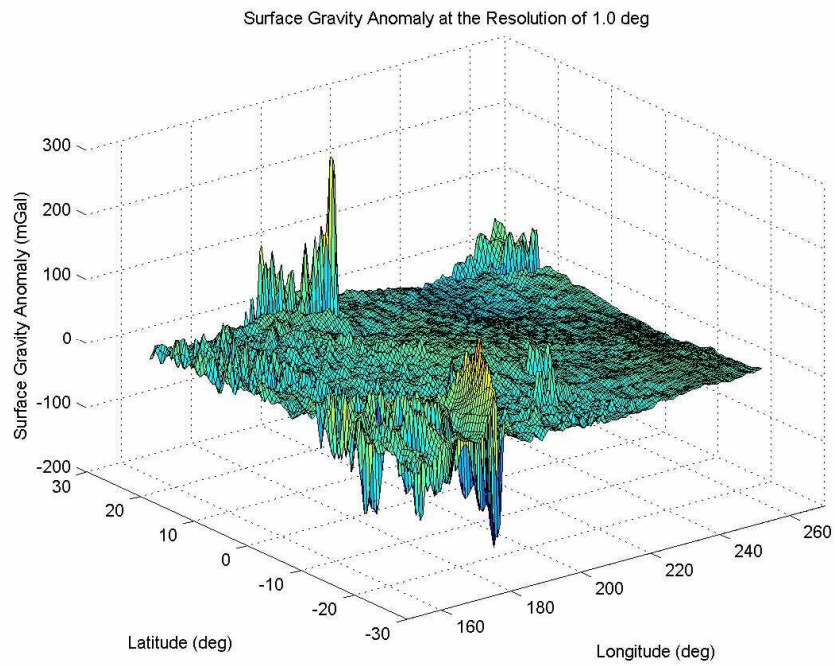


Fig. 6.8. 3-D surface map of the truth data at the spatial resolution 1° and the recovered gravity anomaly for the wavelet resolution level $J = 5$.

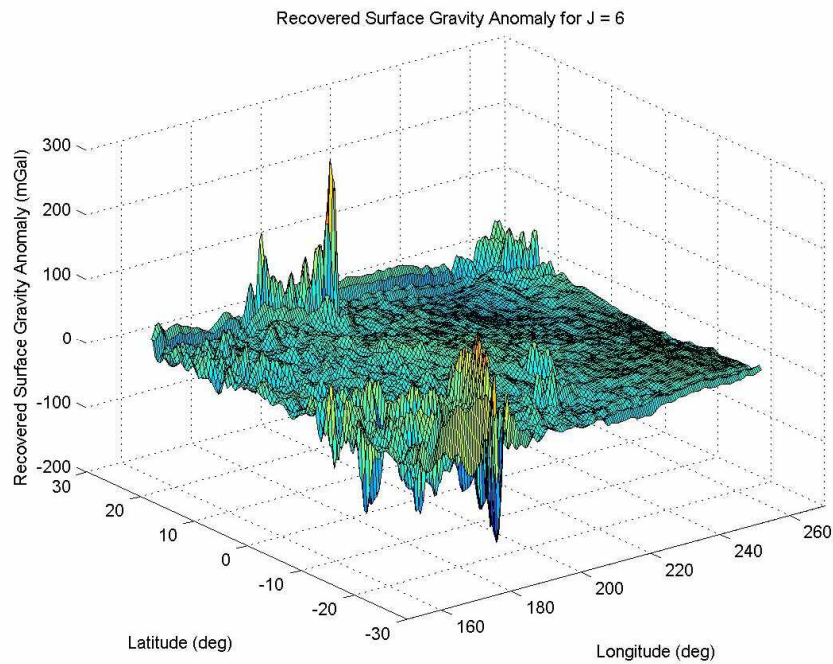
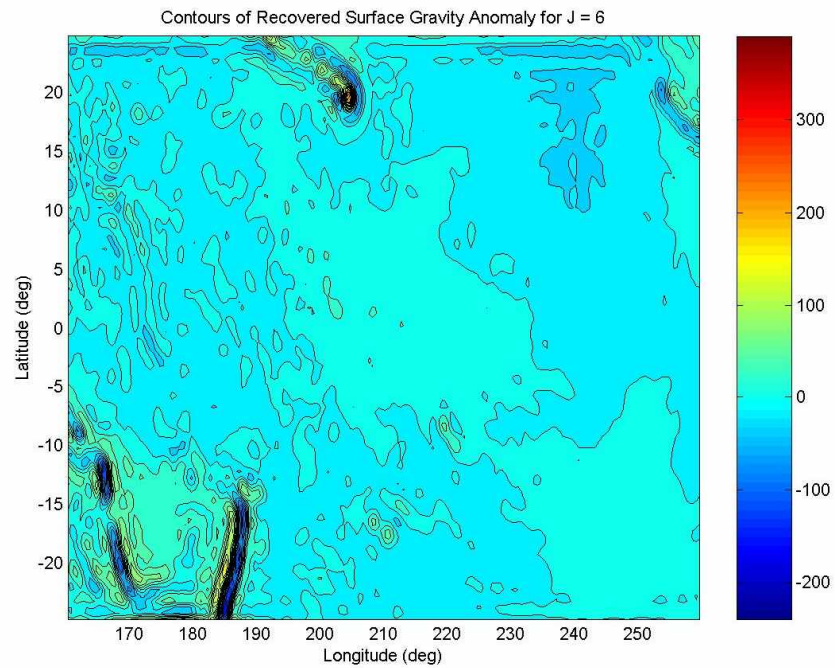


Fig. 6.9. Contour and 3-D surface map of the recovered gravity anomaly for the wavelet resolution level $J = 6$. The interference lines near the horizontal edges caused by “forced” fine signals are more prominent here.

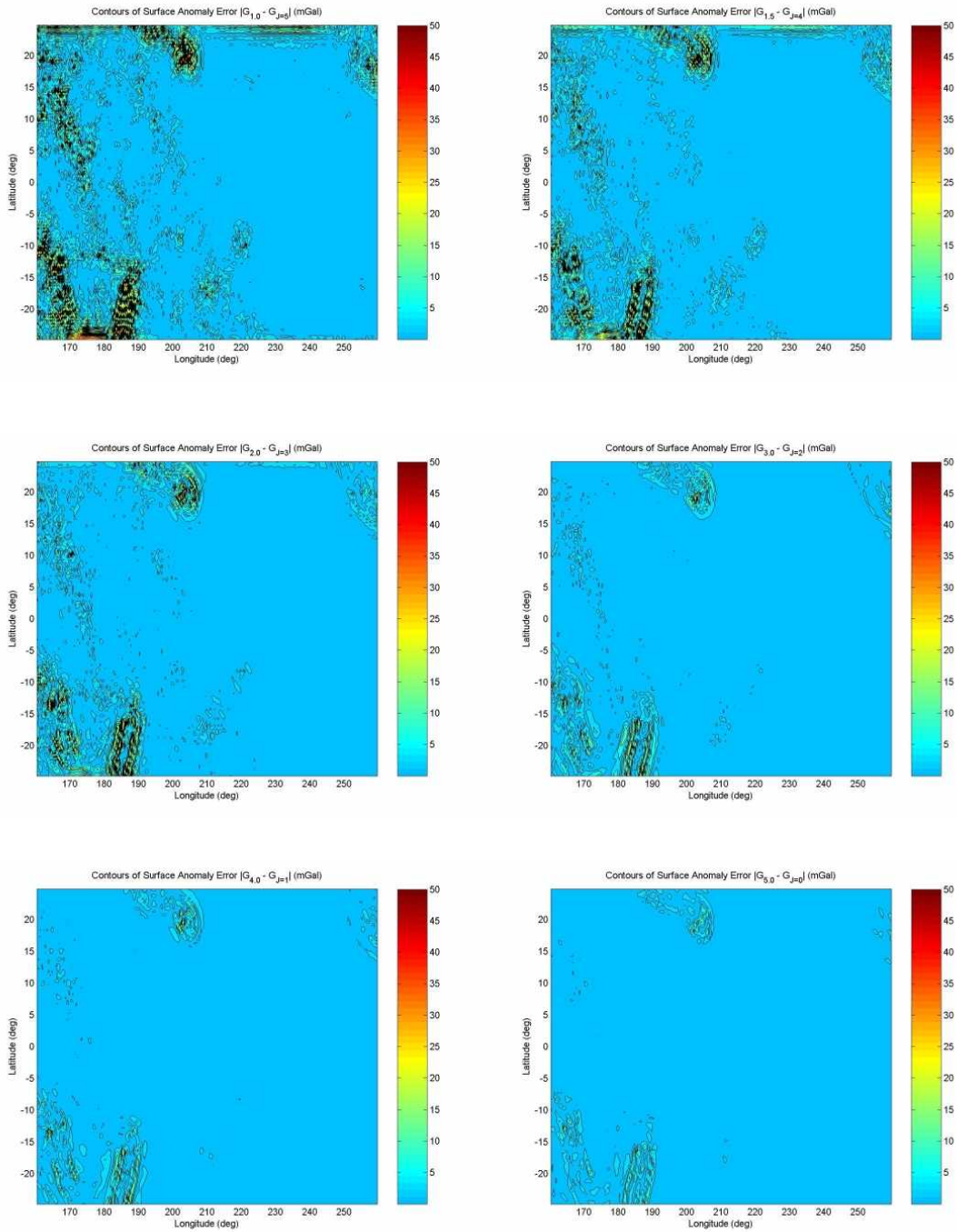


Fig. 6.10. Contour map of the surface gravity anomaly error in different spatial and wavelet resolution levels. The wavelet resolution level J was chosen at each spatial resolution that yields the least RMS error. Each contour represents 3 mGal of difference in gravity anomaly error.

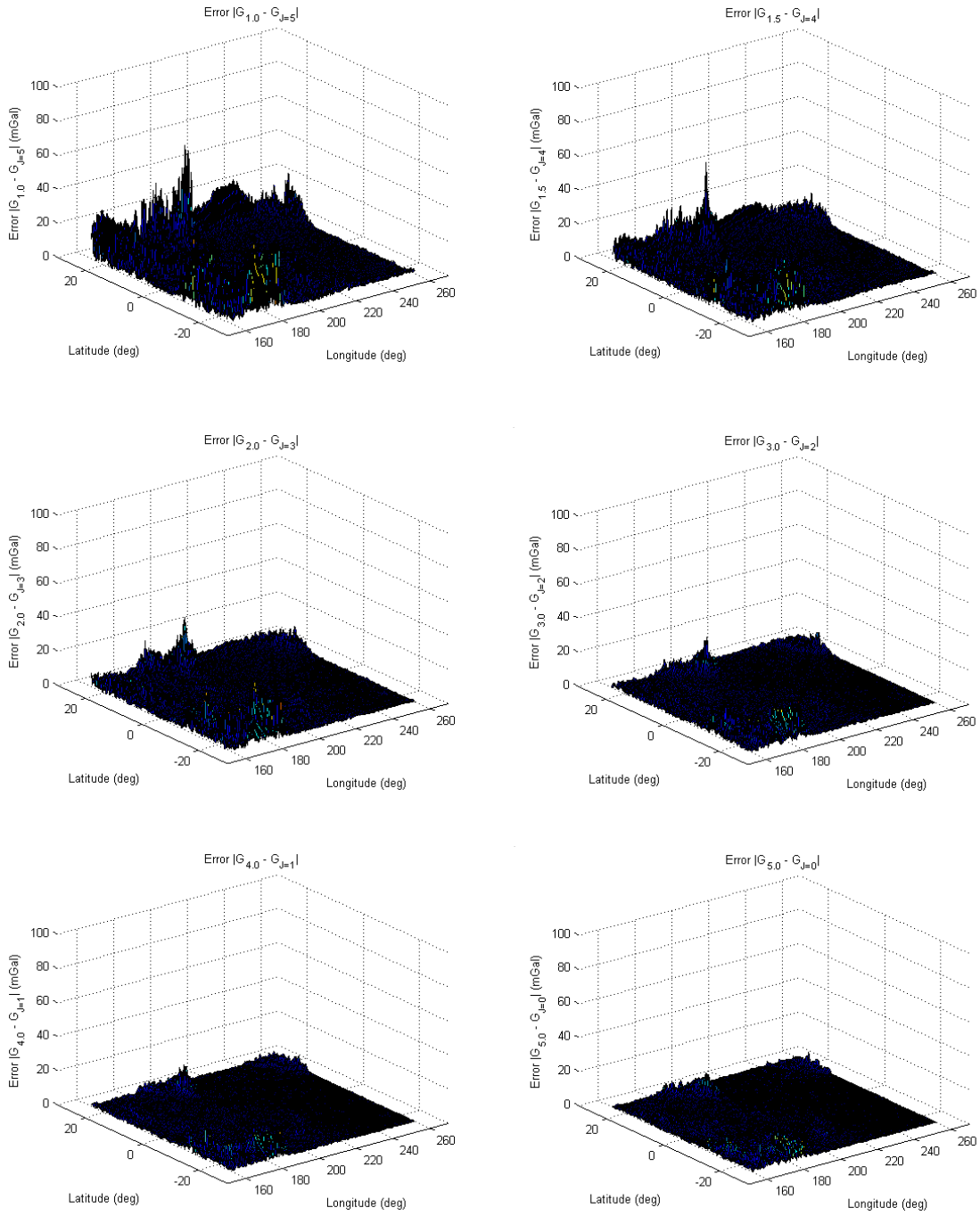


Fig. 6.11. 3-D surface gravity anomaly error plots in different spatial and wavelet resolution levels. The wavelet resolution level J was chosen at each spatial resolution that yields the least RMS error.

The RMS and mean error magnitudes at each wavelet resolution level for different spatial resolutions are listed in **Table 6.1** and **Table 6.2**. The overall RMS error ranges between 5.5 mGal at the spatial resolution 1° and 1.3 mGal at the resolution 5° , while the mean error gradually decreases from 2.8 mGal at the 1° resolution to 0.7 mGal at the 5° resolution, with the large difference between the RMS and mean error indicating the uneven distribution of the error throughout the region.

Table 6.3 to **Table 6.6** provide RMS and mean error of the two sub-regions: $160.25^\circ \sim 195.75^\circ$ in longitude and $-24.75^\circ \sim 7.25^\circ$ latitude and $200.25^\circ \sim 259.75^\circ$ in longitude and $-24.75^\circ \sim 9.75^\circ$ latitude, each representing the area with high and low magnitude gravity gradients. As is observed in previous simulation results, the RMS error is the largest in the region with high gravity gradients (ranging from 10.6 mGal at the resolution 1° to 2.7 mGal at the resolution 5°) and the smallest with the low gradient signals (from 1.8 mGal at the resolution 1° to 0.5 mGal at the resolution 5°).

In this simulation, the size of the at-altitude area, from which the gravity anomaly data is obtained to solve the inverse problem, is only 30% larger (in both longitudinal and latitudinal directions) than the local surface region for which we recovered the gravity anomaly. The volume of the input data we used, hence, is far smaller than what is required to recover the solution as accurately as when the whole global data is used, which demands at least 70% larger (in both directions) than the local solution region, as we briefly mentioned in section 4.2. This may explain the errors that are more prominent near regional boundaries at higher wavelet resolution levels seen in **Fig. 6.5** to **Fig. 6.9**.

Spatial Resolution	$ G - G_0 _{RMS}$	$ G - G_1 _{RMS}$	$ G - G_2 _{RMS}$	$ G - G_3 _{RMS}$	$ G - G_4 _{RMS}$	$ G - G_5 _{RMS}$	$ G - G_6 _{RMS}$
0.5°	17.86	17.41	16.58	14.47	13.06	12.57	12.27
1.0°	11.58	10.94	9.81	7.10	5.64	5.45	6.11
1.5°	9.47	8.75	7.47	4.67	3.79	4.22	5.75
2.0°	7.48	6.65	5.25	3.07	3.94	5.06	7.03
3.0°	4.20	3.20	2.01	4.78	7.46	8.78	10.66
4.0°	2.37	1.60	2.49	7.19	9.81	11.01	12.62
5.0°	1.29	1.96	4.20	8.94	11.11	12.10	13.42

Table 6.1. The RMS surface gravity anomaly error $|G - G_J|_{RMS}$ in mGal at the wavelet resolution level $J = 0$ to $J = 6$ for each spatial resolution of the truth data.

Spatial Resolution	$ G - G_0 _{mean}$	$ G - G_1 _{mean}$	$ G - G_2 _{mean}$	$ G - G_3 _{mean}$	$ G - G_4 _{mean}$	$ G - G_5 _{mean}$	$ G - G_6 _{mean}$
0.5°	7.86	7.68	7.41	6.75	6.38	6.29	6.36
1.0°	4.93	4.66	4.25	3.35	2.91	2.84	3.05
1.5°	4.06	3.74	3.27	2.33	2.02	2.15	2.75
2.0°	3.25	2.88	2.37	1.62	2.03	2.50	3.40
3.0°	1.94	1.50	1.09	2.25	3.44	4.06	5.03
4.0°	1.18	0.88	1.27	3.22	4.40	4.99	5.83
5.0°	0.74	1.05	2.01	3.99	4.95	5.43	6.12

Table 6.2. The mean surface gravity anomaly error $|G - G_J|_{mean}$ in mGal at the wavelet resolution level $J = 0$ to $J = 6$ for each spatial resolution of the truth data.

Spatial Resolution	$ G - G_0 _{RMS}$	$ G - G_1 _{RMS}$	$ G - G_2 _{RMS}$	$ G - G_3 _{RMS}$	$ G - G_4 _{RMS}$	$ G - G_5 _{RMS}$	$ G - G_6 _{RMS}$
0.5°	36.72	35.42	33.14	28.06	24.93	23.91	23.17
1.0°	25.22	23.49	20.51	14.26	11.08	10.63	11.76
1.5°	21.08	19.14	15.84	9.47	7.59	8.31	11.19
2.0°	17.06	14.90	11.33	6.44	8.18	10.25	13.94
3.0°	9.89	7.33	4.33	10.49	15.90	18.36	21.84
4.0°	5.50	3.39	5.64	16.00	21.27	23.52	26.44
5.0°	2.69	4.36	9.91	20.37	24.74	26.60	28.90

Table 6.3. The RMS surface gravity anomaly error $|G - G_j|_{RMS}$ in mGal for the sub-region of $160.25^\circ \sim 195.75^\circ$ in longitude and $-24.75^\circ \sim 7.25^\circ$ in latitude: the region with high gravity gradients profile.

Spatial Resolution	$ G - G_0 _{mean}$	$ G - G_1 _{mean}$	$ G - G_2 _{mean}$	$ G - G_3 _{mean}$	$ G - G_4 _{mean}$	$ G - G_5 _{mean}$	$ G - G_6 _{mean}$
0.5°	20.67	20.01	19.01	16.74	15.43	15.14	15.16
1.0°	14.45	13.46	11.97	9.02	7.43	7.18	7.52
1.5°	12.33	11.22	9.55	6.38	5.19	5.46	7.00
2.0°	10.10	8.85	7.04	4.39	5.54	6.72	9.00
3.0°	6.17	4.64	3.02	6.65	9.94	11.40	13.77
4.0°	3.57	2.38	3.83	9.76	12.96	14.35	16.38
5.0°	1.93	2.96	6.51	12.43	14.96	16.12	17.67

Table 6.4. The mean surface gravity anomaly error $|G - G_j|_{mean}$ in mGal for the sub-region of $160.25^\circ \sim 195.75^\circ$ in longitude and $-24.75^\circ \sim 7.25^\circ$ in latitude.

Spatial Resolution	$ G-G_0 _{RMS}$	$ G-G_1 _{RMS}$	$ G-G_2 _{RMS}$	$ G-G_3 _{RMS}$	$ G-G_4 _{RMS}$	$ G-G_5 _{RMS}$	$ G-G_6 _{RMS}$
0.5°	6.06	5.95	5.78	5.28	4.92	4.76	4.60
1.0°	3.46	3.28	3.02	2.30	1.89	1.76	1.78
1.5°	2.74	2.53	2.23	1.46	1.21	1.25	1.55
2.0°	2.12	1.87	1.54	0.96	1.24	1.50	1.99
3.0°	1.18	0.88	0.67	1.43	2.25	2.63	3.13
4.0°	0.71	0.54	0.82	2.08	2.90	3.23	3.67
5.0°	0.48	0.72	1.29	2.51	3.19	3.46	3.82

Table 6.5. The RMS surface gravity anomaly error $|G-G_J|_{RMS}$ in mGal for the sub-region of $200.25^\circ \sim 259.75^\circ$ in longitude and $-24.75^\circ \sim 9.75^\circ$ in latitude: the region with low gravity gradients.

Spatial Resolution	$ G-G_0 _{mean}$	$ G-G_1 _{mean}$	$ G-G_2 _{mean}$	$ G-G_3 _{mean}$	$ G-G_4 _{mean}$	$ G-G_5 _{mean}$	$ G-G_6 _{mean}$
0.5°	3.33	3.23	3.12	2.88	2.72	2.65	2.61
1.0°	1.98	1.83	1.66	1.30	1.12	1.07	1.07
1.5°	1.62	1.44	1.24	0.88	0.77	0.80	0.94
2.0°	1.31	1.11	0.90	0.62	0.77	0.91	1.17
3.0°	0.80	0.59	0.45	0.87	1.30	1.51	1.81
4.0°	0.50	0.38	0.55	1.24	1.67	1.85	2.12
5.0°	0.35	0.49	0.86	1.55	1.90	2.04	2.25

Table 6.6. The mean surface gravity anomaly error $|G-G_J|_{mean}$ in mGal for the sub-region of $200.25^\circ \sim 259.75^\circ$ in longitude and $-24.75^\circ \sim 9.75^\circ$ in latitude.

Chapter 7. Gravity Solution for SGG Mission

7.1. A Brief Review of SGG Mission

In SGG mission, the gravity signals at the satellite altitude are measured by the onboard gravity gradiometer in the form of the second order derivatives of gravity potential. The basic idea of the gravity gradiometer is to measure the difference in the gravity acceleration (which forms the second derivative gravity gradient tensor known as Eötvös tensor) between the two accelerometers precisely located with respect to each other in the satellite-fixed reference frame. SGG missions, however, have several issues to be solved (Seeber, 2003):

1. The satellite, with the accelerometers in it, rotates.
2. The satellite orbit needs to be precisely known.
3. The orientation of the accelerometers and the satellite with respect to the external frame needs to be known.
4. The measurements are susceptible to errors caused by the external forces (*e.g.* drag, radiation pressure, *etc.*) and the instrumental errors (*e.g.* drift, scale errors, *etc.*).
5. Extremely high accuracy in the measurement is required.

Let us consider an ideal configuration, where the gradiometer is in free fall within a satellite such that the axis of the accelerometer is always along the radial direction. Then the magnitude of the gravity acceleration a measured at the accelerometers' location \bar{x}_A and \bar{x}_B can be defined as

$$a(\bar{x}_A) = \frac{\partial}{\partial r} V(\bar{x}_A) + f_{ext} \quad , \quad (7.1.1)$$

$$a(\bar{x}_B) = \frac{\partial}{\partial r} V(\bar{x}_B) + f_{ext} \quad , \quad (7.1.2)$$

where V is the gravity potential and f_{ext} is the radial component of the acceleration caused by external force. The difference between (7.1.1) and (7.1.2) yields

$$a(\bar{x}_A) - a(\bar{x}_B) = \frac{\partial}{\partial r} V(\bar{x}_A) - \frac{\partial}{\partial r} V(\bar{x}_B) = x_{AB} \frac{\frac{\partial}{\partial r} V(\bar{x}_A) - \frac{\partial}{\partial r} V(\bar{x}_B)}{x_{AB}} \quad , \quad (7.1.3)$$

where x_{AB} is the distance between \bar{x}_A and \bar{x}_B . (7.1.3) then leads to the following equation:

$$a(\bar{x}_A) - a(\bar{x}_B) = x_{AB} \frac{\partial^2}{\partial r^2} V(\bar{x}_{CM}) \quad , \quad (7.1.4)$$

where \bar{x}_{CM} is the position vector of the center of mass of the two accelerometers with respect to the external frame.

The equation (7.1.4) provides the second order radial derivative of the gravity potential on Ω_r , which can be used as an input signal G in the equations (3.2.8) and (3.3.4), along with the spherical symbol of the SGG operator (3.1.4), to obtain the surface gravity potential.

7.2. Simulation Result (Region of 29.82°W ~ 109.82°W and 24.51°S ~ 20.31°N)

In order to test our gravity solution for the SGG type mission, we needed to obtain the second order radial derivative of the gravity anomaly at the satellite altitude. We first re-sampled the global surface gravity anomaly on the 513×257 longitude-latitude grid, where the adjacent grid points are 0.7° apart along the longitude and latitude, from the truth data set on the 720×360 grid by applying Gaussian smoothing on each new grid point \vec{z}_i such that

$$w_g(\vec{y}_j) = \frac{1}{2\pi\sigma_g^2} \exp\left(-\frac{(\vec{z}_i - \vec{y}_j)^2}{2\sigma_g^2}\right) \quad , \quad (7.2.1)$$

$$F_g(\vec{z}_i) = \frac{\sum_j w_g(\vec{y}_j) F(\vec{y}_j)}{\sum_j w_g(\vec{y}_j)} \quad \text{for } |\vec{z}_i - \vec{y}_j| \leq r_g \quad , \quad (7.2.2)$$

where \vec{y}_j is the location of a grid point on the original 720×360 grid set, $F(\vec{y}_j)$ is the surface gravity anomaly at \vec{y}_j , $w_g(\vec{y}_j)$ is the two-dimensional Gaussian filter, $F_g(\vec{z}_i)$ is the Gaussian-smoothed gravity anomaly at \vec{z}_i , r_g is the Gaussian smoothing radius and σ_g is the standard deviation which is about $\frac{r_g}{3}$ for the normal distribution. For our purpose, we set $r_g = 0.7^\circ$ and $\sigma_g = 0.23^\circ$. The number of grid points of 513×257 was chosen partly as a requirement for the extended trapezoidal rule employed in the surface integration routine within the upward continuation code as well as the fact that the grid points of this number would provide a more realistic resolution of the gravity measurement (*i.e.* 0.7°) for the real satellite mission than the 0.5° resolution grid we used

in the previous simulations. For example, the GRACE mission could provide $\sim 1^\circ$ spatial resolution data at the satellite altitude (Tapley, 2008). The RMS value of the surface gravity anomaly (*i.e.* 32.3 mGal) obtained by this Gaussian smoothing and rearranging of the grid points for the Region I from the previous simulation falls between that of the gravity anomaly at 0.5° and 1° spatial resolution, 36.2 mGal for the former and 29.7 mGal for the latter, indicating the spatial resolution of the initial surface gravity field in the SGG simulation to be about 0.7° .

This new global surface gravity anomaly on 513×257 grid set was then used to obtain the second order radial derivative of the gravity anomaly for the local region of $200.35^\circ \sim 20.00^\circ$ in longitude ($20.00^\circ\text{E} \sim 159.65^\circ\text{W}$ clockwise) and $-46.93^\circ \sim 42.72^\circ$ in latitude ($46.93^\circ\text{S} \sim 42.72^\circ\text{N}$) on a 257×129 evenly spaced grid at the satellite altitude of 300 km by solving the upward continuation equation (3.5.8) with the SGG operator (3.5.4), and then multiplied by a factor $\frac{R}{r}$ as is explained in section 4.2. This simulated

data set at the satellite altitude was used afterwards to recover the local surface gravity anomaly on a 115×65 grid for the region of $250.18^\circ \sim 330.18^\circ$ in longitude (equivalent to $29.82^\circ\text{W} \sim 109.82^\circ\text{W}$) and $-24.51^\circ \sim 20.31^\circ$ latitude ($24.51^\circ\text{S} \sim 20.31^\circ\text{N}$), which nearly coincides with the Region I in **Chapter 5**, by solving the equation (3.3.4), the local solution to the inverse problem, setting the spherical symbol of SGG operator (3.1.4) to be σ_n in the Tikhonov spherical regularization scaling function (3.2.9) and wavelet packet (3.2.10). The solution was then multiplied by a factor $\frac{r}{R}$ (see section 4.2).

The contour maps of the surface gravity anomaly at a resolution of 0.7° and the second order radial derivative of gravity anomaly at the satellite altitude of corresponding local area are shown in **Fig. 7.2.1**. The 3-D surface plots are presented in **Fig. 7.2.2**. It is notable that the SGG measurement retains the topography of the surface gravity anomaly fairly well when compared to **Fig. 5.1.1** and **Fig. 5.1.2**, where the gravity signal at the satellite altitude is of the form of gravity anomaly itself (*i.e.* direct upward propagation case). The regularization parameters used in this simulation are $\gamma_0 = 2.0 \times 10^{-12}$, $\gamma_1 =$

7.0×10^{-13} , $\gamma_2 = 2.0 \times 10^{-13}$, $\gamma_3 = 8.0 \times 10^{-14}$, $\gamma_4 = 4.0 \times 10^{-14}$, $\gamma_5 = 2.0 \times 10^{-14}$ and $\gamma_6 = 5.0 \times 10^{-15}$. The maximum degree of the Legendre polynomials was set to be 300.

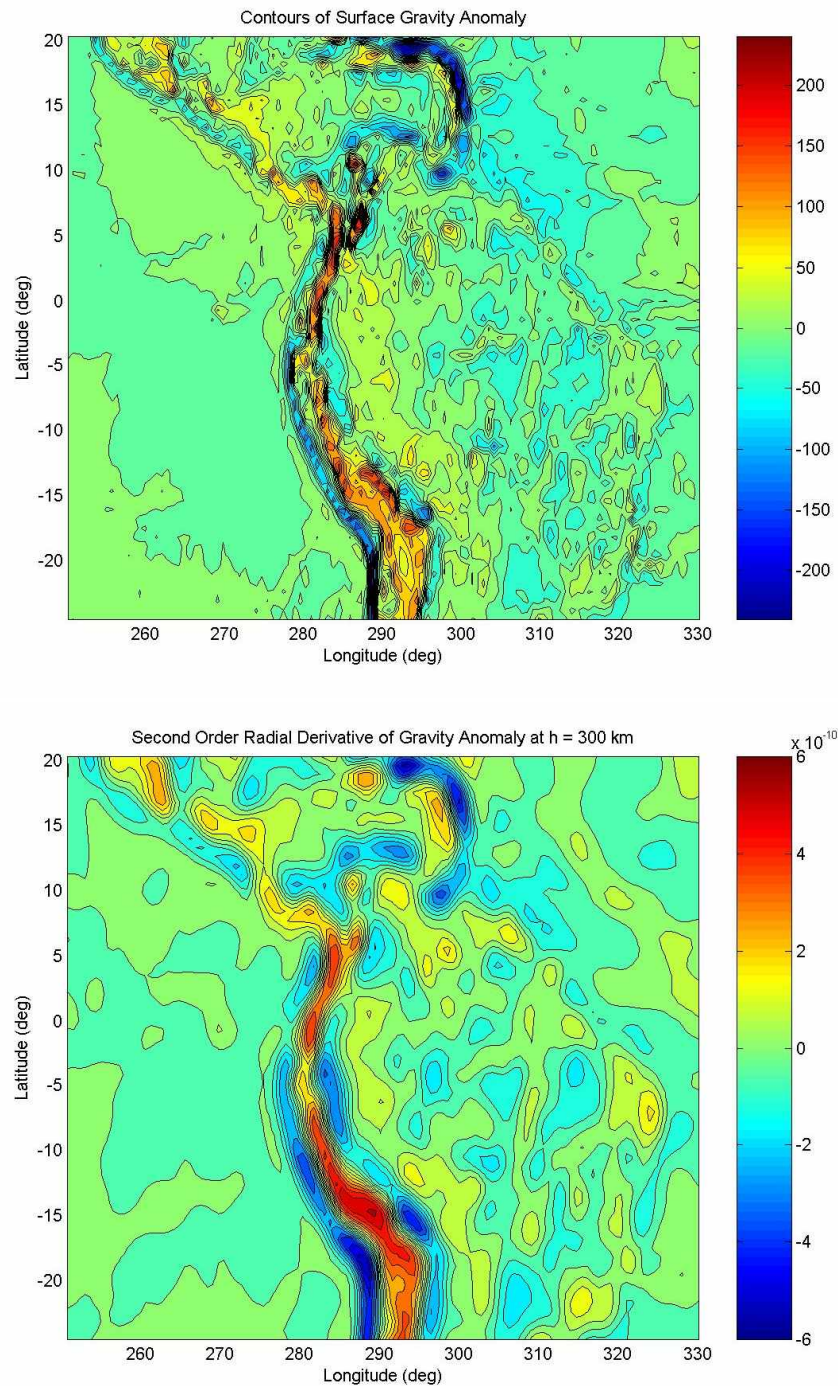


Fig. 7.2.1. The contour map of the surface gravity anomaly at the resolution of 0.7° (upper map), and the corresponding second order radial derivative of the gravity anomaly at the satellite altitude $h = 300$ km obtained by upward continuation (lower map). Each contour represents 20 mGal (upper) and 6.0×10^{-11} mGal/m² (lower) differences.

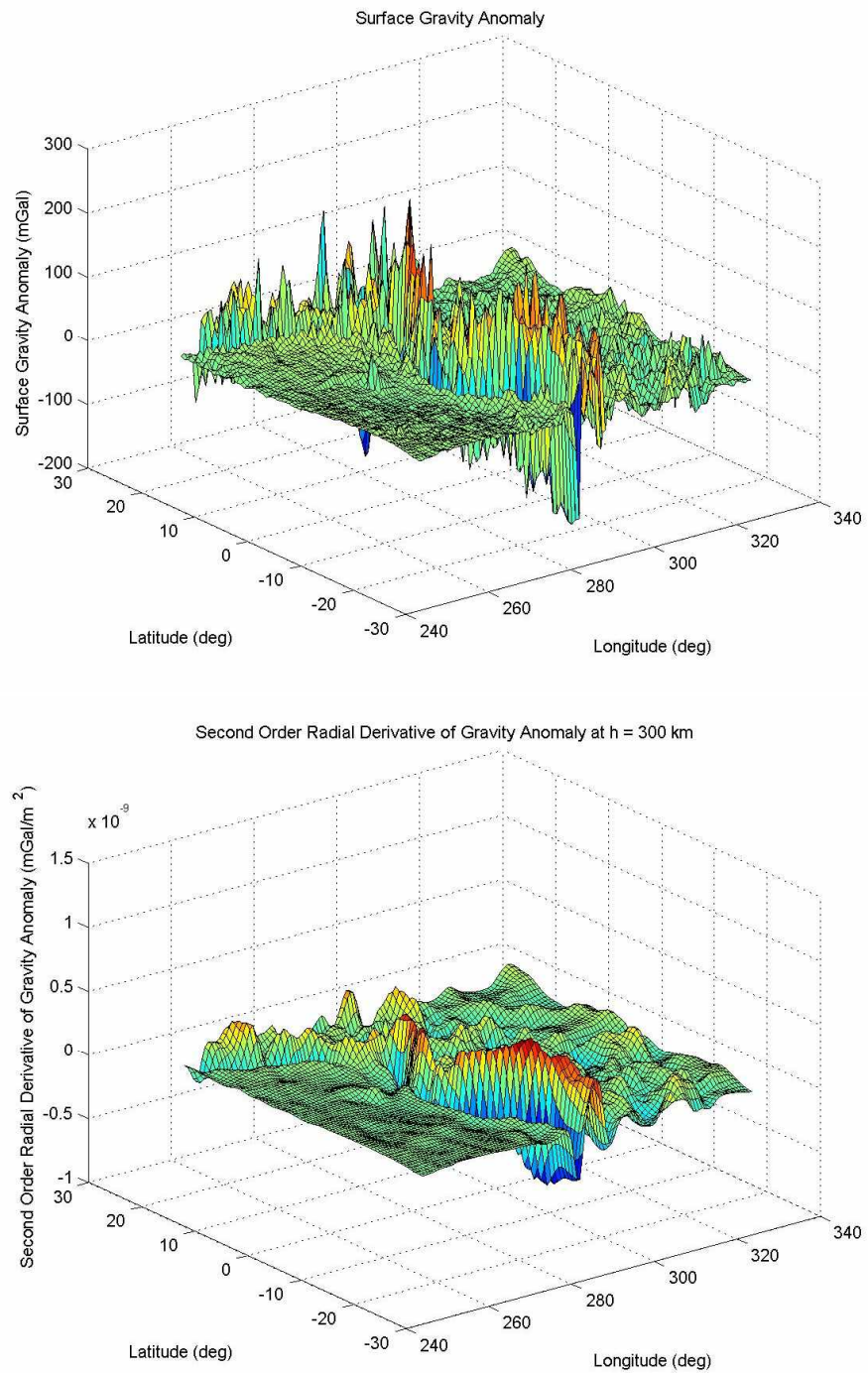


Fig. 7.2.2. 3-D surface plot of the surface gravity anomaly at the resolution of 0.7° and the corresponding second order radial derivative of the gravity anomaly at the satellite altitude $h = 300$ km. The SGG measurement (lower plot) retains the gravity topography of the Earth's surface much more closely than in the direct upward propagation case.

In the SGG case, we found that it is not relevant to compare the recovered surface gravity anomaly with different wavelet resolution levels to the surface gravity anomaly with different spatial resolutions obtained by applying a mean filter to the truth data. As shown in the direct upward propagation case in **Chapter 5** and **Chapter 6**, the mean filter smoothes out the gravity signals as the spatial resolution gets coarser. SGG measurements, however, contain a good deal of gravity detail which is reflected in the recovered gravity anomaly even at low wavelet resolution levels, *i.e.* less ill-posed compared to the direct upward propagation case. Therefore only the direct comparison between the recovered gravity with different wavelet levels to the original surface gravity anomaly at the spatial resolution 0.7° was provided in the following results.

Fig. 7.2.3 to **Fig. 7.2.6** show the contour maps and 3-D surface plots of the recovered surface gravity anomaly at a spatial resolution of 0.7° with different wavelet resolution levels. As in the previous simulations, the finer details are added to the recovered gravity anomaly as the wavelet level J increases until $J = 6$, where low to moderate gravity gradient signals are interfered with the “forced” fine signals induced by the high frequency wavelets.

The contour map and the 3-D plots in **Fig. 7.2.7** and **Fig. 7.2.8** show that $|G - G_J|$, the surface gravity anomaly error, decreases as the wavelet resolution level increases up to $J = 5$. As discussed in the previous chapters, the majority of large errors come from the areas with high gravity gradient signals, once more suggesting a correlation between the error and the gravity gradients.

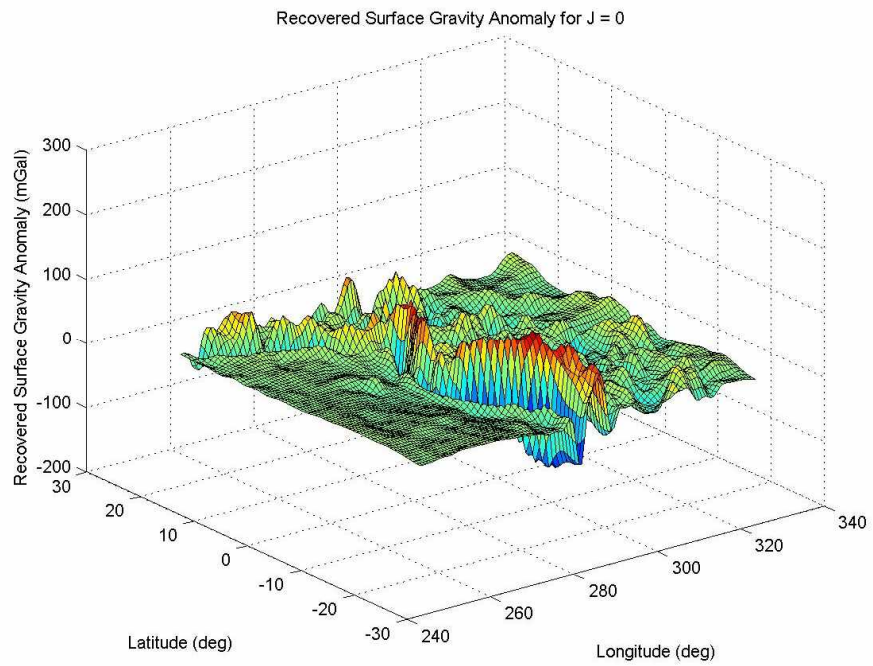
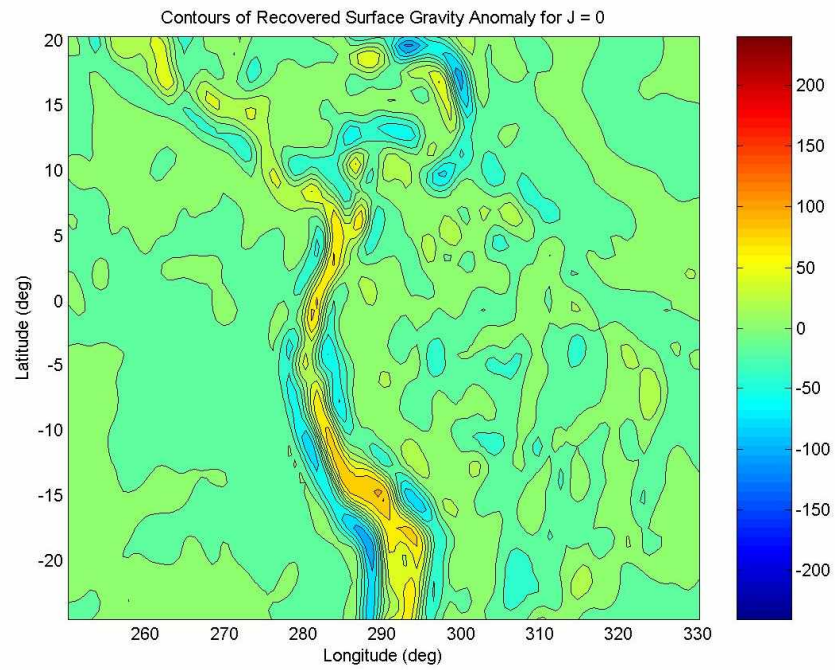


Fig. 7.2.3. Contour and 3-D surface map of the recovered surface gravity anomaly for the wavelet resolution level $J = 0$.

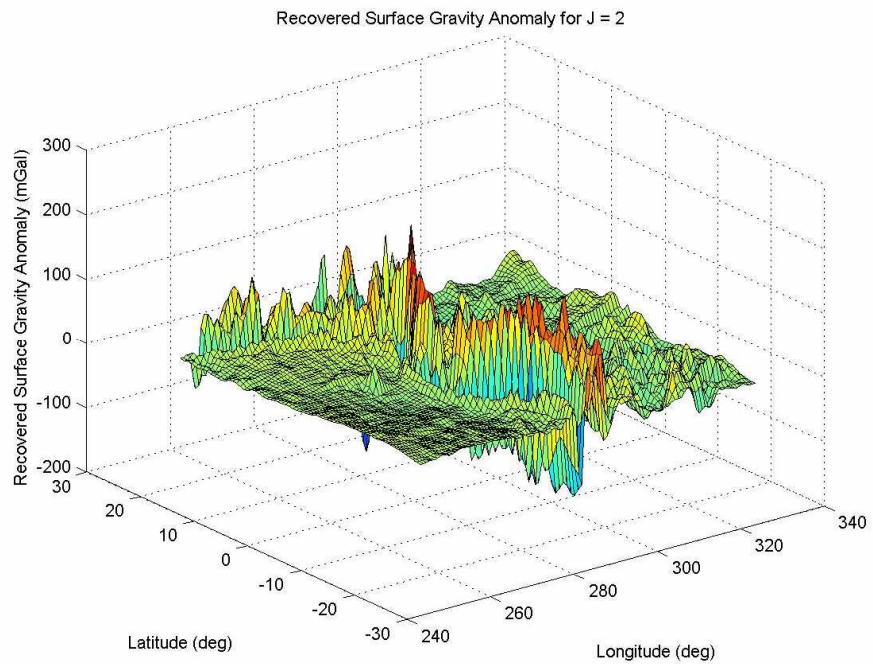
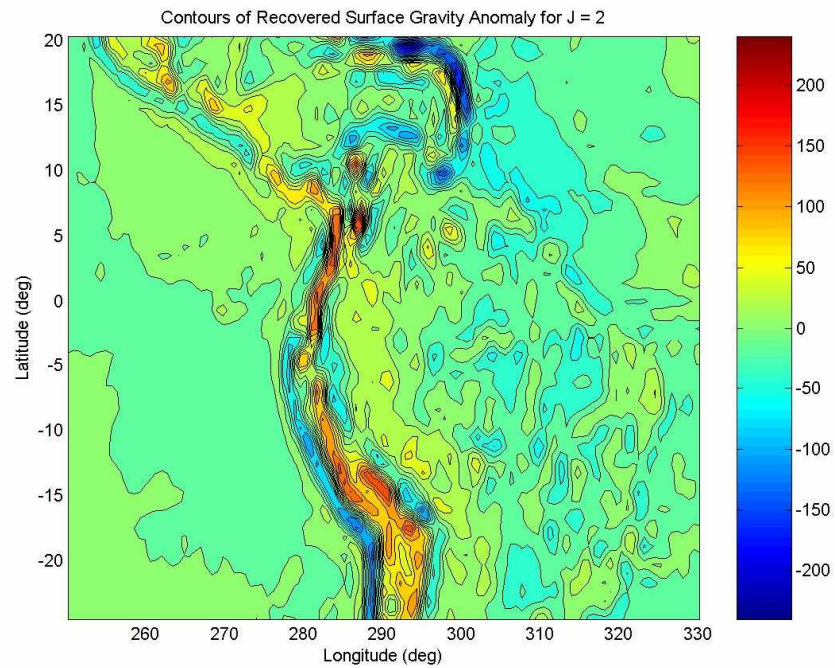


Fig. 7.2.4. Contour and 3-D surface map of the recovered surface gravity anomaly for the wavelet resolution level $J = 2$.

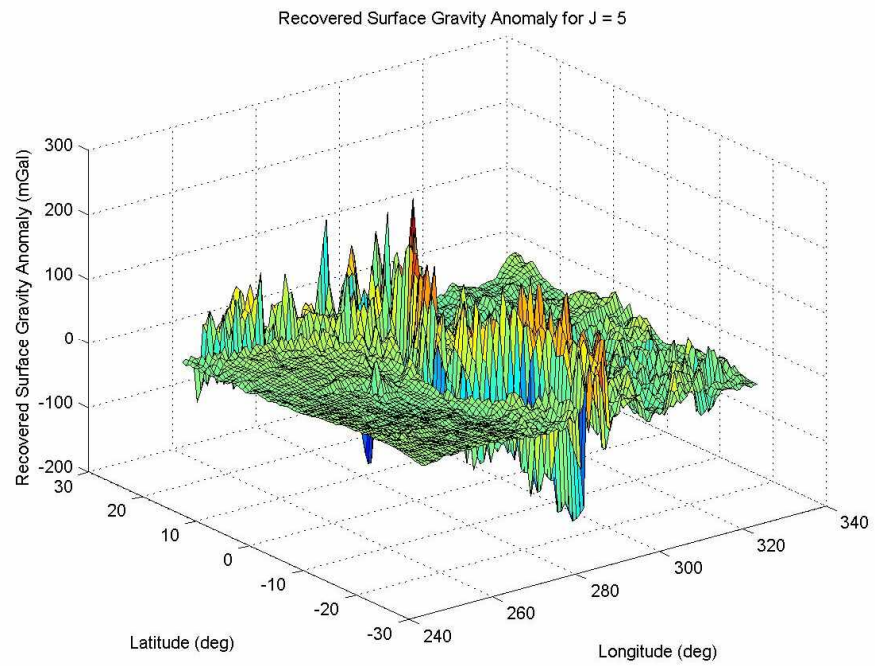
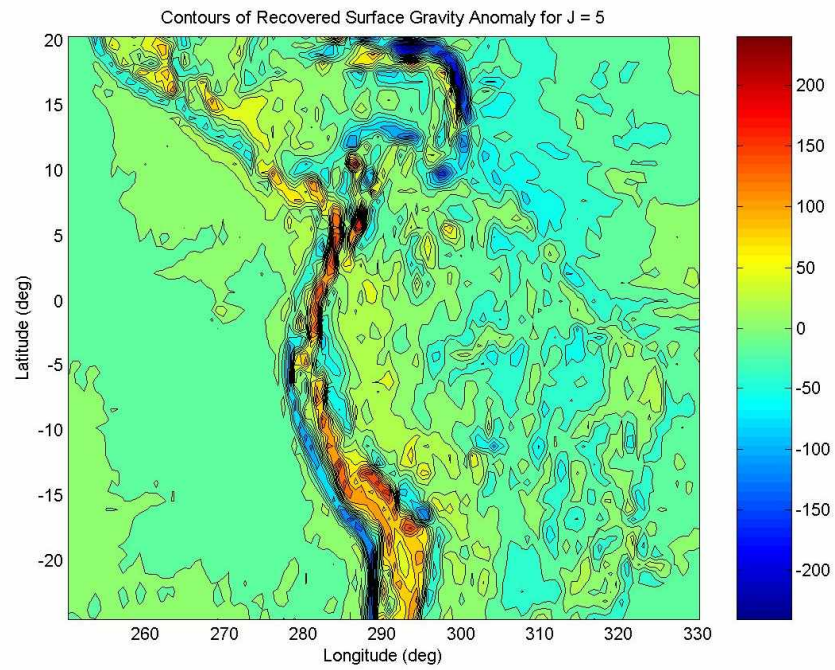


Fig. 7.2.5. Contour and 3-D surface map of the recovered surface gravity anomaly for the wavelet resolution level $J = 5$.

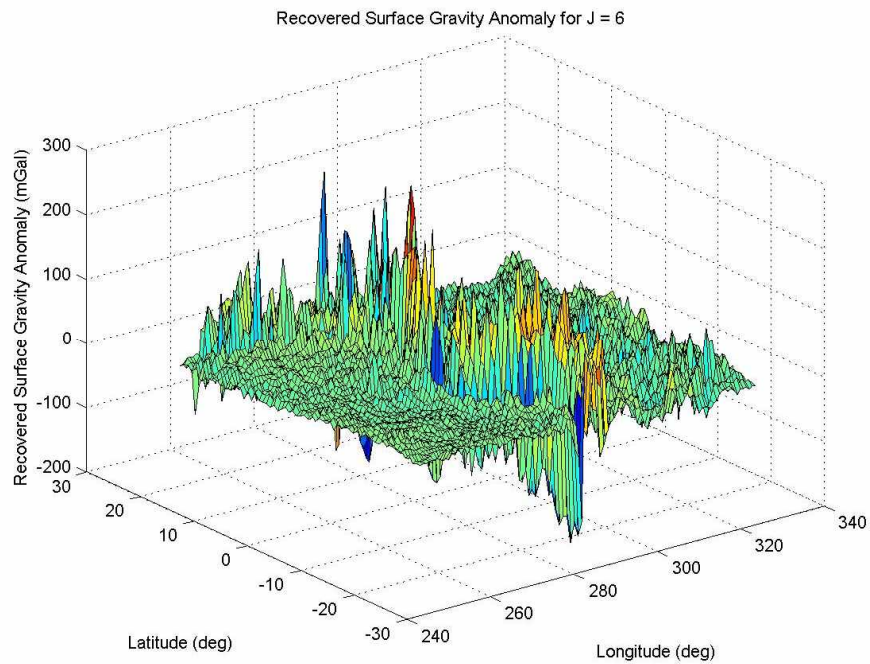
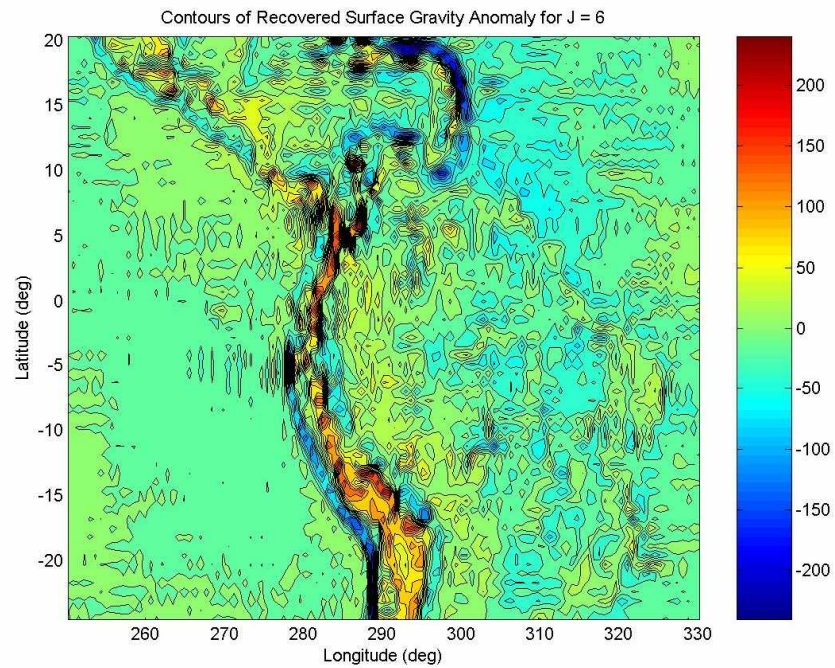


Fig. 7.2.6. Contour and 3-D surface map of the recovered surface gravity anomaly for the wavelet resolution level $J = 6$. The interference from the “forced fine signals” produced by high frequency wavelets is prominent in the low to moderate gravity gradient region.

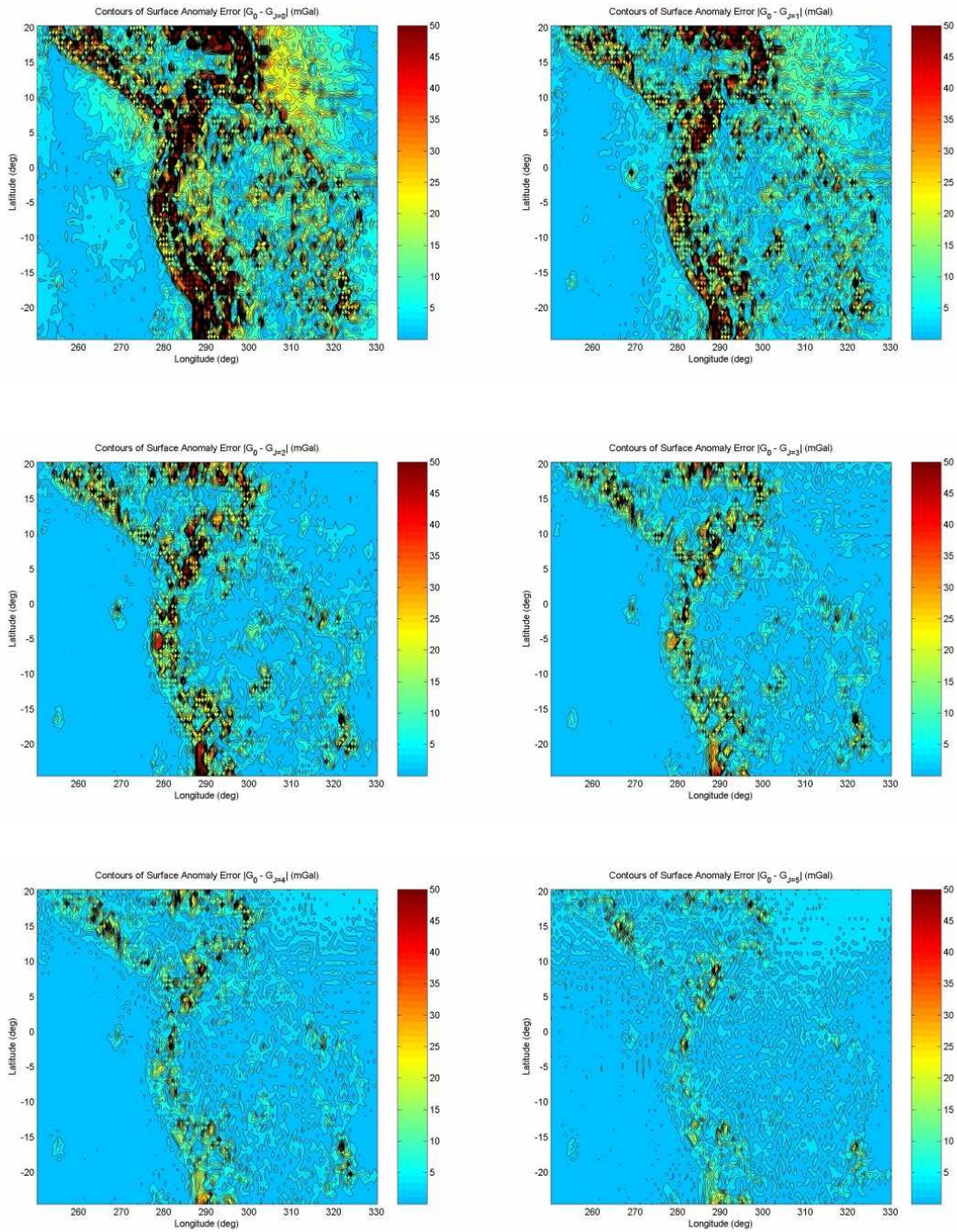


Fig. 7.2.7. Contour map of the surface gravity anomaly error $|G - G_j|$ at a spatial resolution 0.7° with different wavelet resolution levels. The error decreases as the wavelet resolution level J increases. Each contour represents 3 mGal of difference in the error.

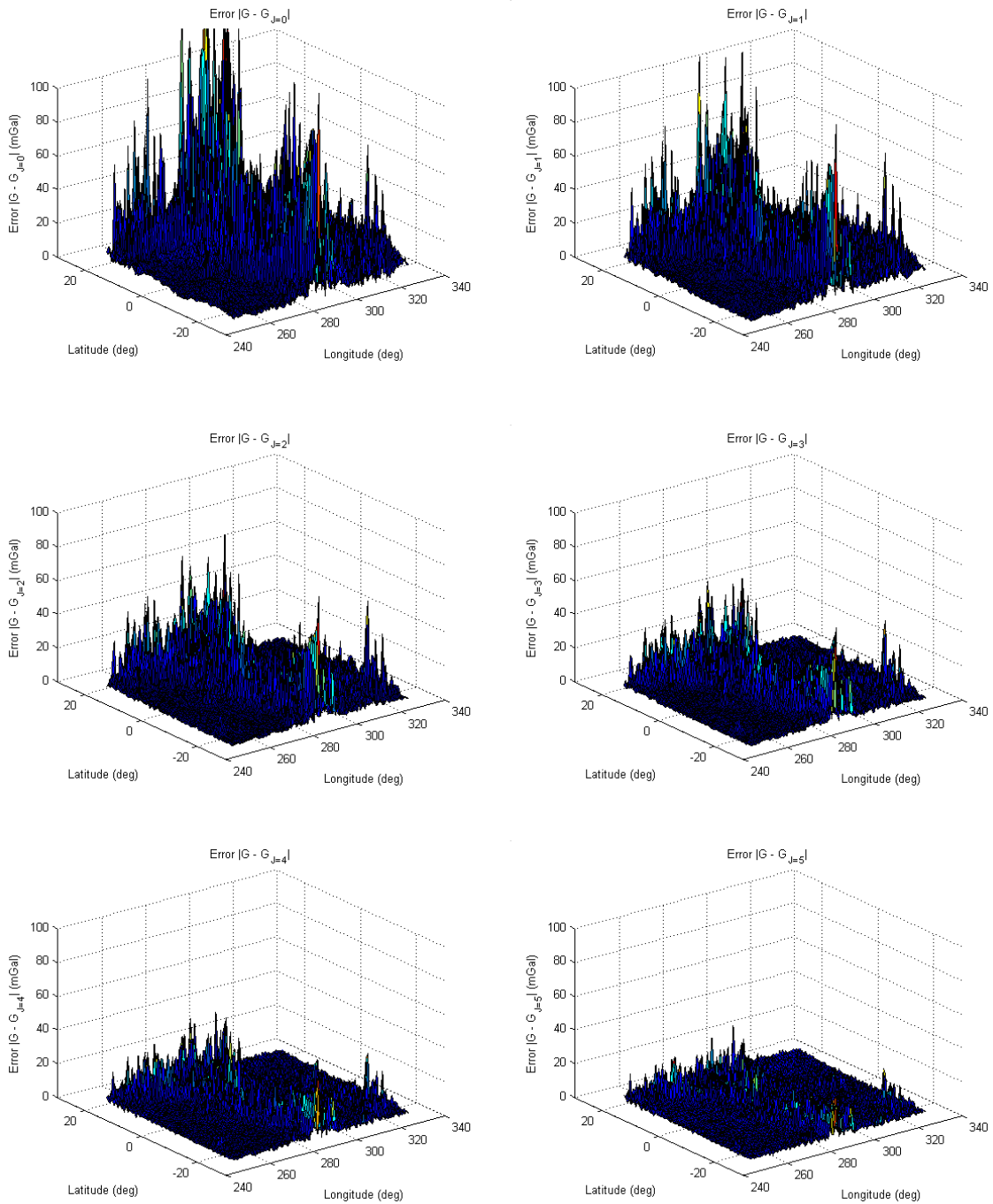


Fig. 7.2.8. 3-D plots of the surface gravity anomaly error $|G - G_J|$ at a spatial resolution 0.7° with different wavelet resolution levels. The error decreases as the wavelet resolution level J increases.

Table 7.2.1 summarizes the result. Bold faced numbers indicate the minimum RMS and mean error magnitude, 4.7 mGal and 3.5 mGal respectively, for the spatial resolution of 0.7° . The SGG solution shows an improvement over the result from section **5.1**, where the RMS error is 13.4 mGal for the spatial resolution 0.5° and 5.9 mGal for the resolution 1° . It is also a better result than that of section **5.2**, the RMS error of which is 12.2 mGal for the resolution 0.5° and 5.6 mGal for the spatial resolution of 1° , where the local region at the satellite altitude, from which the gravity data was retrieved to solve the inverse problem, is larger than for this SGG case. Considering the fact that there should exist an error in the upward continuation process to obtain the second order radial derivative of the gravity anomaly at the satellite altitude (especially the computational error in the surface integration) in addition to that in the process of solving the inverse problem to recover the surface gravity anomaly, the smaller magnitude of error in the gravity solution implies that more accurate gravity recovery can be achieved in SGG type missions.

Table 7.2.2 to **Table 7.2.4** provide RMS and mean error of the three sub-regions with different gravity gradient profiles: $278.25^\circ \sim 299.75^\circ$ in longitude and $-24.75^\circ \sim 19.75^\circ$ latitude, $304.25^\circ \sim 329.75^\circ$ in longitude and $-14.75^\circ \sim 19.75^\circ$ latitude and $250.25^\circ \sim 275.25^\circ$ in longitude and $-20.75^\circ \sim 4.75^\circ$ latitude, respectively indicating the area with high, moderate and low magnitude gravity gradients. The RMS error is the largest in the region with high gravity gradients (6.5 mGal) and the smallest with the low gradient signals (1.5 mGal). Note that for the region with low gravity gradient profile, the gravity solution with lower wavelet resolution level (*i.e.* $J = 3$ instead of $J = 5$) yields a better result (see **Table 7.2.4**), suggesting a possibility of reducing the error in the recovered gravity signal by combining gravity solutions with different wavelet resolution levels for the regions with varying gravity gradients profiles.

J	$ G - G_J _{RMS}$	$ G - G_J _{mean}$
0	20.34	12.75
1	14.11	8.52
2	9.37	5.14
3	7.21	4.17
4	5.86	3.87
5	4.65	3.49
6	12.10	8.58

Table 7.2.1. The RMS surface gravity anomaly error $|G - G_J|_{RMS}$ and mean error $|G - G_J|_{mean}$ in mGal at the spatial resolution $\sim 0.7^\circ$ for the region of $250.18^\circ \sim 330.18^\circ$ in longitude and $-24.51^\circ \sim 20.31^\circ$ in latitude. Bold faced numbers indicate the minimum RMS and mean error magnitude.

J	$ G - G_J _{RMS}$	$ G - G_J _{mean}$
0	32.08	22.57
1	22.25	15.12
2	15.08	10.02
3	11.43	7.71
4	8.91	6.20
5	6.51	4.78
6	17.71	13.12

Table 7.2.2. The RMS surface gravity anomaly error $|G - G_J|_{RMS}$ and mean error $|G - G_J|_{mean}$ in mGal for the sub-region of $278.25^\circ \sim 299.75^\circ$ in longitude and $-24.75^\circ \sim 19.75^\circ$ in latitude: the region with high gravity gradients profile.

J	$ G - G_J _{RMS}$	$ G - G_J _{mean}$
0	14.35	11.76
1	9.28	7.59
2	4.60	3.22
3	3.89	2.93
4	3.67	3.01
5	3.44	3.02
6	9.58	7.69

Table 7.2.3. The RMS surface gravity anomaly error $|G - G_J|_{RMS}$ and mean error $|G - G_J|_{mean}$ in mGal for the region of $304.25^\circ \sim 329.75^\circ$ in longitude and $-14.75^\circ \sim 19.75^\circ$ in latitude: the region with moderate gravity gradients.

J	$ G - G_J _{RMS}$	$ G - G_J _{mean}$
0	3.82	2.96
1	2.66	1.81
2	1.69	1.02
3	1.49	0.98
4	2.02	1.79
5	2.42	2.29
6	5.43	4.29

Table 7.2.4. The RMS surface gravity anomaly error $|G - G_J|_{RMS}$ and mean error $|G - G_J|_{mean}$ in mGal for the sub-region of $250.25^\circ \sim 275.25^\circ$ in longitude and $-20.75^\circ \sim 4.75^\circ$ in latitude: the region with low gravity gradients.

Chapter 8. Effect of Measurement Noise on the Recovered Gravity Anomaly

8.1. Noise and Errors in Satellite Remote Sensing Missions

In a satellite remote-sensing mission, several factors can affect the accuracy of the gravity measurement – the error in the satellite tracking, external non-gravitational forces such as air-drag and radiation pressure, instrumental errors in the accelerometer and the gradiometer sensors, *etc.* Before proceeding further in this chapter, we will first take a brief look at GOCE (Gravity Field and Steady State Ocean Circulation Explorer) to determine the expected measurement error magnitude in a SGG mission.

GOCE satellite carries two primary payload: a Satellite-to-Satellite Tracking Instrument (hereafter SSTI) which incorporates a geodetic GPS (Global Positioning System) receiver for high-low tracking between the GPS satellites and the low-orbit GOCE satellite (mean orbit altitude of 250 km), and an Electrostatic Gravity Gradiometer (hereafter EGG) whose three-axis, six-accelerometer satellite gravity gradiometer provides the gravity gradient tensor as gravity measurements. SSTI and EGG are complemented by two star trackers which provide precise knowledge of the orientation of the spacecraft with respect to the inertial reference frame. The secondary payload consists of an array of Laser Retro-reflector (LRR) cubes, which provide ground-based tracking of the satellite by satellite laser ranging stations. (Drinkwater and Kern, 2006)

GOCE satellite is also equipped with Drag-free Attitude Control System (DFACS) – consisting of Ion Propulsion Assembly (IPA) and magnetotorquers working as actuators as well as multiple sensors such as star trackers, a three-axis magnetometer, a digital sun sensor and a coarse Earth and Sun sensor – which is contrived to compensate for the external non-gravitational forces and to keep the accelerometer drag-free in the along-track direction (Drinkwater *et al.*, 2007).

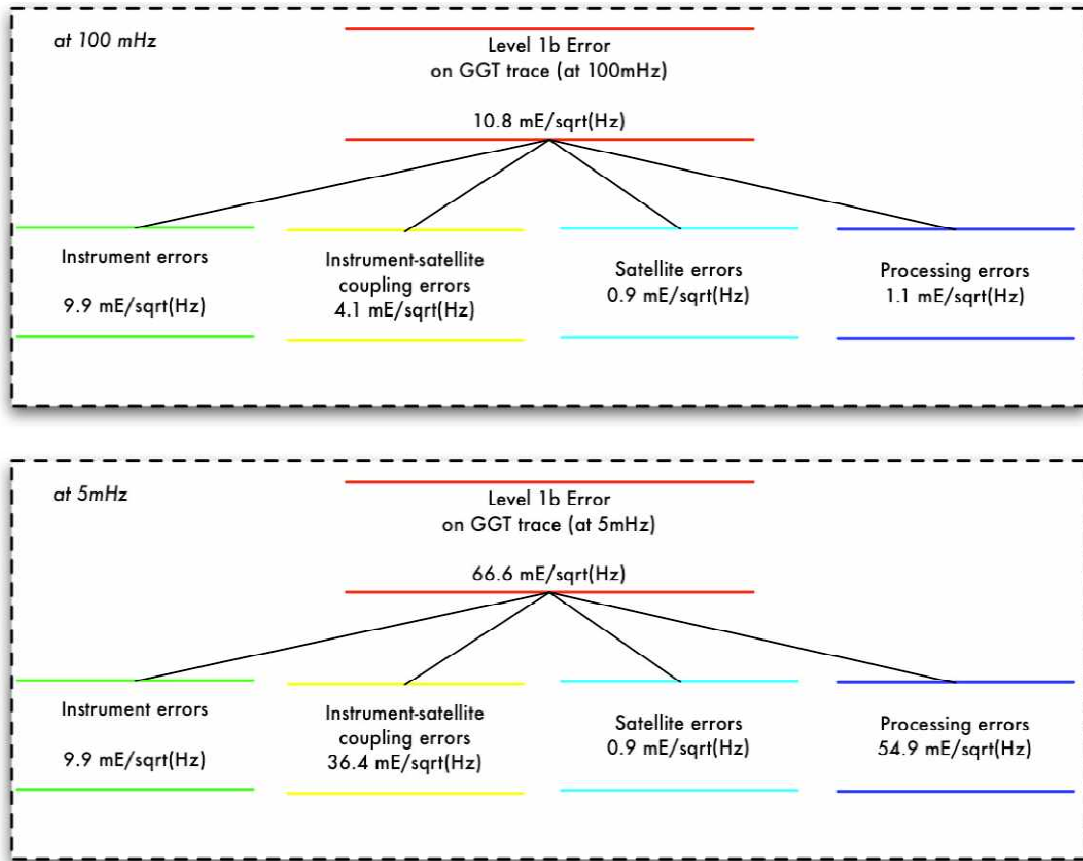


Fig. 8.1.1. Level 1b GOCE gradiometry error budget (Drinkwater and Kern, 2006).

The aforementioned equipment and sensors are designed to minimize the errors in the GOCE data, and the calibration and validation process assesses and quantifies uncertainties in the GOCE measurements to ensure the highest possible quality Level 1b data before it is fed into the Level 2 scientific data products. The error budget and performance criteria for the Level 1b data products are illustrated in **Fig. 8.1.1** and **Fig. 8.1.2** (Drinkwater and Kern, 2006).

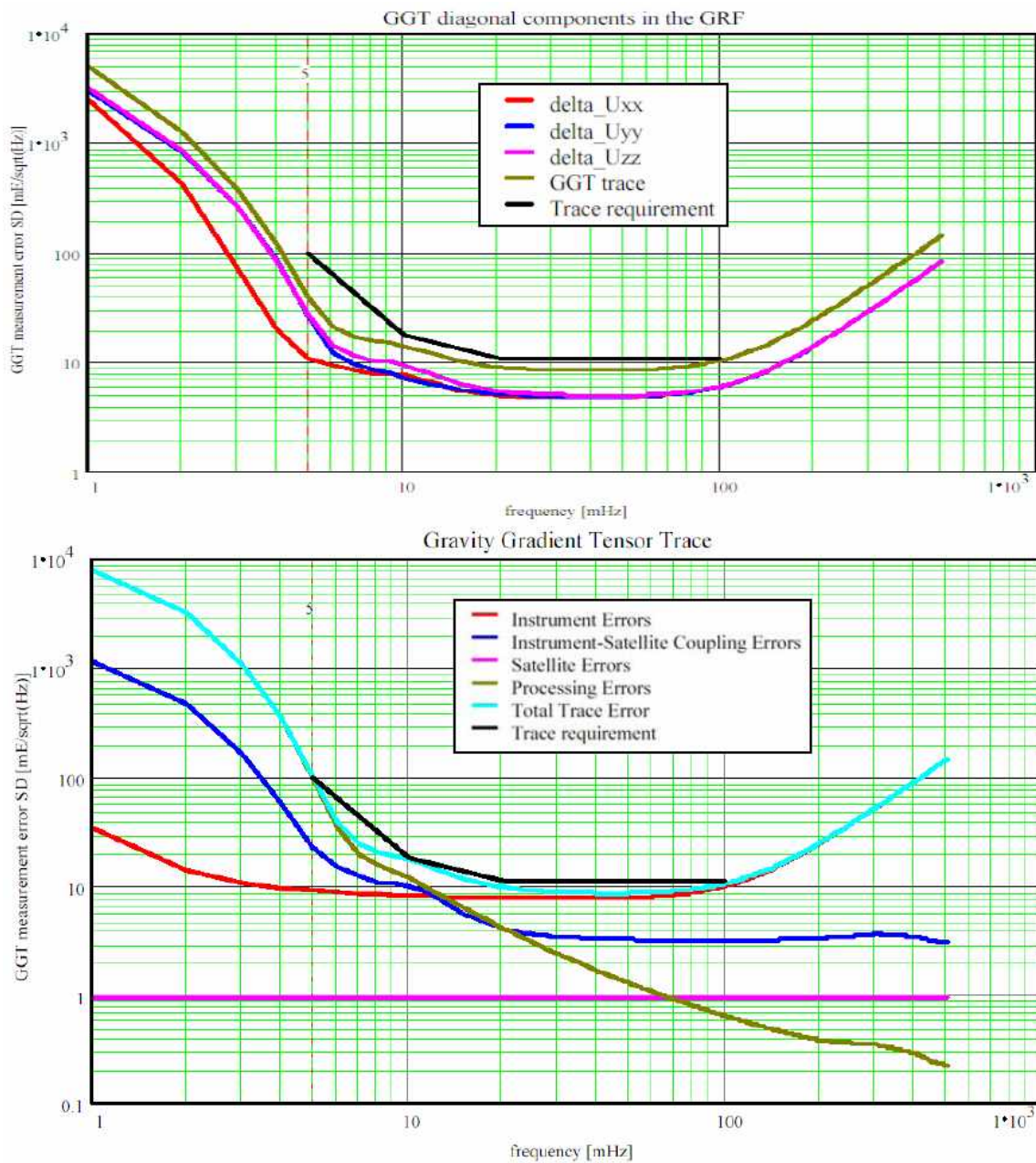


Fig. 8.1.2. Individual contributions to the predicted total Gravity Gradient Trace (GGT) error, based on GOCE system simulations (Drinkwater and Kern, 2006).

The error budget was carefully assigned to meet the mission objectives (Drinkwater *et al.*, 2007):

1. Recovering the Earth's gravity anomaly field with an accuracy better than 1 – 2 mGal.
2. Determining the geoid height with a radial accuracy better than 1 – 2 cm.
3. Achieving both measurements at a spatial resolution of 100 km or less, *i.e.* degree and order higher than 200 in a spherical harmonics expansion.

The calibration steps are taken to ensure the flight-ready accelerometer output is obtained to a certain level of accuracy with an absolute scale factor error within 1%, where the 'scale factor' refers to the accuracy that the individual GOCE accelerometers measure accelerations and gravity gradients along each axis of the gradiometer (Drinkwater and Kern, 2006).

As is apparent from a satellite missions such as GOCE, several components are known to contribute to the accelerometer error, such as accelerometer noise, quantization noise and baseline stability as well as the instrument-satellite coupling errors. In this chapter, we will focus on the measurement error due to accelerometer noise, which is intrinsic to the instrument and thus impossible to avoid completely no matter how accurately the instruments are calibrated and the satellite and processing errors are compensated and corrected.

In order to study the effect of the noise in the measurement data on the recovered gravity solution, we imposed Gaussian random noise on the gravity signal at the satellite altitude. We generated a normalized Gaussian random noise whose mean is 0 and standard deviation is 1. We then found the standard deviation of the magnitude of the gravity signal at the satellite altitude (*i.e.* the upward continued gravity anomaly or the second order radial derivative of it) and added the Gaussian random noise such that

$$G_\varepsilon(\vec{x}_i) = G(\vec{x}_i) + w_\varepsilon \sigma_G N_i \quad , \quad (8.1.1)$$

where \vec{x}_i is the location at the satellite altitude, $G_\varepsilon(\vec{x}_i)$ is the gravity measurement with Gaussian noise error at \vec{x}_i , $G(\vec{x}_i)$ is the error-free gravity signal at \vec{x}_i , N_i is the Gaussian random noise, σ_G is the standard deviation of $G(\vec{x}_i)$ and w_ε is the weight of the error. We investigated two different circumstances, one with 0.1% of Gaussian error (*i.e.* $w_\varepsilon = 0.001$) and the other with 0.5% error (*i.e.* $w_\varepsilon = 0.005$) for the cases with both upward propagated gravity anomaly (*i.e.* the gravity measurement at the satellite altitude is the gravity anomaly itself) and the SGG measurement (*i.e.* the at-altitude measurement is the second order radial derivative of the gravity anomaly). The magnitude of the standard deviation of the error imposed in this manner on the gravity measurements at the altitude of 300 km is equivalent to about 0.01 mGal (0.1% Gaussian error) and 0.05 mGal (0.5% Gaussian error) for the upward propagated gravity anomaly with a spatial resolution 0.5° and 0.7×10^{-13} mGal/m² (0.1% error) and 3.5×10^{-13} mGal/m² (0.5% error) for the SGG measurements with a resolution 0.7° .

The simulation results are discussed in the following sections.

8.2. By Using the Upward Propagated Gravity Anomaly

Fig. 8.2.1 to **Fig. 8.2.6** compare the recovered surface gravity anomaly for the Region I ($30.25^\circ\text{W} \sim 109.75^\circ\text{W}$ in longitude and $24.75^\circ\text{S} \sim 19.75^\circ\text{N}$ in latitude) with the wavelet resolution level $J = 3$ to $J = 5$, when 0.1% and 0.5% Gaussian random noise was imposed on the gravity anomaly at the satellite altitude $h = 300$ km. The regularization parameters used in both cases are the same as the ones in section 5.1, *i.e.* $\gamma_0 = 9.0 \times 10^{-2}$, $\gamma_1 = 5.0 \times 10^{-2}$, $\gamma_2 = 2.0 \times 10^{-2}$, $\gamma_3 = 4.0 \times 10^{-3}$, $\gamma_4 = 1.0 \times 10^{-3}$, $\gamma_5 = 2.0 \times 10^{-4}$ and $\gamma_6 = 5.0 \times 10^{-5}$. The maximum degree of the Legendre polynomials N was set to be 300.

The result shows that the higher the wavelet resolution level is, the more significant the effect of the noise becomes to the recovered gravity anomaly, indicating the high frequency signals are more vulnerable to the measurement errors. It is also very noticeable that the larger the amplitude of the measurement error is, the more corrupted the recovered gravity signal gets. With 0.1% measurement noise, its effect on the gravity solution does not appear until $J = 4$, while 0.5% noise starts to affect the recovered gravity signal from $J = 3$. The 3-D surface plots of the recovered surface gravity anomaly also indicate that the low-moderate amplitude gravity signals get more affected by measurement error.

Table 8.2.1 and **Table 8.2.2** respectively show the RMS surface gravity anomaly error $|G - G_J|_{RMS}$ at the different wavelet resolution levels for each spatial resolution of the truth data with 0.1% and 0.5% Gaussian random noise imposed on the satellite measurement. Comparison to **Table 5.1.1** provides the observation that with 0.1% measurement noise the RMS error increases by 0.2 mGal for the spatial resolution 1.5° , 1.9 mGal for the resolution 1° and 3.1 mGal for the resolution 0.5° . With 0.5% noise the RMS error increases substantially: by 0.2 mGal for 2° resolution, 2.3 mGal for 1.5° resolution, 4.4 mGal for resolution of 1° and 5.7 mGal for the spatial resolution of 0.5° .

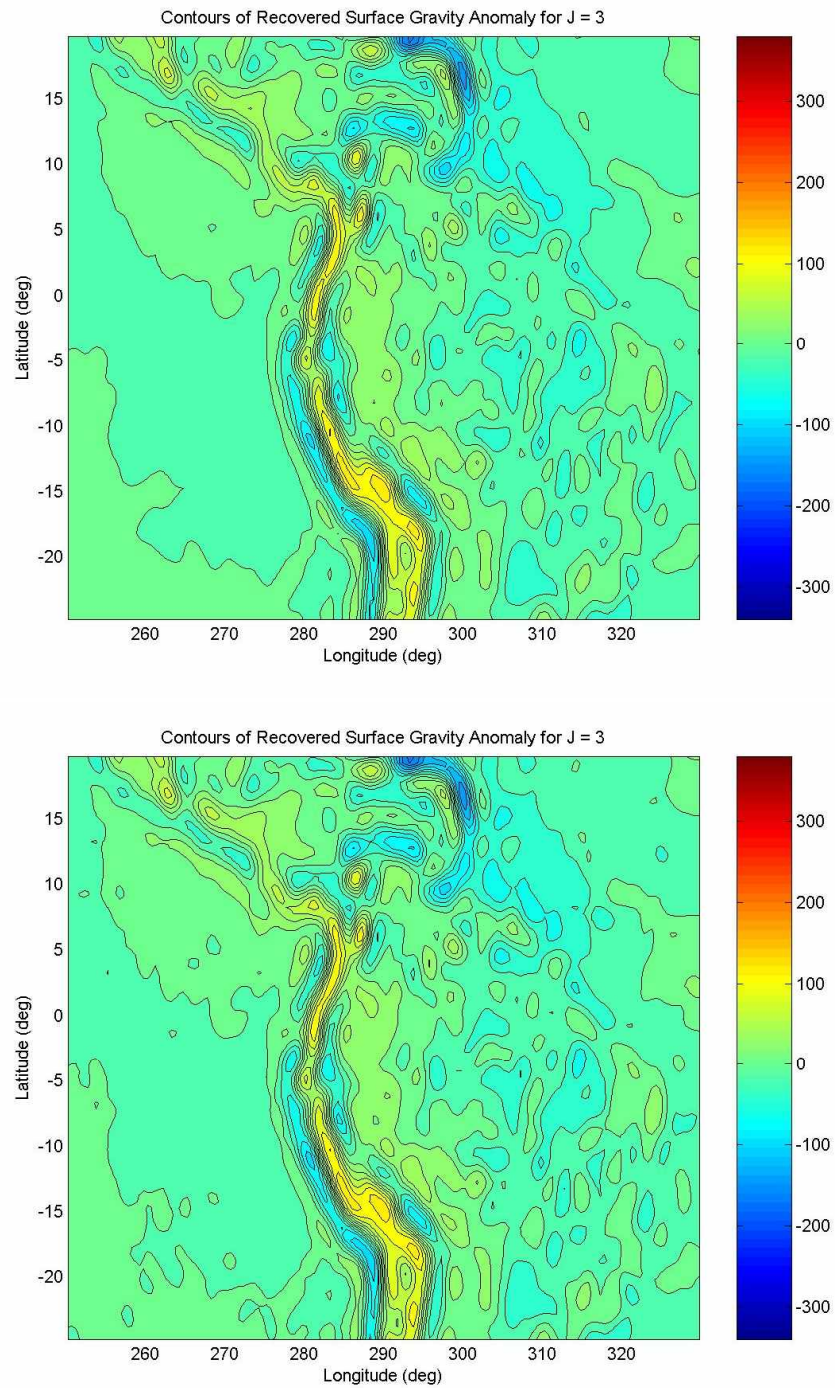


Fig. 8.2.1. The contour map of the recovered surface gravity anomaly for the wavelet resolution level $J = 3$, when 0.1% (top) and 0.5% (bottom) Gaussian random noise was imposed on the gravity anomaly at the satellite altitude $h = 300$ km.

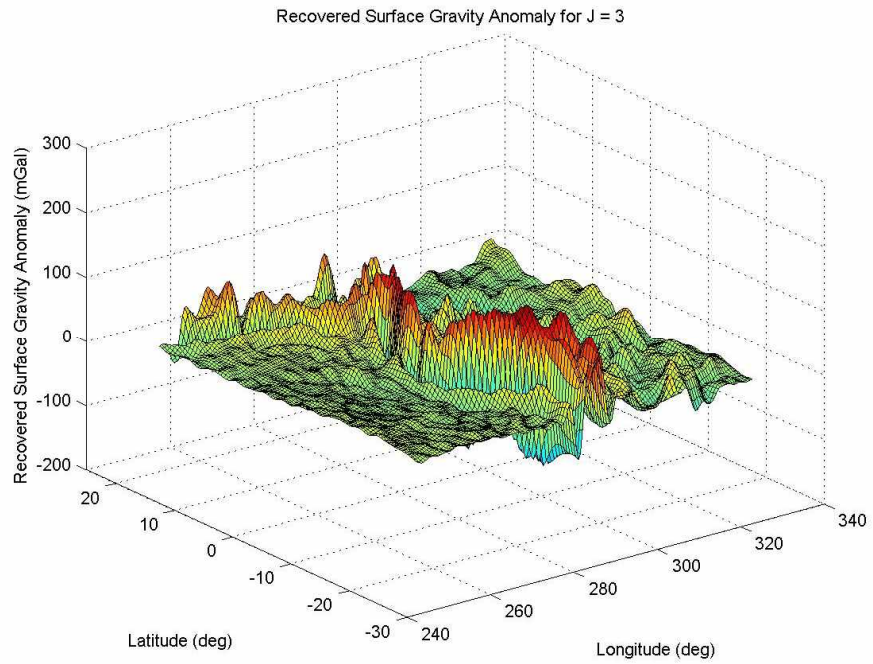
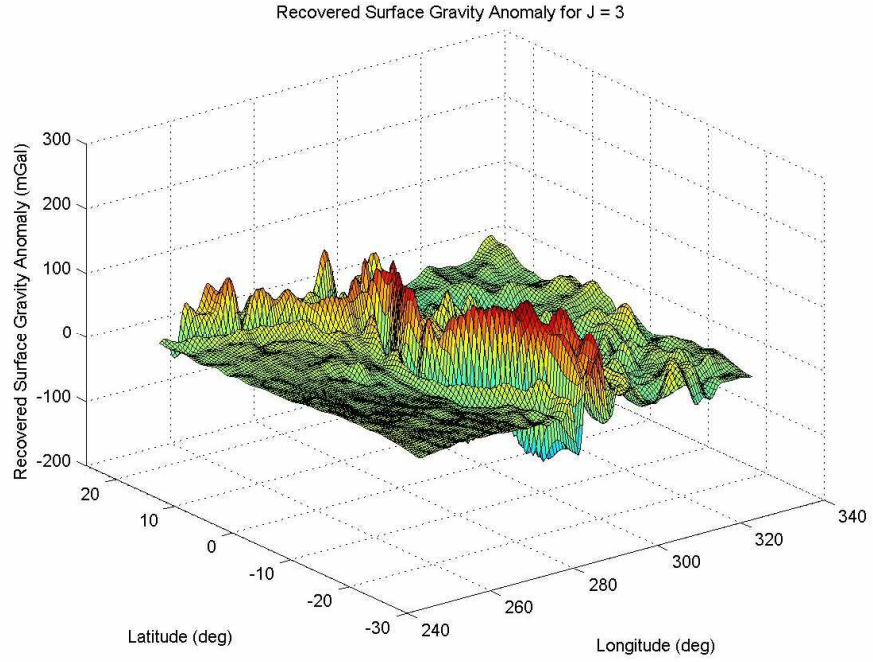


Fig. 8.2.2. 3-D surface map of the recovered surface gravity anomaly for the wavelet resolution level $J = 3$, when 0.1% (top) and 0.5% (bottom) Gaussian random noise was imposed on the gravity anomaly at the satellite altitude $h = 300$ km.

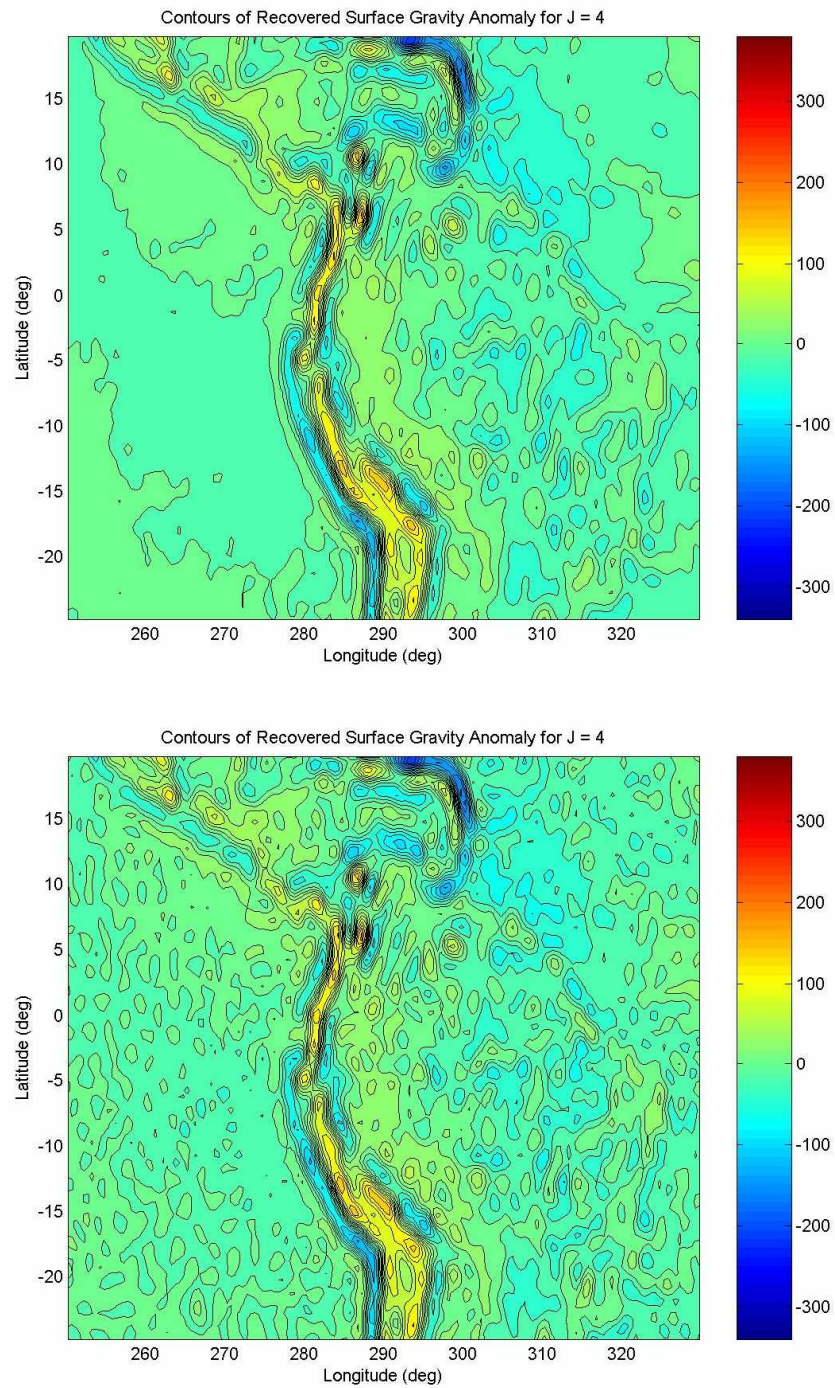


Fig. 8.2.3. The contour map of the recovered surface gravity anomaly for the wavelet resolution level $J = 4$, when 0.1% (top) and 0.5% (bottom) Gaussian random noise was imposed on the gravity anomaly at the satellite altitude $h = 300$ km.

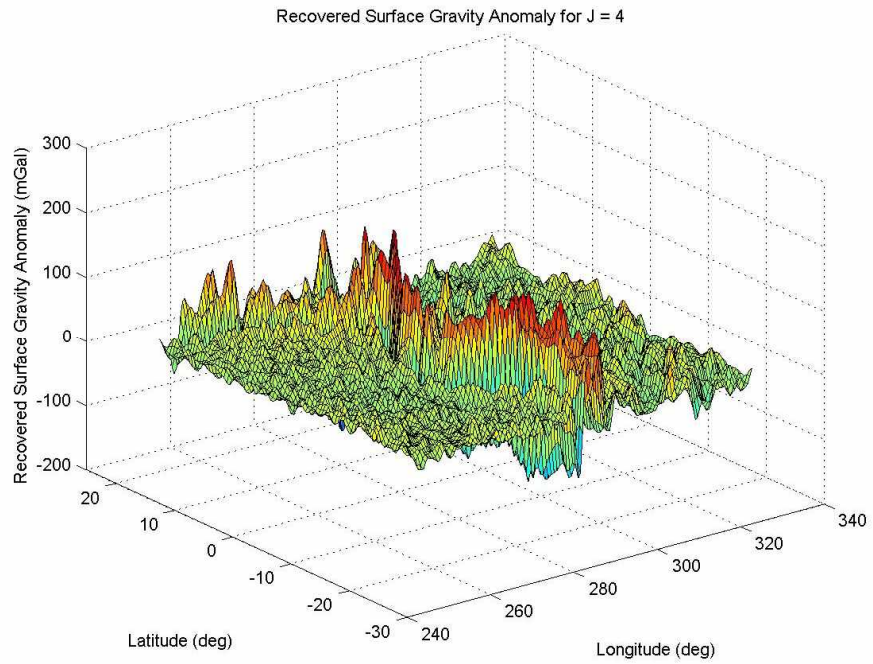
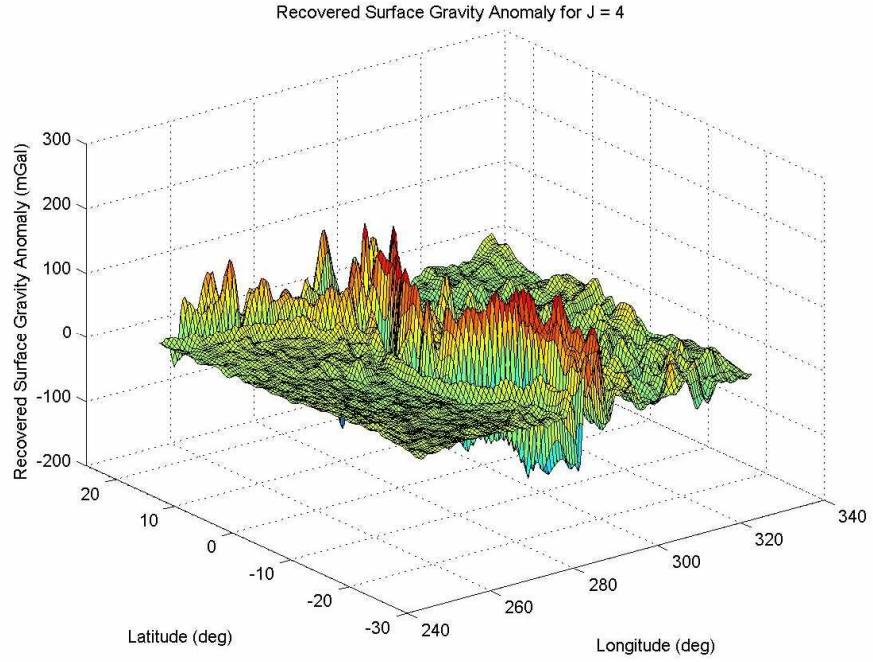


Fig. 8.2.4. 3-D surface map of the recovered surface gravity anomaly for the wavelet resolution level $J = 4$, when 0.1% (top) and 0.5% (bottom) Gaussian random noise was imposed on the gravity anomaly at the satellite altitude $h = 300$ km.

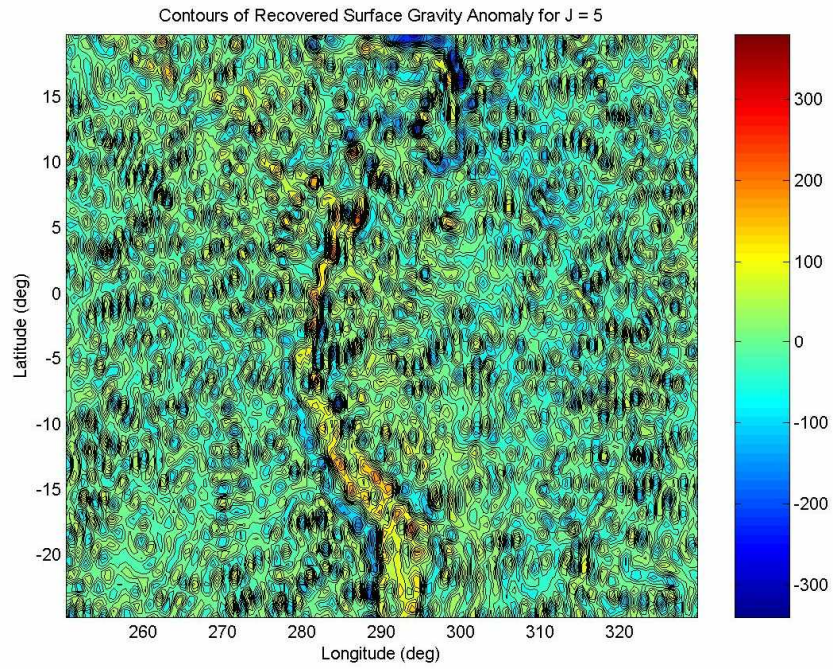
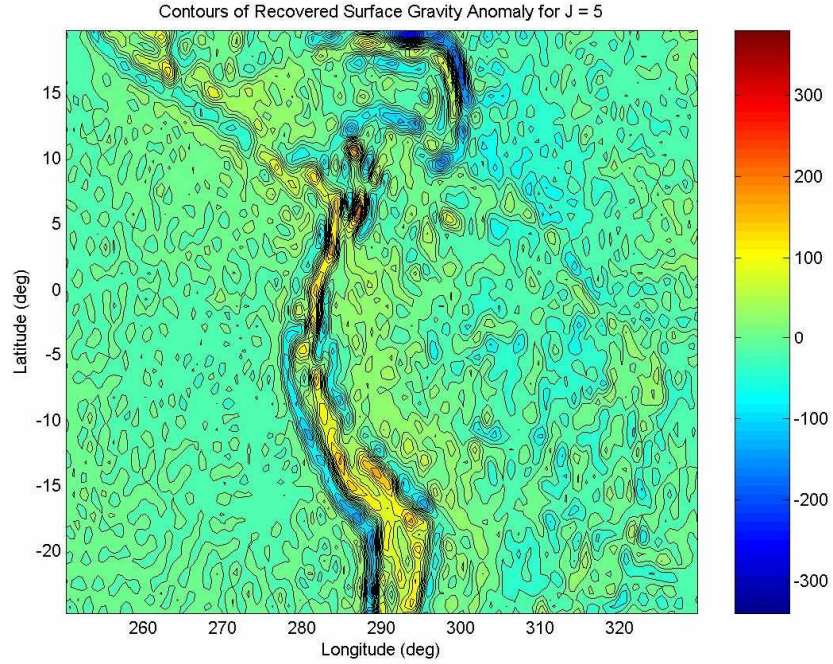


Fig. 8.2.5. The contour map of the recovered surface gravity anomaly for the wavelet resolution level $J = 5$, when 0.1% (top) and 0.5% (bottom) Gaussian random noise was imposed on the gravity anomaly at the satellite altitude $h = 300$ km.

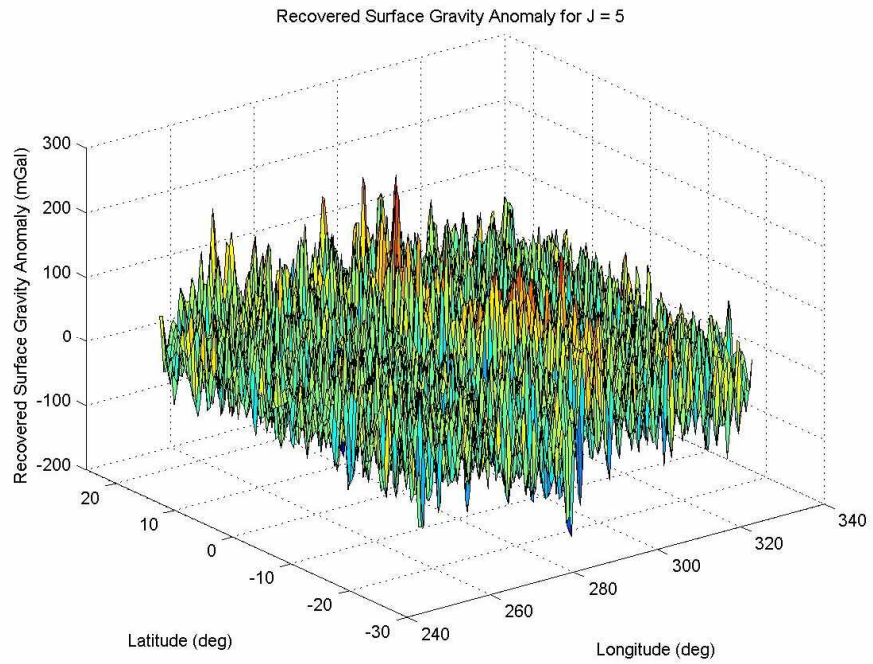
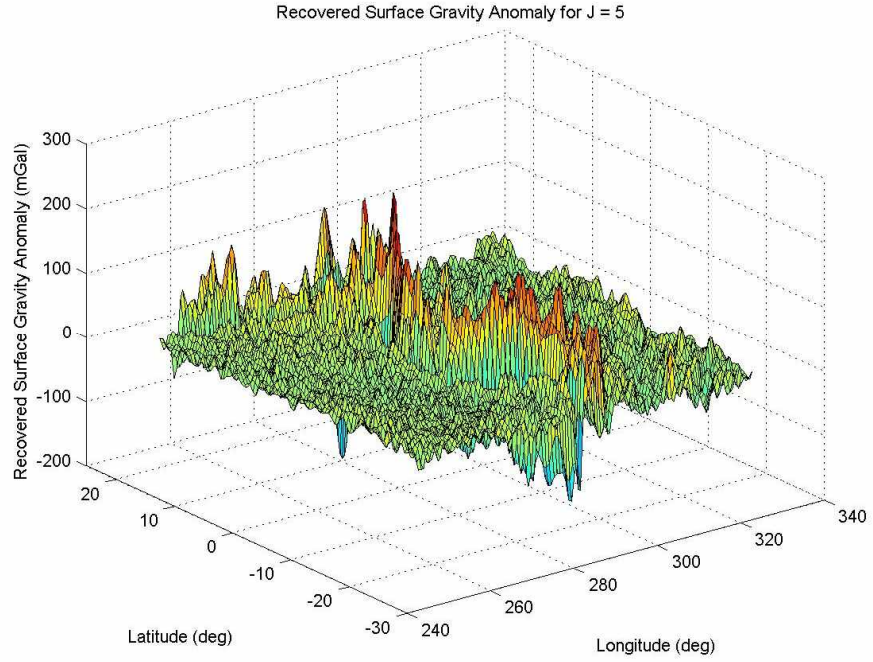


Fig. 8.2.6. 3-D surface map of the recovered surface gravity anomaly for the wavelet resolution level $J = 5$, when 0.1% (top) and 0.5% (bottom) Gaussian random noise was imposed on the gravity anomaly at the satellite altitude $h = 300$ km.

Spatial Resolution	$ G - G_0 _{RMS}$	$ G - G_1 _{RMS}$	$ G - G_2 _{RMS}$	$ G - G_3 _{RMS}$	$ G - G_4 _{RMS}$	$ G - G_5 _{RMS}$	$ G - G_6 _{RMS}$
0.5°	28.90	27.54	25.37	21.27	17.97	16.57	35.86
1.0°	20.51	18.78	16.06	11.11	7.76	9.74	34.19
1.5°	17.26	15.35	12.38	7.32	5.37	10.46	34.85
2.0°	14.13	12.05	8.93	4.97	6.63	12.97	36.01
3.0°	8.05	5.64	3.46	8.12	13.40	19.56	39.26
4.0°	4.29	2.63	5.37	12.79	17.97	23.22	41.10
5.0°	2.29	4.44	9.23	16.61	20.99	25.25	42.18

Table 8.2.1. The RMS surface gravity anomaly error $|G - G_j|_{RMS}$ in mGal for the region of $250.25^\circ \sim 329.75^\circ$ in longitude and $-24.75^\circ \sim 19.75^\circ$ in latitude when 0.1% of Gaussian random noise was imposed on the satellite measurement.

Spatial Resolution	$ G - G_0 _{RMS}$	$ G - G_1 _{RMS}$	$ G - G_2 _{RMS}$	$ G - G_3 _{RMS}$	$ G - G_4 _{RMS}$	$ G - G_5 _{RMS}$	$ G - G_6 _{RMS}$
0.5°	28.90	27.54	25.37	21.30	19.13	41.27	166.44
1.0°	20.51	18.78	16.06	11.18	10.23	39.07	166.01
1.5°	17.26	15.35	12.38	7.44	8.60	39.28	166.12
2.0°	14.13	12.05	8.93	5.17	9.49	40.05	166.32
3.0°	8.05	5.64	3.47	8.27	15.09	42.70	167.04
4.0°	4.29	2.63	5.37	12.89	19.29	44.52	167.50
5.0°	2.29	4.44	9.24	16.69	22.13	45.59	167.78

Table 8.2.2. The RMS surface gravity anomaly error $|G - G_j|_{RMS}$ in mGal for the region of $250.25^\circ \sim 329.75^\circ$ in longitude and $-24.75^\circ \sim 19.75^\circ$ in latitude when 0.5% of Gaussian random noise was imposed on the satellite measurement.

We also recovered the gravity solution for $N = 600$ with 0.1% measurement noise to see if the increased maximum degree of Legendre polynomials would amplify the noise effect. The regularization parameters were identical as in the $N = 300$ case. Comparison between **Table 8.2.1** and **Table 8.2.3** confirms that the increased N in fact reduces the RMS error in the recovered gravity anomaly, although the improvement is insubstantial.

It appears that a little noise in the satellite measurement is amplified in the process of recovering the surface gravity anomaly. It is more conspicuous in the direct upward propagation case where the surface gravity signal is smoothed out a great deal by upward continuation as is mentioned in the previous chapters.

Spatial Resolution	$ G - G_0 _{RMS}$	$ G - G_1 _{RMS}$	$ G - G_2 _{RMS}$	$ G - G_3 _{RMS}$	$ G - G_4 _{RMS}$	$ G - G_5 _{RMS}$	$ G - G_6 _{RMS}$
0.5°	28.90	27.54	25.37	21.27	17.97	16.56	35.68
1.0°	20.51	18.78	16.06	11.11	7.76	9.74	34.02
1.5°	17.26	15.35	12.38	7.32	5.37	10.45	34.70
2.0°	14.13	12.05	8.93	4.97	6.63	12.96	35.85
3.0°	8.05	5.64	3.46	8.12	13.40	19.55	39.12
4.0°	4.29	2.63	5.37	12.79	17.97	23.22	40.96
5.0°	2.29	4.44	9.23	16.61	20.99	25.25	42.04

Table 8.2.3. The RMS surface gravity anomaly error $|G - G_j|_{RMS}$ in mGal for the region of $250.25^\circ \sim 329.75^\circ$ in longitude and $-24.75^\circ \sim 19.75^\circ$ in latitude when 0.1% of Gaussian random noise was imposed on the satellite measurement with the maximum degree of Legendre polynomial N set to be 600.

8.3. By Using the SGG Measurements

We studied the effect of the measurement noise on the recovered gravity solution using the SGG measurements. **Fig. 8.3.1** to **Fig. 8.3.4** show the contour and 3-D surface maps of the recovered surface gravity anomaly for the local region of $250.18^\circ \sim 330.18^\circ$ in longitude ($29.82^\circ\text{W} \sim 109.82^\circ\text{W}$) and $-24.51^\circ \sim 20.31^\circ$ latitude ($24.51^\circ\text{S} \sim 20.31^\circ\text{N}$), which is nearly equivalent to Region I, with the wavelet resolution level $J = 4$ and $J = 5$ when 0.1% and 0.5% Gaussian random noise was imposed on the SGG measurements at the satellite altitude $h = 300$ km. The same regularization parameters in section 7.2 were used in both cases: $\gamma_0 = 2.0 \times 10^{-12}$, $\gamma_1 = 7.0 \times 10^{-13}$, $\gamma_2 = 2.0 \times 10^{-13}$, $\gamma_3 = 8.0 \times 10^{-14}$, $\gamma_4 = 4.0 \times 10^{-14}$, $\gamma_5 = 2.0 \times 10^{-14}$ and $\gamma_6 = 5.0 \times 10^{-15}$. The maximum degree of the Legendre polynomials N was set to be 300.

As is true in section 8.2, the direct upward propagation case, the result from the SGG measurements at the satellite altitude shows that the effect of the measurement error becomes more prominent in the gravity solution as the wavelet resolution level gets higher and thus more detailed, shorter wavelength signals are recovered. The effect of the measurement noise starts to appear at $J = 5$ with 0.1% measurement noise, while it starts to affect the recovered gravity anomaly at $J = 4$ with 0.5% noise.

Table 8.3.1 and **Table 8.3.2** provide the RMS and mean surface gravity anomaly error for the noise-free, 0.1% and 0.5% of imposed measurement noise cases with the different wavelet resolution levels for the spatial resolution of $\sim 0.7^\circ$. It shows that with 0.1% measurement noise the RMS error increases only by 0.1 mGal, whereas with 0.5% noise the RMS error increases by 1.7 mGal. The mean error increases by 0.1 mGal for 0.1% noise and 0.9 mGal for the 0.5% measurement noise case.

Compared to the result from section 8.2, it is obvious that the SGG solution is less influenced by the measurement noise, which is possibly due to the fact that the SGG measurement at the satellite altitude contains a great deal of the detailed information of

surface gravity anomaly and not as smoothed out as in the direct upward propagation case and therefore not as susceptible to the signal amplification during the recovery process.

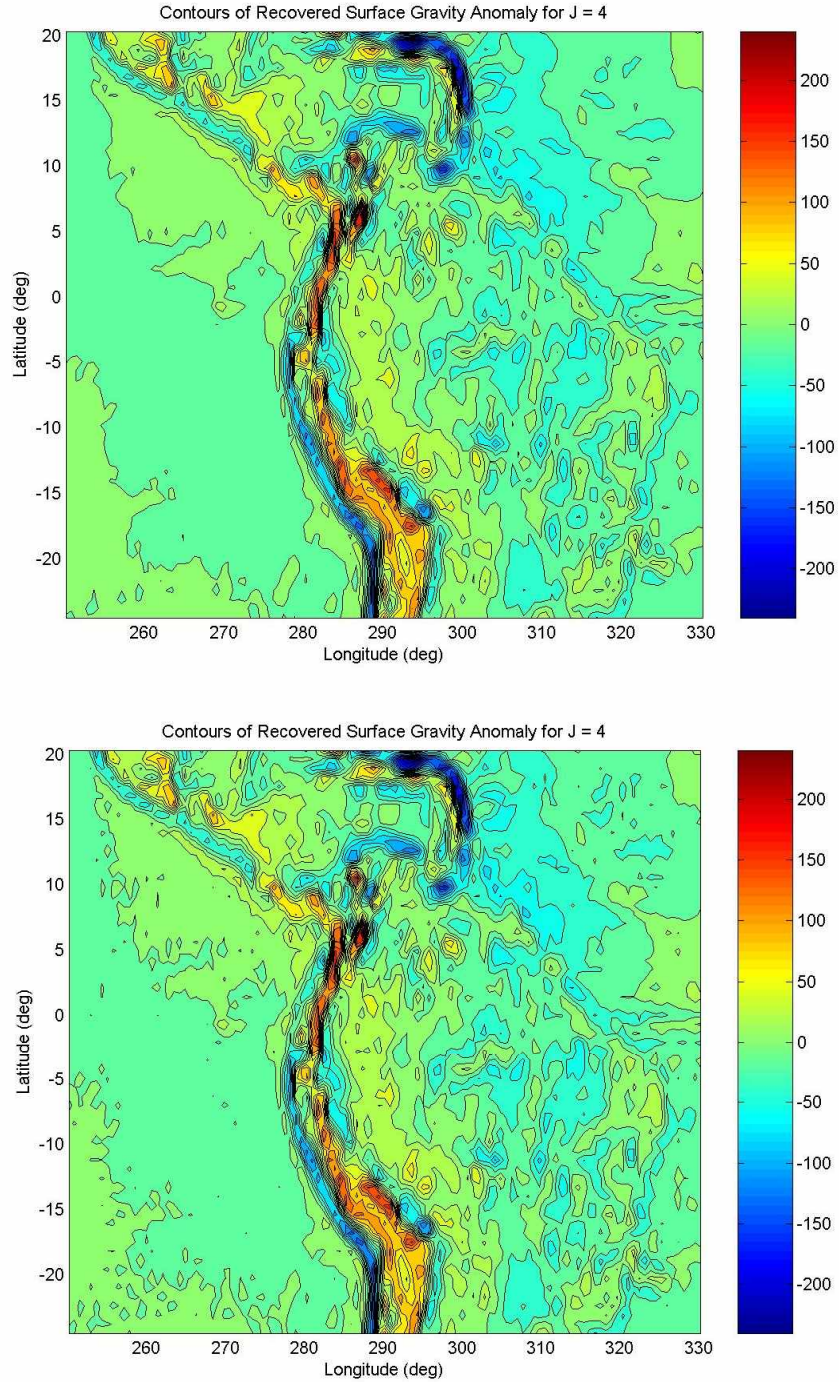


Fig. 8.3.1. The contour map of the recovered surface gravity anomaly for the wavelet resolution $J = 4$, when 0.1% (top) and 0.5% (bottom) Gaussian random noise was imposed on the second order radial derivative of the gravity anomaly at the satellite altitude $h = 300$ km.

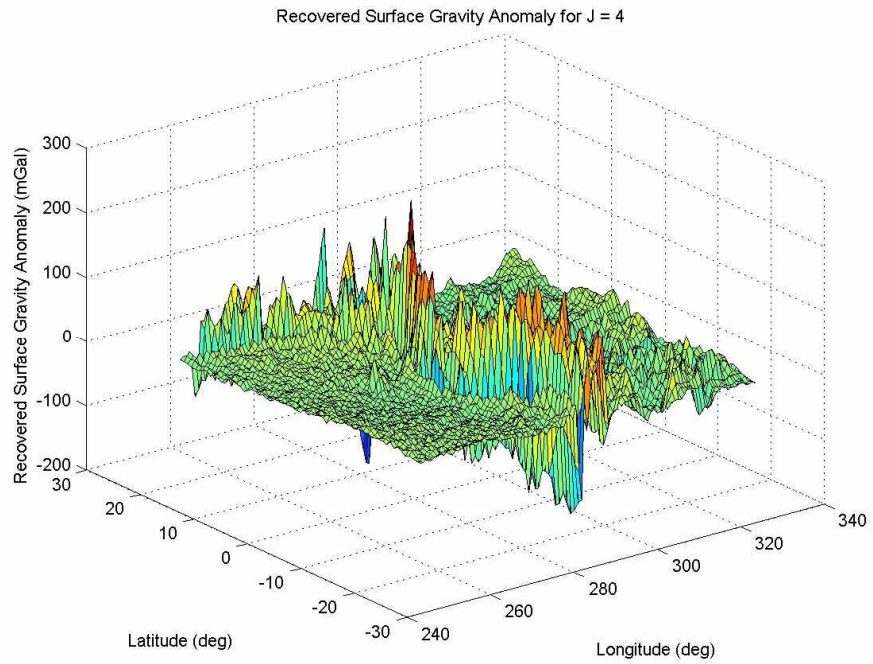
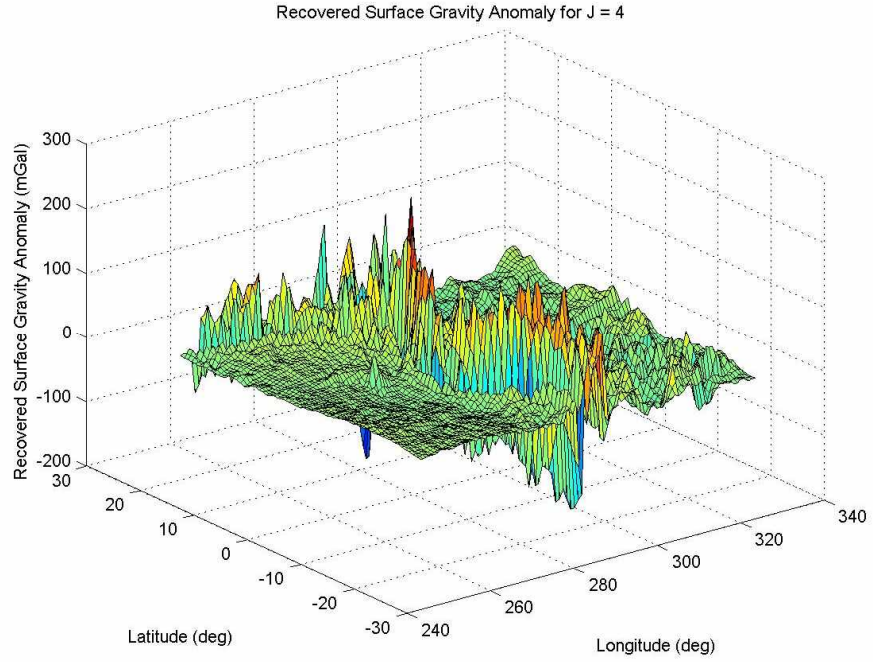


Fig. 8.3.2. 3-D surface map of the recovered surface gravity anomaly for the wavelet resolution $J = 4$, when 0.1% (top) and 0.5% (bottom) Gaussian random noise was imposed on the second order radial derivative of the gravity anomaly at $h = 300$ km.

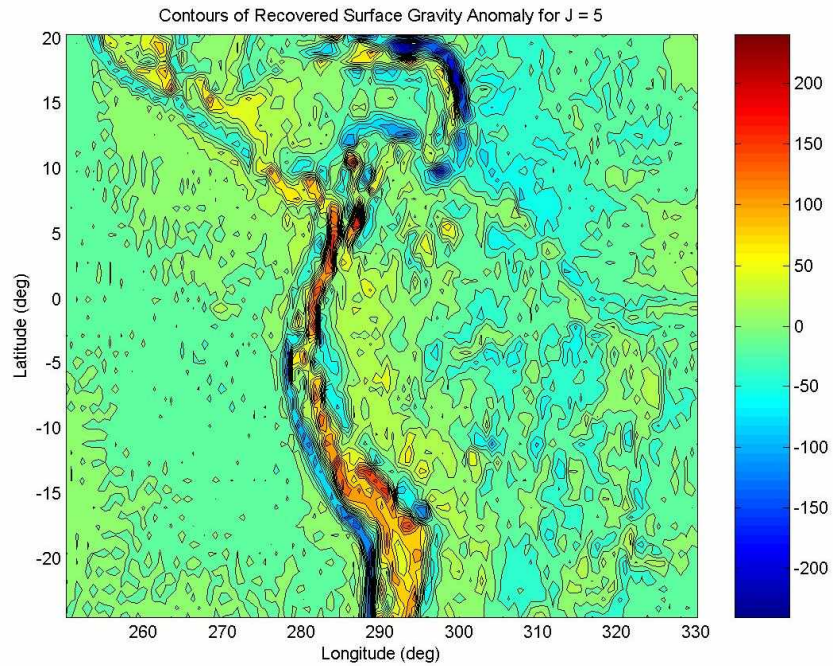
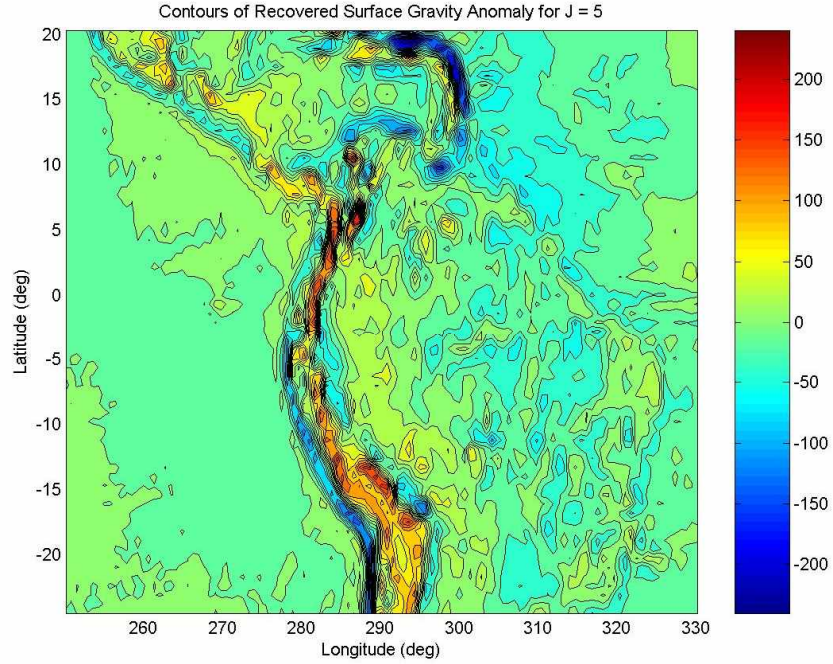


Fig. 8.3.3. The contour map of the recovered surface gravity anomaly for the wavelet resolution $J = 5$, when 0.1% (top) and 0.5% (bottom) Gaussian random noise was imposed on the second order radial derivative of the gravity anomaly at the satellite altitude $h = 300$ km.

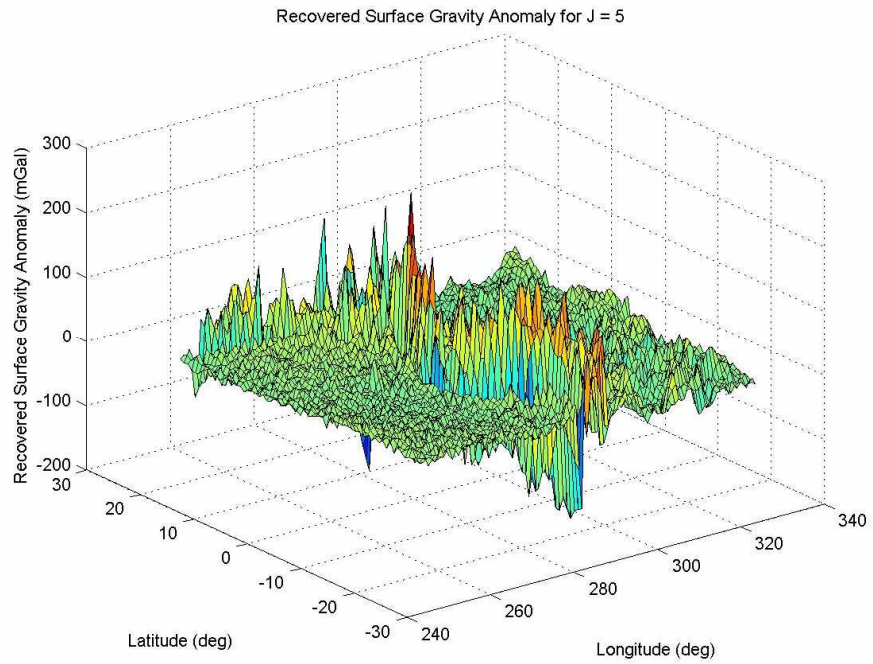
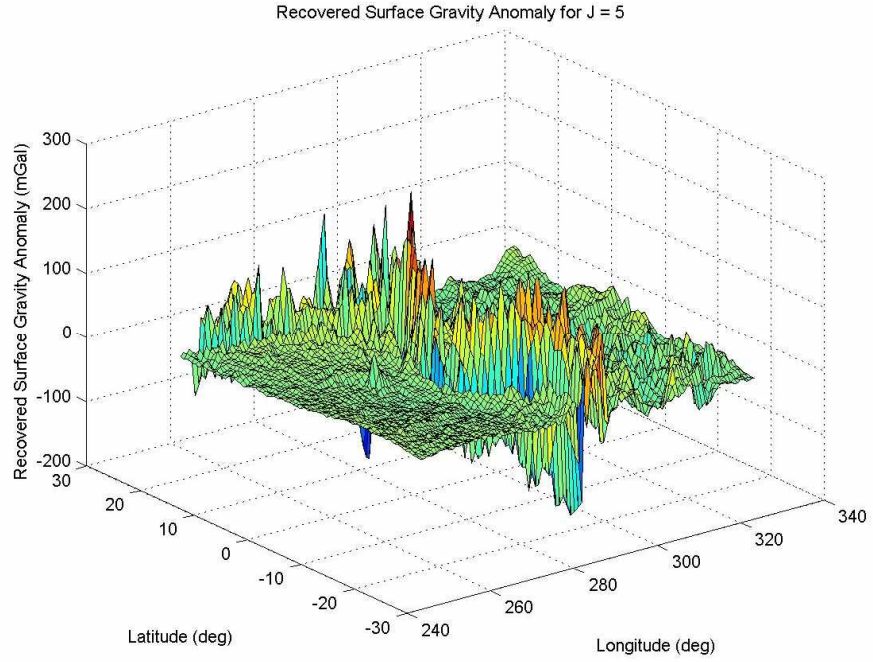


Fig. 8.3.4. 3-D surface map of the recovered surface gravity anomaly for the wavelet resolution $J = 5$, when 0.1% (top) and 0.5% (bottom) Gaussian random noise was imposed on the second order radial derivative of the gravity anomaly at $h = 300$ km.

J	$ G - G_J _{RMS}$	$ G - G_J _{RMS}$ with 0.1% Gaussian noise	$ G - G_J _{RMS}$ with 0.5% Gaussian noise
0	20.34	20.34	20.34
1	14.11	14.11	14.11
2	9.37	9.37	9.37
3	7.21	7.21	7.28
4	5.86	5.88	6.34
5	4.65	4.78	7.11
6	12.10	12.98	25.83

Table 8.3.1. The RMS error $|G - G_J|_{RMS}$ in mGal for the region of $250.18^\circ \sim 330.18^\circ$ in longitude and $-24.51^\circ \sim 20.31^\circ$ in latitude, with zero, 0.1% and 0.5% Gaussian random noise respectively imposed on the satellite measurement.

J	$ G - G_J _{mean}$	$ G - G_J _{mean}$ with 0.1% Gaussian noise	$ G - G_J _{mean}$ with 0.5% Gaussian noise
0	12.75	12.75	12.75
1	8.52	8.52	8.52
2	5.14	5.14	5.16
3	4.17	4.18	4.34
4	3.87	3.89	4.39
5	3.49	3.56	5.54
6	8.58	9.40	20.31

Table 8.3.2. The mean error $|G - G_J|_{mean}$ in mGal for the region of $250.18^\circ \sim 330.18^\circ$ in longitude and $-24.51^\circ \sim 20.31^\circ$ in latitude, with zero, 0.1% and 0.5% Gaussian random noise respectively imposed on the satellite measurement.

Chapter 9. Satellite Gravity Measurement Data on Ground Track

9.1. Satellite Ground Track Data

In previous chapters, we have studied the spherical wavelets gravity model based on the gravity measurement data arranged on a regular grid, *i.e.* evenly spaced grid both in longitude and latitude. In a satellite mission where global coverage is required to map the gravity field of the Earth, such as GRACE and GOCE, the data can be arranged in such a manner in a certain period of time after the launch of the satellite. The freely drifting ground track profile of GRACE enables sufficient global ground track density that is required to meet degree/order 180 solution to be obtained in over 30 days (Bettadpur and Watkins, 2000). In the GOCE satellite's sun-synchronous orbit, the ground track profile shows a 60-day repeat period, where the ground track density after two months ensures that the maximum separation of tracks is less than 40 km (Drinkwater *et al.*, 2007). **Fig. 9.1.1** shows the sample ground track pattern for GOCE satellite. In these satellite missions, once sufficient volume and resolution of data is obtained, a numerical scheme such as polynomial or cubic spline interpolation or data binning technique can be employed to arrange the data on a regular grid.

There are certain occasions or specific regions, however, that arranging the measurement data on a regular grid is not easily achieved, *e.g.* when the region of interest does not have a dense enough ground track coverage during a given period of time. In this chapter, we will study the gravity solution obtained from the measurement data on ground tracks, rather than on a regular grid.

Since the measurement data along the track is dense and relatively regular, it is easily aligned on equally spaced points on the line by one of the aforementioned numerical schemes. The same can be applied to the ground tracks, even if the tracks are farther separated and less dense than the data points along the track. In this chapter, we

will study two different ground track profiles: Track A, where the ground tracks are aligned along the longitude lines at a 1° separation with the measurement data arranged in a 0.5° interval along the track, and Track B, with the same profile as Track A except that the ground tracks are 1.5° apart. Note that the ground tracks can be aligned along either the longitude or the latitude by rotating the reference frame. This will simplify the surface integration process in recovering the numerical solution. Afterwards the coordinate system can be rotated back to the original reference frame.

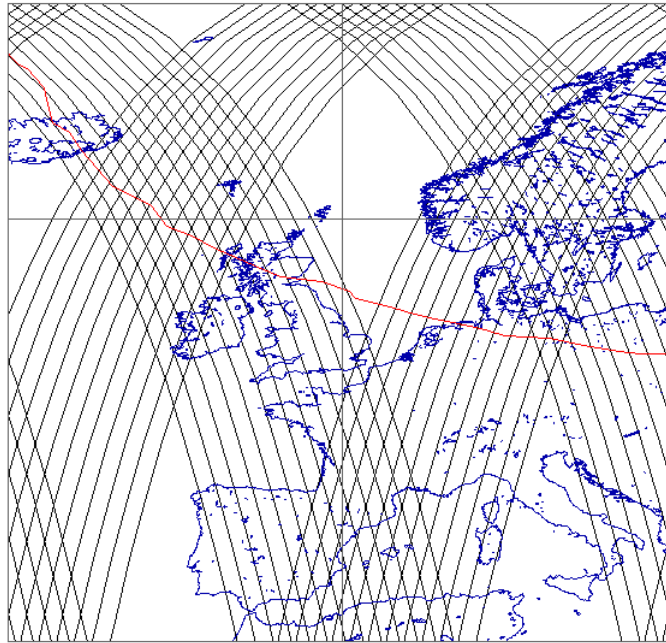


Fig. 9.1.1. GOCE ground track sampling pattern over Europe after 14 days of a 60-day repeat pattern (in the reference orbit configuration). The red line indicates the area within which the satellite is in line-of-sight contact with the Kiruna ground receiving station in northern Sweden (Drinkwater *et al.*, 2007).

9.2. By Using the Upward Propagated Gravity Anomaly

We built three data sets to test our gravity model on the region of $200.25^\circ \sim 19.75^\circ$ in longitude ($19.75^\circ\text{E} \sim 159.75^\circ\text{W}$ clockwise) and $-47.25^\circ \sim 42.25^\circ$ in latitude ($47.25^\circ\text{S} \sim 42.25^\circ\text{N}$) at the satellite altitude $h = 300$ km: a regular 360×180 longitudinal-latitude grid (0.5° separation along the longitude and the latitude), a 180×180 grid (1° separation in longitude and 0.5° in latitude) for Track A, and a 120×180 grid (1.5° separation in longitude and 0.5° in latitude) for Track B. These three different sets of at-altitude gravity anomaly data were then used to solve the inverse problem to recover the surface gravity anomaly for Region I ($30.25^\circ\text{W} \sim 109.75^\circ\text{W}$ in longitude and $24.75^\circ\text{S} \sim 19.75^\circ\text{N}$ in latitude) from the previous chapters. Since the number of abscissas does not meet the $2^n + 1$ requirement (see section 4.1), we employed the single-step trapezoidal rule in the equation (4.1.14) as a numerical integration scheme. The regularization parameters used in all three cases were the same as in section 5.1, *i.e.* $\gamma_0 = 9.0 \times 10^{-2}$, $\gamma_1 = 5.0 \times 10^{-2}$, $\gamma_2 = 2.0 \times 10^{-2}$, $\gamma_3 = 4.0 \times 10^{-3}$, $\gamma_4 = 1.0 \times 10^{-3}$, $\gamma_5 = 2.0 \times 10^{-4}$ and $\gamma_6 = 5.0 \times 10^{-5}$. The maximum degree of the Legendre polynomials N was 300.

Fig. 9.2.1 and **Fig. 9.2.2** are the contour and 3-D surface map of the recovered surface gravity anomaly for Region I at the wavelet resolution level $J = 4$ (corresponding to 1.5° spatial resolution) and $J = 5$ (1° spatial resolution) from the data set arranged on the Track A. The result shows the contours of the gravity anomaly field align along the ground tracks (along the longitude lines) from $J = 5$. The effect seems to be stronger in the high magnitude gravity gradient regions. **Fig. 9.2.3** and **Fig. 9.2.4** are the result from Track B at the wavelet resolution level $J = 2$ (corresponding to 3° spatial resolution) and $J = 3$ (2° spatial resolution). Here the effect of irregularity of the data point arrangement appears from a lower level of wavelet resolution.

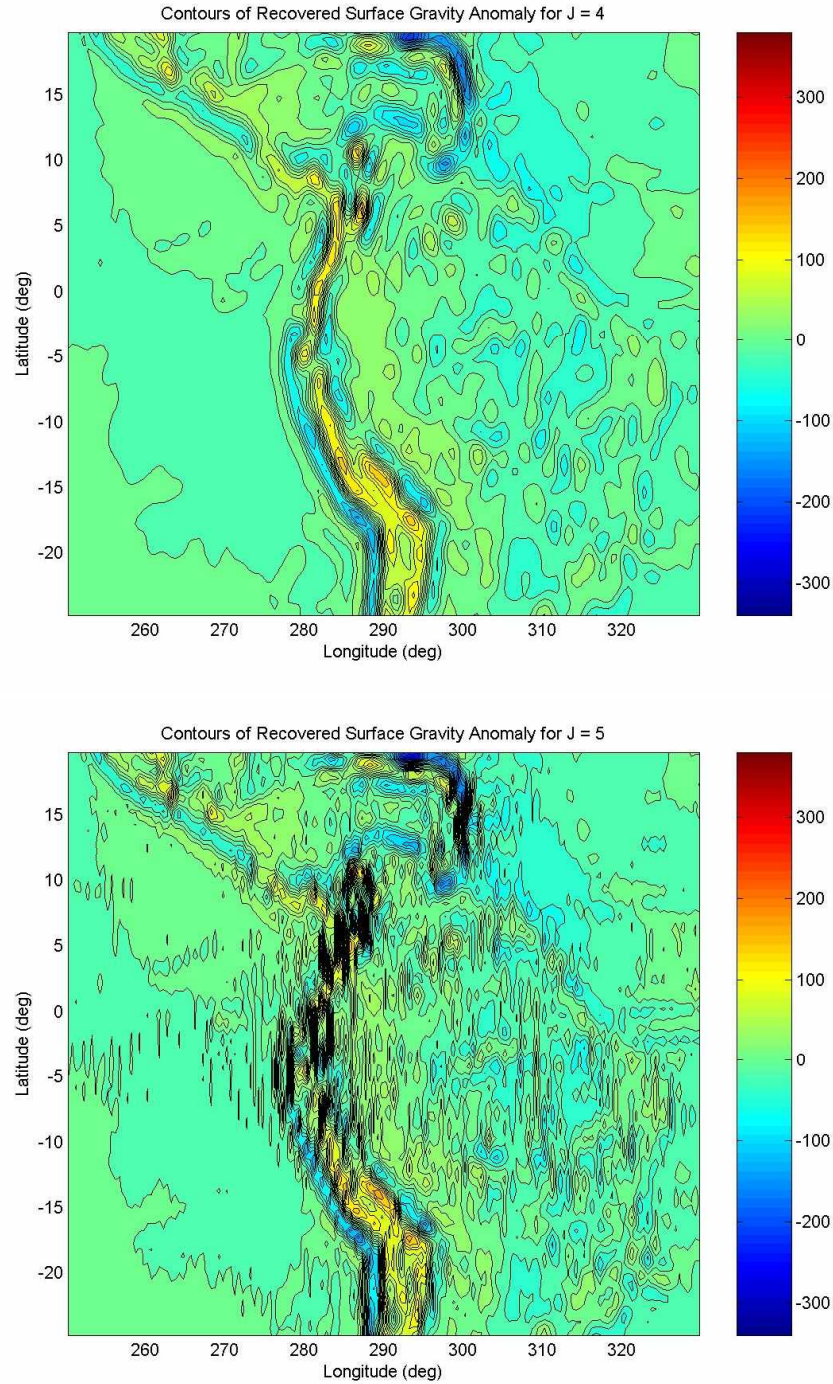


Fig. 9.2.1. The contour map of the recovered surface gravity anomaly for the wavelet resolution level $J = 4$ (top) and $J = 5$ (bottom). The gravity anomaly data at the satellite altitude $h = 300$ km are arranged on Ground Track A where the ground tracks aligned along the longitude lines are separated by 1° .

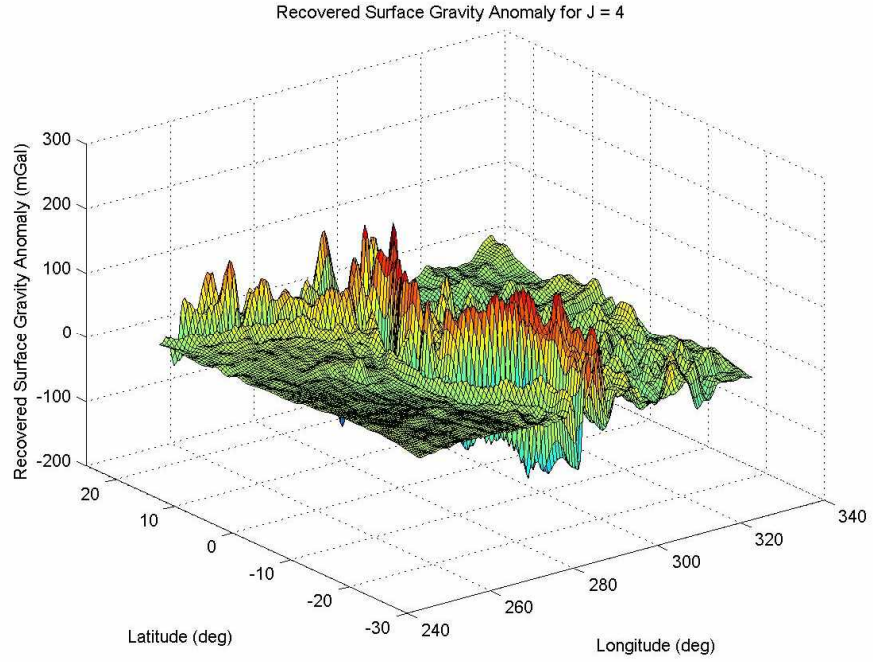


Fig. 9.2.2. 3-D surface map of the recovered surface gravity anomaly for the wavelet resolution level $J = 4$ (top) and $J = 5$ (bottom). The gravity anomaly data at the satellite altitude $h = 300$ km are arranged on Ground Track A where the ground tracks aligned along the longitude lines are separated by 1° .

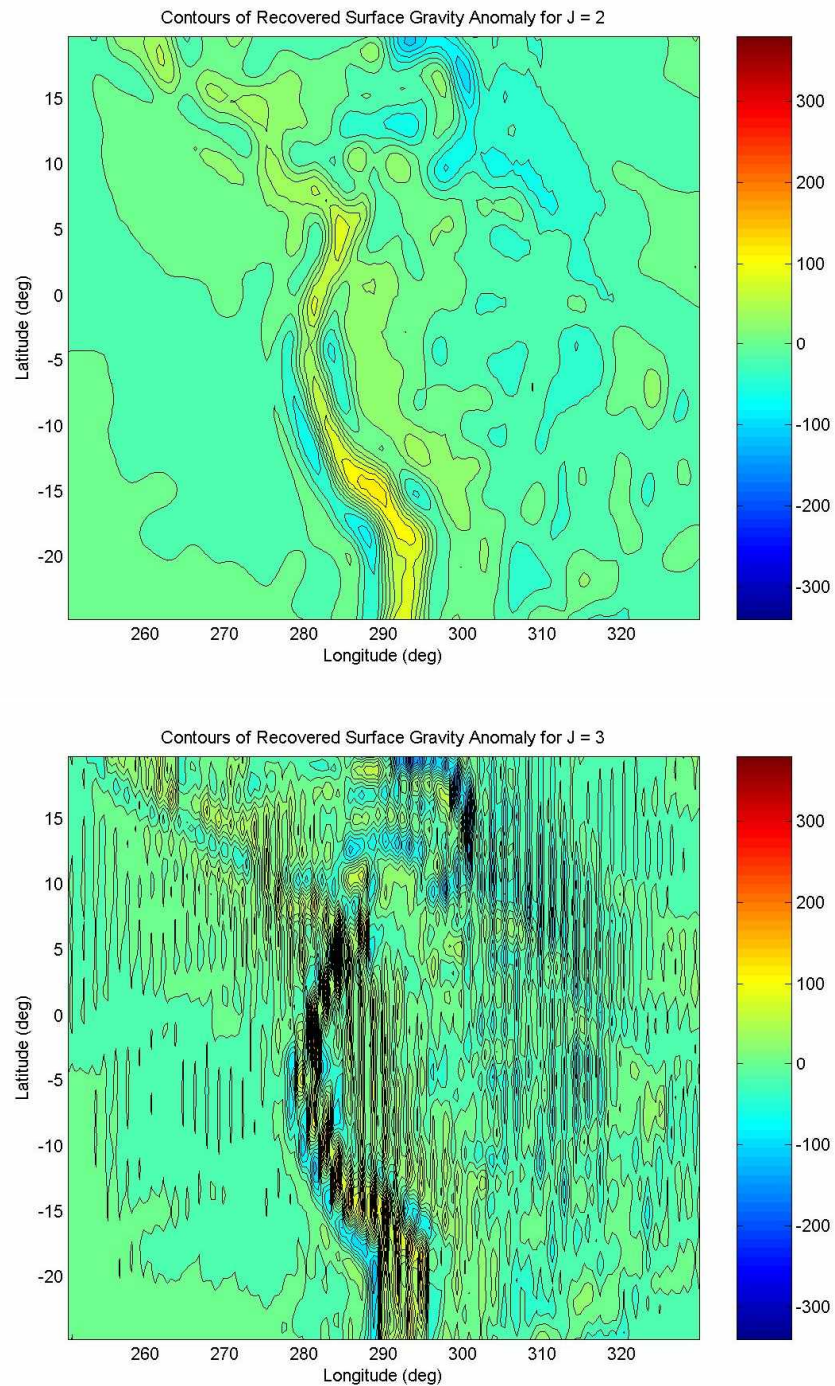


Fig. 9.2.3. The contour map of the recovered surface gravity anomaly for the wavelet resolution level $J = 2$ (top) and $J = 3$ (bottom). The gravity anomaly data at the satellite altitude $h = 300$ km are arranged on Ground Track B where the ground tracks aligned along the longitude lines are separated by 1.5° .

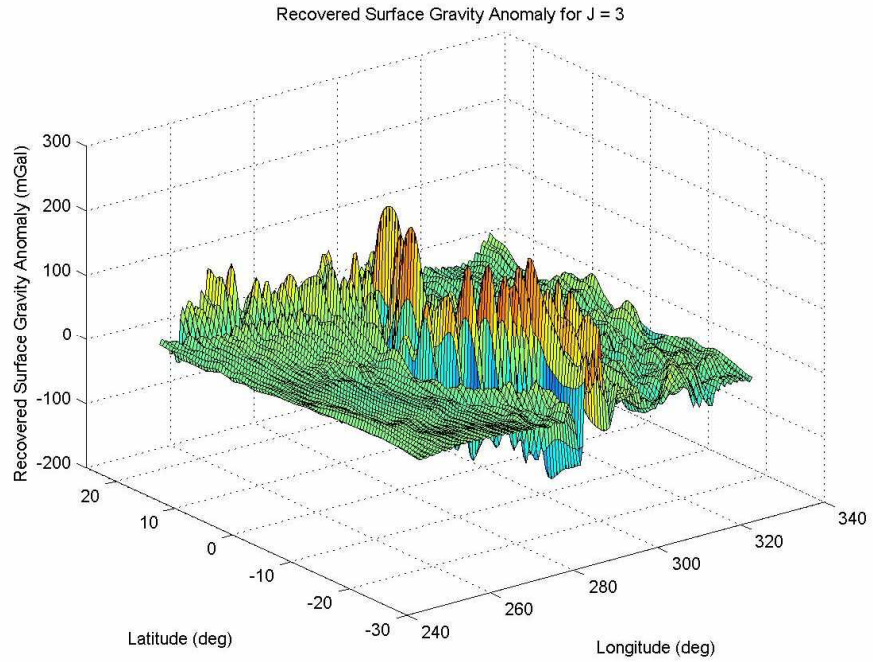
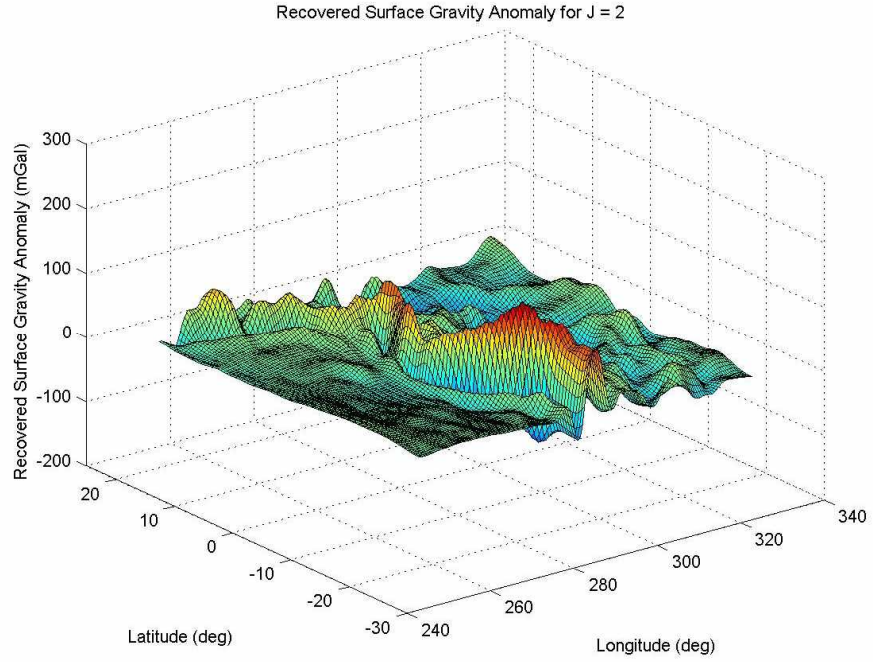


Fig. 9.2.4. 3-D surface map of the recovered surface gravity anomaly for the wavelet resolution level $J = 2$ (top) and $J = 3$ (bottom). The gravity anomaly data at the satellite altitude $h = 300$ km are arranged on Ground Track B where the ground tracks aligned along the longitude lines are separated by 1.5° .

Table 9.2.1 to **Table 9.2.3** provide the RMS surface gravity anomaly error $|G - G_J|_{RMS}$ at the different wavelet resolution levels for each spatial resolution for the altitude gravity anomaly set on a regular grid, on Track A and on Track B, respectively. Comparing the result from Track A and Track B to that from the regular grid confirms that the higher the irregularity of the data arrangement on the grid (the farther the ground tracks are separated), the less fine spatial resolution of the gravity solution that can be recovered. From the data set on the ground tracks that are 1° apart, the surface gravity anomaly could be obtained to the spatial resolution of 1.5° , while a far coarser resolution of 3° solution could be achieved from the gravity data on the ground tracks at a 1.5° separation.

Spatial Resolution	$ G - G_0 _{RMS}$	$ G - G_1 _{RMS}$	$ G - G_2 _{RMS}$	$ G - G_3 _{RMS}$	$ G - G_4 _{RMS}$	$ G - G_5 _{RMS}$	$ G - G_6 _{RMS}$
0.5°	28.90	27.54	25.38	21.28	17.96	14.59	12.23
1.0°	20.51	18.78	16.06	11.13	7.66	5.56	6.10
1.5°	17.27	15.35	12.39	7.34	5.17	6.61	9.16
2.0°	14.13	12.05	8.94	4.98	6.41	10.05	12.94
3.0°	8.05	5.64	3.46	8.10	13.25	17.66	20.25
4.0°	4.29	2.63	5.36	12.77	17.84	21.62	23.58
5.0°	2.29	4.44	9.23	16.59	20.88	23.80	25.41

Table 9.2.1. The RMS surface gravity anomaly error $|G - G_J|_{RMS}$ in mGal for the region of $250.25^\circ \sim 329.75^\circ$ in longitude and $-24.75^\circ \sim 19.75^\circ$ in latitude with the gravity anomaly data at the satellite altitude arranged in a regular grid at a resolution 0.5° both in longitude and latitude.

Spatial Resolution	$ G - G_0 _{RMS}$	$ G - G_1 _{RMS}$	$ G - G_2 _{RMS}$	$ G - G_3 _{RMS}$	$ G - G_4 _{RMS}$	$ G - G_5 _{RMS}$
0.5°	28.90	27.54	25.38	21.28	17.97	18.83
1.0°	20.51	18.78	16.06	11.13	7.69	13.05
1.5°	17.27	15.35	12.39	7.34	5.20	13.48
2.0°	14.13	12.05	8.94	4.98	6.44	15.47
3.0°	8.05	5.64	3.46	8.10	13.26	21.19
4.0°	4.29	2.63	5.36	12.77	17.85	24.58
5.0°	2.29	4.44	9.23	16.59	20.89	26.53

Table 9.2.2. The RMS surface gravity anomaly error $|G - G_j|_{RMS}$ in mGal for the region of 250.25° ~ 329.75° in longitude and -24.75° ~ 19.75° in latitude with the gravity anomaly data at the satellite altitude arranged on Ground Track A where the ground tracks aligned along the longitude lines are separated by 1°.

Spatial Resolution	$ G - G_0 _{RMS}$	$ G - G_1 _{RMS}$	$ G - G_2 _{RMS}$	$ G - G_3 _{RMS}$
0.5°	28.90	27.54	25.35	25.95
1.0°	20.51	18.78	16.04	18.90
1.5°	17.26	15.35	12.37	17.19
2.0°	14.13	12.04	8.92	16.43
3.0°	8.05	5.64	3.52	17.95
4.0°	4.29	2.63	5.41	20.52
5.0°	2.29	4.45	9.26	23.08

Table 9.2.3. The RMS surface gravity anomaly error $|G - G_j|_{RMS}$ in mGal for the region of 250.25° ~ 329.75° in longitude and -24.75° ~ 19.75° in latitude with the gravity anomaly data at the satellite altitude arranged on Ground Track B where the ground tracks aligned along the longitude lines are separated by 1.5°.

9.3. By Using the SGG Measurements

By upward continuation of the global surface gravity anomaly on a 720×360 regular grid with the SGG operator, we first generated three SGG data sets on the same area as described in section 9.2 (the region of $19.75^\circ\text{E} \sim 159.75^\circ\text{W}$ clockwise in longitude and $47.25^\circ\text{S} \sim 42.25^\circ\text{N}$ in latitude at the satellite altitude $h = 300$ km): a 360×180 regular grid with 0.5° spacing in longitude and latitude, a 180×180 grid (1° separation in longitude and 0.5° in latitude) for Track A, and a 120×180 grid (1.5° separation in longitude and 0.5° in latitude) for Track B. These three data sets of the second order radial derivative of gravity anomaly were then downward propagated to recover the surface gravity anomaly for Region I ($30.25^\circ\text{W} \sim 109.75^\circ\text{W}$ in longitude and $24.75^\circ\text{S} \sim 19.75^\circ\text{N}$ in latitude). Both the upward continuation process and the downward propagation, *i.e.* solving the inverse problem, required the implementation of the single-step trapezoidal rule as a numerical integration scheme. The regularization parameters used in this test are: $\gamma_0 = 2.0 \times 10^{-11}$, $\gamma_1 = 2.0 \times 10^{-12}$, $\gamma_2 = 7.0 \times 10^{-13}$, $\gamma_3 = 2.0 \times 10^{-13}$, $\gamma_4 = 8.0 \times 10^{-14}$, $\gamma_5 = 1.0 \times 10^{-14}$ and $\gamma_6 = 5.0 \times 10^{-15}$. The maximum degree of the Legendre polynomials N was set to be 300.

Fig. 9.3.1 and **Fig. 9.3.2** are the contour and 3-D surface map of the surface gravity anomaly for Region I at the wavelet resolution level $J = 3$ and $J = 4$ recovered from the data set arranged on Track A. The alignment of the gravity anomaly contours along the ground track is apparent for $J = 4$, especially in the regions with high magnitude gravity gradients. **Fig. 9.3.3** and **Fig. 9.3.4** are the result from Track B at the wavelet resolution level $J = 1$ and $J = 2$. As was the case in section 9.2, the effect of irregularity of the data arrangement appears at the lower level of wavelet resolution.

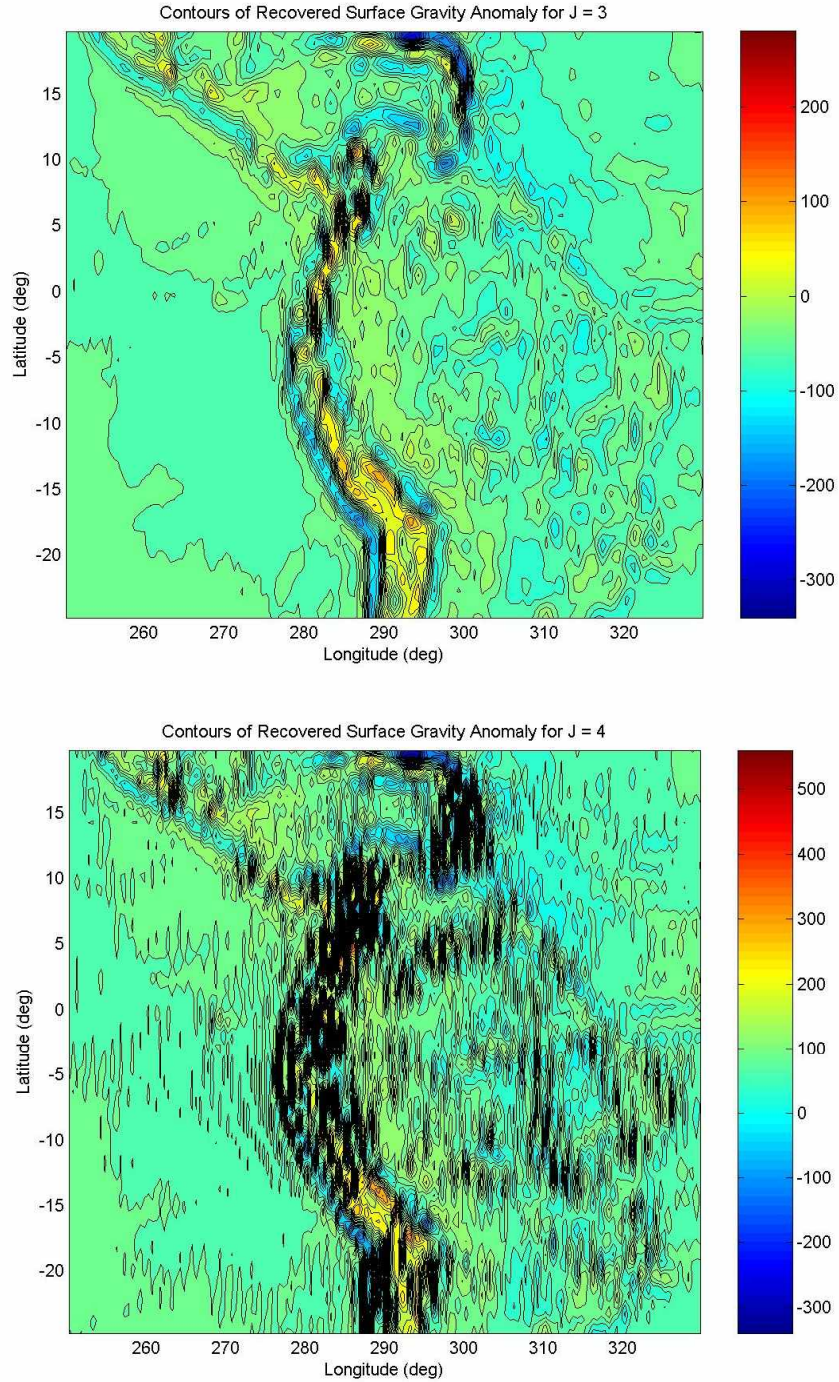


Fig. 9.3.1. The contour map of the recovered surface gravity anomaly for the wavelet resolution level $J = 3$ (top) and $J = 4$ (bottom). The second order radial derivative of the gravity anomaly data at the satellite altitude $h = 300$ km are arranged on Ground Track A where the ground tracks aligned along the longitude lines are separated by 1° .

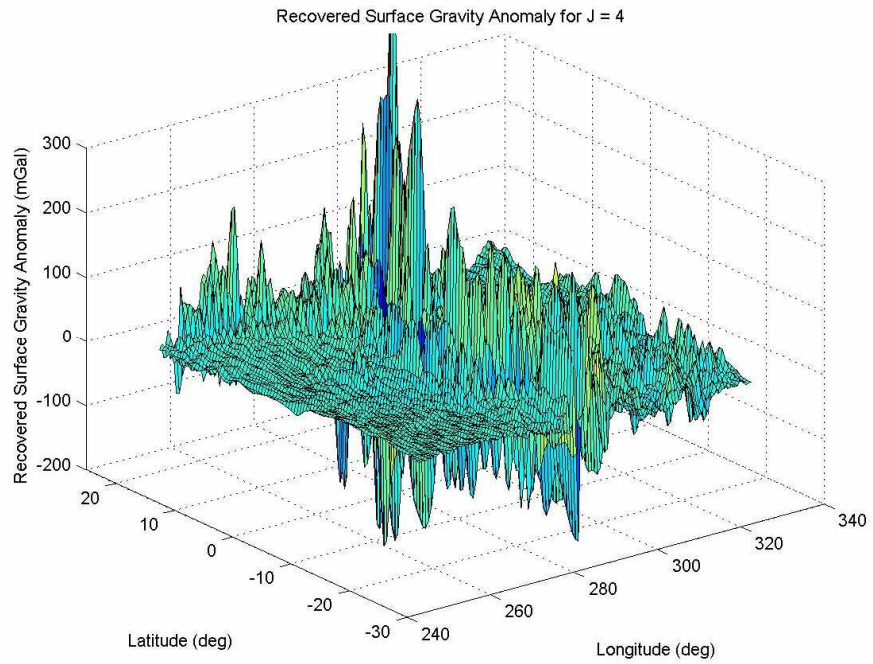
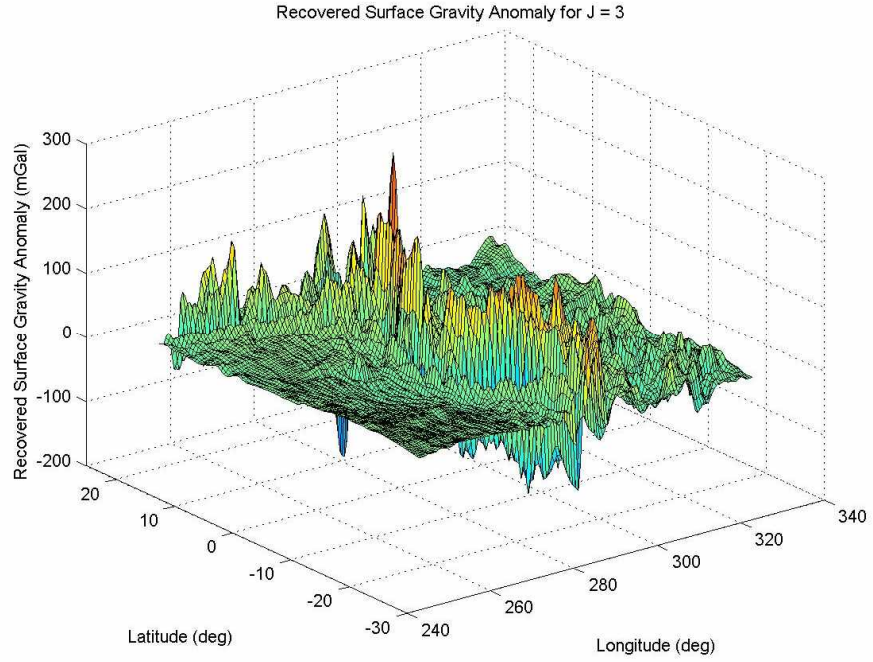


Fig. 9.3.2. 3-D surface map of the recovered surface gravity anomaly for the wavelet resolution level $J = 3$ (top) and $J = 4$ (bottom). The second order radial derivative of the gravity anomaly data at the satellite altitude $h = 300$ km are arranged on Ground Track A where the ground tracks aligned along the longitude lines are separated by 1° .

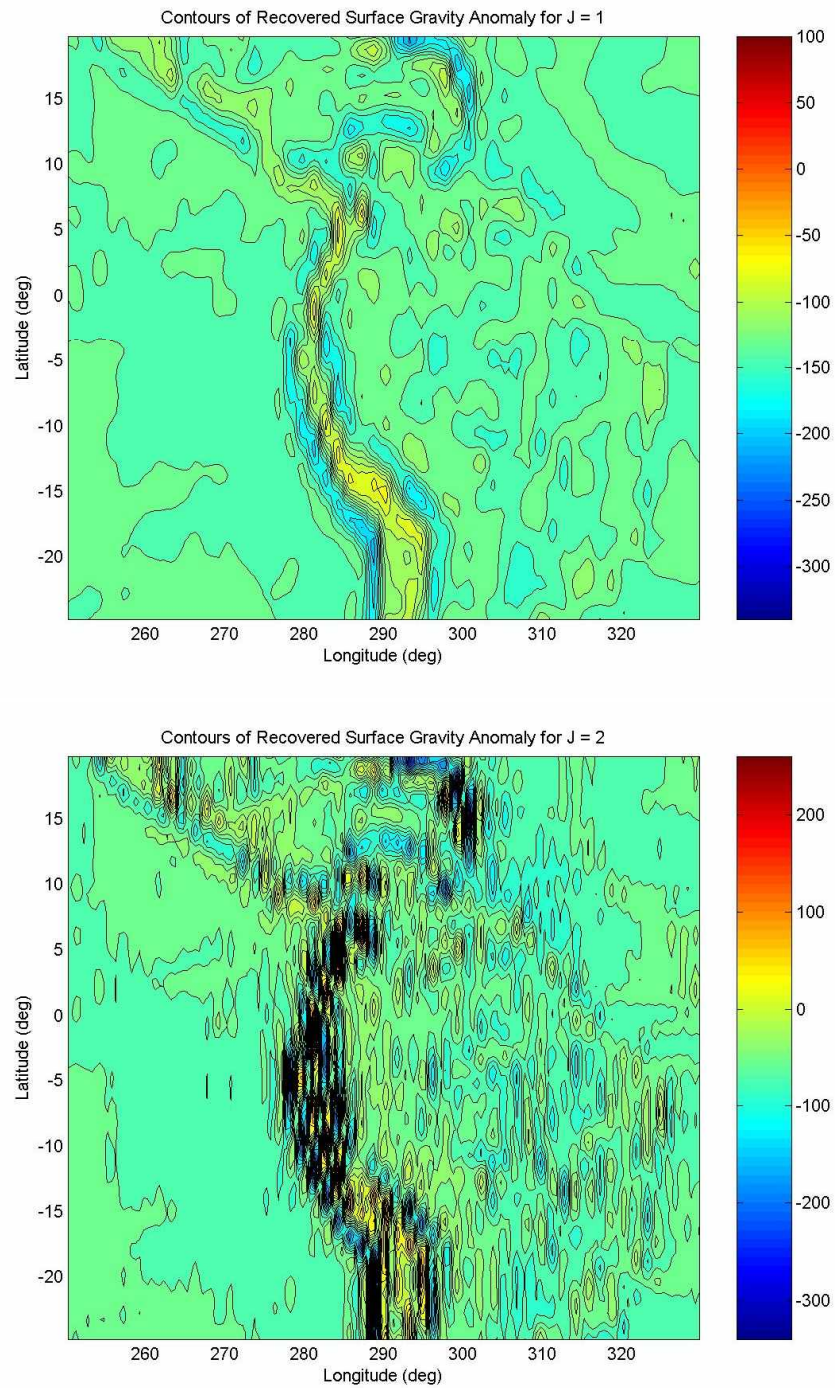


Fig. 9.3.3. The contour map of the recovered surface gravity anomaly for the wavelet resolution level $J = 1$ (top) and $J = 2$ (bottom). The second order radial derivative of the gravity anomaly data at the satellite altitude $h = 300$ km are arranged on Ground Track B where the ground tracks aligned along the longitude lines are separated by 1.5° .

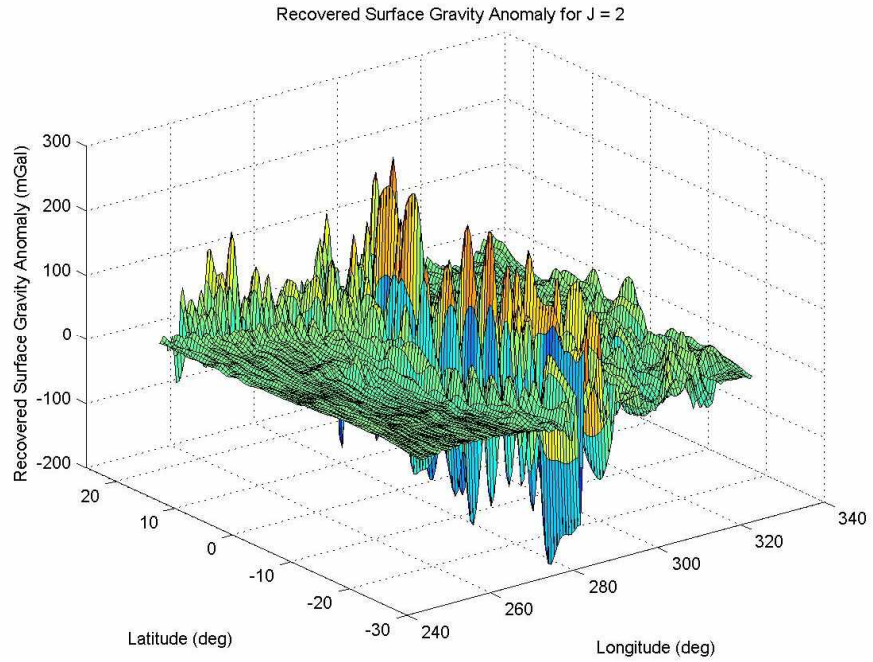
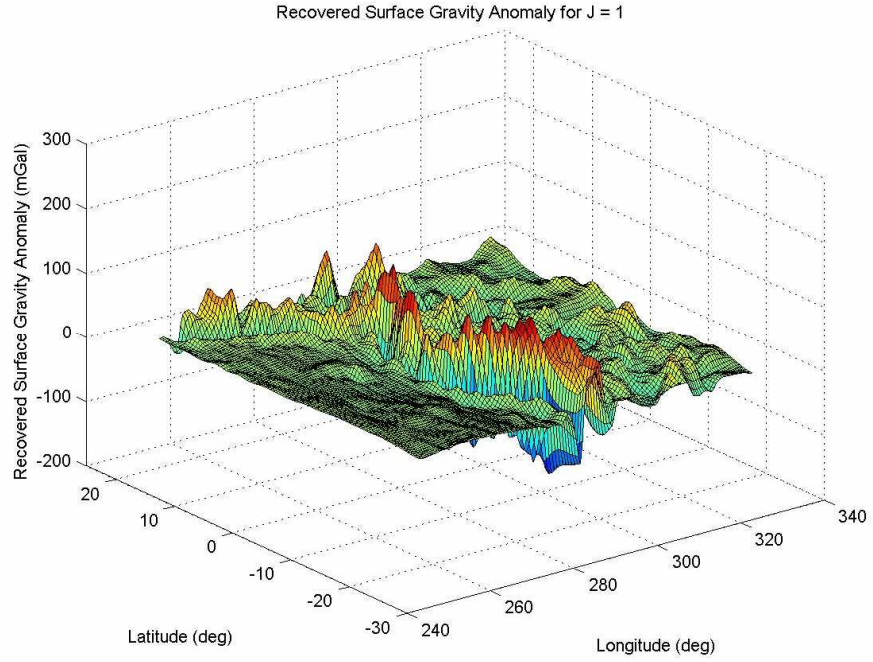


Fig. 9.3.4. 3-D surface map of the recovered surface gravity anomaly for the wavelet resolution level $J = 1$ (top) and $J = 2$ (bottom). The second order radial derivative of the gravity anomaly data at the satellite altitude $h = 300$ km are arranged on Ground Track B where the ground tracks aligned along the longitude lines are separated by 1.5° .

In **Table 9.3.1**, the RMS of the surface gravity anomaly error at the spatial resolution of 0.5° is listed at each wavelet resolution level for the three data sets in our test. As is true with the case when using the direct upward propagated gravity anomaly data, using SGG type data shows that the solution corrupts as the irregularity in the data arrangement increases. As is discussed in **Chapter 7**, the wavelet level of the solution recovered from the SGG type measurement cannot be directly associated with the spatial resolution. We instead applied a mean filter to the gravity solution with the wavelet resolution level yielding the least RMS error (*i.e.* $J = 5$ for the gravity measurements on a regular grid, $J = 3$ for the data arranged along Ground Track A and $J = 1$ along Ground Track B) and compared them to the initial gravity anomaly field at each spatial resolution. **Table 9.3.2** shows the result: The SGG data on a 360×180 regular grid at a 300 km altitude yields the short wavelength gravity solution with the RMS error of 9.2 mGal for the spatial resolution 0.5° and 3.8 mGal for the 1° resolution (Note that it is a far better result to the case in section **9.2**, when direct upward propagated gravity anomaly data was used) and the surface gravity anomaly recovered from the Track A are acceptable as a medium wavelength ($1.5^\circ \sim 3^\circ$) solution, while the result from Track B does not even qualify as a long wavelength solution.

Based on the results from this section as well as the previous one, we have come to the following conclusion: In recovering the surface gravity, the number of data points along one axis is required to be at least half of that along the other for a meaningful solution to be achieved, especially with the SGG type of measurements.

J	$ G - G_J _{RMS}$	$ G - G_J _{RMS}$ Ground Track A	$ G - G_J _{RMS}$ Ground Track B
0	35.46	35.46	35.45
1	24.99	24.99	24.97
2	19.29	19.31	28.07
3	14.87	15.95	154.53
4	12.70	32.63	539.02
5	9.19	1003.55	4584.70
6	9.26	2677.90	9079.93

Table 9.3.1. The RMS error $|G - G_J|_{RMS}$ in mGal for the region of $250.25^\circ \sim 329.75^\circ$ in longitude and $-24.75^\circ \sim 19.75^\circ$ in latitude at a spatial resolution 0.5° , with the second order radial derivative of the gravity anomaly measurement set on a regular grid (left), along Ground Track A (middle) and Ground Track B (right).

Spatial Resolution	$ G - (G_5)_{mean} _{RMS}$	$ G - (G_3)_{mean} _{RMS}$ Ground Track A	$ G - (G_1)_{mean} _{RMS}$ Ground Track B
1.0°	3.80	6.21	17.14
1.5°	3.71	3.27	14.56
2.0°	3.66	2.20	12.93
3.0°	3.52	1.64	11.43
4.0°	3.46	1.16	11.21
5.0°	3.45	1.08	11.10

Table 9.3.2. The RMS error $|G - (G_J)_{mean}|_{RMS}$ in mGal at different spatial resolutions. The gravity solution with the wavelet resolution level yielding the least RMS error in each case ($J = 5$ for the SGG measurement on a regular grid, $J = 3$ along Ground Track A and $J = 1$ along Ground Track B) was smoothed according to the spatial resolution.

Chapter 10. Conclusions and Discussion

Our study shows that the local surface gravity anomaly can be recovered from local gravity measurements at the satellite altitude by the spherical regularization wavelets approximation as a solution to the inverse problem, so long as the input data is arranged on a regular grid. This restriction results from the fact that the solution to the inverse problem takes the convolution form on a spherical surface. It is possible, however, to perform the surface integration on grid points unevenly distributed using Gaussian quadrature or the extended trapezoidal rule with an interpolation scheme, albeit with less accuracy. The regularization of the inverse operator, and hence the employment of regularization wavelets, is essential in solving the inverse problem, as it is ill-posed.

The scale discrete Tikhonov spherical regularization wavelets employed in our model exhibit the characteristics of band pass filters corresponding to the higher frequencies (higher degrees of Legendre polynomials) as the wavelet level increases (see **Fig. 3.2.1** and **Fig. 3.2.2**). The localization property of the wavelets suggests that the higher the wavelet level goes the stronger the localization in scale (see **Fig. 3.2.3** and **Fig. 3.2.4**). This property accounts for the fact that there exists a limit in increasing wavelet level to gain finer details to the recovered signal. When the wavelet's localization goes further than the spatial resolution of the input data itself, the added details become noise, instead of real signal, rendering the solution meaningless. The ill-posed nature of the inverse problem, as well as the computational limits, explains the noise appearing at a slightly lower wavelet level than defined by the localization limit.

When using the upward propagated gravity anomaly at a resolution 0.5° at the altitude of 300 km as simulated input data – where solving the inverse problem becomes a direct downward propagation process – the simulation results from the two different local regions suggest that the local surface gravity anomaly can be recovered at the spatial resolution of 1° with an RMS error of $1 \sim 10$ mGal, depending on the topographic

profile of the gravity field in the region. The error decreases as the spatial resolution becomes coarser, down to $0.5 \sim 2$ mGal at a resolution of 5° . Another notable observation is that the spatial resolution is not the only factor on the recovered gravity solution error. The local nature of the gravity gradients appears to be closely correlated to the achievable accuracy, *i.e.* the higher the magnitude of the gravity gradients, the larger the error. Our investigation of the impact of differing the volume of input data and varying the maximum degree of Legendre polynomials on the accuracy of the recovered gravity solution implies that it is the short wavelength signals and the regions with high magnitude gravity gradients that are most influenced by such alterations.

Our test results from the simulated SGG measurements at the satellite altitude indicate that the gravity solution can be obtained with good accuracy (with RMS error $1 - 7$ mGal at a resolution of 0.7°) by using the relatively detailed at-altitude (hence less ill-posed) SGG signals. The study of the effect of the measurement noise on the recovered gravity anomaly also implies that the SGG solution is less susceptible to measurement errors, attesting to the idea that the SGG type mission would be an ideal choice for implementing our spherical wavelets gravity model. Our study on the impact of the irregularity in the arrangement of the measurement data indicates that the number of data points along one axis is required to be at least half of that along the other for an acceptable solution to be achieved.

As our study focused on recovering the local gravity using only localized data, it became imperative to investigate the local solution of the same region recovered from different sets of input data. Region I and Region II from our simulation share the region of $250.25^\circ \sim 259.75^\circ$ in longitude and $-24.75^\circ \sim 19.75^\circ$ in latitude. Since the latitudinal boundaries in Region II shows large error due to the lack of input data as explained in **Chapter 6**, we concentrated on the region of $250.25^\circ \sim 259.75^\circ$ in longitude and $-19.75^\circ \sim 14.75^\circ$ in latitude for comparison of the both solutions. **Fig. 10.1** shows the contours of the recovered surface gravity anomaly of the overlapping area of Region I and Region II at wavelet level $J = 4$ (equivalent to 1.5° spatial resolution) since it is the highest wavelet level solution with a common regularization parameter.

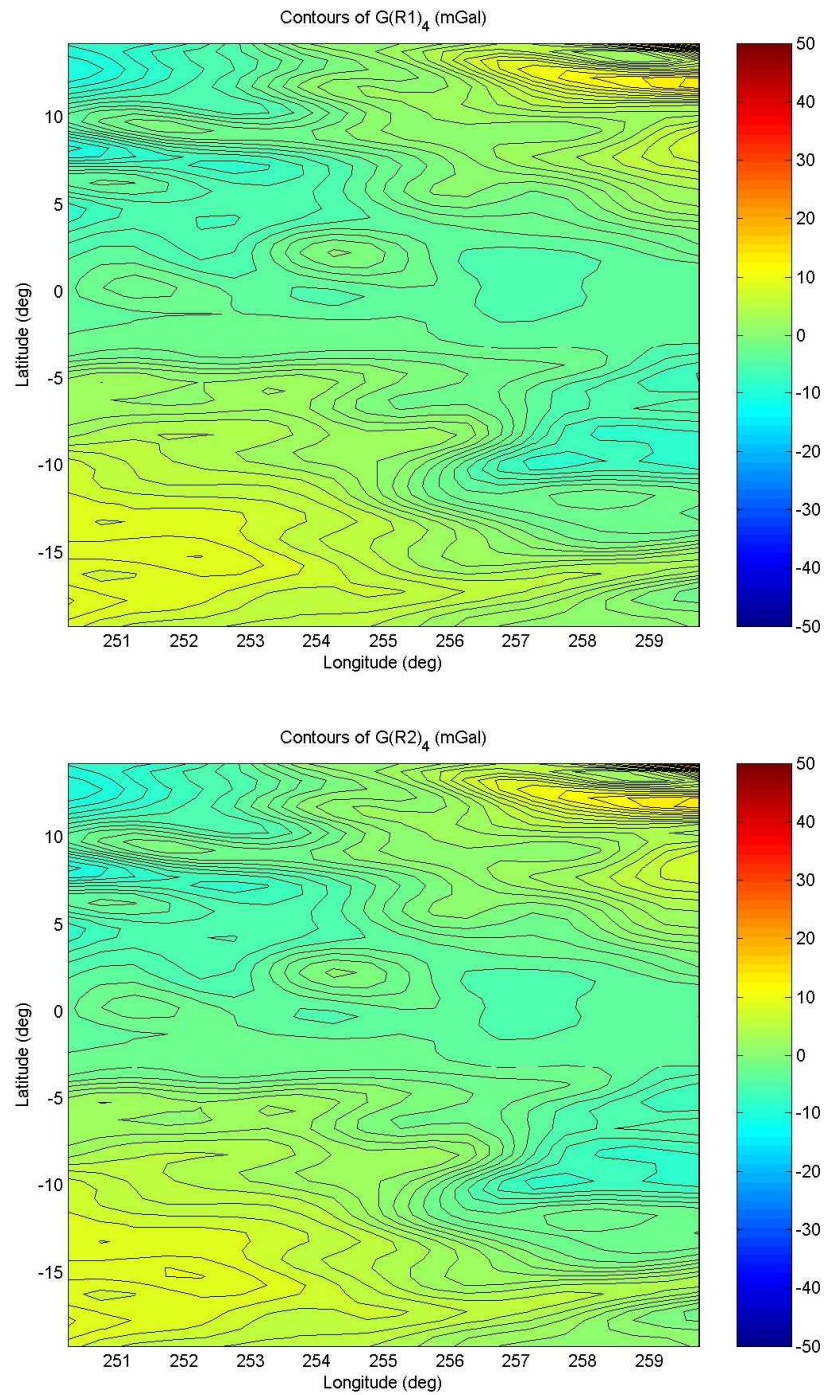


Fig. 10.1. The contours of the recovered surface gravity anomaly of the overlapping area of Region I (top) and Region II (bottom) for the wavelet resolution level $J = 4$ (equivalent to 1.5° spatial resolution). Each contour represents 1 mGal of difference in gravity anomaly.

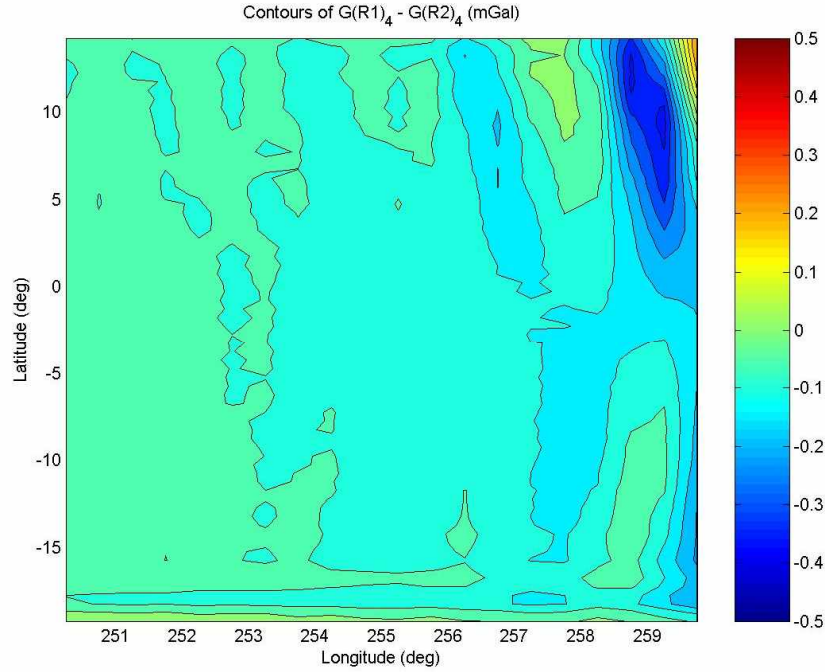


Fig. 10.2. The contours of the surface anomaly difference $G_4(\text{Region I}) - G_4(\text{Region II})$ for the wavelet resolution level $J = 4$. Each contour represents 0.05 mGal gravity anomaly difference.

RMS of Signal $(G_{1.5^\circ})_{RMS}$ at 1.5° spatial resolution	5.03 mGal
Error RMS $ G_{1.5^\circ} - G_{J=4} _{RMS}$ for Region I	8.00×10^{-1} mGal
Error RMS $ G_{1.5^\circ} - G_{J=4} _{RMS}$ for Region II	8.02×10^{-1} mGal
$ G_4(\text{Region I}) - G_4(\text{Region II}) _{RMS}$	9.04×10^{-2} mGal

Table 10.1. The properties of the surface gravity anomaly of the overlapping area (the region of $250.25^\circ \sim 259.75^\circ$ in longitude and $-19.75^\circ \sim 14.75^\circ$ in latitude) for the wavelet resolution level $J = 4$.

Fig. 10.2 shows the contours of the surface gravity anomaly difference $G_4(\text{Region I}) - G_4(\text{Region II})$ for the wavelet resolution level $J = 4$ and **Table 10.1** lists the RMS of the gravity anomaly (from truth data), error RMS for Region I and Region II and the RMS of the gravity anomaly difference between the two solutions for the overlapping area. According to the table, the RMS of the anomaly difference is 0.09 mGal – well below the error range (about 10% of the surface gravity anomaly error). This indicates that the local gravity solution can be obtained with sufficient accuracy despite some differences in the input data, attesting to the validity of our gravity model.

The wavelets model can provide a means to recover the gravity field on a specific local region using only local gravity measurements at the satellite altitude. The accuracy of the solution for long wavelength gravity signals (≥ 500 km), however, might not offer an improvement over an already well-established spherical harmonics gravity model, while the solutions for short wavelength signals (≤ 200 km) could provide finely detailed information of the gravity field which a spherical harmonics model may not be able to recover.

One notable way to improve our spherical wavelets gravity model's accuracy is combining the wavelets solution with a well-established spherical harmonics model such as GGM03C and EGM08 as *a priori*. Instead of using the gravity signal itself as input data, we would utilize the residuals between the actual measurements at the satellite altitude and the upward continued value of the gravity predicted from the well-established gravity model. The solution thus obtained then could be imposed on the surface gravity from the spherical harmonics model as added fine details. Since the error level is somewhat proportional to the amplitude of the signal, using the residuals of gravity measurements will be able to lower the amplitude of the input signal by a considerable amount and the RMS error would be significantly smaller than expected when using the raw signals. The resulting gravity solution could thus provide the short wavelength gravity signals and the fine details missing in the spherical harmonics gravity model.

If we seek to recover the finer scale local gravity field in a much smaller region, *e.g.* $2^\circ \times 2^\circ$, we will need the gravity measurements with very fine resolution at a very low altitude. One of the advantages of the spherical wavelets approach is the capability to support such a mission since only local data is required to recover the gravity field in a target local region. For this purpose, a special aircraft mission can be designed, but this will be left for future study.

Since our model requires radial derivatives of the gravity potential, the satellite mission designed to directly obtain the radial component of the gravity gradients will be the most desirable in implementing our gravity model. The GOCE mission, launched in March 2009, is an SGG mission that seeks to provide global and regional models of the Earth's gravity field with high spatial resolution and accuracy. As is briefly reviewed in **Chapter 8**, the gravity measurements from three pairs of EGG onboard the satellite will provide the radial component of the Earth's gravity gradient tensor after Level 0 and Level 1a/1b processing (Drinkwater *et al.*, 2003). After a 60-day repeat period the satellite's ground track separation will be less than 40 km ($\sim 0.4^\circ$ near the equator), hence ensuring the global coverage in a very fine scale. GOCE aims to recover the Earth's gravity field within the 100 km scale, *i.e.* $\sim 0.9^\circ$ resolution near the equator, with the gravity anomaly error about 1 – 2 mGal (Drinkwater *et al.*, 2007). Our test result using the simulated SGG measurements at a 0.7° resolution at the GOCE satellite's orbit altitude of 250 km (see **Table 10.2** – **Table 10.5**) shows 1 – 5 mGal of gravity anomaly error at a spatial resolution 0.7° (< 80 km on the equator). When the Gaussian noise was imposed on the measurement data, RMS error increases slightly to 1 – 6 mGal for 0.5% Gaussian noise and 2 – 7 mGal for 1.0% noise. Considering these results and the fine spatial resolution of the gravity gradients data expected from the GOCE ground track profile ($\sim 0.5^\circ$), the resulting gravity solution from our spherical wavelets model will be able to meet or exceed the GOCE mission aim.

Presented in **Table 10.2** to **Table 10.5** are the RMS errors of the local gravity anomaly recovered from the simulated SGG measurements at a 0.7° resolution at the satellite altitude of 250 km (GOCE satellite's mean orbit altitude) encompassing the local region of $159.65^\circ \sim 20.00^\circ$ in longitude (counterclockwise) and $-46.93^\circ \sim 42.72^\circ$ in latitude. The regularization used in the simulation are $\gamma_0 = 1.0 \times 10^{-12}$, $\gamma_1 = 7.0 \times 10^{-13}$, $\gamma_2 = 5.0 \times 10^{-13}$, $\gamma_3 = 2.0 \times 10^{-13}$, $\gamma_4 = 1.5 \times 10^{-13}$, $\gamma_5 = 1.0 \times 10^{-13}$ and $\gamma_6 = 9.0 \times 10^{-14}$. The maximum degree of the Legendre polynomials N was set to be 300.

J	$ G - G_J _{RMS}$	$ G - G_J _{RMS}$ with 0.5% Gaussian noise	$ G - G_J _{RMS}$ with 1.0% Gaussian noise
0	12.20	12.19	12.19
1	10.18	10.18	10.18
2	8.52	8.52	8.53
3	4.99	5.06	5.27
4	4.09	4.27	4.74
5	3.55	4.05	5.21
6	3.70	4.30	5.66

Table 10.2. The RMS surface gravity anomaly error $|G - G_J|_{RMS}$ in mGal for the region of $250.18^\circ \sim 330.18^\circ$ in longitude and $-24.51^\circ \sim 20.31^\circ$ in latitude, with zero, 0.5% and 1.0% Gaussian random noise respectively imposed on the satellite measurements.

J	$ G - G_J _{RMS}$	$ G - G_J _{RMS}$ with 0.5% Gaussian noise	$ G - G_J _{RMS}$ with 1.0% Gaussian noise
0	18.35	18.34	18.33
1	15.41	15.39	15.38
2	13.06	13.04	13.03
3	7.88	7.89	7.99
4	6.43	6.52	6.81
5	5.39	5.76	6.67
6	5.55	6.03	7.14

Table 10.3. The RMS surface gravity anomaly error $|G - G_J|_{RMS}$ in mGal for the sub-region of $278.25^\circ \sim 299.75^\circ$ in longitude and $-24.75^\circ \sim 19.75^\circ$ in latitude: the region with high gravity gradients profile, with zero, 0.5% and 1.0% Gaussian random noise.

J	$ G - G_J _{RMS}$	$ G - G_J _{RMS}$ with 0.5% Gaussian noise	$ G - G_J _{RMS}$ with 1.0% Gaussian noise
0	9.98	9.99	9.99
1	8.00	8.01	8.02
2	6.15	6.16	6.19
3	2.55	2.69	3.07
4	2.06	2.38	3.16
5	2.24	2.97	4.45
6	2.47	3.32	4.99

Table 10.4. The RMS surface gravity anomaly error $|G - G_J|_{RMS}$ in mGal for the sub-region of $304.25^\circ \sim 329.75^\circ$ in longitude and $-14.75^\circ \sim 19.75^\circ$ in latitude: the region with moderate gravity gradients, with zero, 0.5% and 1.0% Gaussian random noise.

J	$ G - G_J _{RMS}$	$ G - G_J _{RMS}$ with 0.5% Gaussian noise	$ G - G_J _{RMS}$ with 1.0% Gaussian noise
0	2.62	2.62	2.63
1	2.34	2.34	2.37
2	1.86	1.88	1.95
3	1.10	1.38	2.01
4	0.92	1.48	2.50
5	1.02	2.06	3.74
6	1.17	2.31	4.18

Table 10.5. The RMS surface gravity anomaly error $|G - G_J|_{RMS}$ in mGal for the sub-region of $250.25^\circ \sim 275.25^\circ$ in longitude and $-20.75^\circ \sim 4.75^\circ$ in latitude: the region with low gravity gradients, with zero, 0.5% and 1.0% Gaussian random noise.

As our model proves its capability to recover the fine scale local gravity solution, it is natural to speculate whether it can detect the time-varying gravity anomaly and water mass changes. The water mass variability in particular regions such as the Amazon Basin has been of great scientific interest. To investigate this prospect, we evaluated the error-to-signal ratio of the Region I with the gravity solution obtained from simulated SGG gravity measurements at GOCE satellite's mean altitude of 250 km. **Fig. 10.3** shows the distribution of error-to-signal ratio for the solution with the wavelet level $J = 4$, where the mean value of the error-to-signal ratio is the minimum. Although it is not as straightforward as the relation between the surface anomaly error and the magnitude of the gravity gradients, error-to-signal ratio also displays a certain degree of correlation with the gravity gradients – the region with high gravity gradients tends to yield high error-to-signal ratio.

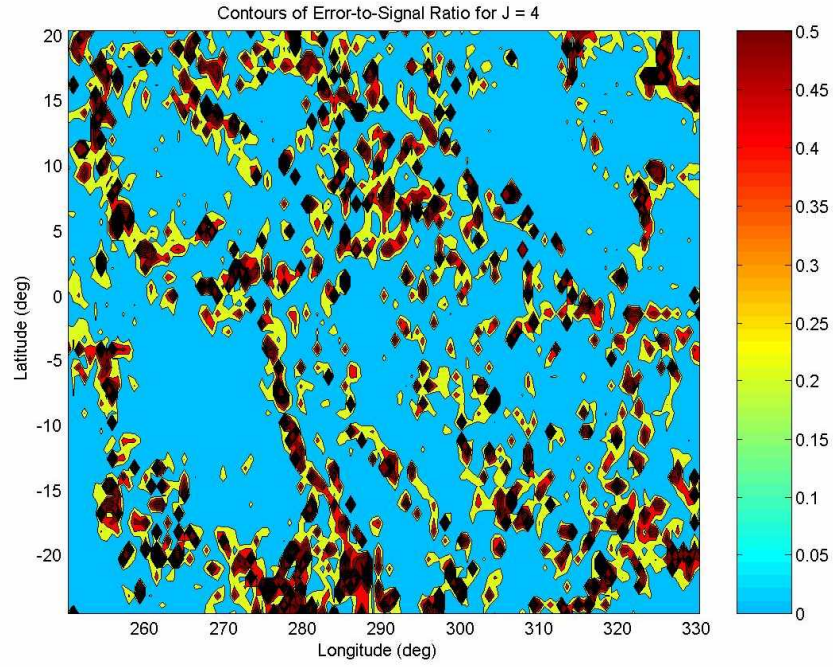


Fig. 10.3. The contours of the error-to-signal ratio for Region I at a 0.7° spatial resolution with the wavelet resolution level $J = 4$.

$\frac{ G - G_{J=5} _{RMS}}{ G _{RMS}}$ for the overall region	0.11
$\frac{ G - G_{J=4} _{RMS}}{ G _{RMS}}$ for the Pacific Ocean	0.07
$\frac{ G - G_{J=5} _{RMS}}{ G _{RMS}}$ for the Amazon Basin	0.11
$\frac{ G - G_{J=4} _{RMS}}{ G _{RMS}}$ for the Amazon River	0.09

Table 10.6. The ratio of RMS error to RMS of signal in different regions.

Table 10.6 provides the ratio of RMS error to RMS value of the signal for the chosen regions at a 0.7° spatial resolution, *i.e.* less than 80 km scale: the Pacific Ocean ($255^\circ \sim 270^\circ$ in longitude, $-15^\circ \sim 5^\circ$ in latitude), the Amazon Basin ($290^\circ \sim 310^\circ$ in longitude, $-15^\circ \sim 0^\circ$ in latitude) and the Amazon River vicinity ($290^\circ \sim 305^\circ$ in longitude, $-5^\circ \sim 0^\circ$ in latitude). The ratios were computed from the gravity solution with the wavelet level yielding the least RMS error for each region. According to the table, the error-to-signal ratio is about 10% of the magnitude of the signal in most of the regions, except the Pacific Ocean where the ratio is down to 7%. This result implies that the gravity changes (whether seasonal or inter-annual) less than 10% of the gravity signal cannot be validly detected with our model. For the Amazon Basin, the RMS of the surface gravity anomaly is 25 mGal indicating the gravity change less than 2.5 mGal on 80 km scale is undetectable using our solution. With the spherical harmonics gravity model, GRACE satellites could capture the changes in ground water with an accuracy of $0.4 \mu\text{Gal}$ on the spatial scales longer than 1300 km (Anderson and Hinderer, 2005). The Amazon Basin is one of the regions with largest inter-annual gravity changes ($> 1 \mu\text{Gal}$) on that scale. Although we cannot directly compare GRACE's large-scale gravity solution to our model's fine-scale one, the criteria of 10% signal RMS seems too large for the realistic gravity changes despite the fact that the gravity changes on 80 km scale will be considerably larger than $1 \mu\text{Gal}$ on 1300 km scale. However, there still exists a possibility that our model is capable of discerning fine-scale gravity changes in regions with very large water mass change if we can lower the error significantly by employing *a priori* solution as mentioned previously in this chapter. Further study on this subject will be explored.

Although our spherical regularization wavelets gravity model shows its strength in recovering local gravity on a fine scale, it must be pointed out that the downward propagation process in some way deteriorates the gravity measurements taken at satellite altitude due to its ill-posed nature, which means the surface gravity solution is not as accurate as the at-altitude gravity measurements. Spherical harmonics gravity model, on the other hand, is free from this effect for it can compute the spherical harmonics

coefficients that best fit the orbit elements of the satellite at its altitude, fully capable of utilizing the integrity of the measurement data. This is one of the advantages of spherical harmonics approach over our spherical wavelets method and must be taken into account in comparing the two different approaches regarding the determination of the gravity field.

As previously mentioned, the most ready application of our model will be toward the SGG measurements from GOCE satellite. The six accelerometers on board GOCE satellite can provide three components of the second derivative gravity gradients tensors (second order derivatives of gravity potential). Our gravity model takes the radial component of the tensors as input in solving the inverse problem. The other two components whose magnitude is not as significant as their radial counterpart, however, contain the regional non-radial topographic information of the gravity field. A possible means to utilize these non-radial components of the gravity tensors is to exploit them to impose local corrections on the surface gravity solution obtained from the radial component. Further study in this prospect will be left for the future work.

Using the spherical wavelets gravity model, we could recover the local gravity anomaly to a fine level of spatial resolution on the order of a hundred kilometers or less ($\leq 1^\circ$). The model also exhibits superior performance in edge detection by accurately modeling the boundaries between the ocean and a sea cliff. With its capability in recovering fine resolution gravity signals using only localized gravity measurements, the application potential of our spherical wavelets gravity model is extensive, including determination of the surface gravity potential and anomaly at finer scales than could be achieved by a spherical harmonics model approach. Future study will be pursued to apply our wavelet solution in conjunction with the spherical harmonics model to GOCE's EGG data in support of increasing the accuracy of our knowledge of the Earth's gravity field.

BIBLIOGRAPHY

- Anderson, O. B. and J. Hinderer, *Global Inter-Annual Gravity Changes from GRACE: Early Results*, Geophysical Research Letters, 32, L01402, 2005
- Bettadpur, S. and M. Watkins, *GRACE Gravity Science & Its Impact on Mission Design*, Presentation in the AGU 2000 Spring Meeting, GP51C-11, 2000
- Beylkin, G. and R. Cramer, *Toward Multiresolution Estimation and Efficient Representation of Gravitational Fields*, Celestial Mechanics and Dynamical Astronomy, v. 84, 1, 87-104, 2002
- Daubechies, I., *Ten Lectures on Wavelets*, CBMS-NSF Regional Conference Series in Applied Mathematics, 61, SIAM, Philadelphia, 1992
- Daubechies, I. and A. Gilbert, *Harmonics Analysis, Wavelets and Applications in Hyperbolic Equations and Frequency Interactions*, Luis Cafarelli and Weinan E, eds., IAS/Park City Mathematics Series, Vol. 5, 1998
- Drinkwater, M. R. and M. Kern, *GOCE Calibration & Validation Plan for L1b Data Products*, GOCE Project Technical Report EOP-SM/1363/MD-md, Issue 1.2, 2006
- Drinkwater, M. R., R. Floberghagen, R. Haagmans, D. Muzi and A. Popescu, *GOCE: ESA's First Earth Explorer Core Mission*, Space Science Reviews, 108, 419-432, 2003
- Drinkwater M. R., R. Haagmans, D. Muzi, A. Popescu, R. Floberghagen, M. Kern and M. Fehringer, *The GOCE Gravity Mission: ESA's First Core Earth Explorer*, Proceedings of 3rd International GOCE User Workshop, pp. 1-8, 6-8 November, 2006, Frascati, Italy, ESA SP-627, 2007
- Èskin, G. I., *Boundary Value Problems for Elliptic Pseudo-differential Equations*, Translations of Mathematical Monograph, 52, American Mathematical Society, Providence, Rhode Island, 1981
- Freeden, W., *Über eine Klasse von Integralformeln der Mathematischen Geodäsie*, Veröff. Geod. Inst. RWTH Aachen, Heft, Germany, 1979

- Freeden, W. and U. Windheuser, *Spherical Wavelet Transform and Its Discretization*, Advances in Computational Mathematics, 5, 51-94, 1996
- Freeden, W. and U. Windheuser, *Combined Spherical Harmonic and Wavelet Expansion – A Future Concept in Earth's Gravitational Determination*, Applied and Computational Harmonic Analysis, 4, 1-37, 1997
- Gilbert, J., Personal Communication, 2001
- Grossman, A. and J. Morlet, *Decomposition of Hardy Functions into Square-integrable Wavelets of Constant Shape*, SIAM Journal of Mathematical Analysis, 15, 723-736, 1984
- Kaiser, G., *A Friendly Guide to Wavelets*, Birkhäuser, Boston, Basel, Berlin, 1994
- Louis, A. K., *Inverse und schlecht gestellte Probleme*, B. G. Teubner, 1989
- Mallat, S. G., *A Theory for Multiresolution Signal Decomposition: The Wavelet Representation*, IEEE Transactions on Pattern Analysis and Machine Intelligence, v. 11, n. 7, 674-693, 1989
- Meyer, Y., *Wavelets and Operators*, Cambridge University Press, Cambridge, England, 1993
- Morozov, V. A., *The Error Principle in the Solution of Operational Equations by the Regularization Method*, USSR Computational Mathematics and Mathematical Physics, 8, 2, 63-87, 1966
- Müller, C., *Spherical Harmonics*, Lecture Notes in Mathematics, 17, Springer-Verlag, Berlin, Heidelberg, New York, 1966
- National Imagery and Mapping Agency, *Department of Defense World Geodetic System 1984, Its Definition and Relationships With Local Geodetic Systems*, NIMA Technical Report TR8350.2, Third Edition, Amendment 1, 2000
- Press, W., B. Flannery, S. Teukolsky and W. Vetterling, *Numerical Recipes*, Cambridge University Press, Cambridge, England, 1986
- Schneider, F., *Inverse Problems in Satellite Geodesy and Their Approximate Solution by Splines and Wavelets*, Dissertation, Universität Kaiserslautern, Shaker Verlag, Germany 1997

Seeber, G., *Satellite Geodesy: Foundations, Methods and Applications*, Walter de Gruyter, Berlin, 2003

Svensson, L., *Pseudo-differential Operators – a New Approach to the Boundary Value Problems of Physical Geodesy*, *Manuscripta Geodaetica*, 8, 1-40, 1983

Tapley, B., J. Ries, S. Bettadpur, D. Chambers, M. Cheng, F. Condi, B. Gunter, Z. Kang, P. Nagel, R. Pastor, T. Pekker and F. Wang, *GGM02 – An Improved Earth Gravity Field Model from GRACE*, *Journal of Geodesy*, 79, 467-478, 2005

Tapley, B., Personal Communication, 2008

Vermeer, M., *Observation Equations For SST And SGG*, Technical Report, National Survey and Cadastre of Denmark, 1989

VITA

Harrey Jeong Shuler was born in October, 1970, in Seoul, Korea. Upon graduating from Young-Dong Girls' High School in 1989, she entered Seoul National University in Seoul, Korea, where she received the degree of Bachelor of Science in Astronomy in February, 1993. During the years 1993 and 1994 she attended the Graduate Programs in the College of Natural Sciences at Seoul National University and earned the degree of Master of Science in Astronomy in February, 1995. After teaching math and physics at several institutes during the following years, she moved to the United States to pursue her study in Aerospace Engineering at The University of Texas at Austin in 1998, where she met her future spouse. She married Andrew Shuler in April, 2001, in Austin, and was admitted to candidacy for the doctoral degree in Aerospace Engineering in June, 2002. She gave birth to her son Jeremy in December, 2003, in Austin. The author currently resides in Dallas, Texas, with her family.

Permanent address: 6975 Regatta Dr., Grand Prairie, TX 75054

This dissertation was typed by the author.